CITY-SCALE MODELLING OF FACTORS AFFECTING URBAN PLUVIAL FLOOD HAZARD IN RAPIDLY DEVELOPING CITIES USING GLOBAL DATA

Victor Olajubu

Submitted in accordance with the requirements for the degree of
Doctor of Philosophy

The University of Leeds

Water & Public Health Engineering (WPE)
School of Civil Engineering

July 2022

The candidate confirms that the work submitted is his/her own and that appropriate credit has been given where reference has been made to the work of others.

Or (in those cases where work which has formed part of ***jointly****-authored publications has been used to form the basis of a chapter or chapters):*

The candidate confirms that the work submitted is his/her own, except where work, which has formed part of jointly authored publications, has been included. The contribution of the candidate and the other authors to this work has been explicitly indicated below. The candidate confirms that appropriate credit has been given within the thesis where reference has been made to the work of others.

(i). The chapter of the thesis based on work from jointly-authored publications is

Chapter 4.

The publication details are as follows:

Olajubu, V., Trigg, M., Berretta, C., Sleigh, A., Chini, M., Matgen, P., Mulligan. J., Mojere, S., 2020. Earth Science Informatics (Springer Journal). Urban correction of global DEMs using building density for Nairobi, Kenya. (details TBC).

(ii) The following aspects of the publication are attributable to me: hypothesis, aims & objectives, writing of methods, results and discussion.

The co-authors reviewed all aspects of the paper prior to publication and provided comments, which I acted upon to develop the paper.

AKNOWLEDGEMENTS

I would first like to take this opportunity to first thank the Sovereign God for giving me the strength, health, knowledge, ability, and opportunity to undertake this research and to persevere and complete it satisfactorily.

I would like to thank my supervisors Dr. Mark Trigg, Dr. Christian Berretta and Dr. Andrew Sleigh for their help, advice, invaluable supervision, support, and tutelage during the course of my PhD degree.

I would particularly like to single out my supervisor, Dr. Mark Trigg. Mark, I want to thank you for your treasured support which was influential and invaluable in shaping the research questions, methodology and critiquing my results. You provided me with the tools that I needed to choose the right direction. Your insightful feedback pushed me to sharpen my thinking and brought my work to a higher level. From the first meeting I had with you in the fall of 2016, precisely October the 17th and the first *"hi Victor"* that followed, it has been an incredible journey. I have been extremely lucky to have a supervisor who cared so much about my work, responded to my questions and queries so promptly, and who took interest in my family, career and wellbeing.

Finally, I am forever indebted to Theo Henderson, to my family and friends, and especially Modupe, for her understanding, support, endless patience, and encouragement throughout my time as a student at the University of Leeds.

ABSTRACT

Flooding is the most prevalent disaster worldwide accounting for 43% of all recorded global disaster events in the past 20 years leading up to 2018 Choy (2018). While migration from rural settlements to urban areas often mirrors economic advancement, it also presents socioeconomic and environmental challenges. Rapid urban growth strains existing infrastructure and also discourages the preservation of natural habitat in favour of building more developments causing urban flooding. Climate change and urbanisation have been reported as the major contributors to the increasing damaging effects of flooding to lives and livelihoods worldwide (Aerts et al., 2014). There is lack of adequate research focused on the dual impacts of climate change and urbanisation on urban flooding and water quality in rapidly developing urban areas of the world – a gap that will result in an increase in fluvial and pluvial flood risk, and further reduction in water quality (Miller and Hutchins, 2017).

This study highlights the importance of the use of free global datasets in the development of a city-scale 2D hydraulic model that assesses the impact of land use change and climate change on urban pluvial flooding in rapidly developing cities. This thesis presents three key results chapters assessing the ability of a simplified city-scale hydrological and hydraulic models to estimate urban pluvial flood inundation in a large catchment, before going on to establish the impacts of climate change and land use change on flood hazard. Topography has been identified as a key dataset of estimating flood extent (Horritt and Bates, 2001) and models of flood extent rely on DEMs in order to simulate paths of water flow, flood extent and depth. Errors in Digital Elevation Models (DEMs) can substantially affect the results of flood models (Stephens et al., 2012, Hawker et al., 2018).

Therefore, in order to increase the accuracy of the outputs from the hydrological and hydraulic models used in this study, a methodology for the correction of building error in DEMs was developed in Chapter 4 for removing building elevation artefacts from six global DEMs namely: (i) NASADEM, (ii) SRTM, (iii) MERIT, (iv) ALOS, (v) TanDEM-X 12 m, and (vi) TanDEM-X 90 m. The findings show that the removal of building elevation artefacts/error from global DEMs resulted in the improvement of the vertical height accuracy of global DEMs. The findings show that building density has an influence on vertical accuracy of global digital elevation models (DEMs).

This finding was a key step prior to research undertaken in subsequent chapters. In chapter 5, a city-scale hydrological and hydraulic model of the Nairobi catchment is built. The purpose of creating the models is to use the raw DEM and corrected global DEM derived in Chapter 4 to estimate the impact of land use change and climate change on urban pluvial flood hazard at city-scale level using global datasets.

The HEC-RAS software is used to create five categories of models for the extreme rainfall event of 1st to 13th of March 2018; a baseline model (S1-Baseline), S2-2000LU model, S3-CP4uplift model, S4-P25uplift model, and the S5-RawDEM model. The five sets of models are created in 2D and make use of the diffusive wave equation for simplification. The results showing a lot of promises by providing evidence for the hypothesis that urban flood models built at city-scale level using free global datasets have a good level of skill and are proficient enough to accurately estimate urban flood inundation depth and extent in rapidly developing cities characterised by sparsity of data.

Chapter 6 discusses the results of the flood inundations and flood hazard vulnerability maps from the HEC-RAS 2D hydraulic model under 5 different scenarios. It is found that topography plays an important role in flood inundation maps and that the accuracy of flood inundation maps can be improved simply by using urban corrected DEMs over raw DEMs as key input data when conducting both hydrological and hydraulic modelling. The findings also show that urban pluvial flooding is affected by both change in climate change and land use change, however, climate change is found to contribute significantly to surface water runoff and exacerbate the problems of urban flooding. The results also show that the baseline model using the urban corrected DEM as input data produced flood inundation and flood hazard vulnerability maps with better accuracy in comparison to a similar baseline model using the raw DEM as key input data.

Chapter 7 further explored the influence of climate change and land use change that is due to rapid urbanization on urban pluvial flood hazard. Chapter 7 focuses on the synthesis of the results obtained from the results of the 5 set of 2D hydraulic models discussed in chapter 6. Results demonstrated that climate change had more influence on urban pluvial flood hazard than land use change. It is found that climate change, rather than land use change is a bigger threat to urban area in terms of flood risk. Specifically, the effects induced by climate change under the CP4 and P25 climate rainfall models are much higher than the effects induced by land use change due to urbanisation in Nairobi from 2000 to 2020.

The findings show that the changes caused by current and future changes in rainfall intensities and frequencies are most likely to render most large urban areas vulnerable to extreme rainfall and pluvial flooding due to lack of resilience in existing drainage infrastructure and flood mitigation systems. Assessment of land use changes alone cannot fully account for hydrological and hydraulic alterations in the urban context and it is important for policy makers and people with responsibilities for managing urban flood risks to consider adaptation and mitigation strategies that considers increasing threat of urban flooding emanating from increased runoff from climate change rainfall.

This thesis has subsequently enhanced our understanding of the value of free global hydrological and hydraulic models developed at city-scale to model the impacts of climate change and land use change on urban pluvial flood hazard in data-sparse context of rapidly developing cities where availability of high-quality data for urban flood studies are a rarity. Finally, one of the key findings of this study is that in the context of conducting urban flood modelling in data sparse regions in rapidly developing cities across the world, it is possible to leverage the opportunities provided by the growing availability of free, global datasets to develop urban flood models. Traditional urban flood models rely on the use of high-quality datasets as key input data and require computers with high computational efficiency to run detailed flood inundation models. Most importantly, the study has demonstrated that it is possible to achieve a trade-off between complexity and resolution by the use of simplified 2D hydraulic flood models that use global dataset as key input data.

Table of Contents

1.0 INTRODUCTION 23

1.1 Background 23

1.2 Significance of this study 24

1.3 Research Aims and Objectives 24

Aim 1: 24

Aim 2: 25

Aim 3: 25

To build and test a city scale urban pluvial flood model with global datasets using Nairobi as a test city. 25

Aim 4: 26

1.4 Thesis structure 26

2.0 LITERATURE REVIEW 28

2.1 Global flood model data scarcity challenge 28

2.2 Urbanization, land use change and pluvial flooding 29

2.3 Climate change and urban flooding 31

2.4 Global Digital Elevation Models (DEMs) and correction 33

2.5 Urban flood models 35

2.6 Summary 37

3.0 METHODS & DATA 41

3.1 Introduction 41

3.2 Urban Flood Modelling Tools 42

3.3 2D Hydrodynamic Model Choice 42

Criteria for Choice of Model 43

3.4 Shallow Water Equation Based Models 44

3.5 HEC-RAS Hydrodynamic Model for Surface Water Runoff 44

3.6 HEC-HMS Hydrologic Model 51

3.7 The March 2018 Rainfall Events 52

3.8 Weighted Average Curve Number 52

3.9 Model Validation 53

3.10 Extension of Controls and Topographic/Levelling Survey 53
3.11 CP4 & P25 Africa Rainfall Models 54
3.12 Summary 56
4.0 URBAN CORRECTION OF GLOBAL DEMS 59
4.1 Introduction 59
4.2 Study Site 61
4.3 Dataset Description 63
4.4 Global DEMs 64
4.5 Facebook High Resolution Settlement Layer (HRSL) Data 66
4.6 Sentinel-1 SAR Data Derived Global Building Map 67
4.7 Reference Topography Relief Map Data 67
4.8 Methodology 67
4.9 Procedure for urban correction of global DEMs 67
5.0 Results and Discussion 73
5.1 Distribution of Vertical Errors 73
5.2 DEM Error and Building Density Relationships 75
5.3 Analysis of DEM error versus building density relationships for Kibera slum area and Embakasi residential area. 80
5.4 Summary 86
6.0 CITY-SCALE MODELLING OF THE NAIROBI CATCHMENT 88
6.1 Hydrologic Modelling System (HEC-HMS) of the Study Area 89
6.2 The March 2018 Rainfall Events 92
6.3 Weighted Average Curve Number 92
6.4 Pre-processing of Raster Data 93
6.5 Reclassification of Land use map 94
6.6 Combination of Land use and HSG soil group raster files 94
6.7 Net / excess rainfall values from HEC-HMS 94
6.8 HEC-RAS 2D Hydraulic Model Computational Setting 96
6.9 Watershed and Stream Network Delineation 98

6.10 Flood Hazard Assessment 105

7.0 SCENARIO ANALYSIS 110

7.1 Land use change and Climate change impact scenario analysis 113

7.2 Urban Land Use Transition 117

7.3 Hazard Vulnerability Classification of Land Use Change and Climate Change 123

7.4 CREATION OF ADDITIONAL SIX MODEL SIMULATION SCENARIOS USING URBAN CORRECTED GLOBAL AND LOCAL DEMs. 129

JICA Reference DEM Model 130

SRTM DEM Model. 130

ALOS DEM Model 130

NASA DEM Model 131

TanDEM-X 12m DEM Model 131

TanDEM-X 90m DEM Model 131

7.5 Model Validation 146

7.6 Survey errors 147

8.0 SYNTHESIS OF RESEARCH FINDINGS 153

8.1 Work on Urban Correction of Global DEM and Impacts on Urban Flood Modelling. 153

8.2 Impacts of Land use change on Pluvial Flooding. 159

8.3 Impacts of climate change on urban pluvial flooding 165

8.4 Discussion of study in the context of wider literature 170

8.5 Summary 173

9.0 CONCLUSIONS AND RECOMMENDATIONS 176

9.1 Reflection of study objectives 179

9.2 Summary 180

9.3 Research contribution to science and literature 180

9.4 Computational efficiency of 2D city-scale hydraulic flood models that use global datasets as key input data. 180

9.5 Urban correction of global DEMs 181

9.6 Contribution to thinking around urban flood projections using future climate change precipitation dataset 181

9.7 Quantification of Vulnerability of People and Built Environment to Urban Flood Hazard 182

9.8 Study Limitations and Recommendations for Future Research 183

10.0 REFERENCES 186

11.0 LIST OF APPENDICES 195

List of Figures

Figure 1. A concept of trade-off between bias (grey) and uncertainty (black) in model complexity. Adapted from (Di Baldassarre, 2012a.). 44

Figure 2. Map of the study area showing Nairobi 62

Figure 3. Difference between DSM and DTM (both DEMs) 63

Figure 4. Visual comparison of the six global DEMs, applied in Nairobi. 64

Figure 5. Flowchart of the datasets and methodology used to correct building density errors in global DEMs in our five-step method. This can be applied to any spatial extent. 68

Figure 6. Error map of global DEMs at 90 m resolution 69

Figure 7. Building density raster of Nairobi derived from (a) the Facebook HRSL population density map, and (b) global urban building map. 71

Figure 8. Map of the Central Business District (CBD), Nairobi 72

Figure 9. Comparison of density distribution plots for the six global DEMs: ALOS (AW3D30), SRTM, MERIT, NASADEM, TanDEM-X 12m, and TanDEM-X 90 m 74

Figure 10. Scatter plots of building density with DEM error, with superimposed linear regression lines of best fit for the tested global DEMs, applied to Nairobi: (a) ALOS; (b) SRTM; (c) MERIT; (d) NASADEM; (e) TanDEM-X 12 m and (f) TanDEM-X 90. 78

Figure 11. (a) Building density error raster for SRTM DEM, (b) urban-corrected SRTM DEM. 78

Figure 12. Scatter plots of building density with DEM error, with superimposed linear regression lines of best fit for the tested global DEMs, applied to Central Business District (CBD): (a) ALOS; (b) SRTM; (c) MERIT; (d) NASADEM; (e) TanDEM-X 12 m 79

Figure 13. Map of the Kibera slum area of Nairobi city 81

Figure 14. Map of the Embakasi residential area of Nairobi city 81

Figure 15. Scatter plots of building density with DEM error, with superimposed linear regression lines of best fit for the tested global DEMs, applied to Central Business District (CBD): (a) ALOS; (b) SRTM; (c) MERIT; (d) NASADEM; (e) TanDEM-X 12 m 83

Figure 16. Scatter plots of building density with DEM error, with superimposed linear regression lines of best fit for the tested global DEMs, applied to the Kibera slum area of Nairobi city: (a) ALOS; (b) SRTM; (c) MERIT; (d) NASADEM; (e) TanDEM-X 12 m 84

Figure 17. Scatter plots of building density with DEM error, with superimposed linear regression lines of best fit for the tested global DEMs, applied to the Embakasi residential area of Nairobi city: (a) ALOS; (b) SRTM; (c) MERIT; (d) NASADEM; (e) TanDEM-X 12 m 85

Figure 18. Six-step method flowchart of the datasets and methodology used to create the five model scenarios (S1-Baseline, S2-2000LU model, S3-CP4uplift model, S4-P25uplift model, and the S5-RawDEM model.) using HEC-HMS and HEC-RAS software. 89

Figure 19. Typical representation of watershed runoff within the HEC-HMS hydrologic model (U.S. Army Corps of Engineering, 2016) 90

Figure 20. A screenshot from the HEC-HMS hydrologic model showing the sub-basins and reach of the Nairobi catchment. 95
Figure 21. Five-step method flowchart of the datasets and methodology used to create the five model scenarios (S1-Baseline, S2-2000LU model, S3-CP4uplift model, S4-P25uplift model, and the S5-RawDEM model.) using the software. 96
Figure 22. A screenshot from the HEC-RAS model showing the set-up of the 2D flow area boundary used for the five model scenarios. 97
Figure 23. 2D flow area computational points created within the HEC-RAS model. 97
Figure 24. Computational settings used in the HEC-RAS 2D hydraulic simulation model. 98
Figure 25. Advance time step settings used in the HEC-RAS 2D hydraulic simulation model. 98
Figure 26. A screenshot from QGIS software environment showing the Strahler order of each stream segment, sub-watershed draining into each stream segment (reach). 99
Figure 27. Delineated Watershed and Stream Network of Study Area 100
Figure 28. A screenshot from the HEC-RAS hydraulic model software of the land cover data types, Manning's roughness coefficient values data for the 2008 & 2018 land maps for the study area and their respective Manning's value. 104
Figure 29. A screenshot from the HEC-RAS 2D hydraulic model of the Manage Layer Association showing the association of Land Cover/Manning's n layer with a specific Geometry data set. 104
Figure 30. Combined flood hazard curve developed by (Smith et al., 2014). 106
Figure 31. The Australian Rainfall and Runoff guidelines raster calculator script (Smith et al., 2014), 2014) used for the calculation of flood hazard mapping in the HEC-RAS model. 107
Figure 32. Rainfall hydrographs for the five sets of models (S1-Baseline, S2-2000LU, S3-CP4uplift, S4-P25uplift and S5-RawDEM) developed in this study for the 1st to 13th March rainfall evens of 2018. 110
Figure 33. A screenshot from QGIS software of the overall catchment area (C1) used in the model. 111
Figure 34. A screenshot from QGIS software of the Kiambu sub-catchment area (C2) used in the model. 112
Figure 35. A screenshot from QGIS software of the Nairobi district sub-catchment area (C3) used in the model. 112
Figure 36. A screenshot from the QGIS software of the Machakos sub-catchment area (C4) used in the model. 112
Figure 37. A screenshot showing the results of the various type of inundation maps (Depth(max), Velocity(max), Water Surface Elevation, WSE(max), D*V(max), and Flood Hazard Maps) generated using the RAS Mapper within the HEC-RAS software application. 113
Figure 38. A screenshot from the HECRAS model of flow hydrograph for C1 outlet to River Athi. 114
Figure 39. A screenshot from the HECRAS model of flow hydrograph for C2-Kiambu outlet to River Athi. 114
Figure 40. A screenshot from the HECRAS model of flow hydrograph for C3-Nairobi outlet to River Athi. 114
Figure 41. A screenshot from the HECRAS model of flow hydrograph for C4-Machakos outlet to River Athi. 115
Figure 42. A screenshot from the HECRAS model of maximum flow depth (left) and velocity (right) for S1-Baseline over C1 catchment. 115
Figure 43. A screenshot from the HECRAS model of maximum flow depth (left) and velocity (right) for S2-2000LU over C1 catchment. 116

Figure 44. A screenshot from the HECRAS model of maximum flow depth (left) and velocity (right) for S3-CP4uplift over C1 catchment. 116
Figure 45. A screenshot from the HECRAS model of maximum flow depth (left) and velocity (right) for S4-P25uplift over C1 catchment. 117
Figure 46. Year 2000 land use map for C1 catchment, (B) Year 2020 landuse map for C1 catchment, (C) Urban area transition landuse map for C1 catchment between 2000 and 2020. 118
Figure 47. Year 2000 landuse map for C2 sub-catchment, (B) Year 2020 landuse map for C2 sub-catchment, (C) Urban area transition landuse map for C2 sub-catchment between 2000 and 2020. 119
Figure 48. Year 2000 landuse map for C3 sub-catchment, (B) Year 2020 landuse map for C3 sub-catchment, (C) Urban area transition landuse map for C3 sub-catchment between 2000 and 2020. 119
Figure 49. (A) Year 2000 landuse map for C4 sub-catchment, (B) Year 2020 landuse map for C4 sub-catchment, (C) Urban area transition landuse map for C4 sub-catchment between 2000 and 2020. 120
Figure 50. A screenshot from the HEC-RAS model showing the generation of calculated flood hazard raster layers for the five model scenarios by adding the hazard curves onto the results. 123
Figure 51. Cell to cell flow paths of simulated floods for the S3-CP4 model. 124
Figure 52. A screenshot from the HECRAS model of the flood hazard category map for A: S1-Baseline; B: S2-2000LU; S3-C: CP4uplift; and D: S4-P25uplift over C1 catchment. 126
Figure 53. (A) Flood Hazard Category map for S1_Baseline and (B) Flood Hazard Category map for S2-200LU for C3 Nairobi sub-catchment area processed within the QGIS software. 127
Figure 54. (C) Flood Hazard Category map for S3_CP4uplift and (D) Flood Hazard Category map for S4-P25uplift for C3 Nairobi sub-catchment area processed within the QGIS software. 127
Figure 55. Comparison of Flood Hazard Vulnerability Classification (H1) for seven DEMs under the S4-P25uplift Model Scenario. 140
Figure 56. Comparison of Flood Hazard Vulnerability Classification (H2) for seven DEMs under the S4-P25uplift Model Scenario. 140
Figure 57. Comparison of Flood Hazard Vulnerability Classification (H3) for seven DEMs under the S4-P25uplift Model Scenario. 141
Figure 58. Comparison of Flood Hazard Vulnerability Classification (H4) for seven DEMs under the S4-P25uplift Model Scenario. 141
Figure 59. Comparison of Flood Hazard Vulnerability Classification (H5) for seven DEMs under the S4-P25uplift Model Scenario. 142
Figure 60.Comparison of Flood Hazard Vulnerability Classification (H6) for seven DEMs under the S4-P25uplift Model Scenario. 142
Figure 61. Comparison of Flood Hazard Vulnerability Classification (H1) for seven DEMs under the S2-2000LU Model Scenario. 143
Figure 62. Comparison of Flood Hazard Vulnerability Classification (H2) for seven DEMs under the S2-2000LU Model Scenario. 143

Figure 63. Comparison of Flood Hazard Vulnerability Classification (H3) for seven DEMs under the S2-2000LU Model Scenario 144
Figure 64. Comparison of Flood Hazard Vulnerability Classification (H4) for seven DEMs under the S2-2000LU Model Scenario 144
Figure 65. Comparison of Flood Hazard Vulnerability Classification (H5) for seven DEMs under the S2-2000LU Model Scenario 145
Figure 66. Comparison of Flood Hazard Vulnerability Classification (H6) for seven DEMs under the S2-2000LU Model Scenario 145
Figure 67. A screenshot from the QGIS software showing locations of three flooding hotspots in (1). Westgate Shopping Mall, Westlands, Nairobi. (2). Lindi Area, Kibera. (3). Thika Super Highway and Industrial Area in Nairobi where model validation data were collected between 20th and 27th July 2018. 147
Figure 68. Offloading of survey equipment (researcher) from car on arrival at the Westgate Shopping Mall flooding hotpot site to undertake topographic survey – 27th March 2018. 148
Figure 69. A hired local surveyor (Stanley Kimani) of the Kenya National Survey authority, Nairobi, with highly technical surveying knowledge providing support during the survey exercise. 149
Figure 70. Setting up of the survey equipment by the survey team at one of the survey sites. 150
Figure 71. Survey in progress at the Westgate Shopping Mall flooding hotspot showing a breach of the shopping mall fence line during the March 2018 flooding event to allow the passage of floodwater – brick rubble can be seen visible behind the gaping hole in fence wall in the background. 150
Figure 72. Measurement of flood historic flood depth levels at flooding hotspot site. 151
Figure 73. A screenshot from the HEC-RAS model showing hazard vulnerability classification map for the S5-RawDEM model that used raw DEM data instead of the corrected MERIT DEM 155
Figure 74. Cmparison of the flow hydrograph for the S1-Baseline model and S5-RawDEM model. 156
Figure 75. (A) Flood Hazard Category map for the S1-Baseline and (B) Flood Hazard Category map for S5-RawDEM models for C3 Nairobi sub-catchment area 158
Figure 76. Comparison of Hazard Vulnerability Classification between S1-Baseline model and S5-RawDEM model for the Nairobi C3 sub-catchment. 159
Figure 77. A screenshot from the HEC-RAS software showing comparison of flood hydrographs for the S1-Baseline model and the S2-2000LU model. 161
Figure 78. Comparison of Hazard Vulnerability Classification between S1-Baseline model and S2-2000LU model for the Nairobi C3 sub-catchment. 161
Figure 79. Comparison of Hazard Vulnerability Classification, H1 for the S2-2000LU model and the S1-Baseline model 162
Figure 80. Comparison of Hazard Vulnerability Classification, H2 for the S2-2000LU model and the S1-Baseline model 163
Figure 81. Comparison of Hazard Vulnerability Classification, H3 for the S2-2000LU model and the S1-Baseline model 163

FIGURE 82. COMPARISON OF HAZARD VULNERABILITY CLASSIFICATION, H4 FOR THE S2-2000LU MODEL AND THE S1-BASELINE MODEL. 163
FIGURE 83. COMPARISON OF HAZARD VULNERABILITY CLASSIFICATION, H5 FOR THE S2-2000LU MODEL AND THE S1-BASELINE MODEL. 164
FIGURE 84. COMPARISON OF HAZARD VULNERABILITY CLASSIFICATION, H6 FOR THE S2-2000LU MODEL AND THE S1-BASELINE MODEL. 164
FIGURE 85. A SCREENSHOT FROM THE HEC-RAS SOFTWARE SHOWING COMPARISON OF FLOOD HYDROGRAPHS FOR THE S1-BASELINE MODEL, S3-CP4UPLIFT MODEL AND THE S4-P25UPLIFT MODEL. 167
FIGURE 86. COMPARISON OF HAZARD VULNERABILITY CLASSIFICATION BETWEEN S1-BASELINE MODEL AND S3-CP4UPLIFT MODEL FOR THE NAIROBI C3 SUB-CATCHMENT. 167
FIGURE 87. COMPARISON OF HAZARD VULNERABILITY CLASSIFICATION BETWEEN S1-BASELINE MODEL AND S4-P25UPLIFT MODEL FOR THE NAIROBI C3 SUB-CATCHMENT. 168
FIGURE 88. COMPARISON OF HAZARD VULNERABILITY CLASSIFICATION, H1 FOR S1-BASELINE MODEL VS S3-CP4UPLIFT MODEL VS S4-P25UPLIFT MODEL. 168
FIGURE 89. COMPARISON OF HAZARD VULNERABILITY CLASSIFICATION, H2 FOR S1-BASELINE MODEL VS S3-CP4UPLIFT MODEL VS S4-P25UPLIFT MODEL. 168
FIGURE 90. COMPARISON OF HAZARD VULNERABILITY CLASSIFICATION, H3 FOR S1-BASELINE MODEL VS S3-CP4UPLIFT MODEL VS S4-P25UPLIFT MODEL. 169
FIGURE 91. COMPARISON OF HAZARD VULNERABILITY CLASSIFICATION, H4 FOR S1-BASELINE MODEL VS S3-CP4UPLIFT MODEL VS S4-P25UPLIFT MODEL. 169
FIGURE 92. COMPARISON OF HAZARD VULNERABILITY CLASSIFICATION, H5 FOR S1-BASELINE MODEL VS S3-CP4UPLIFT MODEL VS S4-P25UPLIFT MODEL. 169
FIGURE 93. COMPARISON OF HAZARD VULNERABILITY CLASSIFICATION, H6 FOR S1-BASELINE MODEL VS S3-CP4UPLIFT MODEL VS S4-P25UPLIFT MODEL. 170
FIGURE 94. A SCREENSHOT FROM HEC-RAS SOFTWARE SHOWING WATER SURFACE ELEVATION MAP (WSE) FOR THE S1-BASELINE MODEL. 195
FIGURE 95. A SCREENSHOT FROM HEC-RAS SOFTWARE SHOWING WATER SURFACE ELEVATION MAP (WSE) FOR THE S2-2000LU MODEL. 196
FIGURE 96. A SCREENSHOT FROM HEC-RAS SOFTWARE SHOWING WATER SURFACE ELEVATION MAP (WSE) FOR THE S3-CP4UPLIFT MODEL. 197
FIGURE 97. A SCREENSHOT FROM HEC-RAS SOFTWARE SHOWING WATER SURFACE ELEVATION MAP (WSE) FOR THE S4-P25UPLIFT MODEL. 198
FIGURE 98. A SCREENSHOT FROM HEC-RAS SOFTWARE SHOWING WATER SURFACE ELEVATION MAP (WSE) FOR THE S5-RAWDEM MODEL. 199
FIGURE 99. A SCREENSHOT FROM HEC-RAS SOFTWARE SHOWING FLOOD DEPTH FOR THE S1-BASELINE MODEL. 200
FIGURE 100. A SCREENSHOT FROM HEC-RAS SOFTWARE SHOWING FLOOD DEPTH FOR THE S2-2000LU MODEL. 201
FIGURE 101. A SCREENSHOT FROM HEC-RAS SOFTWARE SHOWING FLOOD DEPTH FOR THE S3-CP4UPLIFT MODEL. 202
FIGURE 102. A SCREENSHOT FROM HEC-RAS SOFTWARE SHOWING FLOOD DEPTH FOR THE S4-P25UPLIFT MODEL. 203

FIGURE 103. A SCREENSHOT FROM HEC-RAS SOFTWARE SHOWING FLOOD DEPTH FOR THE S5-RAWDEM MODEL. 204

FIGURE 104. A SCREENSHOT FROM HEC-RAS SOFTWARE SHOWING FLOOD VELOCITY FOR THE S1-BASELINE MODEL. 205

FIGURE 105. A SCREENSHOT FROM HEC-RAS SOFTWARE SHOWING FLOOD VELOCITY FOR THE S2-2000LU MODEL. 206

FIGURE 106. A SCREENSHOT FROM HEC-RAS SOFTWARE SHOWING FLOOD VELOCITY FOR THE S3-CP4UPLIFT MODEL. 207

FIGURE 107. A SCREENSHOT FROM HEC-RAS SOFTWARE SHOWING FLOOD VELOCITY FOR THE S4-P25UPLIFT MODEL. 208

FIGURE 108. A SCREENSHOT FROM HEC-RAS SOFTWARE SHOWING FLOOD VELOCITY FOR THE S5-RAWDEM MODEL................ 209

List of Tables

TABLE 1. A SUMMARY OF THE CHARACTERISTICS PERTINENT TO URBAN FLOOD MODELS (KAIHUA ET AL., 2021). 47

TABLE 2. COMPARATIVE SUMMARY OF THE RELATIVE ADVANTAGES AND DISADVANTAGES OF DIFFERENT URBAN FLOOD MODELS (KAIHUA ET AL., 2021). 49

TABLE 3. KEY INPUT DATA FOR THE HEC-HMS HYDROLOGIC RAINFALL RUNOFF MODEL. 51

TABLE 4. OBSERVED RAINFALL DATA (MARCH 2018) AT FIVE RAINFALL STATIONS IN NAIROBI, KENYA. 52

TABLE 5. CHARACTERISTICS OF THE SIX GLOBAL DEMS USED IN THE STUDY. 64

TABLE 6. STATISTICAL ERROR PARAMETERS FOR THE GLOBAL DEMS, IN METRES, BEFORE (AND AFTER) URBAN CORRECTION 74

TABLE 7. STATISTICAL ERROR PARAMETERS FOR SRTM & TANDEM-X 90 M DEMS IN NAIROBI CITY WIDE AND THE CBD AREA, IN METRES, BEFORE (AND AFTER) URBAN CORRECTION 76

TABLE 8. CORRECTION ERROR OF GLOBAL DEMS AT HIGHEST AND LOWEST MEASURED BUILDING DENSITIES (BD) 77

TABLE 9. STATISTICAL ERROR PARAMETERS FOR THE GLOBAL DEMS IN THE CBD AREA, IN METRES, BEFORE (AND AFTER) URBAN CORRECTION 80

TABLE 10. STATISTICAL ERROR PARAMETERS FOR SRTM DEM IN NAIROBI CITY WIDE, CBD, KIBERA SLUM AND THE EMBAKASI RESIDENTIAL AREA, IN METRES, BEFORE (AND AFTER) URBAN CORRECTION 82

TABLE 11. P VALUES FOR DEM ERROR VS BUILDING DENSITY RELATIONSHIPS FOR THE NAIROBI CITY, NAIROBI CENTRAL BUSINESS DISTRICT (CBD), KIBERA SLUM AREA AND EMBAKASI RESIDENTIAL AREA. 86

TABLE 12. CHARACTERISTICS OF FIVE SETS OF MODEL SCENARIOS CREATED IN HEC-RAS 2D V6.0.0 SOFTWARE USING THE DIFFUSIVE WAVE EQUATION. 88

TABLE 13. KEY INPUT DATA INTO THE HEC-HMS HYDROLOGIC RAINFALL RUNOFF MODEL 92

TABLE 14. OBSERVED RAINFALL DATA (MARCH 2018) AT FIVE RAINFALL STATIONS IN NAIROBI, KENYA (SOURCE KENYA METEOROLOGICAL SERVICE) 92

TABLE 15. LANDUSE AND LANDCOVER (LULC) CLASSIFICATION 93

TABLE 16. HEC HMS NET MODEL OUTPUT FLOW RESULT 95

TABLE 17. EXAMPLE MANNING'S N VALUES FOR VARIOUS NLCD LAND COVER TYPES. 101

TABLE 18. COMBINED HAZARD CURVES – VULNERABILITY THRESHOLD CLASSIFICATION LIMITS. 108

TABLE 19. TRANSITION MATRIX SHOWING LANDUSE AND LANDCOVER (LULC) CHANGE IN C1-COMBINED CATCHMENT BETWEEN 2000 & 2020. 121

TABLE 20. TRANSITION MATRIX SHOWING LANDUSE AND LANDCOVER (LULC) CHANGE IN C2-KIAMBU SUB-CATCHMENT BETWEEN 2000 & 2020. 121

TABLE 21. TRANSITION MATRIX SHOWING LANDUSE AND LANDCOVER (LULC) CHANGE IN C3-NAIROBI SUB-CATCHMENT BETWEEN 2000 & 2020. 122

TABLE 22.TRANSITION MATRIX SHOWING LANDUSE AND LANDCOVER (LULC) CHANGE IN C4-MACHAKOS SUB-CATCHMENT BETWEEN 2000 & 2020. 122

TABLE 23. AREAS OF EACH HAZARD VULNERABILITY CLASSIFICATION FOR S4-P25UPLIFT MODEL FOR C3: NAIROBI SUB-CATCHMENT AREA. 128

TABLE 24. AREAS OF EACH HAZARD VULNERABILITY CLASSIFICATION FOR S3-CP4UPLIFT MODEL FOR C3: NAIROBI SUB-CATCHMENT AREA. 128

TABLE 25. AREAS OF EACH HAZARD VULNERABILITY CLASSIFICATION FOR S2-2000LU MODEL FOR C3: NAIROBI SUB-CATCHMENT AREA. 128
TABLE 26. AREAS OF EACH HAZARD VULNERABILITY CLASSIFICATION FOR S1-BASELINE MODEL FOR C3: NAIROBI SUB-CATCHMENT AREA. 129
TABLE 27. HAZARD VULNERABILITY CLASSIFICATION FOR THE S4-P25UPLIFT JICA REFERENCE MODEL FOR C3: NAIROBI CATCHMENT AREA. 133
TABLE 28. HAZARD VULNERABILITY CLASSIFICATION FOR THE S3-CP4UPLIFT JICA REFERENCE MODEL FOR C3: NAIROBI CATCHMENT AREA. 133
TABLE 29. HAZARD VULNERABILITY CLASSIFICATION FOR THE S2-2000LU JICA REFERENCE MODEL FOR C3: NAIROBI CATCHMENT AREA. 134
TABLE 30. HAZARD VULNERABILITY CLASSIFICATION FOR THE S1-BASELINE JICA REFERENCE MODEL FOR C3: NAIROBI CATCHMENT AREA. 134
TABLE 31. HAZARD VULNERABILITY CLASSIFICATION FOR THE S4-P25UPLIFT SRTM MODEL FOR C3: NAIROBI SUB-CATCHMENT AREA. 134
TABLE 32. HAZARD VULNERABILITY CLASSIFICATION FOR THE S3-CP4UPLIFT SRTM MODEL FOR C3: NAIROBI CATCHMENT AREA. 135
TABLE 33. HAZARD VULNERABILITY CLASSIFICATION FOR THE S2-2000LU SRTM MODEL FOR C3: NAIROBI CATCHMENT AREA. ... 135
TABLE 34. HAZARD VULNERABILITY CLASSIFICATION FOR THE S1-BASELINE SRTM MODEL FOR C3: NAIROBI CATCHMENT AREA.... 135
TABLE 35. HAZARD VULNERABILITY CLASSIFICATION FOR THE S4-P25UPLIFT TM12 MODEL FOR C3: NAIROBI SUB-CATCHMENT AREA. 135
TABLE 36. HAZARD VULNERABILITY CLASSIFICATION FOR THE S3-CP4UPLIFT TM12 MODEL FOR C3: NAIROBI SUB-CATCHMENT AREA. 136
TABLE 37. HAZARD VULNERABILITY CLASSIFICATION FOR THE S2-2000LU TM12 MODEL FOR C3: NAIROBI SUB-CATCHMENT AREA. 136
TABLE 38. HAZARD VULNERABILITY CLASSIFICATION FOR THE S1-BASELINE TM12 MODEL FOR C3: NAIROBI SUB-CATCHMENT AREA. 136
TABLE 39. HAZARD VULNERABILITY CLASSIFICATION FOR THE S4-P25UPLIFT TM90 MODEL FOR C3: NAIROBI SUB-CATCHMENT AREA. 136
TABLE 40. HAZARD VULNERABILITY CLASSIFICATION FOR THE S3-CP4UPLIFT TM90 MODEL FOR C3: NAIROBI SUB-CATCHMENT AREA. 137
TABLE 41. HAZARD VULNERABILITY CLASSIFICATION FOR THE S2-2000LU TM90 MODEL FOR C3: NAIROBI SUB-CATCHMENT AREA. 137
TABLE 42. HAZARD VULNERABILITY CLASSIFICATION FOR THE S1-BASELINE TM90 MODEL FOR C3: NAIROBI SUB-CATCHMENT AREA. 137
TABLE 43. HAZARD VULNERABILITY CLASSIFICATION FOR THE S4-P25UPLIFT NASADEM MODEL FOR C3: NAIROBI SUB-CATCHMENT AREA. 137
TABLE 44. HAZARD VULNERABILITY CLASSIFICATION FOR THE S3-CP4UPLIFT NASADEM MODEL FOR C3: NAIROBI SUB-CATCHMENT AREA. 138

TABLE 45. HAZARD VULNERABILITY CLASSIFICATION FOR THE S2-2000LU NASADEM MODEL FOR C3: NAIROBI SUB-CATCHMENT AREA. 138
TABLE 46. HAZARD VULNERABILITY CLASSIFICATION FOR THE S1-BASELINE NASADEM MODEL FOR C3: NAIROBI SUB-CATCHMENT AREA. 138
TABLE 47. HAZARD VULNERABILITY CLASSIFICATION FOR THE S4-P25UPLIFT ALOS MODEL FOR C3: NAIROBI SUB-CATCHMENT AREA. 138
TABLE 48. HAZARD VULNERABILITY CLASSIFICATION FOR THE S3-CP4UPLIFT ALOS MODEL FOR C3: NAIROBI SUB-CATCHMENT AREA. 138
TABLE 49. HAZARD VULNERABILITY CLASSIFICATION FOR THE S2-2000LU ALOS MODEL FOR C3: NAIROBI SUB-CATCHMENT AREA. 139
TABLE 50. HAZARD VULNERABILITY CLASSIFICATION FOR THE S1-BASELINE ALOS MODEL FOR C3: NAIROBI SUB-CATCHMENT AREA. 139
TABLE 51. COMPARISON OF THE HAZARD VULNERABILITY CLASSIFICATIONS (H1 TO H6) FOR ALL SEVEN DEMS FOR THE S4-P25UPLIFT MODEL FOR THE NAIROBI SUB-CATCHMENT AREA – (ALL VALUES IN SQUARE KM) 139
TABLE 52. MODEL VALIDATION: COMPARISON OF SITE SURVEY DATA ACROSS THREE FLOODING HOTSPOTS AREAS OF NAIROBI WITH MODEL RESULTS OF THE SEVEN DEM MODELS 146
TABLE 53. MODEL VALIDATION: COMPARISON OF SITE SURVEY DATA ACROSS THREE FLOODING HOTSPOTS AREAS OF NAIROBI WITH MODEL RESULTS 151
TABLE 54. COMPARISON OF FLOOD HEIGHT LEVELS BETWEEN THE S1-BASELINE AND S5-RAWDEM MODELS WITH ACTUAL SURVEY DATA AT FLOODING HOTSPOT SITES. 157
TABLE 55: AIM 1: IDENTIFICATION OF GLOBAL DATASETS AND MODELS THAT COULD BE USED FOR MODELLING OF CITY SCALE-PLUVIAL FLOOD HAZARD IN DATA SCARCE AREAS 210
TABLE 56: AIM 2: DERIVATION OF URBAN CORRECTED DEMS WITH GLOBAL DATASETS USING NAIROBI AS A TEST CITY 211
TABLE 57. AIM 3: BUILD AND TEST A CITY SCALE URBAN PLUVIAL FLOOD MODEL WITH GLOBAL DATASETS USING NAIROBI AS A TEST CITY 212
TABLE 58. AIM 4: TEST IF MODEL IS SUITABLE FOR EXPLORING FACTORS AFFECTING PLUVIAL URBAN FLOODING BY SCENARIO ANALYSIS. 213

List of Equations

EQUATION 1 45
EQUATION 2 45
EQUATION 3 45
EQUATION 4 45
EQUATION 5 45
EQUATION 6 45
EQUATION 7 69
EQUATION 8 69
EQUATION 9 69
EQUATION 10 69
EQUATION 11 91
EQUATION 12 91
EQUATION 13 91

List of Abbreviations / Acronyms

Advance Land Observing Satellite	(ALOS)	34
Advanced Spaceborne Thermal Emission and Reflection Radiometer	(ASTER)	33, 60
Airborne Laser Scanning	(ALS)	34
Airborne Light Detection and Ranging	(LiDAR)	34
ALOS World 3D-30m	(AW3D30)	34
Building Density	(BD)	77
Central Business District.	(CBD)	67
Centre for International Earth Science Information	(CIESEN)	66
Combined Sewer Overflow	(CSO)	166
Curve Number	(CN)	90
Digital surface models	(DSMs)	60
Digital Surface Models	(DSMs)	34
Digital Terrain Model	(DTM)	61
Earth Gravitational Model 1996	EGM96	66
Environment Agency	(EA)	30
Geographic Information System	(GIS)	68
Geospacial Data Abstraction Library	(GDAL)	94
German SAR satellite mission for scientific and commercial applications	TerraSAR-X	67
Global DEM	(GD)	70
Global Hydrologic Soil Groups	(HSG)	93
Global Precipitation Climatology Centre	(GPCC)	92
Global Urban Footprint	(GUF)	67
Interferometric Synthetic Aperture Radar	(InSAR)	67
Japan Aerospace Exploration Agency	(JAXA)	66
Japanese International Co-operation Agency	(JICA)	67
Linear Error	(LE)	64
Luxe bough Institute of Science & Technology	(LIST)	70
Mean Average Error	(MAE)	64
Multi-Error-Removed Improved-Terrain DEM	(MERIT DEM)	33
National Aeronautics & Space administration Digital Elevation Model	(NASADEM)	33
October November December	(OND)	32
Open Street Map	(OSM)	34
Quantum Geographic Information System	(QGIS)	70
Root Mean Square Error	(RMSE)	34
Shuttle Radar Topography Mission	(SRTM)	33
Soil Conservation Service	(SCS)	90
Standard Deviation		

(SD) 67
TerraSAR-X- Add-oN for Digital Elevation Model
Measurement
(TanDEM-X) 28
The high resolution settlement layer
(HRSL) 66
Three-dimensional
(3) 63
Triangular Irregular Networks
(TIN) 67
Two-Dimensional
2D 60
United Kingdom
(UK) 30
Version 1
(v1) 65
Version 2.1
(v2.1) 65
Version 3
(V3) 65
World Geodetic System 1984
WGS84 68

1.0 INTRODUCTION

1.1 Background

Land use change due to increasing urbanisation is a major cause of pluvial flooding in urban areas. Pluvial flooding occurs when surface water runoff accumulating from the result of intense rainfall saturates the urban drainage system, and the excess water cannot be absorbed. Climate change and urbanisation pose significant threats for flooding and water quality in urban areas (Miller and Hutchins, 2017). The flooding experienced in many urban areas of the world is significantly influenced by the changes to the timing and magnitude (flood extent, depth, and velocity) of rainfall brought about by climate change (Ashley et al., 2005a, Wheater and Evans, 2009). Changes in land use and land management affect the hydrology that determines flood hazard, water and the transport and dilution of pollutants and it is increasingly recognised that the management of land and water are inextricably linked (Wheater and Evans, 2009). Similarly, (Suriya and Mudgal, 2012) found that the rapid increase in population and the change in land use patterns are the major reasons for occurrence of flooding in the Thirusoolam sub watershed.

Whilst urbanisation generally increases the size and frequency of floods and expose communities to increasing flood hazards, various studies have highlighted the difficulties in modelling flood inundation extent in data sparse regions of the globe (Komi et al., 2017). Until recent years, flood mapping and forecasting tools were available only in few areas of the globe, given their high demand of resources and data for development and maintenance (Dottori et al., 2016). However, the situation is changing nowadays: the development of high-resolution flood hazard models have become feasible at continental and global scale, and their application in developing countries and especially data-scarce regions is becoming extremely helpful to increase preparedness of populations and reduce catastrophic impacts of floods.

1.2 Significance of this study

The impact of pluvial flooding can be very devastating especially in densely populated areas of rapidly developing cities. With increasing infrastructure development and building density, increase in paved areas, ageing drainage infrastructure and climate change come increased frequency of pluvial flooding. The lack of reliable data in urban centres of developing countries constitute the biggest challenge to urban pluvial flood modelling (Gebremichael and Hossain 2010). The general aim of the PhD study is to develop a city-scale hydrologic and hydraulic model to model the impact of climate change and land use change on pluvial flood hazard in the context of rapidly developing cities by using global datasets. Specific aims and objectives of the study are reported below including research matrix tables in Appendix 1 of the thesis.

1.3 Research Aims and Objectives

Aim 1:

To identify global datasets and models that could be used for modelling of city scale-pluvial flood hazard in data scarce areas.

Objectives

- Types of data sets (remote sensing-based sources for: climate change rainfall, digital elevation model (DEM), and urban land use etc) required to build a city scale model will be identified and extracted from *open* sources.
- Data appropriate numerical flood model for city scale urban flood modelling - identify physical processes that are required in model, and their appropriate application scale. Compare available models for computation speed, and process representation.
- The data from both sets will be synthesised and harmonised together to prepare for use as key input data sets in a city scale model.

Aim 2:

To derive urban corrected DEMs with global datasets using Nairobi as a test city.

Objectives

- Using Nairobi as a case study, raster data for six global DEMs will be pre-processed, resampled and transformed to the WG WGS84 (G1150) ellipsoid to EGM96 Geoid using the NOAA's VDatum transformation tool.
- DEM error for six global DEMs will be calculated including calculation of building density using – use of QGIS raster algebra tool to calculate the vertical accuracy for the six global DEMs and creation of DEM error maps and building density maps.
- The data sets and outputs from above will be used to determine DEM error relationship with building density using QGIS tools - plots of DEM error versus building density will be created for all six global DEMs.
- The error relationship determined above will be applied to derive urban corrected global DEMs.
- The same procedure described above for the Nairobi city and the central business district area will be applied to the Kibera slum area and the Embakasi residential area of Nairobi.

Aim 3:

To build and test a city scale urban pluvial flood model with global datasets using Nairobi as a test city.

Objectives

- Outputs from the processes described above will be extracted to build a city scale model using Nairobi as a test location - baseline model and different model scenario will be developed, run and analysed using historical flood events.
- Local data sets relating to urban flooding will be collected across government offices, private firms, NGOs, and International organisations headquartered in Nairobi city.
- Sensitivity of model behaviour, results of choice of datasets, assumptions made in model build etc will be quantified.
- The model will be validated by comparison of baseline model results with historical flooding observations.

Aim 4:

To test if the model is suitable for exploring factors affecting urban pluvial flooding by scenario analysis.

Objectives

- The impacts of climate change on urban flooding will be investigated.
- S3-CP4uplift and S4-P25uplift models will be created and run using inputs from climate rainfall models.
- The impacts of land use change on urban flooding will be investigated.
- S1-Baseline and S2-2010LU land use models will be created and run using inputs from landuse maps for 2010 and 2020 for the test location.

1.4 Thesis structure

Chapter 1 introduces the research, with the background of the study, problem statement, research aim & objectives, research questions and the hypothesis. In **Chapter 2** the literature is reviewed. **Chapter 3** covers the general methods & data used in the study. The urban correction of global DEMs using building density for Nairobi, Kenya is developed in **Chapter 4**. **Chapter 5** covers the development of hydrologic & hydraulic models to simulate the impact of climate change and land use change on urban pluvial flood hazard in rapidly developing cities using Nairobi, Kenya as a case study. **Chapter 6** covers the scenario analysis of the five scenarios of the HEC-RAS 2D hydraulic models developed in Chapter 5. **Chapter 7** is a synthesis of the findings for the whole thesis together with discussion. In **Chapter 7,** conclusions are drawn, contributions of this study to the research community are highlighted, limitations are identified, and recommendations for further research outlined.

2.0 LITERATURE REVIEW

2.1 Global flood model data scarcity challenge

The key challenge for urban flood studies in many of the world's rapidly developing cities is sparsity of data (Hawker et al., 2018). Even if there was data, the context is evolving so rapidly that it would be out of date within few years. Terrain and hydrological data are scarce in many developing regions of the world and the absence of flow gauges on flood-prone reaches make flood inundation modelling challenging in these regions (Komi et al., 2017). With the advent of computational methods and computer processing power, the ability to tackle urban floods at the catchment level is clearly emerging, making it possible to apply an integrated approach to modelling rainfall-runoff processes along with surface flows (Courty et al., 2018). Thus, new datasets through remote sensing and modelling as well as faster computing are transforming our capability to model flooding globally and could be a potential solution to the rapidly developing urban contexts where there is little data. The development of a reliable approach to adequately describe urban floods processes has been recognized as a challenging task (Coulthard, et al. 2015 & Courty et al. 2017).

The growing availability of remotely senses data has fostered the implementation of hydraulic flood modelling in poorly gauged regions leading (Domeneghetti, 2016, Donald Houston, 2011) to test two different procedures for inferring the river bathymetry under water surface level by assessing the suitability of spaceborne topographic and remotely sensed altimetry data for implementing and calibrating hydrodynamic models. Results showed the efficiency of the statistical metrics of satellite borne data similar to those obtained with benchmark models.

(Gutenson et al., 2017) provided insight into how recent advances in generation of global datasets is improving the capability to model riverine inundation at nearly any location on Earth. The authors demonstrated how flood inundation model can be developed on a large scale by combining continental scale hydrologic simulations, the TanDEM-X DEM data, and the AutoRoute software. The study showed how together these data and models function to quickly and effectively model inundation on large geographic scales in data sparse environments.

2.2 Urbanization, land use change and pluvial flooding

Land use change due to increasing urbanisation is a great contributor to pluvial flooding in urban areas. Pluvial flooding occurs when surface water runoff accumulating from the result of intense rainfall saturates the urban drainage system, and the excess water cannot be absorbed by the ground. Pluvial flood risk accounts for approximately one-third of flood risk in the UK, whilst, approximately 2 million people in UK urban areas are exposed to an annual pluvial flood risk of 0.5 per cent or greater ('1-in-200 year' event), (Houston, 2011). Today, the most urbanized regions of the world include Northern America (with 82% of its population living in urban areas in 2018), Latin America and the Caribbean (81%), Europe (74%) and Oceania (68%) (UN, 2019). The level of urbanization in Asia is now approximating 50%. In contrast, Africa remains mostly rural, with 43% of its population living in urban areas (UN, 2019). It is very clear from these statistics that most of future urban growth will be witnessed in developing regions of the world where cities continue upward growth in population and outward growth in boundary.

Flooding is the most prevalent disaster worldwide accounting for 43% of all recorded global disaster events in the past 20 years leading up to 2018 (Choy, 2018). While migration from rural settlements to urban areas often mirrors economic advancement, it also presents socioeconomic and environmental challenges. Rapid urban growth strains existing infrastructure and also discourages the preservation of natural habitat in favor of building more developments causing urban flooding. The urban population in 2015 accounted for 54% of the total global population, up from 30% in 1950 This figure is expected to increase to 60% of world population by 2030 and the global urban population is expected to grow approximately 1.84% per year between 2015 and 2020 (UN, 2019). By 2030, the world is projected to have 43 megacities with more than 10 million inhabitants, most of them in developing regions. However, some of the fastest-growing urban agglomerations are cities with fewer than 1 million inhabitants, many of them located in Asia and Africa. While one in eight people live in 33 megacities worldwide, close to half of the world's urban dwellers reside in much smaller settlements with fewer than 500,000 inhabitants (UN, 2019).

According to (Schmid, 2015), the challenge is to improve our understanding of contemporary urbanization processes and to decipher their implications and effects. The increase in impervious areas disrupts the natural water balance. Reduced infiltration increases runoff and leads to higher flood peaks and volumes even for short duration low intensity rainfall events (Suriya and Mudgal, 2012). For example, urbanization is taking place rapidly in Nairobi, Kenya as the city experiences dramatic growth. The increase in human settlements is as a result of increased migration from rural areas into the city, with its population pushing upward and its boundaries pushing outward in Kiambu, Machakos, and Kajiado counties that form the Nairobi metropolitan area.

Various researches have highlighted how rapid urbanization processes have influenced flood behaviour and contributed to flooding (Braud et al., 2013, Chen et al., 2017b, Donald Houston, 2011, Miller and Hutchins, 2017, Sanyal et al., 2014, Suriya and Mudgal, 2012). They found that physical growth of urban areas, amongst others characterized by the increase of impervious surfaces lead to the decrease in infiltration rate thus to an increase of overland flow. Removing vegetation and soil, grading the land surface, and constructing drainage networks increase runoff to streams from rainfall and snowmelt. As a result, the peak discharge, volume, and frequency of floods increase in nearby streams. Roads and buildings constructed in flood-prone areas are exposed to increased flood hazards, including inundation and erosion, as new development continues. Floodplains can alter the capacity of a channel to convey water and can increase the height of the water surface corresponding to a given discharge. In particular, structures that encroach on the floodplain, such as bridges, can increase upstream flooding by narrowing the width of the channel and increasing the channel's resistance to flow. As a result, the water is at a higher stage as it flows past the obstruction, creating a backwater that will inundate a larger area upstream.

(Konrad, 2003) observed sediment and debris carried by floodwaters can further constrict a channel and increase flooding whilst (Sliuzas, 2013) found similar hazard is greatest for upstream of culverts, bridges, or other places where debris collects. Small stream channels can be filled with sediment or become clogged with debris, because of undersized culverts. This creates a closed basin with no outlet for runoff. A very modest rainstorm that earlier would be absorbed by soil storage in a rural catchment produces more surface runoff in an urban catchment. Also, (Miller and Hutchins, 2017) reviewed the evidence concerning the combined impacts of urbanization and climate change on the urban water environment of inland catchments of the United Kingdom and found climate change and urbanization pose significant threats for flooding and water quality in urban areas. In addition, the study also found urban densification and inadequate urban drainage design to be primary drivers of pluvial and sewer flooding in the UK. Detailed estimates of UK pluvial flood risk indicate approximately 2 million people are exposed to a 0.5% AEP risk (Houston, 2011) and the figures from the Environment Agency (EA) suggests that as many as two thirds of all the flooding events of summer 2007 across the UK was attributed to inadequacies in surface water drainage systems (Pitt, 2008).

(Suriya and Mudgal, 2012) found that the rapid increase in population and the change in land use pattern between 1976 and 2005 are the major reasons for occurrence of flooding at the Thirusoolam sub watershed in Chennai, China. The land use pattern of the Thirusoolam was classified into a built-up area and the results reflect that the increase in impervious area has altered the water cycle and obstructed natural runoff, which in turn led to flood risks to inhabitants. Similarly, (Konrad, 2003) found, generally, urbanization increases the size and frequency of floods and expose communities to increasing flood hazards. Urbanisation affects hydrological processes, often detrimentally and the growth of urban population, combined with an increase of extreme rainfall events due to climate change call for a better understanding and representation of urban floods (Courty et al., 2018). One of the key aims of this study is to assess the impact of urbanization and the consequent changes in land use and land cover on pluvial flooding at a city-scale.

2.3 Climate change and urban flooding

Flooding in urban areas is characterized by strong intensity and a short response time that would cause enormous human and economic losses (Apel et al., 2009). With changes in global climate and urbanization, urban flood is increasing, and resultant damage has been reported worldwide (Aerts et al., 2014). Flood dynamics across urbanized areas are difficult to understand because of the complex urban infrastructures, underlying surface conditions and drainage systems (Wu et al., 2018). Urbanisation affects hydrological processes, often detrimentally and the growth of urban population, combined with an increase of extreme rainfall events due to climate change call for a better understanding and representation of urban floods (Courty et al., 2018). Without proper planning and management can lead to increases in peak flows.

Africa is acutely vulnerable to the effects of climate change (Dunning, 2018). The large proportion of the population dependent upon rain-fed agriculture for their source of income and subsistence means that future changes in rainfall over Africa have high potential for detrimental socioeconomic consequences. Climate change and urbanization pose significant threats for flooding and water quality in urban areas (Miller and Hutchins, 2017). Previous studies have examined the impact of climate change on annual or seasonal rainfall totals over Africa, (Dunning, 2018, Hunt and Watkiss, 2011, Kundzewicz et al., 2014, Miller and Hutchins, 2017, Murray and Ebi, 2012), (Dunning, 2018), highlighting the challenges posed by a combination of climate change and rapid urban development on urban flooding. (Dunning, 2018) found over the Horn of Africa rainfall during the “short rains” season is projected to increase by over 100 mm on average by the end of the twenty-first century under the RCP8.5 scenario. Average rainfall per rainy day is projected to increase, while the number of rainy days in the wet season declines in regions of stable or declining rainfall (western and southern Africa) and remains constant in central Africa, where rainfall is projected to increase.

Rapid urban growth puts strain on existing infrastructure and discourages the preservation of natural habitat in favour of new housing developments, shopping malls, urban infrastructure, etc. that can exacerbate the problem of urban flooding. Flooding is the most prevalent natural disaster, often characterised as a high intensity event that requires rapid emergency service response in order to minimise substantial human and economic losses (Apel et al., 2009). Climate change and urbanisation have been reported as the major contributors to the increasing damaging effects of flooding to lives and livelihoods worldwide (Aerts et al., 2014). There is lack of adequate research focused on the dual impacts of climate change and urbanisation on urban flooding and water quality in rapidly developing urban areas of the world – a gap that will result in an increase in pluvial and pluvial flood risk, and further reduction in water quality (Miller and Hutchins, 2017). Changes in the seasonality of precipitation over Africa have high potential for detrimental socioeconomic impacts due to high societal dependence upon seasonal rainfall.

(Dunning, 2018) found that over the Horn of Africa rainfall during the "short rains" season is projected to increase by over 100 mm on average by the end of the twenty-first century under the RCP8.5 scenario. Average rainfall per rainy day is projected to increase, while the number of rainy days in the wet season declines in regions of stable or declining rainfall. (Miller and Hutchins, 2017) reviewed the evidence concerning the combined impacts of urbanization and climate change on the urban water environment on inland catchments in the United Kingdom and reached a conclusion that there is an acceptance that combined population and climate change projections are a pressing challenge and represent critical urban flood risks. The uncertainty of climate change projection and suitability are part of recurring factors that limit the utility of evidence for managing the urban environment. One of the main aims of this research is to assess the current and future combined impacts of urbanization and climate change on pluvial flooding in rapidly developing cities of the world using global data.

In the period from 1951 to 2012, global temperature increased at the rate of 0.8 C to 0.14 C (IPCC, 2014a). (Mirza, 2011) found the frequency of extreme floods to be on the rise in Bangladesh, India and Pakistan due to climate change. Climate change has led to increasing temperature in some places while increasing precipitation and streamflow at the other places (Khadka and Pathak, 2016). Recent studies have shown there is a strong link between climate change and increase in the intensity of rainfall over Africa due to increase in global warming (Finney et al., 2020, Kendon et al., 2019). Various studies focusing on climate models have predicted a significant increase in East African rainfall (Shongwe et al., 2011a, Wainwright et al., 2021, Otieno et al., 2018, Kent et al., 2015). In particular, the IPCC projections suggest the increase in rainfall over the Horn of Africa as a sign of climate change (Collins et al., 2013).The short rains witnessed in East Africa between October – December [OND] in 2019 were one of the wettest in recent decades, adversely affecting over 2.8 million people across the region (Wainwright et al., 2021). East Africa is prone to climate and weather extremes with a highly variable climate, and the Long-Rains wet season of March–May (MAM) over Kenya in 2018 was one of the wettest on record (Kilavi et al., 2018). The strong sub-seasonal variability in the Long-Rain has been linked to the irregular impact of the Madden–Julian Oscillation (MJO) influenced by climate change (Zaitchik, 2017).

2.4 Global Digital Elevation Models (DEMs) and correction

Rapid urban growth puts strain on existing infrastructure and discourages the preservation of natural habitat in favour of new housing developments, shopping malls, urban infrastructure, etc. that can exacerbate the problem of urban flooding. Flooding is the most prevalent natural disaster, often characterised as a high intensity event that requires rapid emergency service response in order to minimise substantial human and economic losses (Apel et al., 2009). Climate change and urbanisation have been reported as the major contributors to the increasing damaging effects of flooding to lives and livelihoods worldwide (Aerts et al., 2014). Topography has been identified as a key method of estimating flood extent (Horritt and Bates, 2001) and many models of flood extent rely on DEMs in order to simulate paths of water flow, flood extent and depth. Errors in DEMs can substantially affect the results of flood models (Stephens et al., 2012, Hawker et al., 2018).

Global DEMs used in flood models are representations of physical ground surface and the spatial resolution of a DEM refers to the area of land being represented by single regular or irregular grid, with the value of each grid element representing the height of the ground at the corresponding datum (Vaze et al., 2010). There are many open access global scale DEMs such as the Shuttle Radar Topography Mission (SRTM), and its derivatives, the Multi-Error-Removed Improved-Terrain DEM (MERIT DEM) and NASA DEM (NASADEM), as well as Advanced Spaceborne Thermal Emission and Reflection Radiometer (ASTER) DEM and TerraSAR-X add-on for Digital Elevation Measurement (TanDEM-X 90m) etc. The global coverage of these DEMs makes them highly suitable for use in scientific applications where they are used extensively in flood models and have been critical in facilitating important flood studies, particularly in data-sparse areas, where local data is often difficult to access or unavailable (Hawker et al., 2018).

Chen and Hill (Chen and Hill, 2007) investigated the influence of DEM resolution on flood hazard modelling in urban areas and found that both vertical height error and spatial resolution of DEMs can impact on flood inundation depth and extent in urban flood modelling. Although, spaceborne DEMs provide fundamental input to many geoscience studies, they suffer from non-negligible height errors (Yamazaki et al., 2017). Sources of error in spaceborne DEMs include: (i) incomplete spatial sampling; (ii) measurement errors, such as positional inaccuracy, data entry errors; and (iii) processing errors such as computational numerical errors, interpolation errors, and classification and generalisation errors (Burrough, 1986). Global DEMs suffer from many different types of errors, some of which are significant at local scales; for example, (Rodríguez et al., 2006) reported a global mean and standard vertical height error of 8.2 ± 0.7 and 6.9 ± 0.5 m for SRTM X- and C-band data, respectively. There is a number of published work on the correction of errors in global DEMs, especially vegetation errors. (Falorni et al., 2005, Bhang et al., 2007, Dong et al., 2015, Gallant et al., 2012, Baugh et al., 2013, O'Loughlin et al., 2016, Chen et al., 2018). Also, there are many previous studies focused on the assessment of the vertical height accuracy of DEMs by comparing elevation values of DEMs to that of a reference local DEM having a higher vertical accuracy. A more accurate reference DEM such as the Light Detection and Ranging (LiDAR) is required in order to make an assessment of the vertical accuracy of global DEMs (Dong et al., 2015, Wessel et al., 2018, Acharya et al., 2018).

Although many studies (Robinson et al., 2014, Yamazaki et al., 2012, Yamazaki et al., 2017) have developed new vegetation-corrected DEMs, by either editing or adjusting existing global DEMs. However, despite significant advances in developing vegetation-corrected DEMs, there is limited understanding of DEM errors that can be attributed to building heights and building density in urban areas. Local DEMs that are based on airborne light detection and ranging (LiDAR) are preferential over open access, global DEMs due of their superior vertical accuracy, horizontal resolution, and ability to distinguish between ‘bare earth’ from built structures and vegetation (Yamazaki et al., 2017). However, (LiDAR) DEMs (<10 m horizontal resolution) are only available for a very small percentage of Earth's land surface (~0.005%), and data acquisition is often expensive (Hawker et al., 2018).

Building heights and building density inhibit the ability of radar signals to penetrate land surfaces, especially in densely populated urban areas where higher DEM resolution does not necessarily ensure accurate mapping (Rossi et al., 2012). Gridded elevation datasets, such as the radar-measurement-derived SRTM, exhibit signal reflection from built structures and vegetation so that further data processing may be required to enable accurate flood modelling (Sanders, 2007b). (Kim et al., 2020) selected the SRTM and Sentinel 2 multispectral imagery to train the artificial neutral network in order to improve the quality of SRTM DEM and then evaluated the performance of the resulting SRTM DEM over two dense urban cities. The ‘new’ DEM (iSRTM) showed better results than the original SRTM, achieving 38% reduction in the root mean square error (RMSE). Similarly, (Klonner et al., 2015) leveraged on the advantages of the Airborne Laser Scanning (ALS) and the Open Street Map (OSM) to create an up-to-date Digital Surface Model (DSM) combining 2D OSM and ALS data.

Digital surface models (DSMs) can provide a good source of high quality data for the extraction of building height maps in urban areas and (Alganci et al., 2018) explored the feasibility of using open access DSMs, such as the Advance Land Observing Satellite, ALOS (AW3D30), ASTER, and SRTM datasets, for extracting digital building height models and compared their accuracy. The potential for

DSMs as a rich data source for the extraction of building height data has been highlighted as a significant challenge in their use at the same time as representations of DTM in urban flood modelling (Alganci et al., 2018). Despite efforts made in the processing of global DEM data prior to making the data publicly accessible, DEMs frequently contain artefacts such as spikes, holes and line errors. (Hirt, 2018) recommended that all DEM datasets undergo a complete global screening for artefacts prior to public release, further advising users to check quality before using global DEMs. Despite recent advances in removing error components from DEMs, such as tree height bias, speckle noise, stripe noise and absolute bias, much work remains in the urban correction of building biases in global DEMs.

According to (Hawker et al., 2018), there is no forthcoming high-accuracy open-access global DEM, therefore, for the foreseeable future, the primary means of improving flood simulation will be to use editing or stochastic simulation using existing DEM data. Urban correction of existing global DEMs remains a key research challenge. One of the key aims of this research is to develop a methodology for the urban correction of global DEMs, using building density data. This methodology was applied to the city of Nairobi, Kenya.

2.5 Urban flood models

In (Dawson et al., 2008) pluvial flooding in urban areas represents a particular challenge to modellers and flood risk managers because of the complex interactions of surface water flow, inadequate urban drainage system, poor planning, land use change etc. The prevalence of flooding events and the associated risk in the urban areas is an increasingly important issue of global significance and more critical for the developing countries where's there's sparsity of data for urban flood modelling (Nkwunonwo et al., 2020). (Komi et al., 2017) highlighted the difficulties in modelling flood inundation extent in data scarce areas, particularly in generating realistic flood flows. The study explored a methodology for simulating flood extent in data scarce areas using a hydrological model and flood inundation model. Hydrological and hydraulic models are required to first simulate peak flows or high-water levels and then simulate inundation to identify flood prone areas. With the advent of computational methods and computer processing power, the ability to tackle urban floods at the catchment level is clearly emerging, making it possible to apply an integrated approach to modelling rainfall-runoff processes along with surface flows (Courty et al., 2018). Thus, new datasets through remote sensing and modelling as well as faster computing are transforming our capability to model flooding globally and could be a potential solution to the rapidly developing urban contexts where there is little data. The development of a reliable approach to adequately describe urban floods processes has been recognized as a challenging task (Li et al., 2021).

(Trigg et al., 2016) highlighted how quantifying flood hazard is an essential component of resilience planning, emergency response, and mitigation, including insurance. The study further highlighted how global flood hazard models are becoming a practical reality due to improvements in numerical algorithms, global datasets, computing power, and coupled modelling frameworks. Outputs of these models are vital for consistent quantification of global flood risk and in projecting the impacts of climate change. (Chowdhury and Akter, 2021) developed a city-scale flood hazard map through using the Hydrologic Engineering Centre-hydrologic modelling system (HEC-HMS) developed by the US Army Corps of Engineers. The simulated runoff showed a reasonable match with field records at three different outlets with R2 values of 0.782, 0.719 and 0.768 respectively. (Guo et al., 2021)

(Trigg et al., 2016) compared multi-probability flood hazard maps for Africa from six global models and the results showed wide variation in their flood hazard, economic loss and exposed population estimates, which has serious implications for model credibility. Results from the study, which was the first study to compare flood hazard models showed that even at continental scales, there are significant differences in hazard magnitude and spatial pattern between models, notably in deltas, arid/semi-arid zones and wetlands. The study presented an important step towards a better understanding of modelling global flood hazard, which is urgently required for both current risk and climate change projections. Flood models used for assessing the impacts of climate change on global flood risk will require credible skill at representing currently observed flooding before climate change impacts can be predicted with certainty. As models are improved, there is a parallel need to address scale and accuracy limitations in exposure and vulnerability datasets, which are used together with the flood model output for global scale risk assessments. One of the aims of this research is to address this gap.

(Sanyal et al., 2013) observed there is a lack of focus on flooding as a natural hazard when it comes to hydraulic modelling in data sparse regions. When tools for flood predictions and warnings are developed, they are conventionally focussed on modelling extreme flow events with an accuracy that is acceptable in flood management and planning practices. Whilst the study noted the use of the global DEMs for routing high magnitude floods at a regional scale is likely to require some additional reference data in order to correct the systematic bias and noise present in them and increase the details of topographic representations where it is absolutely necessary. However, in spite of all the constraints associated with use of global datasets for hydraulic flood models, there is an increasing trend of utilising freely available terrain data for hydraulic modelling of pluvial floods (Sanyal et al., 2014). Hydrological modelling usually provides an excellent basis regarding the generation of surface runoff for drainage network planners, designers and engineers and one of the aims of this study is to leverage on the opportunities provided by the user-friendly tools of the HEC-HMS to derive net precipitation data for use as key input data for the HEC-RAS hydraulic model and generate surface runoff over the catchment area.

2.6 Summary

Topography has been identified as a key dataset of estimating flood extent (Horritt and Bates, 2001) and models of flood extent rely on DEMs in order to simulate paths of water flow, flood extent and depth. Errors in Digital Elevation Models (DEMs) can substantially affect the results of flood models (Stephens et al., 2012, Hawker et al., 2018). Open-access global DEMs are not only useful tools for estimating flood risks, but they also provide baseline data for flood studies. Urban flood models that use ground height surface models, such as Digital Elevation Models (DEMs), to predict flood inundation rely on DEM accuracy for predicting flood events, extent, and depth. Global DEMs have a significant influence on the outcome of flood modelling, with higher levels of DEM vertical accuracy resulting in more accurate flood modelling.

The accuracy of such DEMs is a key point for these applications and DEM is one of the most important inputs in hydrodynamic models as it controls the accuracy of the model outputs (Sanders, 2007a) in particular flood extents and depths. (Carabajal and Harding, 2005) validated the SRTM DEM using ICESat, a satellite laser altimeter, and discovered that the errors in SRTM increased with increasing tree cover. This was because the C-band radar used by SRTM could not fully penetrate the vegetation canopy to the ground. (Berry et al., 2007) utilised satellite radar altimeters to validate the SRTM DEM and supports the findings of (Carabajal and Harding, 2005).

While these errors can clearly be attributed to vegetation, their correction requires knowledge about canopy heights and radar penetration depths. The correction of vegetation biases associated with these DEMs require global vegetation height map that was only first published in 2010 (Lefsky, 2010), followed by a more accurate vegetation map the following year (Simard et al., 2011). Despite the importance of Artefact removal methods have been very important in correcting vegetation errors in SRTM data but was found to have been rather simple and have only applied static corrections, i.e. they removed a spatially uniform fixed percentage of vegetation height from the DEM (O'Loughlin et al., 2016). Therefore, (O'Loughlin et al., 2016) developed the first global ‘Bare-Earth’ Digital Elevation Model (DEM) based on the Shuttle Radar Topography Mission (SRTM) for all landmasses between 60N and 54S.

The new ‘Bare-Earth’ SRTM DEM combines multiple remote sensing datasets, including point-ground elevations from NASA's laser altimeter ICESat, a database of percentage of tree cover from the MODIS satellite as a proxy for penetration depth of SRTM and a global vegetation height map in order to remove the vegetation artefacts present in the original SRTM DEM. The final ‘Bare-Earth’ SRTM product showed global improvements greater than 10 m in the bias over the original SRTM DEM in vegetated areas compared with ground elevations determined from ICESat data with a significant reduction in the root mean square error from over 14 m to 6 m globally.

(Zhao et al., 2018) used a linear regression based method to estimate the original SRTM DEM error and therefore corrected the SRTM DEM data. The results showed that the original SRTM DEM data is around 6 m higher than the actual land surfaces on average across all vegetation types. (Yamazaki et al., 2017) Introduced a high-accuracy global DEM at 3″ resolution (~90 m at the equator) by eliminating major error components from existing DEMs. The study separated absolute bias, stripe noise, speckle noise, and tree height bias of the original SRTM DEM by using multiple satellite data sets and filtering techniques to create the Multi-Error-Removed Improved-Terrain DEM (MERIT). After the error removal, land areas mapped with ±2 m or better vertical accuracy were increased from 39% to 58%. Significant improvements were found in flat regions where height errors larger than topography variability, and landscapes such as river networks and hill-valley structures, became clearly represented. The newly developed MERIT DEM has enhanced many geoscience applications which are terrain dependent.

The previous studies dealt only with vegetation biases and do not develop methodologies for the correction or removal of biases due to built structures in urban areas. Despite recent advances in developing vegetation corrected DEMs, the effect of building height errors in DEMs in urban areas are still poorly understood, and their correction remains a challenge. This study will present the first urban corrected global DEM using building density data, locally for Nairobi, Kenya. By comparing six global DEMs (SRTM, MERIT, AW3DD30, NASADEM, TanDEM-X 12 m, and TanDEM-X 90 m DEM) with a local reference DEM for the study area, a relationship is established between building density, derived from urban footprint map of the study area, and DEM error.

Despite recent advances in developing vegetation corrected DEMs, the effect of building height errors in DEMs in urban areas are still poorly understood, and their correction remains a challenge. There is lack of adequate research focused on the impact of building density on the vertical accuracy of global DEMs and how these errors can be assessed and corrected especially for urban areas. This research will aim to address this research gap by deriving a methodology for correcting building errors in freely available global DEMs with Nairobi, Kenya as a case study and can be applied to any other case study anywhere in the world where building density data and local reference DEM data are available.

Flooding is the most prevalent disaster worldwide accounting for 43% of all recorded global disaster events in the past 20 years leading up to 2018 Choy (2018). Rapid urban growth strains existing infrastructure and also discourages the preservation of natural habitat in favour of building more developments causing urban flooding. Climate change and urbanisation have been reported as the major contributors to the increasing damaging effects of flooding to lives and livelihoods worldwide (Aerts et al., 2014). There is lack of adequate research focused on the dual impacts of climate change and urbanisation on urban flooding and water quality in rapidly developing urban areas of the world – a gap that will result in an increase in fluvial and pluvial flood risk, and further reduction in water quality (Miller and Hutchins, 2017). This research aims to focus on the dual impacts of climate change and land use change (urbanization) of pluvial flooding in rapidly developing cities of the world in order to address this research gap and by doing so contribute to existing knowledge in this area.

This research will aim to highlight the importance of the use of free global datasets in the development of a city-scale 2D hydrodynamic models that assesses the impacts of land use change and climate change on urban pluvial flooding in rapidly developing cities. The built of a city scale hydrodynamic models will aim to assess the ability of a simplified city-scale hydrological and hydraulic models to estimate urban pluvial flood inundation in a large catchment, before going on to establish the impacts of climate change and land use change on flood hazard.

3.0 METHODS & DATA

3.1 Introduction

This study describes the development and testing of the HECRAS (2D) hydraulic model in terms of its ability to simulate surface water flows in rapidly developing urban cities using global datasets. Flood mapping is a crucial element of flood risk management since it provides the delineation of flood depth and extent in flood-prone areas. The creation of flood maps is usually performed using a combination of hydrologic and hydraulic models (Vojtek et al., 2019). Therefore, this study involves the development, testing and validation of hydrologic (HEC-HMS) and hydraulic (HEC-RAS) 2D flood model scenarios developed at a city-scale to simulate the impact of climate change and land use change on urban pluvial flood hazard in rapidly developing cities by using global datasets.

Five specific model scenarios (S1-S5) are developed and applied to a 5751 km^2 catchment (C1) of the city of Nairobi and environs. The **S1-Baseline** scenario uses the urban corrected DEM, 2020 land use map and March 2018 precipitation data as key input data. The **S2-2010LU** scenario is developed using the same key input data as S1-Baseline model apart from using land use the 2010 land use map for the catchment. The **S3-CP4uplift** scenario is developed using the 2020 land use map, the urban corrected DEM and future CP4 climate change rainfall model. The **S4-P25uplift** model uses the 2020 land use map, the urban corrected DEM and future P25 climate change rainfall model. The **S5-RawDEM** model is similar to the S1-Baseline model but uses a raw DEM as key input data instead of an urban corrected DEM. The five model scenarios are developed to simulate the impact of climate change and land use change on urban pluvial flood hazard in Nairobi, Kenya.

S1-S3 use a historic rainfall event between 1st and 13th March 2018, i.e. the S1-Baseline, S2-2010LU, and S5-RawDEM scenarios. The simulation of future flood events under climate change scenarios was undertaken using uplift factors derived from the CP4 and P25 climate rainfall models for the development of the S3-CP4uplift and S4-P25uplift models respectively. Also, this study involves the analysis of the scenario outputs for three sub-catchments (C2-Kiambu, C3-Nairobi, C4-Machakos), 804 km^2, 1015 km^2, and 723 km^2 respectively within the within the (C1) main catchment, Figure 33, Figure 34, Figure 35, and Figure 36. The purpose of the more focused analysis on the sub-catchments is to understand impacts more locally in different types of catchments.

3.2 Urban Flood Modelling Tools

Flood hazard and flood risk maps are key elements for flood risk management around the world. They are an essential tool for flood warning, mitigation of property damage and loss of life and for flood risk communication to the stakeholders (Costabile et al., 2020). Global climate is changing with increases in the frequency and intensity of extreme events, such as coastal flooding, extreme precipitation and heat waves (IPCC, 2014). This, together with rapid urbanisation and land use change, will cause even more severe floods and damage to urban areas in the near future (Zhou et al., 2012). Urban flooding has become one of the most significant natural hazards due to climate change and rapid urbanization (Wang et al., 2018) and significant efforts have been made to improve accuracy and efficiency of urban flood modelling through enhanced methodology and numerical methods (Bates et al., 2010). Therefore, the utilisation of computer models to simulate flood extent, depth, duration and flow velocity and their associated damages, using many flooding scenarios i.e. future climates and landuse change due to urbanization, is paramount (Jamali et al., 2018). Hydrodynamic models are applied to simulate fluvial and pluvial flooding. In pluvial applications, water is routed through typically urban areas and is driven by water originating from rainfall (Sampson et al., 2013).

3.3 2D Hydrodynamic Model Choice

A summary of the characteristics pertinent to urban flood models and a comparative summary of the relative advantages and disadvantaged of different models is presented in Table 1 and Table 2. A comparison of the HEC-HMS & HEC-RAS models used in this study with other shallow water equation models is presented in the tables. Urban flood modelling tools are in demand to predict surface water inundation caused by intense rainfall and to manage associated flood risks in urban areas. Kalihua et al. (2021) presented a comprehensive review of the advanced urban flood models and emerging approaches for predicting urban surface water driven intense rainfall. Hydrodynamic, shallow water-based models built upon simplified or full shallow water equations (SWEs) have demonstrated strong capabilities in providing more detailed flood information in urban areas, such as distributed floodwater depths and velocities.

Hunter et al. (2008) undertook the benchmark testing of six two-dimensional (2D) hydraulic models in terms of their ability to simulate surface water flows in a densely urbanize area and found all the models tested produced plausible results. Terrain data used as part of the study were found to be sufficiently accurate and resolved for simulating urban flows. Even though the simulations show that flows in urban environments are characterised by numerous transitions to supercritical flow and numerical shocks. However, the study found the effects of these are localised and they do not appear to affect overall wave propagation.

Criteria for Choice of Model

For the purpose of this research, the 2D hydraulic model used was selected based on the following criteria:

Rain on grid capabilities.
Suitability for a data sparse context of rapidly developing cities Not found to be data intensive i.e.
Ability to represent flood inundation over a large city-scale catchment
Computational efficiency to run multiple scenarios simulations at city-scale.
Less complexity and can achieve a trade-off between model complexity and resolution.

The HEC-HMS hydrological and HEC-RAS (U.S. Army Corps of Engineering, 2016) models are chosen for this study based on these criteria. The HEC-RAS model is a rain on grid model that is suitable and appropriate for extremely large catchment such as Nairobi, Kenya – the case study area. According to (Di Baldassarre, 2012a.), and as shown in Figure 1, as the model complexity increases, the bias (error) tends to decrease, but the uncertainty tends to increase. The main objective of choosing the 2D hydraulic model is to identify a modelling tool that will achieve a trade-off between model complexity and resolution of the input datasets. Model resolution can have a large impact on simulation time because model simulation time can increase by an order of magnitude by halving the model resolution (Savage et al., 2015).

Model computational time and model computational efficiency were a big factor in the choice of the modelling tools and the model should ideally take in order of minutes to hours to run at different resolutions under all the modelling scenarios considered in this study. When considering model application, data available, computational resources, time available, and the other criteria listed above, the HEC-HMS hydrologic and the HEC-RAS hydraulic models became the best models that give the required information and achieve the intended outcomes, whilst reasonably fitting the data. Because of the above, the choice of HEC-HMS and HEC-RAS models is justified. The models don’t rely on sophisticated data inputs making them appropriate for data-sparse environments similar to the case study area considered in this study.

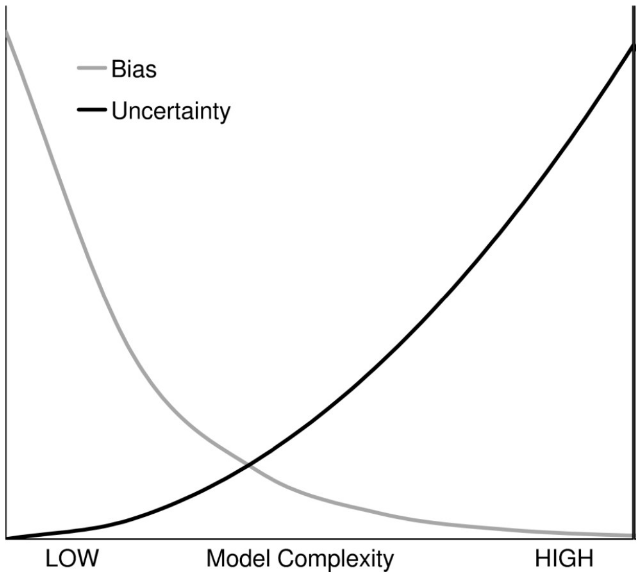

Figure 1. A concept of trade-off between bias (grey) and uncertainty (black) in model complexity. Adapted from (Di Baldassarre, 2012a.).

3.4 Shallow Water Equation Based Models

In recent years, hydrodynamic simulation of overland flows based 2-D shallow water equations (SWEs) has become increasingly popular and SWE models have proven to be capable of reproducing surface water flow reasonably well for flooding in urban areas, accurately predicting velocity, flood extent and water elevation level (Kaihua et al., 2021). Simplified SWE-based models have been typically used in larger-scale urban flood modelling with coarser grids and simplified treatment of urban features at city/continental scale because of the relatively low computational costs and the capability in simulating surface water dynamic (Yu et al., 2016, Xia et al., 2017). Consideration was given to the use of the HEC-HMS and HEC-RAS in this study, given the city-scale nature of the catchment and the coarse nature of the input datasets.

3.5 HEC-RAS Hydrodynamic Model for Surface Water Runoff

The HEC-RAS model has the ability to perform two-dimensional unsteady flow routing with either the full Shallow Water Equations (SWE) or the Diffusion Wave approximation of the SWE (DWE). HEC-RAS has three separate solvers that can be used to solve for the flow moving over the computational mesh, the Diffusion Wave equations; the original Shallow Water equations (SWE-ELM, which stands for Shallow Water Equations, Eulerian-Lagrangian Method), and a new Shallow Water equations solution that is more momentum conservative (SWE-EM, which stands for Shallow Water Equations, Eulerian Method). The 2D flood inundation modelling for this study was carried out using HEC-RAS 2D (U.S. Army Corps of Engineering, 2016). The HEC-RAS software is a 2D model grid model that is capable of simulating flooding caused by rainfall as well as river flooding (U.S. Army Corps of Engineering, 2016). The HEC-RAS 2D hydraulic model solves the full 2D Saint Venant equations and the 2D diffusive wave equation as described below (U.S. Army Corps of Engineering, 2016). The shallow water equations are shown in Equation 1, Equation 2 and Equation 3 and the diffusive wave equations used in this study are shown in equations 4 and Equation 5.

$$\frac{\partial h}{\partial t} + \frac{\partial}{\partial x}(uh) + \frac{\partial}{\partial y}(vh) = 0$$

Equation 1

$$\frac{\partial h}{\partial t} + \frac{\partial}{\partial x}(uh) + \frac{\partial}{\partial y}(vh) = 0$$

Equation 2

$$\frac{\partial}{\partial t}(uh) + \frac{\partial}{\partial x}(u^2h) + \frac{\partial}{\partial y}(uvh) = gh\left[S_{Ox} - \frac{\partial h}{\partial x} - S_{fx}\right]$$

Equation 3

$$\frac{\partial}{\partial t}(vh) + \frac{\partial}{\partial x}(uvh) + \frac{\partial}{\partial y}(v^2h) = gh\left[S_{Oy} - \frac{\partial h}{\partial v} - S_{fy}\right]$$

Equation 4

Where *t* is time, *u* and *v* are the velocity components in the x- and y- direction respectively, g is acceleration due to gravity and S_f represents slope of the energy grade line.

The diffusive wave equation is a simplification of the shallow water equation wherein inertial forces are neglected and only considers pressure, gravity and frictional forces. The diffusive wave equation option is the default option in HEC-RAS and gives a model output with better flood extent.

$$\frac{\partial h}{\partial t} + \nabla(uh) = R$$

Equation 5

$$\frac{\partial u}{\partial t} + (u\nabla)u + \frac{V_t}{h}(h\nabla u) + g\nabla(h + z) = g\,S_f$$

Equation 6

Where g is acceleration due to gravity, V_t is the Eddy viscosity coefficient, R is the hydraulic radius, S_f represents slope of the energy grade line, ∇ is the vector of the partial derivative operators represents bed slope and u,h represent velocity components under X and Y axis respectively.

Table 1. A summary of the characteristics pertinent to urban flood models (Kaihua et al., 2021).

Representative models		Model Equations	Acceleration Method	Rainfall runoff	drainage network module	Status
Drainage network models	Djordjevic et al. (1999)	ID Saint-Venant equations	No	No	Yes	Research
	Schmitt et al. (2004)	ID Saint-Venant equations	No	No	Yes	Research
SWE-based models	FloodMap (Yu, 2010)	2D diffusive wave model	MPI	Yes		Research
	LISFLOOD-FP (Bates et al. 2010)	Inertial formulation of 2D SWEs	OpenMP	No		Research
	[JIM (Chen et al. 2012)	2D diffusive wave model	No	Yes	HEC- 1	Research
	P-DWave (Leandro et al. 2016)	2D diffusive wave model	OpenMP	Yes	ID SaintVenant equations	Research
	PRIMo (Sanders et al. 2019)	2D SWEs based on upscaled grids	single process multiple data parallel algorithm	Yes	No	Research
	RMA (Rao 2005)	simplified 2D SWEs	MPI	Yes		Research
	UPFLOOD (Huang et al. 2019)	2D diffusive wave model	No	Yes	No	Research
	TRENT (Villanueva et al. 2006)	21) full SWEs	No	No	No	Research

Representative models		Model Equations	Acceleration Method	Rainfall runoff	drainage network module	Status
	Porosity-based models (e.g. Guinot et al., 2017; Bruwier et al., 2017)	2D full SWEs with porosity in coarse grids	No	No	No	Research
	CityCAT (Glenis et al. 2018)	2D full SWEs	Amazon Cloud	Yes	MFPmodel (Bourdarias et al. 2011)	Research
	Hou et al. (2018)	2D full SWEs	GPU	Yes	No	Research
	HiPIMS (Xia et al. 2019)	2D full SWEs	GPU	Yes	ID SaintVenant equations	Research
	Henonin et al (2015)	2D full SWEs	No	Yes	No	Research
	Liu et al. (2019)	2D full SWEs	GPU	Yes	No	Research
	HEC-RAS (Brunner, G. 2016)	2D full SWEs and diffusive wave equations.	No	Yes	No	Research
Hydrogeomorphic approaches	Nardi et al (2018)	hydrogeomorphic paradigm	No	Yes	No	Research
	GeoFlood (Zheng et al. 2018)	hydrogeomorphic paradigm	No	Yes	No	Research
Other methods	CADDIES-caflood (Guidolin et al., 2016)	cellular automata	GPU	No	No	Research
	Bermudez et al. (2018)	ANNs	No	Yes	Yes	Research

Table 2. Comparative summary of the relative advantages and disadvantages of different urban flood models (Kaihua et al., 2021).

Method		Strength	Limitation	Suitability
Drainage network models		computationally efficient suitable for various temporal and spatial scale evaluations quantification of flow in drainage systems	coarse spatiotemporal resolution no/little flow dynamics validation is very data and time demanding (large number of drainage nodes and pipes)	drainage system design and evaluation quantification of outflow of urban catchments a reference for other inundation models a tool coupled with surface water model
2D SWE based models	Simplified SWEsbased models	dynamic simulation of urban flooding within relative cheaper computational cost	cannot capture shock flood wave Less numerical accuracy compared with full SWEs no pipe flow consideration	urban flood mapping without high requirement on detailed flow dynamics faster urban flood simulations
	Full SWEsbased models	• full dynamic simulation shock-captured be able to simulate the flow infrastructure interactions	computationally expensive • high requirement for data inputs no pipe flow consideration or over assumption	quantification of local urban flood dynamics without pipe urban flood model in urban areas with high-quality DEM/DSM • design and evaluation of flood infrastructures
	Coupled with drainage network	can simulate drainage floods have potential to simulate urban flooding more accurately	computationally expensive requirement of good-quality data input	• quantification of drainage flooding simulation of local urban flood dynamics with pipe urban drainage design and evaluation
	Coupled with hydrological methods	computational efficient plus the strength of its coupled hydraulic models	currently no pipe consideration plus the limitation of its coupled hydraulic models	large-scale catchments where natural areas have equal runoff contribution with urban areas

Method	Strength	Limitation	Suitability
Hydro-geomorphic approaches	Less sensitive to data scarcity and time series data unnecessary Computationally efficient	cannot include the role of infrastructures and altered geomorphic signature in urban areas uncertainty of empirical data no flow dynamics re resentation	Preliminary identify inundation areas a reference for physically representative models.

3.6 HEC-HMS Hydrologic Model

The HEC-HMS (Centre for Hydrological Engineering - Hydrological Modelling Systems, US Army Corps of Engineers) rainfall runoff model is a software program that models the complete hydrologic process of dendritic watershed systems. The HEC-HMS software includes hydrologic analysis procedures such as event infiltration, unit hydrographs, and hydrologic routing including procedures necessary for continuous simulation of evapo-transpiration, snowmelt, and soil moisture accounting. HEC-HMS deals with the basic water balance equation and the transformation of the runoff from precipitation in the HEC-HMS model is governed by landuse, soil type, evapotranspiration, and storage.

The purpose of using the HEC-HMS hydrologic model for this study is to obtain runoff (net precipitation) from the precipitation data with HEC-HMS model. The obtained net runoff data is then simulated in HEC-RAS model and the output of HEC-RAS exported to QGIS software for flood plain mapping and analysis. The HEC-RAS 2D hydraulic model can simulate runoff based on channel morphology and generate flood inundation extent within the catchment. However, coupling the two models will aid in the assessment of flood inundation of the study area for the March 2018 storm event. The coupled model will be used for landuse change and climate change flood plain mapping with the future rainfall climate change rainfall data and landuse change scenarios described in chapter 5 and chapter 6. Details of the rainfall data, terrain data, soil types and landuse data used in the HEC-HMS model are shown in Table 3.

It is worth noting that the latest version of HEC-RAS (v6.1), available after this work for this thesis was completed, allows calculation of infiltration losses which could be used instead of using HEC-HMS in calculate net rainfall.

Table 3. Key Input Data for the HEC-HMS hydrologic rainfall runoff model.

SN	Data	Data source
1.	3 arc second MERIT Digital elevation Model (DEM)	Multi-Error-Removed Improved-Terrain DEM (MERIT DEM)http://hydro.iis.u-tokyo.ac.jp/~yamadai/MERIT_DEM/
2.	Land use data 2020	Globeland 30m resolution landuse data. http://www.globeland30.org/
3.	Soil type Data	FAO/UNESCO Soil Map of the World. https://www.fao.org/soils-portal/data-hub/soil-maps-and-databases/faounesco-soil-map-of-the-world/en/
4.	Rainfall, Evapotranspiration data	Kenya Meteorological Services. Ngong Road. Nairobi. Kenya.

3.7 The March 2018 Rainfall Events

Over the greater Nairobi region and indeed Kenya as a whole, 2018 saw the wettest March, April and May seasons over the 119-year record of the Global Precipitation Climatology Centre (GPCC) data, and the 118 years of CenTrends data (Kilavi et al., 2018). Locally in Nairobi, the capital city of Kenya, total rainfall values at the five stations exceeded the normal amounts by two to three times in March and one to two times in April (Kilavi et al., 2018). Precipitation data for the watershed was obtained from the Kenya Metrological Service for the March 2018 extreme rainfall from four rainfall-gauging stations at different locations within the watershed and shown in Table 4.

Table 4. Observed rainfall data (March 2018) at five rainfall stations in Nairobi, Kenya.

STATION	March Total Rainfall (mm)	Source
Dagoretti	260.3	Kenya Meteorological Service
JIKA	216.8	
Machakos	236.8	
Thika	375.3	

3.8 Weighted Average Curve Number

The SCS (NRCS) Curve Number is used for the quantification of infiltration loss during runoff calculation and can range from 0 (100% infiltration) to 100 (impervious, no infiltration). The overall CN of a watershed is the area-weighted average CN of each combination of soil type and land cover type. A weighted average curve number for the watershed will be required for use as input in the HEC-HMS model. Therefore, a three-step method for calculating area-weighted average curve number from landuse and hydrologic soil group (HSG) data was developed.

Step 1: Pre-process raster data. Global land cover map for 2019 and soil data for the study area were downloaded from https://lcviewer.vito.be/2019 and the Global Hydrologic Soil Groups (HSG) for Curve Number-Based Runoff Modelling website https://webmap.ornl.gov/ogc/dataset.jsp?ds_id=1566 respectively. The Global land cover data are 100 m resolution global maps of land cover & cover changes of different areas over certain years. The HYSOGs250m represents a global, gridded dataset of hydrologic soil groups (HSGs) with a resolution of approximately 250 m. It is important that the landuse raster file has the same extent, projected coordinate reference system and resolution value as the HSG raster file so that the two files can align together to create a Curve Number raster file. Therefore, the landuse and soil group data were resampled to 30 m using raster calculator tools in QGIS

Step 2: Reclassification of Landuse map. Using the Reclassify by layer tool in QGIS, the landuse raster file is reclassified to reduce landuse types to 4 and a CSV txt file for landuse class breaks is created and added to QGIS layer panel. The reason for the reclassification of the of the landuse categories is to simplify and streamline the curve number CN calculation procedure. The original landuse data for the study area in its 12 different types of land cover types will end up with 12 x 3 = 36 different combinations for CN assignment when combined with HSG soil types (1, 2, & 3).

Step 3: Combination of land cover raster file and soil HSG raster file. The final step involved the combination of the two raster files described above using GDAL Raster calculator of QGIS to create a Curve Number (CN) raster file. A simple logic equation expression is created for the CN calculation. Finally, using Zonal statistics tool of QGIS, a watershed boundary shapefile was loaded and parameters count, sum and mean are selected for statistics to calculate and use Curve Number (CN). Three new fields are added to the watershed boundary shapefile and the area-weighted average (curve Number (CN) for the watershed area is calculated as 86.122.

3.9 Model Validation

An essential component of hydrodynamic model evaluation is the ability to validate the predictions against previous recorded measurements. A one-week filed visit was undertaken to three flooding hotspots located within the study area between 20th and 27th March 2018 and involved travelling from Leeds, UK to Nairobi, the capital city of Kenya. The purpose of the site visit was to collect historic flood height level data to compare with the results of the models. The methodology for the setup of survey equipment and collection, pre-processing and processing of survey data is described below.

3.10 Extension of Controls and Topographic/Levelling Survey

The Control survey was undertaken using Differential Global Navigation Satellite Systems (DGNSS) technique. The GNSS Receiver used was a set of Topcon GR3 model with Serial Numbers 1888, 223. The existing control points were far from the some of the flooding hotspot sites visited, therefore, extension of controls was set up at the Westgate car park and at a location near the Thika super highway, and control points fixed. Geodetic GNSS receivers in static mode were used to do the observations. The points were established and fixed using iron pins in concrete (IPC). One set of the GNSS receivers was used as the base receiver whilst the other two receivers were set as the rovers.

The established points were continuously observed for two hours. During the observation, raw data were automatically recorded in the equipment after every ten seconds. The recorded raw data files were then downloaded from the equipment in TPS files being the file format for the Topcon equipment. The TPS files were then converted to rinex format using the toplink software. The rinex format files were then post-processed using Kolida Geo Office (KGO) post processing software to get the XYZ coordinates for the point.

3.11 CP4 & P25 Africa Rainfall Models

The Long-Rains wet season of March–May (MAM) over Kenya in 2018 was one of the wettest on record. Nairobi is frequently hit by large storms, which pose an immense threat to life and destruction of infrastructure. Due to climate change, the frequency and intensity of these events are increasing. Using the river catchments of Nairobi River & the Ngong River, the main aim of this chapter was to investigate and model the extent to which rapid urbanization and climate change increases flood hazard vulnerability to the local residents and infrastructure in Nairobi. The impact of climate change on the future pluvial flood hazard for the Nairobi & Ngong river catchment in Nairobi was investigated using future climate change rainfall uplift factors of 48% & 96% for 24-hour, 48-hour, 72-hour, 96-hour, 120-hour and 144-hour duration provided from the CP4 Africa & P25 future climate models (Stratton et al., 2018).

The CP4-Africa uses a 4.5-km horizontal grid spacing at the equator and run without a convection parameterization, nested within a global atmospheric model driven by observations at the sea surface, which does include a convection scheme. The results from the CP4-Africa simulation show substantial improvements in JJA average rainfall compared to the parameterized convection models, with most notably a reduction in the persistent dry bias in West Africa, giving an indication of the benefits gained from running a convection-permitting simulation over the whole of African continent. The model realistically captures hourly rainfall characteristics, unlike coarser resolution models. CP4A shows greater future increases in extreme 3-hourly precipitation compared to a convection-parameterised 25 km model (R25).

The dataset simulating current climate over Africa with a CP model at 4.5-km grid spacing (CP4), and a parameterized convection model at ~25-km grid spacing (P25), has been shown to improve the representation of both intensity and timing of rainfall associated with deep convection (Kendon et al., 2019). CP4A also shows future increases in dry spell length during the wet season over western and central Africa, weaker or not apparent in R25. These differences relate to the more realistic representation of convection in CP4A, and its response to increasing atmospheric moisture and stability (Stratton et al., 2018). One of the key objectives of this research is to model the impact of climate change i.e. climate rainfall on urban pluvial flooding at cityscale. Therefore, to achieve this objective, the CP4 Africa & P25 rainfall models have been adapted for use in the development of the S3-CP4uplift model and the S4-P25uplift model used in this study

The model produced current (MAM 2018) and future pluvial flood maps for a range of durations, which were then combined into the current and future lower & upper band worst-case scenarios for the CP4 Africa & P25 models respectively. These were used to assess the impact of climate change on pluvial flood hazard in the catchment. This included analysis on flood extent, depth, velocity, and hazard, comparing by current and future worst-case and by duration. The Long-Rains wet season of March–May (MAM) over Kenya in 2018 was one of the wettest on record. This paper examines the nature, causes, impacts, and predictability of the rainfall events, and considers the implications for flood risk management.

Several studies have been undertaken to examine eastern African climate change concluding on a broad range of rainfall projections (Cook and Vizy, 2013, Giannini et al., 2018, Ongoma et al., 2018, Osima et al., 2018, Rowell et al., 2016, Shongwe et al., 2011b, Thiery et al., 2016). The fast-growing population in East Africa is vulnerable to changing rainfall and extremes. (Finney et al., 2020), investigated both climate change response of key mesoscale drivers of eastern African rainfall, such as sea and lake breezes, and the spatial heterogeneity of rainfall responses. The results of the explicit model showed widespread increases at the end of the century in mean (~40%) and extreme (~50%) rain rates across the region. The effects of climate change are potentially disastrous for East Africa (Bornemann et al., 2019). (Nicholson, 2017), examined several aspects of the climate of eastern Africa and found that because of long-term climatic change, the region has become a major focus of meteorological research in recent years. Eastern Africa comprises of majorly ten countries including Rwanda, Kenya, Djibouti, Burundi, South Sudan, Uganda, Ethiopia, Somalia, Eritrea & Tanzania. The region has a history of extreme and devastating floods and out of the seven most flood-prone countries in Africa, five are in eastern Africa (Li et al., 2016).

These extreme rainfall events especially events which occur from March to May (MAM) have had devastating effects on the population in the region, especially when occurring in the same year (Nicholson, 2017). There is serious concern for the region's future because of the strong consensus that climate change will have a major effect on rainfall (Nicholson, 2017). East Africa is particularly vulnerable to extreme weather and climate events, due to limited resources and low adaptation capacity and (Bornemann et al., 2019) described the spatial character and large intermodel uncertainty of changes in temperature and rainfall metrics in the region. (Yang et al., 2014), examined how the East African long rains will respond to the warming climate forced by anthropogenic emissions of greenhouse gases (GHGs) and suggested the wet area getting wetter and the dry area getting drier. (Thiery et al., 2016), showed that Lake Victoria is projected to be a hotspot of future extreme precipitation intensification by using new satellite-based observations, a high-resolution climate projection for the African Great Lakes and coarser-scale ensemble projections. The study found the future increase in extremes over Lake Victoria is about twice as large relative to surrounding land under a high-emission scenario, highlight a major hazard associated with climate change over East Africa and underline the need for high-resolution projections to assess local climate change.

Rapid urban sprawl is taking place in East Africa, and according to (UN-DESA, 2018) the urban population in East Africa increased from 21 to 27% during 2000 to 2015, and the expectation is that the trend will continue by 2030 to reach 34% resulting in increased pressure on urban infrastructure and frequent urban flooding. Nairobi, Kenya is chosen as the case study city for this research because it is imperative that urban flood modelling tools that can model the impacts of urbanization and climate change on flooding (LREA) of the MAM months are available for use to decision makers, policy makers etc. within a framework that enables prioritisation of climate-resilient development, utilising cost-effective measures to tackle risks.

Until CP4, future climate projections across Africa have been provided by relatively coarse resolution (order 10–100 -km grid spacing) climate models (Christensen et al., 2007). These models rely on a parameterisation scheme to represent the average effects of convection that introduces error into the model, especially in the tropics where convection is integral to circulation and extremes (Kendon et al., 2019). Convection parameterisation schemes often produce very intermittent rainfall and fail to capture organised propagating systems, instead simulating unrealistically widespread light daily total and insufficient heavy rain (Stephens et al., 2010). The uncertainty with climate change-projection for Africa makes it difficult to predict the impacts of climate change and develop adaptation strategies (Rowell et al., 2016). The Pan-African Convection-Permitting Regional Climate Simulation with the Met Office Unified Model: CP4-Africa is a convection-permitting multiyear regional climate simulation using the Met Office Unified Model has been run for the first time on an Africa-wide domain. The model was run as part of the Future Climate for Africa (FCFA) Improving Model Processes for African Climate (IMPALA) project (Stratton et al., 2018).

3.12 Summary

This chapter has outlined methods and approaches of how floods are modelled and a provided a discussion of the choice of HEC-HMS and HEC-RAS for the hydrodynamic modelling used in this thesis. Further discussion of the setting up and development of the HEC-HMS and the HEC-RAS models are described in further detail in subsequent chapters. This chapter also covers the climate model choices for future climate scenarios and field work methods used for model validation. Further chapter specific methods and data are detailed in each chapter as needed.

4.0 URBAN CORRECTION OF GLOBAL DEMS

4.1 Introduction

Rapid urban growth puts strain on existing infrastructure and discourages the preservation of natural habitat in favour of new housing developments, shopping malls, urban infrastructure, etc. that can exacerbate the problem of urban flooding. Flooding is the most prevalent natural disaster, often characterised as a high intensity event that requires rapid emergency service response in order to minimise substantial human and economic losses (Apel et al., 2009). Climate change and urbanisation have been reported as the major contributors to the increasing damaging effects of flooding to lives and livelihoods worldwide (Aerts et al., 2014). Topography has been identified as a key method of estimating flood extent (Horritt and Bates, 2001) and many models of flood extent rely on DEMs in order to simulate paths of water flow, flood extent and depth. Errors in DEMs (DEMs) can substantially affect the results of flood models (Stephens et al., 2012, Hawker et al., 2018).

Global DEMs used in flood models are representations of physical ground surface and the spatial resolution of a DEM refers to the area of land being represented by single regular or irregular grid, with the value of each grid element representing the height of the ground at the corresponding datum (Vaze et al., 2010). There are many open access global scale DEMs such as the Shuttle Radar Topography Mission (SRTM), and its derivatives, the Multi-Error-Removed Improved-Terrain DEM (MERIT DEM) and NASA DEM (NASADEM), as well as Advanced Spaceborne Thermal Emission and Reflection Radiometer (ASTER) DEM and TerraSAR-X add-on for Digital Elevation Measurement (TanDEM-X 90m) etc. The global coverage of these DEMs makes them highly suitable for use in scientific applications where they are used extensively in flood models and have been critical in facilitating important flood studies, particularly in data-sparse areas, where local data is often difficult to access or unavailable (Hawker et al., 2018).

Chen and Hill (Chen and Hill, 2007) investigated the influence of DEM resolution on flood hazard modelling in urban areas and found that both vertical height error and spatial resolution of DEMs can impact on flood inundation depth and extent in urban flood modelling. Although, spaceborne DEMs provide fundamental input to many geoscience studies, they suffer from non-negligible height errors (Yamazaki et al., 2017). Sources of error in spaceborne DEMs include: (i) incomplete spatial sampling; (ii) measurement errors, such as positional inaccuracy, data entry errors; and (iii) processing errors such as computational numerical errors, interpolation errors, and classification and generalisation errors (Burrough, 1986). Global DEMs suffer from many different types of errors, some of which are significant at local scales; for example, (Rodríguez et al., 2006) reported a global mean and standard vertical height error of 8.2 ± 0.7 and 6.9 ± 0.5 m for SRTM X- and C-band data, respectively. There is a number of published work on the correction of errors in global DEMs, especially vegetation errors. (Falorni et al., 2005, Bhang et al., 2007, Dong et al., 2015, Gallant et al., 2012, Baugh et al., 2013, O'Loughlin et al., 2016, Chen et al., 2018). Also, there are many previous studies focused on the assessment of the vertical height accuracy of DEMs by comparing elevation values of DEMs to that of a reference local DEM having a higher vertical accuracy. A more accurate reference DEM such as the Light Detection and Ranging (LiDAR) is required in order to make an assessment of the vertical accuracy of global DEMs (Dong et al., 2015, Wessel et al., 2018, Acharya et al., 2018).

Although many studies (Robinson et al., 2014, Yamazaki et al., 2012, Yamazaki et al., 2017) have developed new vegetation-corrected DEMs, by either editing or adjusting existing global DEMs. However, despite significant advances in developing vegetation-corrected DEMs, there is limited understanding of DEM errors that can be attributed to building heights and building density in urban areas. Local DEMs that are based on airborne light detection and ranging (LiDAR) are preferential over open access, global DEMs due of their superior vertical accuracy, horizontal resolution, and ability to distinguish between ‘bare earth’ from built structures and vegetation (Yamazaki et al., 2017). However, (LiDAR) DEMs (<10 m horizontal resolution) are only available for a very small percentage of Earth's land surface (~0.005%), and data acquisition is often expensive (Hawker et al., 2018).

Building heights and building density inhibit the ability of radar signals to penetrate land surfaces, especially in densely populated urban areas where higher DEM resolution does not necessarily ensure accurate mapping (Rossi et al., 2012). Gridded elevation datasets, such as the radar-measurement-derived SRTM, exhibit signal reflection from built structures and vegetation so that further data processing may be required to enable accurate flood modelling (Sanders, 2007b). (Kim et al., 2020) selected the SRTM and Sentinel 2 multispectral imagery to train the artificial neutral network in order to improve the quality of SRTM DEM and then evaluated the performance of the resulting SRTM DEM over two dense urban cities. The ‘new’ DEM (iSRTM) showed better results than the original SRTM, achieving 38% reduction in the root mean square error (RMSE). Similarly, (Klonner et al., 2015) leveraged on the advantages of the Airborne Laser Scanning (ALS) and the Open Street Map (OSM) to create an up-to-date Digital Surface Model (DSM) combining 2D OSM and ALS data.

Digital surface models (DSMs) can provide a good source of high quality data for the extraction of building height maps in urban areas and (Alganci et al., 2018) explored the feasibility of using open access DSMs, such as the ALOS (AW3D30), ASTER, and SRTM datasets, for extracting digital building height models and compared their accuracy. The potential for DSMs as a rich data source for the extraction of building height data has been highlighted as a significant challenge in their use at the same time as representations of DTM in urban flood modelling (Alganci et al., 2018). Despite efforts made in the processing of global DEM data prior to making the data publicly accessible, DEMs frequently contain artefacts such as spikes, holes and line errors. (Hirt, 2018) recommended that all DEM datasets undergo a complete global screening for artefacts prior to public release, further advising users to check quality before using global DEMs. Despite recent advances in removing error components from DEMs, such as tree height bias, speckle noise, stripe noise and absolute bias, much work remains in the urban correction of building biases in global DEMs.

According to (Hawker et al., 2018), there is no forthcoming high-accuracy open-access global DEM, therefore, for the foreseeable future, the primary means of improving flood simulation will be to use editing or stochastic simulation using existing DEM data. Urban correction of existing global DEMs remains a key research challenge. In this context, the present paper develops a methodology for the urban correction of six global DEMs, tested using building density data from the city of Nairobi, Kenya. Although the scope of this study is currently limited to the use of building density data, however, we anticipate that once building height data becomes globally available, our methodology can be extended to urban correction of DEMs using building height data.

4.2 Study Site

Nairobi is the capital and largest city of Kenya and chosen as the study area for this research due to its rapid urban expansion within the last two decades, Figure 2. Nairobi has witnessed a population growth from 0.51 to 4,397,073 million people at a growth rate of 3 to 4% per year in past 50 years leading up to the 2019 national census (KNBS, 2019). The lies within an administrative area of 696 km^2 (269 sq mi), whilst the metropolitan area has a population of 9,354,580. The city lies on the River Athi in the southern part of the country and has an elevation of 1,795 metres (5,889 ft) above sea level (Nippon, 2014). Approximately 2 million people that make up nearly half the population of Nairobi live in the informal settlement area (5%) of the city occupying meagre 1% of the total 696 km^2 land area (Amnesty-International, 2019)

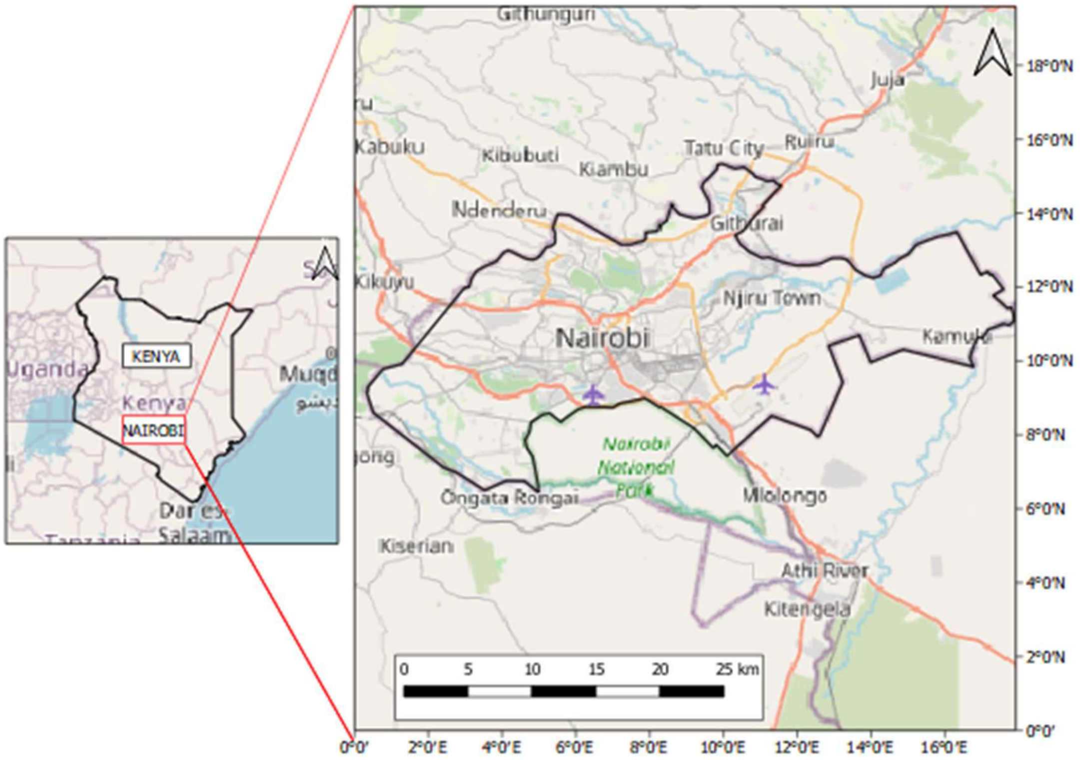

Figure 2. Map of the study area showing Nairobi

In their recent work (Henderson et al., 2016), developed a dynamic model of a growing city that shows the urban expansion of Nairobi, Kenya. The study highlighted the nature of the intensified land use within Nairobi and its increasing building heights, with a key distinction between formal and informal, or slum sectors. The study painted a picture of the built environment of Nairobi, both in the spatial cross-section and its evolution through time between 2003 and 2015. The built volume of the whole city increased at 3.9% p.a., expanding by 59% between 2003 and 2015. The growth and expansion within the central business district and formal sector redevelopment increased building volume by 35%. The expansion in the city was achieved by the demolition of over one third of buildings and redevelopments that saw three times increase in building heights. The study painted a picture of a monocentric city with tall but variable building height at the centre and then diminishing moving away from the centre of the city.

4.3 Dataset Description

Global DEMs derived from spaceborne and remote sensing data, and which are used in many global flood studies, are important data sources of ground surface height information (Hawker et al., 2018). DEMs are a type of raster, regular or irregular grids of spot heights that provide a three-dimensional (3D) model of the earth surface that can be categorised into two groups: (i) digital terrain models DTMs, which are free of trees, buildings, and all other types of object; and (ii) digital surface models DSMs (Figure 3), which reflect the earth's surface, including all man-made, natural objects and other features elevated above the 'Bare Earth' (Martha et al., 2010, Maune and Nayegandhi, 2017).

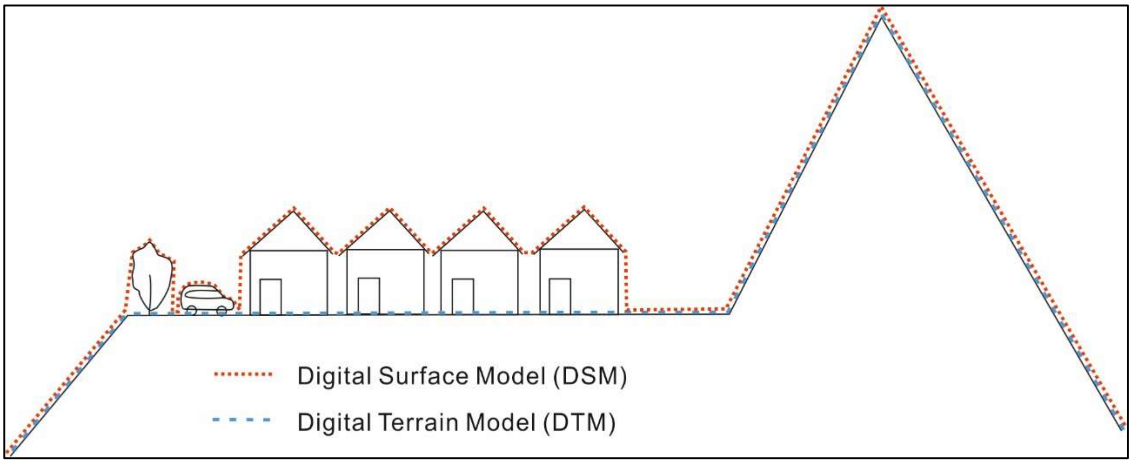

Figure 3. Difference between DSM and DTM (both DEMs)

DTMs are obtained by different methods such as the interpolation of contour lines that include not only heights and elevations, but also other geographical elements and natural features such as rivers, ridge lines, and so on (Moore et al., 1991). Whilst DSMs are mostly used for landscape modelling and applications for projection of cities in 3D, etc, DTMs have applications for global flood modelling, geoscience studies, drainage modelling, land use studies etc (Rayburg et al., 2009, Alganci et al., 2018). In this study, we focused on six of the most widely used global DEMs as fundamental input for many geoscience studies: SRTM; MERIT; ALOS; NASADEM; TanDEM-X 12 m; and TanDEM-X 90 m. Figure 4 provides an illustration of the visual comparison of the six global DEMs over the study area of Nairobi, Kenya whilst Table 5 shows a summary of the characteristics of the global DEMs used in this study.

Table 5. Characteristics of the six global DEMs used in the study.

DEM	Resolution (m)	Vertical accuracy (m)	Reference
SRTM	90	6 m (MAE)[a]	(Farr et al., 2007)
MERIT	90	5 m (LE90)[b]	(Yamazaki et al., 2017)
ALOS	30	4.4 m	(Tadono et al., 2016)
NASADEM	30	< 6 m ((MAE)[a])	(Buckley et al., 2020)
TanDEM-X	12 & 90	<10 m	(Mason et al., 2016)

[a] Mean error

[b] 90th percentile linear error

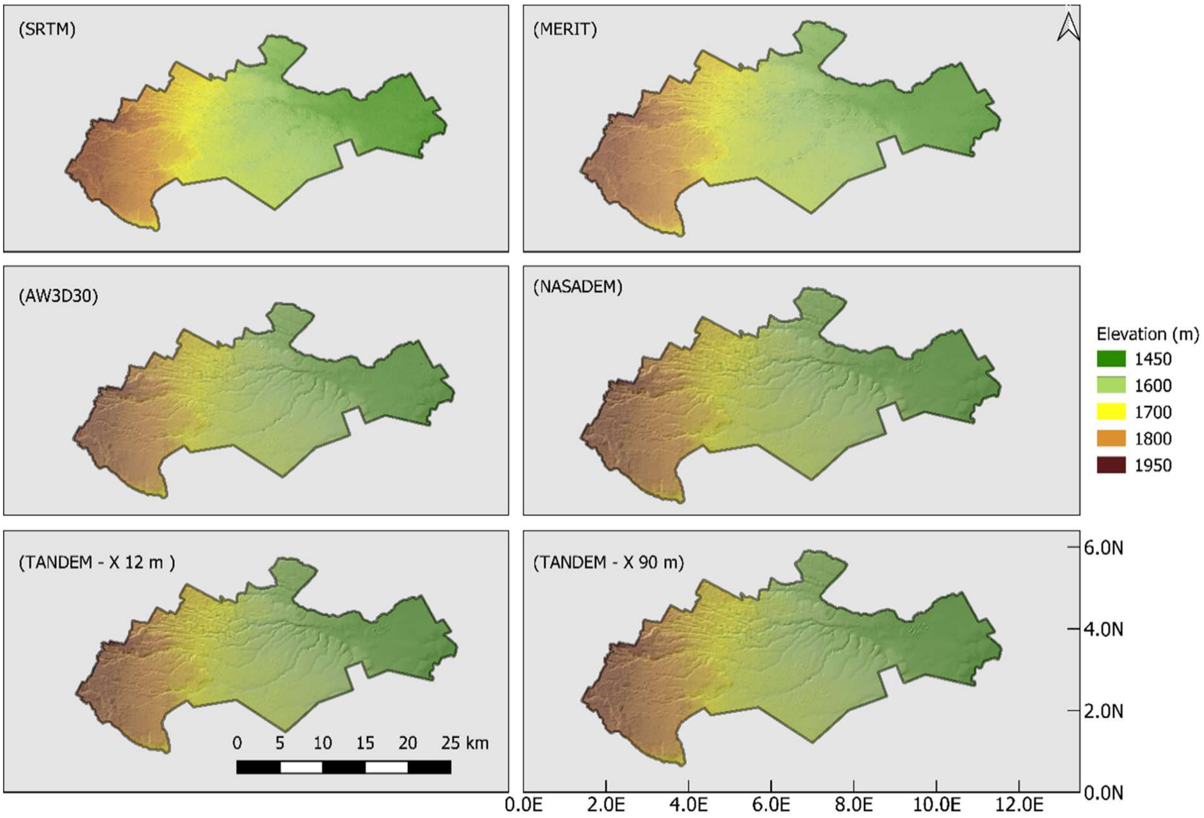

Figure 4. Visual comparison of the six global DEMs, applied in Nairobi.

4.4 Global DEMs

The Shuttle Radar Topography Mission (SRTM) was a joint endeavour of NASA, the National Geospatial-Intelligence Agency, and the German and Italian Space Agencies that flew in February 2000. It used dual radar antennas to acquire interferometric radar data, processed to digital topographic data at 1 arc sec resolution (Farr et al., 2007). Three official versions of SRTM have been released. Version 1.0 is the (almost) raw data obtained during the mission and its quality is considered research-grade. The Non-Void Filled version 2.1 is the data from Version 1 cleaned-up to correct processing errors and to clip data to water boundaries. This version still contains "void" areas for which there is no elevation data. These void areas are due to problems obtaining data using the radar methodology, such as in areas with steep terrain, and areas of low reflectivity such as flat deserts. The last official version of the SRTM (V3 or "SRTM Plus")) data with 01″ resolution (~30 m at the Equator) removes all of the void areas by incorporating data from other sources such as the ASTER GDEM and was publicly released in 2014 (Kolecka and Kozak, 2014).

The Multi Error removed Improved Terrain (MERIT) DEM was developed by removing multiple error components (absolute bias, stripe noise, speckle noise, and tree height bias) from the existing spaceborne DEMs (SRTM3 v2.1 and AW3D-30m v1) using multiple satellite data sets and filtering techniques (Yamazaki et al., 2017). MERIT represents the terrain elevations at a 3sec resolution (~90m at the equator), and covers land areas between 90N-60S, referenced to EGM96 geoid. Following the removal of the various error components, land areas mapped with ±2 m or better vertical accuracy were
increased from 39% to 58%. Significant improvements were found in flat regions where height errors larger than topography variability, and landscapes such as river networks and hill-valley structures, became clearly represented (Yamazaki et al., 2017).

SRTM produced an unprecedented near-global DEM of the world (Farr et al., 2007). Since its release, the SRTM DEM is widely used in many research studies, commercial, and military applications. The objective of the NASADEM project was to improve the SRTM DEM vertical height accuracy and data coverage. The improvements were achieved by reprocessing the original SRTM radar echoes and telemetry data with updated algorithms and auxiliary data not available at the time of the original SRTM production (Crippen et al., 2016, Vaka et al., 2019). One known issue of the SRTM DEM is the observed height ripples caused by uncompensated SRTM antenna boom motion. The NASADEM compensate for these elevation ripples based on a high-resolution correction of strip data in radar geometry (Crippen et al., 2016). The NASADEM data is available for download via https://lpdaac.usgs.gov.

The TanDEM-X (TerraSAR-X add-on for Digital Elevation Measurements) is a spaceborne radar interferometer that is based on two TerraSAR-X radar satellites flying in close formation since 2010 to map all land surfaces at least twice and difficult terrain mapped even up to four times. Krieger et al. (2007). The TanDEM-X Digital Elevation Model (DEM) is a DEM with a complete global coverage at 3 arc-seconds resolution (~90 m at the equator) of the earth's surface (Zink et al., 2016). The TanDEM-X 90 m resolution DEM product is open and free for download from https://download.geoservice.dlr.de/TDM90/ but the 0.4 arc second (12 m resolution) version is only free to the science community for educational purpose. An application was made to the German Aerospace Centre for the release of TanDEM-X 12 m DEM used in this study.

Accuracy assessment of the TanDEM-X 90 m DEM used in this study has been undertaken by different studies to determine their suitability for global flood modelling and found the TanDEM-X DEM has improved flood inundation predictive capacity when compared to other DEMs, but not MERIT (Wang et al., 2012, Yan et al., 2015, Mason et al., 2016). (Hawker et al., 2019), carried out error accuracy assessment of the TanDEM-X DEM on the freely available TanDEM-X 90 for selected floodplain sites in comparison to other popular global DEMs with results indicating that the average vertical accuracy of TanDEM-X 90 and MERIT are similar and are both a significant improvement on SRTM. Also, results suggested that TanDEM-X 90 is the most accurate global DEM in all land cover categories tested except short vegetation and tree-covered areas where MERIT is demonstrably more accurate.

The ALOS World 3D – AW3D30 (ALOS) global DEM data were produced using the data acquired by the Panchromatic Remote Sensing Instrument for Stereo Mapping (PRISM) operated on the ALOS from 2006 to 2011 (Takaku et al., 2016). The operator of the satellite is the Japan Aerospace Exploration Agency (JAXA) and the mission led to the production of the global ALOS DEM using approximately 3 million images. The free version of the DEM has a 1″ resolution, which is equivalent to approximately 30 m at the Equator and model is downloadable in 1°×1° tiles. The grid elevations (m) are referenced to the EGM96 geoid and the geographic coordinates are referenced to the GRS80 ellipsoid (Caglar et al., 2018). The dataset is downloadable from: www.eorc.jaxa.jp/ALOS/en/aw3d30.

4.5 Facebook High Resolution Settlement Layer (HRSL) Data

Facebook, in partnership with the Centre for International Earth Science Information Network (CIESEN) at Columbia University developed population grids dataset for 140 countries by using machine learning applied to high resolution satellite imagery (Tiecke et al., 2017). The high resolution settlement layer (HRSL) provides estimates of human population distribution at a resolution of 1 arc-second (approximately 30 m) using population estimates assigned to settlements delineated by machine learning algorithm in both urban and rural areas. Each 30 m grid has a population value assigned to an identified structure. For building density purposes, the data assumes grids with no population have no buildings and those with population have a building covering the whole grid. The Data is accessible via https://data.humdata.org/dataset/highresolutionpopulationdensitymaps

4.6 Sentinel-1 SAR Data Derived Global Building Map

(Chini et al., 2018), introduced a technique for automatically mapping built-up areas using synthetic aperture radar (SAR) backscattering intensity and interferometric multi-temporal coherence generated from Sentinel-1 data. The data represents global building maps in 20 m resolution and derived from multi-temporal InSAR coherence, a systematic and consistent feature that allows for a better characterization of urban areas. The urban footprint data are on average in 92% agreement with the Global Urban Footprint (GUF) map derived from the TerraSAR-X mission data (Chini et al., 2018).

4.7 Reference Topography Relief Map Data

As a reference raster, we used data from an interpolated contour map of Nairobi, which has an estimated vertical error of ± 2 m and is derived from aerial photogrammetry. The detailed contour map was produced- in 2003 by the Japanese International Co-operation Agency (JICA) for the government of Kenya (Nippon, 2014). In 2003, JICA performed an aerial triangulation that mapped the entire city of Nairobi (595 km^2), excluding the Nairobi National Park (~107 m^2); the mission required 15 aerial photography flight strips over Nairobi, including 20 GPS validation photo points. The standard deviation (SD) of the final coordinates of all the newly installed photo control points was within an acceptable limit (within 30 cm vertical height error). JICA released this data for use in the present study, providing the original topography contour map as a vector file which we converted to a raster elevation file using the TIN Interpolation plugin conversion tool in QGIS.

4.8 Methodology

4.9 Procedure for urban correction of global DEMs

A five-step method is developed for removing building density error from the six global DEMs namely: (i) NASADEM, (ii) SRTM, (iii) MERIT, (iv) ALOS, (v) TanDEM-X 12 m, and (vi) TanDEM-X 90 m. presents a flowchart of the datasets and methodology used in the five-step method, and each step is also described in detail.

This five-step method is first applied to the whole of greater Nairobi area, followed by a separate application to just the Central Business District. The CBD area is the commercial hub of Nairobi and is composed of tall buildings, skyscrapers, government offices etc. and it should provide some insights into the effect of building heights on DEM errors.

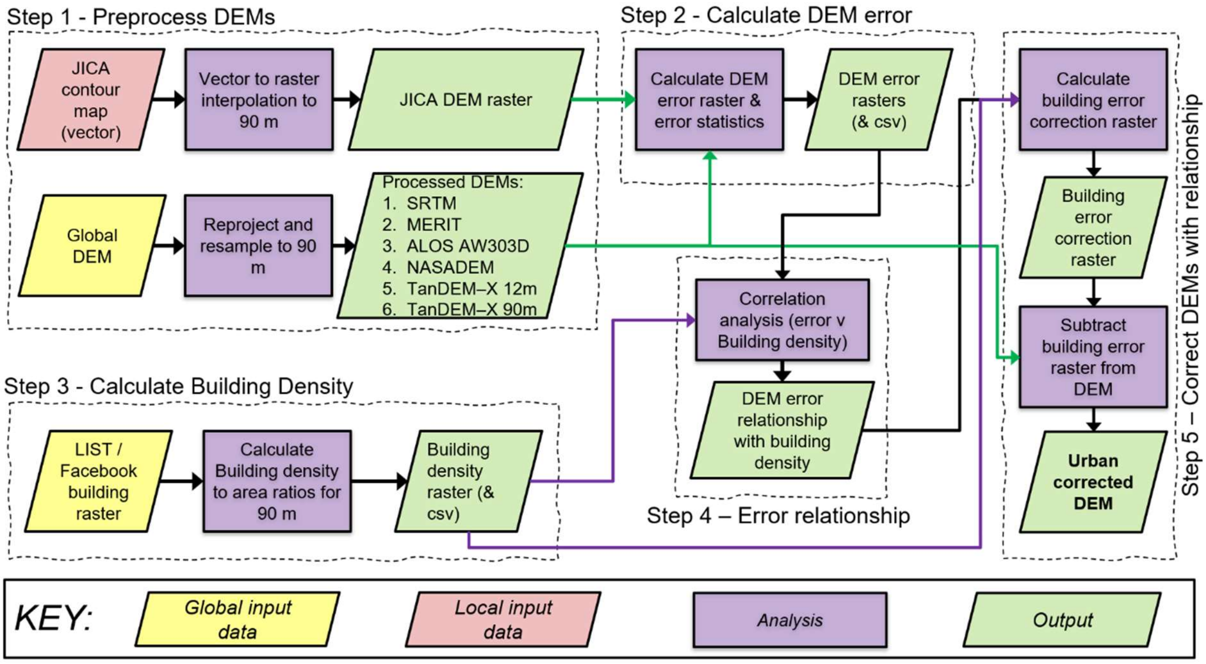

Figure 5. Flowchart of the datasets and methodology used to correct building density errors in global DEMs in our five-step method. This can be applied to any spatial extent.

Step 1: Pre-process raster data. To allow for consistent geospatial analysis, all six global DEMs data were transformed to the EGM96 Geoid, if not already, and resampled to a 90 m raster resolution. This was carried out for all six global DEMs and for the reference DEM. The resampling was carried out using the bilinear method using QGIS (v3.12) raster resampling tools. The SRTM, MERIT, ALOS, NASADEM elevation data are orthometric heights referenced to the EGM96 Geoid, whilst the TanDEM-X 12 & 90 m elevations are referenced to the WGS84 (G1150) ellipsoid. Therefore, in order to compare elevations, the TanDEM-X 12 m & TanDEM-X 90 elevations were transformed to the EGM96 Geoid using the NOAA’s VDatum transformation tool, version 4.0.1 accessible via (https://vdatum.noaa.gov/). Using QGIS Triangulated Irregular Network (TIN) interpolation plugin tool, we created a DEM raster map of the study area from the original topography contour map of the study area to serve as the reference DEM, resampled to 90 x 90 m grids to match the horizontal resolution of the global DEMs.

Step 2: Calculate global DEM error. Using the GIS raster algebra tool, vertical accuracy is calculated for the six global DEMs by creating error maps as shown in Figure 6. The error rasters are produced by subtracting elevations of the JICA reference DEM, which has a higher vertical accuracy, from the six global DEMs of the study area, (Equation 1). The root-mean square error (RMSE), mean error (ME), standard deviation (SD) and median (M) are then calculated for each global DEM. The differences in the elevations of global DEMs are analysed by using error metrics, density distribution plots and the DEM error maps.

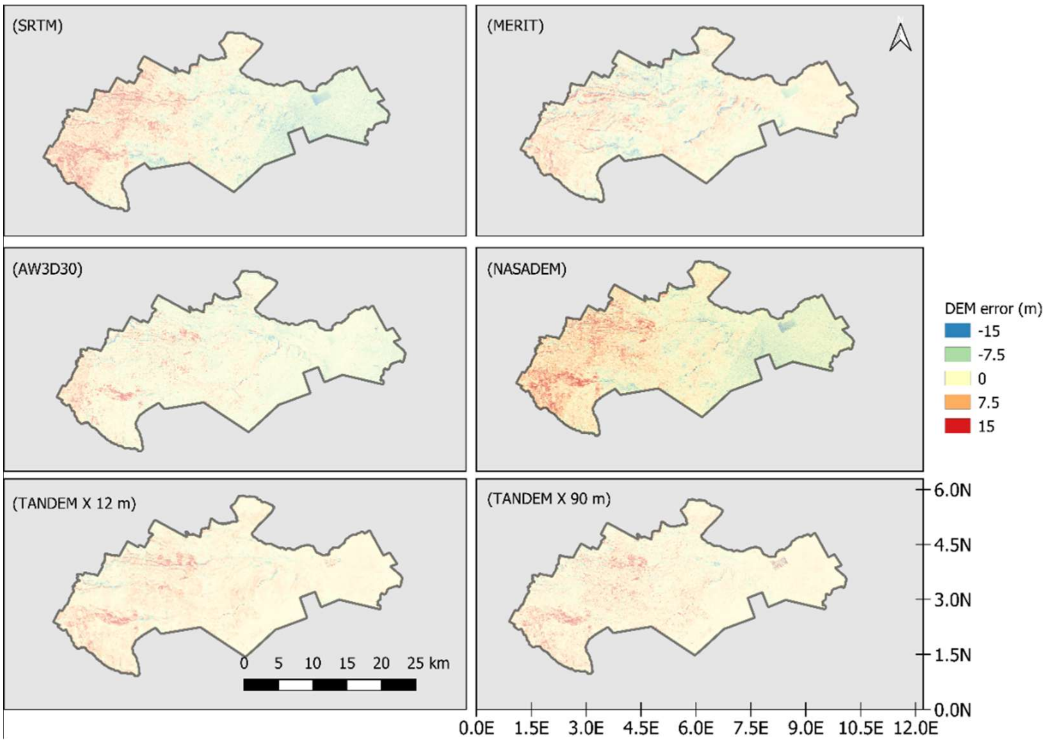

Figure 6. Error map of global DEMs at 90 m resolution

$$Error\ of\ DEM = Y_{GD} - Y_{ref}$$

Equation 7

$$ME = \frac{1}{n}\sum_1^n Y_{GD} - Y_{ref}$$

Equation 8

$$RMSE = \sqrt{\frac{\sum_1^n \left(Y_{GD} - Y_{ref}\right)^2}{n}}$$

Equation 9

$$SD = \sqrt{\frac{\sum_1^n \left(\left(Y_{GD} - Y_{ref}\right) - ME\right)^2}{n}}$$

Equation 10

where *Y* is elevation in metres, *GD* refers to the global DEM, and *ref* refers to the reference JICA elevation.

Step 3: Calculate building density. The building density rasters are calculated by processing the Facebook high-resolution settlement layer data (HRSL) and the Sentinel-1 SAR urban footprint map developed by LIST to generate building density maps. We resampled the HRSL and Luxe bough Institute of Science & Technology (LIST) building maps to a coarser grid size and using GIS raster aggregation tools, an aggregate is computed over all of the input raster grids whose centres lie within the output grid of a coarser resolution (270 x 270 m) urban footprint map of the study area. QGIS tools (qgis/grass/*r.resamp.stats) are used to resample the building maps to a* coarser grid using aggregation to generate building density maps. An aggregate is computed over all of the input raster grids whose centres lie within the output cell. The aggregate uses the values from all input raster grid cells of 20 m resolution of the LIST building map which intersect the coarser resolution (270 m) output cell, weighted according to the proportion of the source cell which lies inside the output cell to generate building density maps for the study area. The aggregate uses the weighted values to create a building density raster with a building to land area fraction within the study area of between 0 and 1 Figure 7.

A visual comparison of the Facebook HRSL and the LIST data with google earth image of the study area show that the LIST urban footprint map is of better agreement with building footprint of the study area. Therefore, the building density map derived from the LIST urban footprint map is found to be of higher accuracy in comparison to the output building density map derived from the HRSL population density map, Figure 7. The higher resolution nature of the LIST data i.e. 20 m compared to the 30 m for the Facebook HRSL data is a plausible explanation for the differences in the results and accuracy of the two output maps. Consequently, the study is progressed based on the use of the building density map derived from the LIST urban footprint map for the study area.

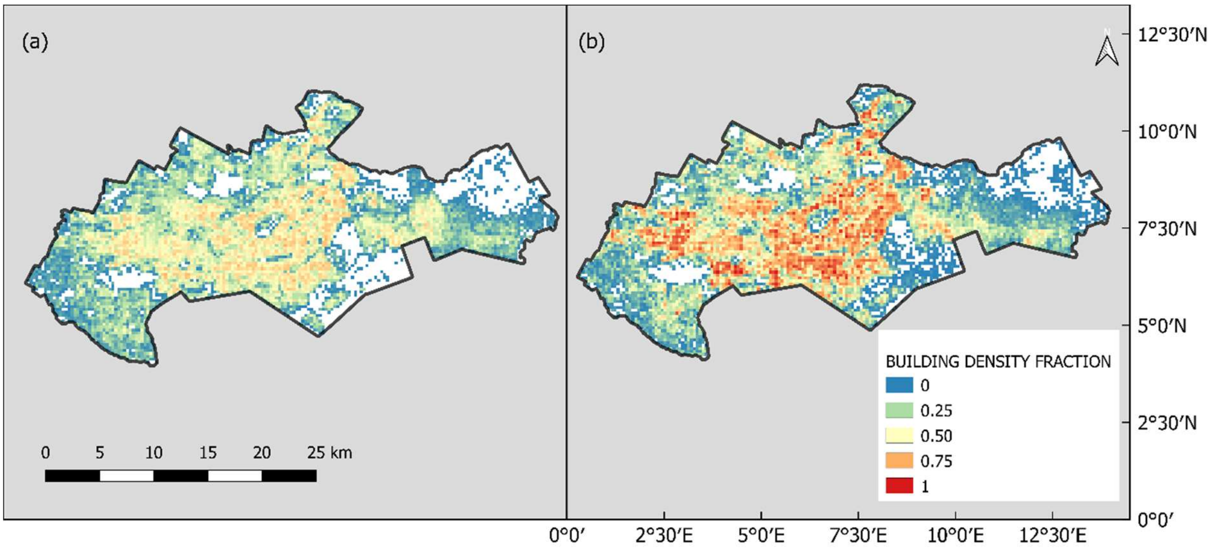

Figure 7. Building density raster of Nairobi derived from (a) the Facebook HRSL population density map, and (b) global urban building map.

Step 4: Determine DEM error relationship with building density. In order to calculate the building density error for each tile of the global DEMs, a relationship is established between DEM error and building density. Using the gdalqxyz plugin in QGIS tools, raster values for the error maps and building density maps are exported from the GIS platform and converted the exported data to csv format for further processing. Plots of DEM error versus building density are created for all six global DEMs represented by a linear regression fit and R^2 values as illustrated in Figure 10. As is common in other DEM correction studies, a linear relationship is used due to the noisiness of the data (Baugh et al., 2013) and (O'Loughlin et al., 2016). The resulting DEM error coefficient for each DEM represented increases in mean error measured in meters for every increase in building density and set between 0 and 1, with zero representing areas of no buildings at all and value of 1 for very dense areas respectively.

Step 5: Apply error relationship to correct global DEM. The next step is to remove the fraction of vertical error component that is associated with building density. This is calculated for each DEM grid, grid-by-grid from the linear regression functions by using the DEM error coefficient, building density predictor, and a constant value, (Figure 10). The procedure is repeated for all six global DEMs. Subsequently, using the raster calculator tool in QGIS, a building density error map is created for each of the global DEMs with an example for the SRTM DEM shown in Figure 11a. The building density error maps are created using the linear regression function for each of the global DEMs and the building density map derived from the LIST urban building map. To create the new urban corrected DEM for all six global DEMs, building density error map is subtracted from the original global DEM to arrive at the final product illustrated with the SRTM DEM in Figure 11b. The new product is the urban corrected NASADEM, SRTM, MERIT, ALOS, TanDEM-X 12 m, TanDEM-X 90 m DEM for Nairobi, Kenya.

The Central Business District (CBD) area (Figure 8) of Nairobi features many tall buildings, government offices, skyscrapers etc. and we wanted to understand if taller buildings will provide some further insights into the nature of the error. Therefore, the analysis of the urban correction of the global DEMs is extended to the CBD area by repeating the 5 steps described above for the CBD area.

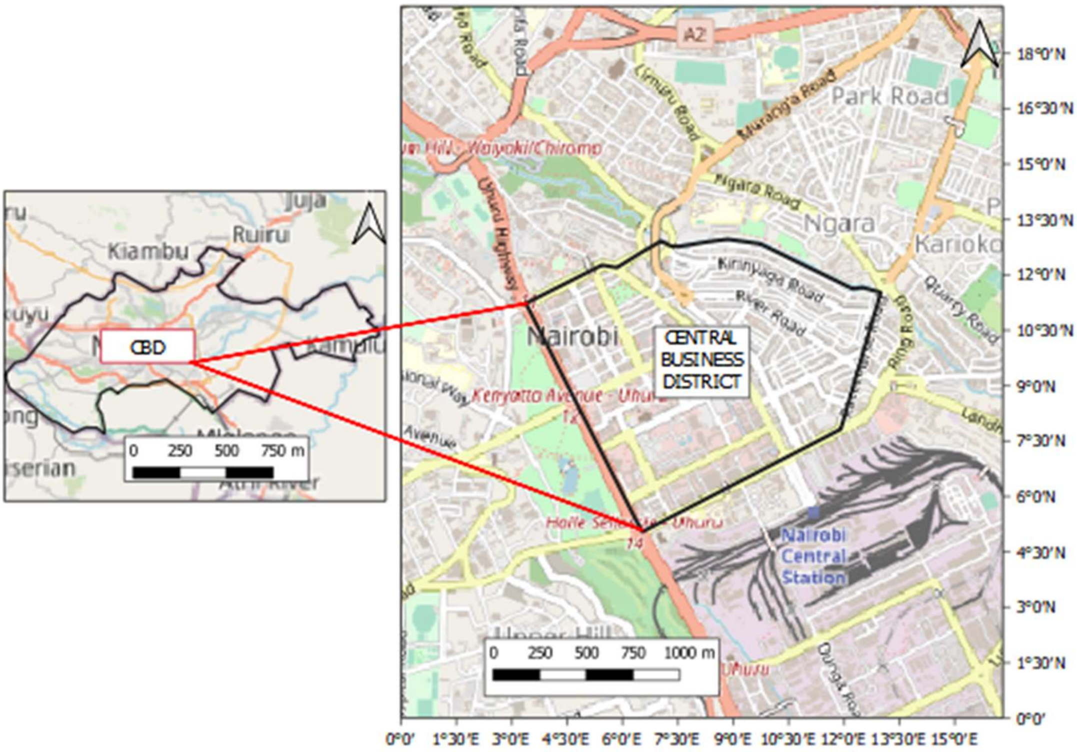

Figure 8. Map of the Central Business District (CBD), Nairobi

5.0 Results and Discussion

5.1 Distribution of Vertical Errors

The results show the MERIT DEM with the smallest vertical height deviation from the reference DEM, with an SD of 2.97 m, followed by TanDEM-X 12 and TanDEM-X 90, which had similar SDs of 3.03 m and 3.29 m, respectively. Figure 9 provides an illustration of comparison of density distribution plots for the six global DEMs. The error statistics for the six global DEMs are shown in Table 6. The SRTM, NASADEM & ALOS DEMs show a standard deviation of 5.92 m, 3.46 m, and 4.34 m respectively.

The results show that the MERIT and TanDEM-X 12 m & 90 m global DEMs have lower vertical height errors in comparison to the NASADEM, SRTM & ALOS DEMs if the SD metric only is considered. In addition, if the RMSE metric of the errors is considered alongside mean and median values, MERIT still provides lowest overall values and highest accuracy of all six global DEMs. The MERIT DEM is a multiple error-reduced improved version of SRTM (Chen et al., 2018) with tree height bias, stripe noise, absolute bias, and speckle noise removed from the original SRTM. MERIT is a corrected version of the SRTM, therefore, providing a plausible explanation for its higher accuracy.

(Hawker et al., 2019) investigated the vertical height accuracy of the TanDEM-X DEM 90 m, in comparison to other popular global DEMs by using high resolution (<10 m) LiDAR (Light Detection and Ranging) DEMs as a reference dataset. Their results show mean error values of 1.09 m, 1.30 m and 1.06 m for the MERIT, SRTM and TanDEM-X 90 DEMs respectively. The results correspond well with our own mean error magnitudes of 0.77 m, 0.87 m, and 1.72 m for the MERIT, SRTM and TanDEM-X 90 m DEMs.

The density distribution plot for all six global DEMs shown in Figure 9 demonstrates that all six global DEMs have a unimodal distribution, except for SRTM which shows a weak bi-modal distribution. The kurtosis of the error distribution for all six global DEMs are generally positive for MERIT, NASADEM, ALOS, TanDEM-X 12 and TanDEM-X 90 m DEMs, but is less positive for the SRTM DEM by showing a less acute peak around the mean than the other DEMs. SRTM, MERIT, and NASADEM DEMs show a nearly symmetric error distribution with a near zero skewness whilst ALOS, TanDEM-X 12 and TanDEM-X 90 m DEMs all have positive skewness and show more extreme positive outliers than negative ones.

The while the SRTM DEM shows a relatively low positive mean error (+0.87 m), this is only as a result of averaging cancelling out a large positive and negative spread of errors, evidenced by the highest Standard Deviation (5.32 m) of all the DEMS. The MERIT and NASADEM are derivatives of the SRTM DEM, with improvements made to reduce errors and in MERIT's case also remove vegetation bias. Unsurprisingly therefore these have better error characteristics than SRTM. However, neither MERIT nor NASADEM have been corrected for urban bias and this perhaps explains some of the remaining positive error bias (overprediction of elevation), which is larger for the NASADEM (+1.99 m) compared to the MERIT (+0.77 m). The higher mean error of NASADEM is likely explained by the lack of vegetation correction compared to MERIT. TanDEM-X, another radar instrument derived dataset also suffers from a similar positive error bias (for 12 and 90 m, 1.83 and 1.87 m respectively) presumably also for the lack of vegetation and urban error correction.

There are only minor differences between the 12 m and 90 m TanDEM-X DEMs in our analysis, unsurprising as the 90 m DEM is derived from the 12 m DEM in the first place. However, we might expect if we were resampling from 12 m to 90m this may reduce random noise error due to the averaging process. This does not seem to be the case here, indicating that the positive bias is indeed related to a systematic bias, likely vegetation and urban artefacts (and possibly other errors). The most unusual error characteristics are observed in the ALOS DEM.

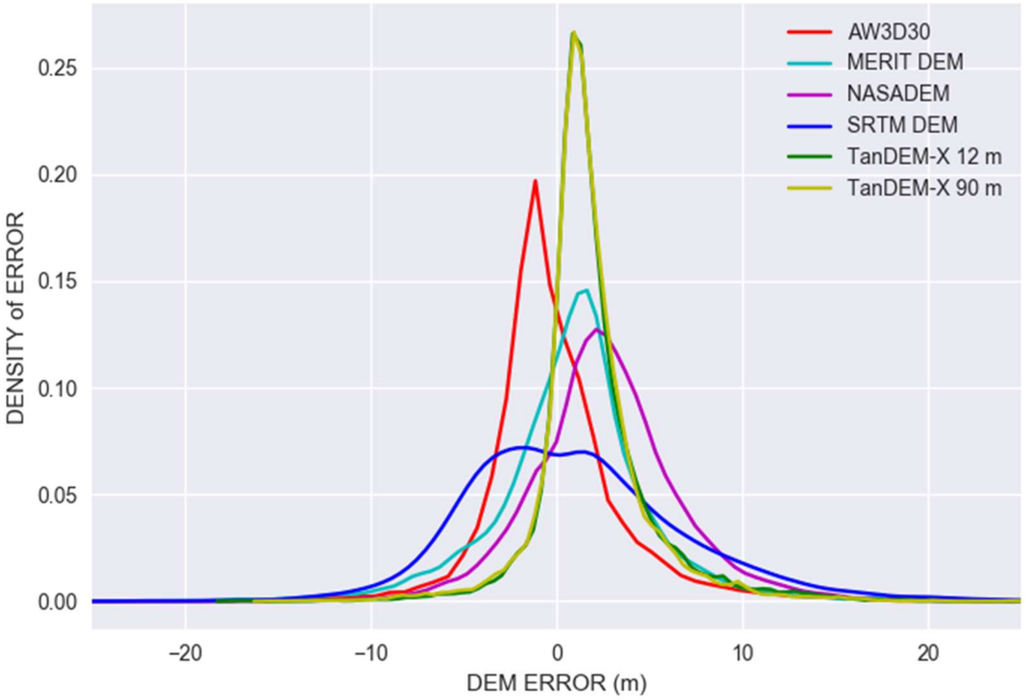

Figure 9. Comparison of density distribution plots for the six global DEMs: ALOS (AW3D30), SRTM, MERIT, NASADEM, TanDEM-X 12m, and TanDEM-X 90 m

Table 6. Statistical error parameters for the global DEMs, in metres, before (and after) urban correction

DEM	SRTM	MERIT	NASADEM	ALOS	TanDEM-X 12	TanDEM-X 90
Mean	-0.87 (-0.72)	0.77 (0.35)	1.99 (1.76)	-1.92 (-1.25)	1.83 (1.68)	1.87 (1.72)
RMSE	0.99 (0.85)	0.88 (0.48)	1.41 (1.33)	1.54 (0.92)	1.35 (1.22)	1.37 (1.28)
SD	5.92 (5.32)	2.97 (2.53)	3.46 (3.28)	4.34 (3.53)	3.03 (2.89)	3.29 (2.60)
Median	-0.41 (-0.36)	1.02 (0.70)	1.45 (1.19)	-1.39 (-1.26)	1.28 (0.98)	1.42 (1.17)

The error statistics for our urban corrected global DEMs are also shown in Table 6 along with the original DEM error statistics to allow direct comparison.

5.2 DEM Error and Building Density Relationships

We found that there is a linear and positive, but noisy relationship between DEM error and building density Figure 10. All the DEMs show a noisy relationship; with SRTM having the noisiest Figure 10(b)) and TanDEM-X DEMs the least noisy (Figure 10(e) & (f)). At zero building density the DEM error is not necessarily zero. For each DEM, the highest error in all DEMs is found at the highest building density of 1 as shown in Table 8.

The CBD features many of Nairobi's important buildings, government offices, headquarters of business and corporations – both national & international, skyscrapers etc. The scatter plots of building density of the CBD area against DEM error for the six global DEMs is shown in Figure 10. The analysis of the urban correction of the global DEM for the Central Business District area (Figure 8) of Nairobi consisting of taller buildings provided some further insights into the nature of the errors. Similar to the results of the analysis undertaken at a city scale for Nairobi, we found that there is a linear and positive, but noisy relationship between DEM error and building density. All the DEMs show a noisy relationships and the statistical error parameters for the six global DEMs both before (and after) the urban correction for the CBD area is shown in Table 6.

The relationships for both CBD area and Nairobi appear to be weak when the values of the R^2 are considered. However, the very sensitive nature of the impacts of vertical height accuracy on DEMs means that these results are real and can be significant. We noticed a higher error for the CBD area across all error metrics of ME, RMSE, and SD for all six global DEMs. For example, Table 7 shows a comparison of the error parameters for the SRTM and the TanDEM-X 90 m DEMs for Nairobi city wide and for the CBD area both before and after the urban correction. The error parameters in the CBD area is between 15 to 45 percent higher than those of the Nairobi city wide area for the DEMs. The very tall nature of the buildings in the CBD area appears to have contributed to the percentage increase in the errors. The focus of this study is on building density error and the results obtained for the CBD area show building heights can be an important contributor to DEM errors in urban areas and is worthy of further study.

Table 7. Statistical error parameters for SRTM & TanDEM-X 90 m DEMs in Nairobi city wide and the CBD area, in metres, before (and after) urban correction

DEM	SRTM (Nairobi)	SRTM (CBD)	TanDEM-X 90 (Nairobi)	TanDEM-X 90 (CBD)
Mean	-0.87 (-0.72)	-1.25 (-1.04)	1.87 (1.72)	2.49 (2.01)
RMSE	0.99 (0.85)	1.39 (1.02)	1.37 (1.28)	2.18 (1.85)
SD	5.92 (5.32)	6.84 (6.24)	3.29 (2.60)	4.84 (4.04)
Median	-0.41 (-0.36)	-0.88 (-0.49)	1.42 (1.17)	1.94 (1.52)

We corrected the DEMs by applying a correction based on the linear error relationship fitted to each DEM (Table 8). For example, to correct the SRTM DEM we calculated the vertical error for the given building density of a corresponding DEM grid using the regression equation in Table 8 to create a building density error raster Figure 11a. Subsequently, the building density error map is subtracted from the original DEM to create the urban corrected DEM in Figure 11b.

It should be noted that there will be the requirement for a local reference DEM data of vertical height accuracy higher than the global DEMs before the methodology described in this paper can be adapted for similar urban case study areas. Accuracy assessment of the global DEMs will involve the subtraction of elevation values belonging to each grid cell of the reference DEM from the corresponding cells of the global DEMs. Also, the six global DEMs and the reference DEM datasets used in the study were acquired over different periods spanning decades and could be a possible factor influencing the higher accuracy of the most recent DEMs.

Building error DEM artefacts in urban areas have two major components: building density and building height. Ideally, both of these components should be removed from DEM data; however, building height data is unavailable on a global scale. Therefore, this paper only addresses errors due to building density biases. Our results show that global DEMs can be usefully corrected for building density errors in urban areas, even where specific building height data are not available.

Table 8. Correction error of global DEMs at highest and lowest measured building densities (BD)

DEM	Regression equation	Correction error (m) at highest BD	Correction error (m) at lowest BD
SRTM	4.73x + 0.34	5.07	0.34
MERIT	0.73x + 0.52	1.25	0.54
NASADEM	2.21x + 2.26	4.47	2.26
ALOS	0.53x + 1.74	2.27	1.74
TanDEM-X 12	1.49x + 1.56	3.05	1.56
TanDEM-X 90	1.53x + 1.81	3.34	1.81

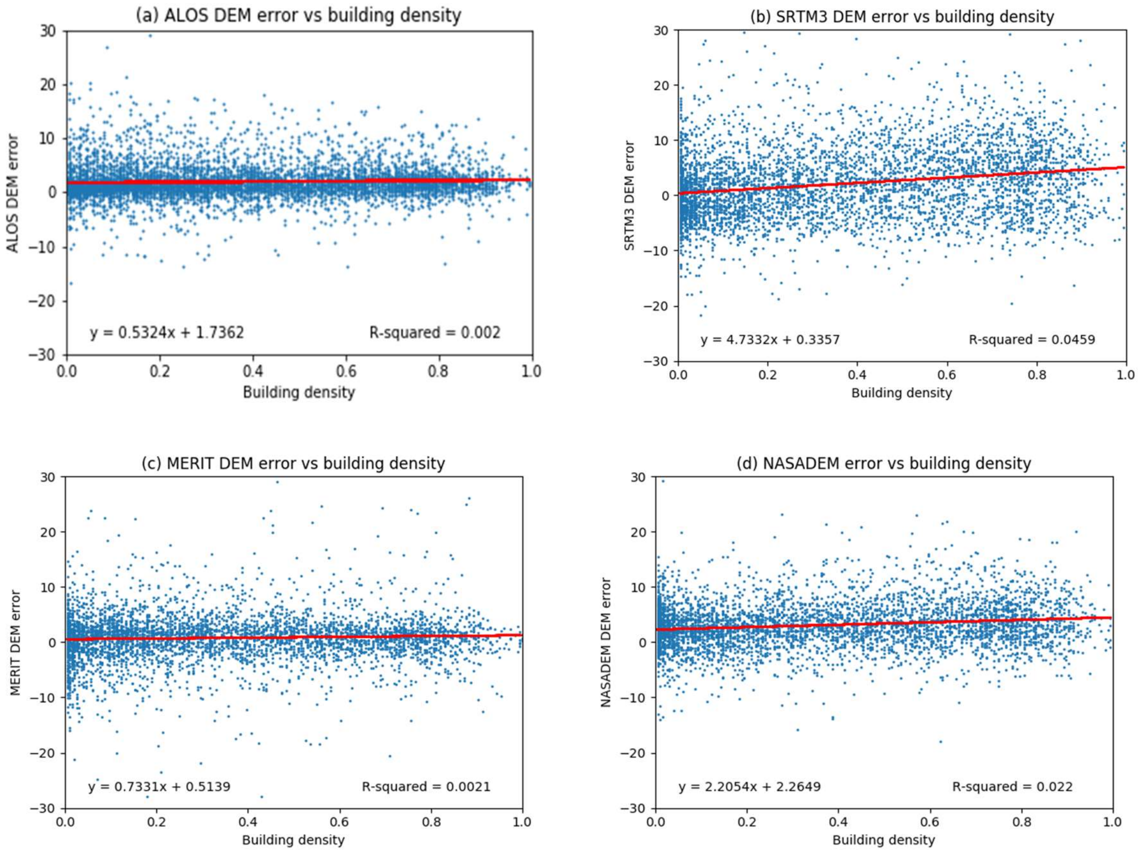

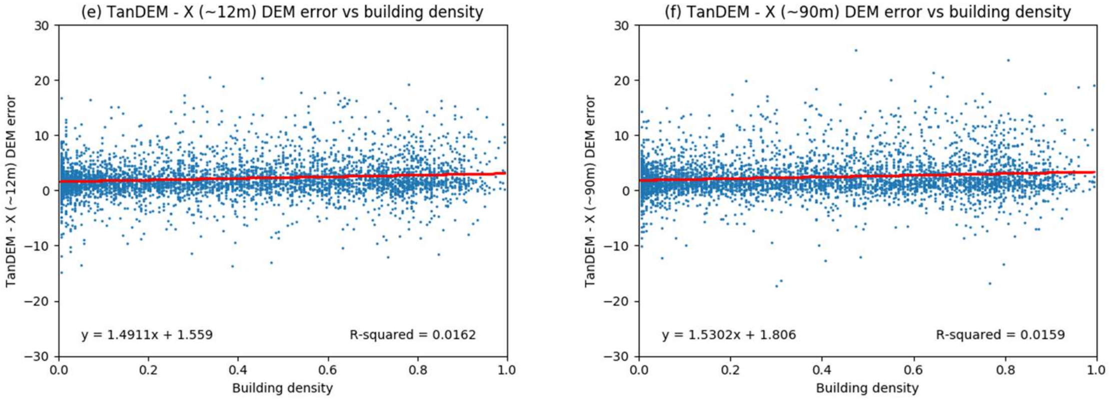

Figure 10. Scatter plots of building density with DEM error, with superimposed linear regression lines of best fit for the tested global DEMs, applied to Nairobi: (a) ALOS; (b) SRTM; (c) MERIT; (d) NASADEM; (e) TanDEM-X 12 m and (f) TanDEM-X 90.

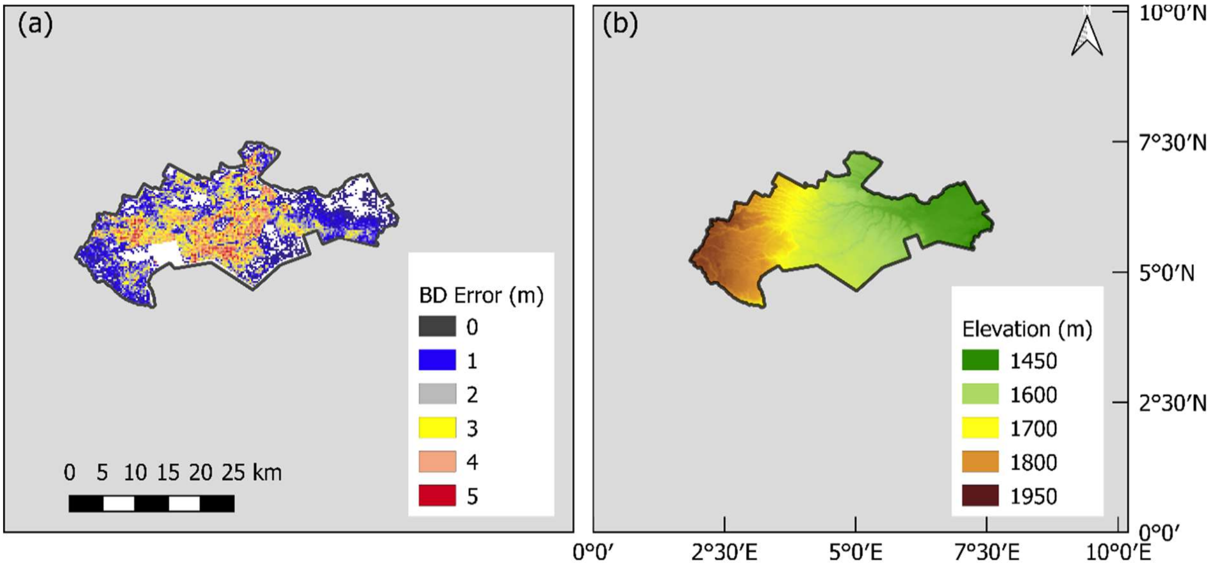

Figure 11. (a) Building density error raster for SRTM DEM, (b) urban-corrected SRTM DEM.

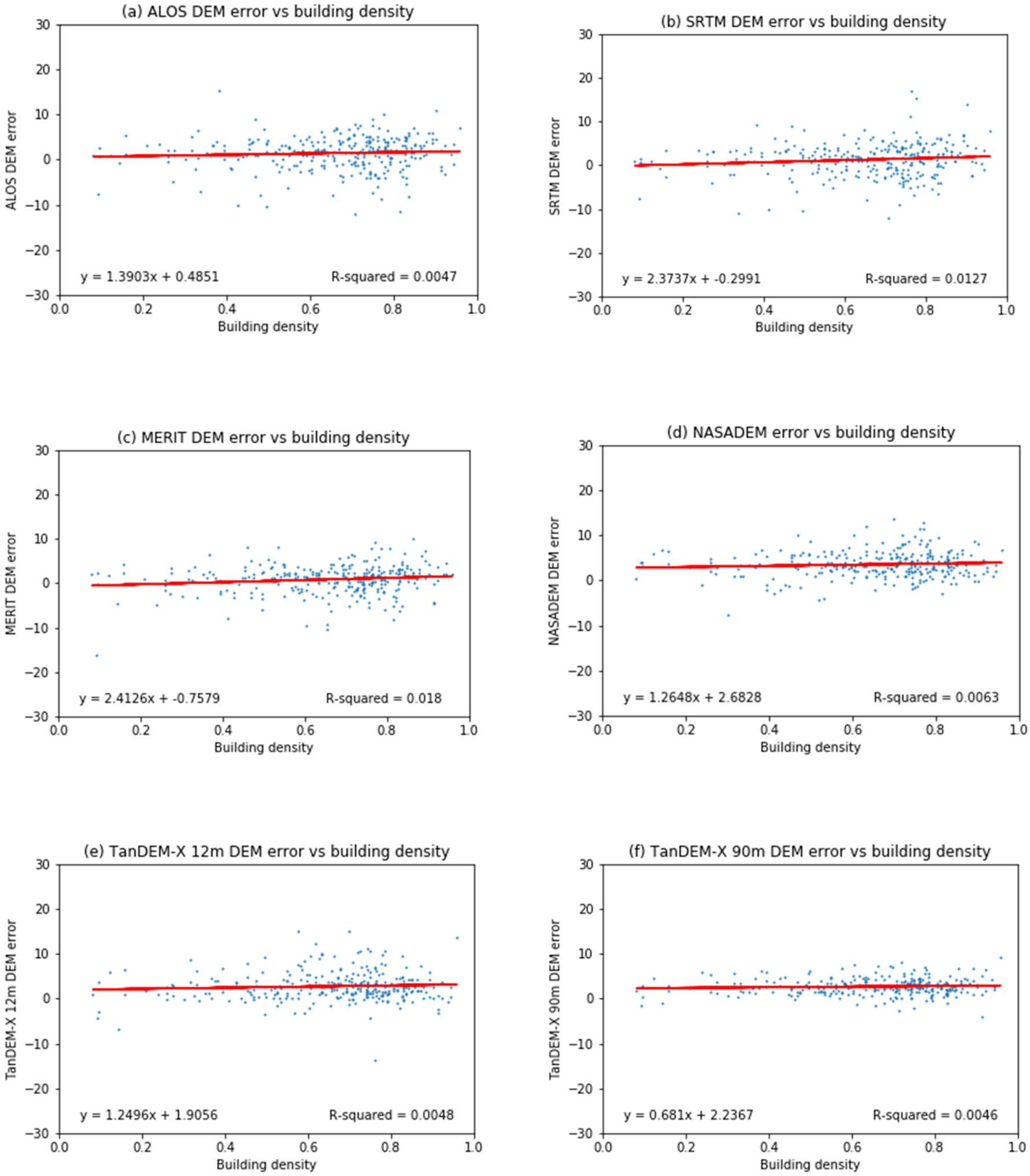

Figure 12. Scatter plots of building density with DEM error, with superimposed linear regression lines of best fit for the tested global DEMs, applied to Central Business District (CBD): (a) ALOS; (b) SRTM; (c) MERIT; (d) NASADEM; (e) TanDEM-X 12 m

Table 9. Statistical error parameters for the global DEMs in the CBD area, in metres, before (and after) urban correction

DEM	SRTM	MERIT	NASADEM	ALOS	TanDEM-X 12	TanDEM-X 90
Mean	-1.25 (-1.04)	1.05 (0.68)	2.47 (1.96)	-2.32 (-1.46)	2.15 (1.87)	2.49 (2.01)
RMSE	1.39 (1.02)	1.28 (0.88)	2.06 (1.73)	2.19 (1.43)	2.09 (1.72)	2.18 (1.85)
SD	6.84 (6.24)	3.02 (2.87)	3.98 (3.60)	4.95 (3.99)	4.36 (3.73)	4.84 (4.04)
Median	-0.88 (-0.49)	1.33 (0.91)	1.98 (1.64)	-1.74 (-1.51)	1.61 (1.15)	1.94 (1.52)

5.3 Analysis of DEM error versus building density relationships for Kibera slum area and Embakasi residential area.

The Central Business District (CBD) area of Nairobi is characterised by tall buildings, office towers, historical buildings, parking lots and less housing compared to other areas within the city. Buildings from 0-1 km of the Nairobi city centre average 10 stories, at about 3m, a storey. (Henderson et al., 2016). In order to determine the extent of the residual building height error remaining in the corrected DEMs, the analysis for the correction of the global DEMs is extended to the Kibera slum area (Figure 13) and the Embakasi residential area (Figure 14) of the city of Nairobi.

Kibera is a large slum area to the southwest of the central business district of Nairobi city and often referred to as Africa's largest slum (Henderson et al., 2016). The slum of Kibera is located directly south-west of the centre, ranging from about 3-5 km of the central business district. The majority (about 55%) of housing walls are corrugated iron sheets and building height values ranging from 2m to maximum 4 m high (Henderson et al., 2016)

Embakasi is located east of the CBD of Nairobi. Embakasi district neighbours Mihango estate to the east, Embakasi and Fedha estates to the south, Kayole and Donholm estates to the West. Embakasi is considered part of Nairobi's Eastlands area, lying 15km to the south-east of Nairobi province. Jomo Kenyatta International Airport, the main airport of Nairobi is located in Embakasi. As a residential estate it houses mostly middle to lower income citizens. Most of the residential houses are four to eight storey flats.

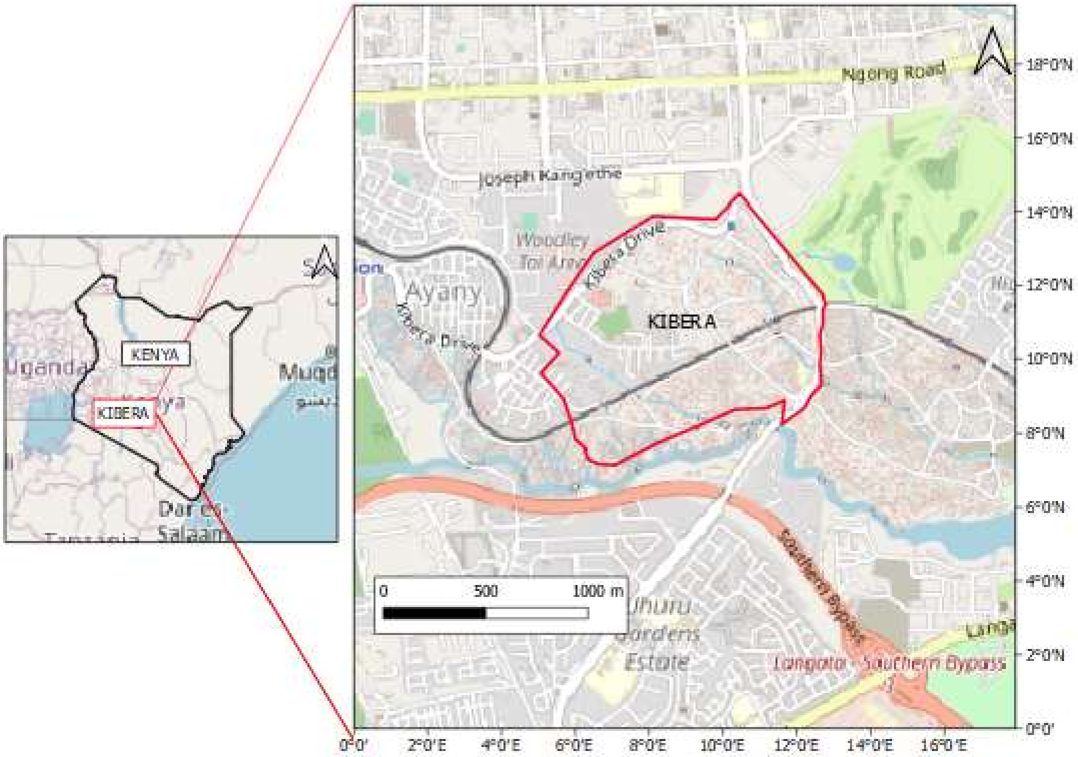

Figure 13. Map of the Kibera slum area of Nairobi city

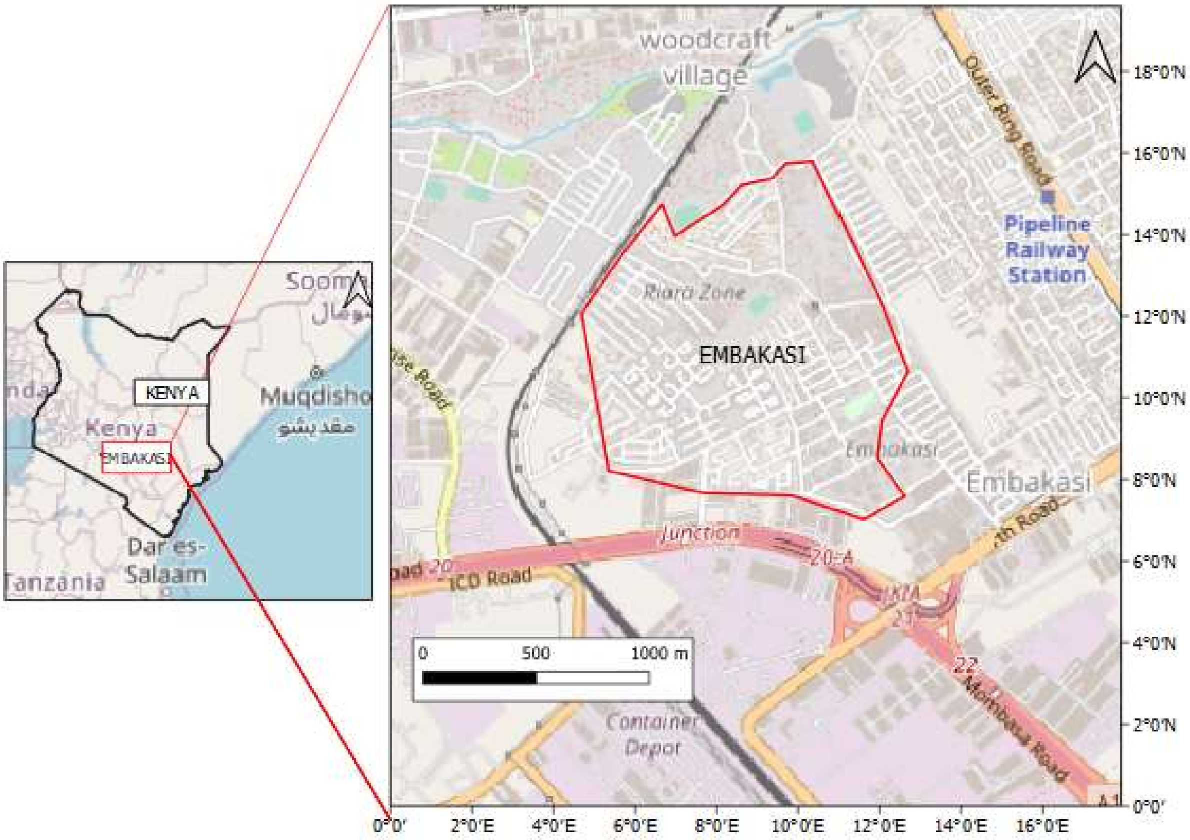

Figure 14. Map of the Embakasi residential area of Nairobi city

The scatter plots of building density of the Kibera slum area and Embakasi residential dwelling area against DEM error for the six global DEMs is shown in *Figure 16* and *Figure 17*. Similar to the results of the analysis undertaken at a city scale level and for the central business district area of the city, the results show that there is a linear and positive, but noisy relationship between DEM error and building density for the Kibera and Embakasi area. However, the results of the relationships for the Kibera slum area and Embakasi residential area appear to be stronger when the values of the R^2 are considered against the results for the central business district area and the results for the Nairobi city analysis. A comparison of the scatter plots for all four areas of Nairobi investigated in this study reflects the nature of the settlements (density) across the four areas and the specific impacts building density can have on DEM error.

The very sensitive nature of the impacts of vertical height accuracy on DEMs means that these results are real and can be significant, especially in very densely populated areas where the ratio of building density to available space is very high and up to the value of 1. The results show a higher error for the Kibera slum area followed by the Embakasi area, the Central CBD and lastly the Nairobi city wide area across all error metrics of ME, RMSE, and SD for all six global DEMs. For example, Table 10 shows a comparison of the error parameters for the SRTM DEM for Nairobi city wide area, CBD area, Kibera slum area, and Embakasi residential area, both before and after the urban correction of the DEMs.

The *p* values (with a threshold of 0.05) for the DEM error versus building density for the analysis the Kibera slum area and the Embakasi residential area is shown in Table 11. When comparing *p* values for the Kibera slum area and the Embakasi residential area, the results show the relationships for the Kibera area with more significance than the DEM error vs building density relationships for the Embakasi residential area. It is concluded that the very high building density of the Kibera area is responsible for the smaller *p* values of the shown in the DEM error versus building error relationships for the area when compared to the Embakasi residential area. A comparison of the *p* values for all four study areas (Nairobi city wide; Nairobi Central Business District (CBD); Kibera slum area; and the Embakasi residential area) is also shown in Table 11. The results show the Kibera slum area with the smallest *p* values for the error relationships for all DEMs followed by the Embakasi residential area, the central business district (CBD) and the Nairobi citywide scenario.

Table 10. Statistical error parameters for SRTM DEM in Nairobi city wide, CBD, Kibera slum and the Embakasi residential area, in metres, before (and after) urban correction

DEM	SRTM (Nairobi)	SRTM (CBD)	SRTM (Kibera)	SRTM (Embakasi)

Mean	-0.87 (-0.72)	-1.25 (-1.04)	1.88 (1.09)	2.16 (1.62)
RMSE	0.99 (0.85)	1.39 (1.02)	1.76 (1.27)	1.42 (1.05)
SD	5.92 (5.32)	6.84 (6.24)	4.17 (3.89)	4.46 (4.31)
Median	-0.41 (-0.36)	-0.88 (-0.49)	1.69 (1.21)	1.83 (1.49)

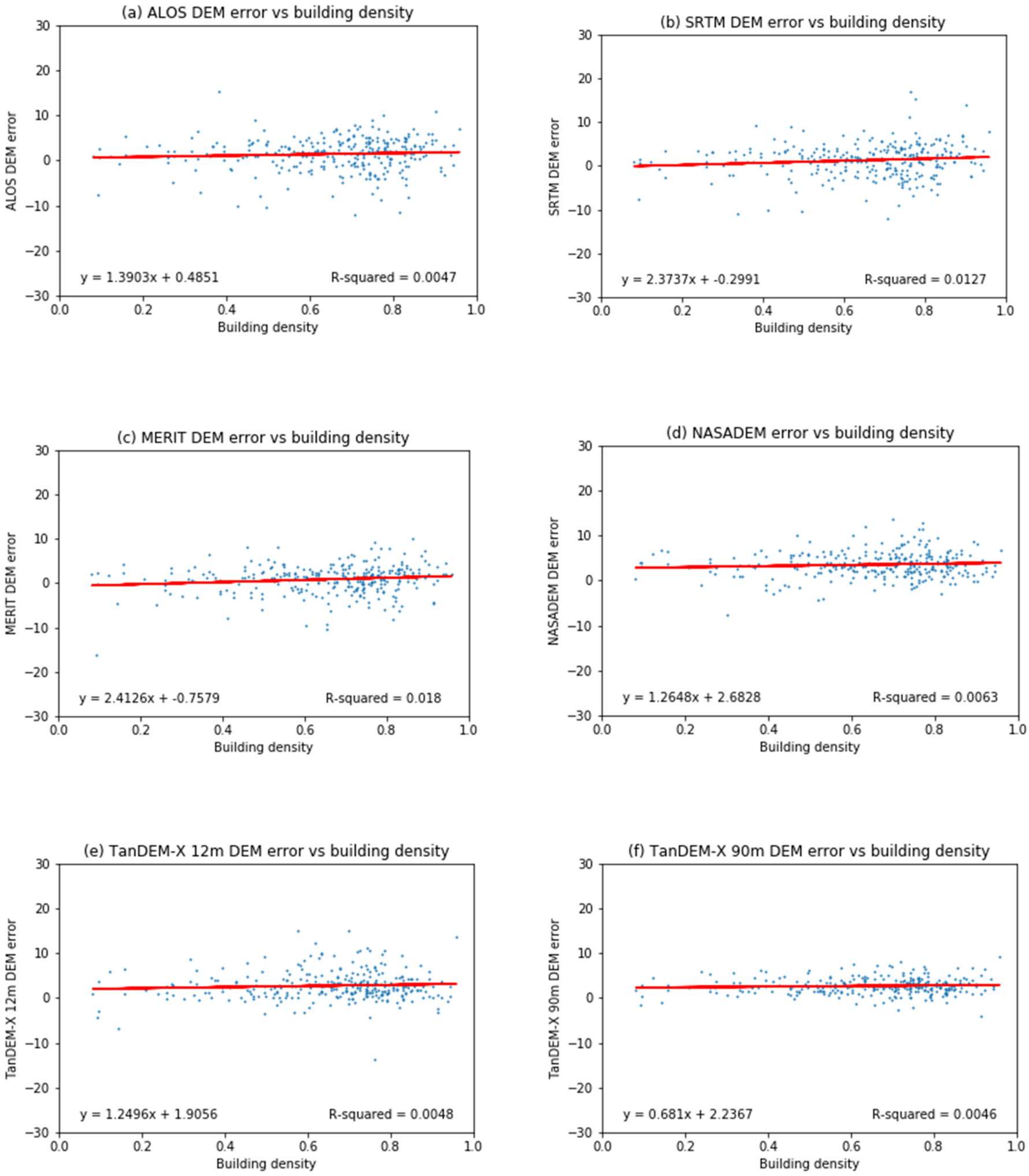

Figure 15. Scatter plots of building density with DEM error, with superimposed linear regression lines of best fit for the tested global DEMs, applied to Central Business District (CBD): (a) ALOS; (b) SRTM; (c) MERIT; (d) NASADEM; (e) TanDEM-X 12 m

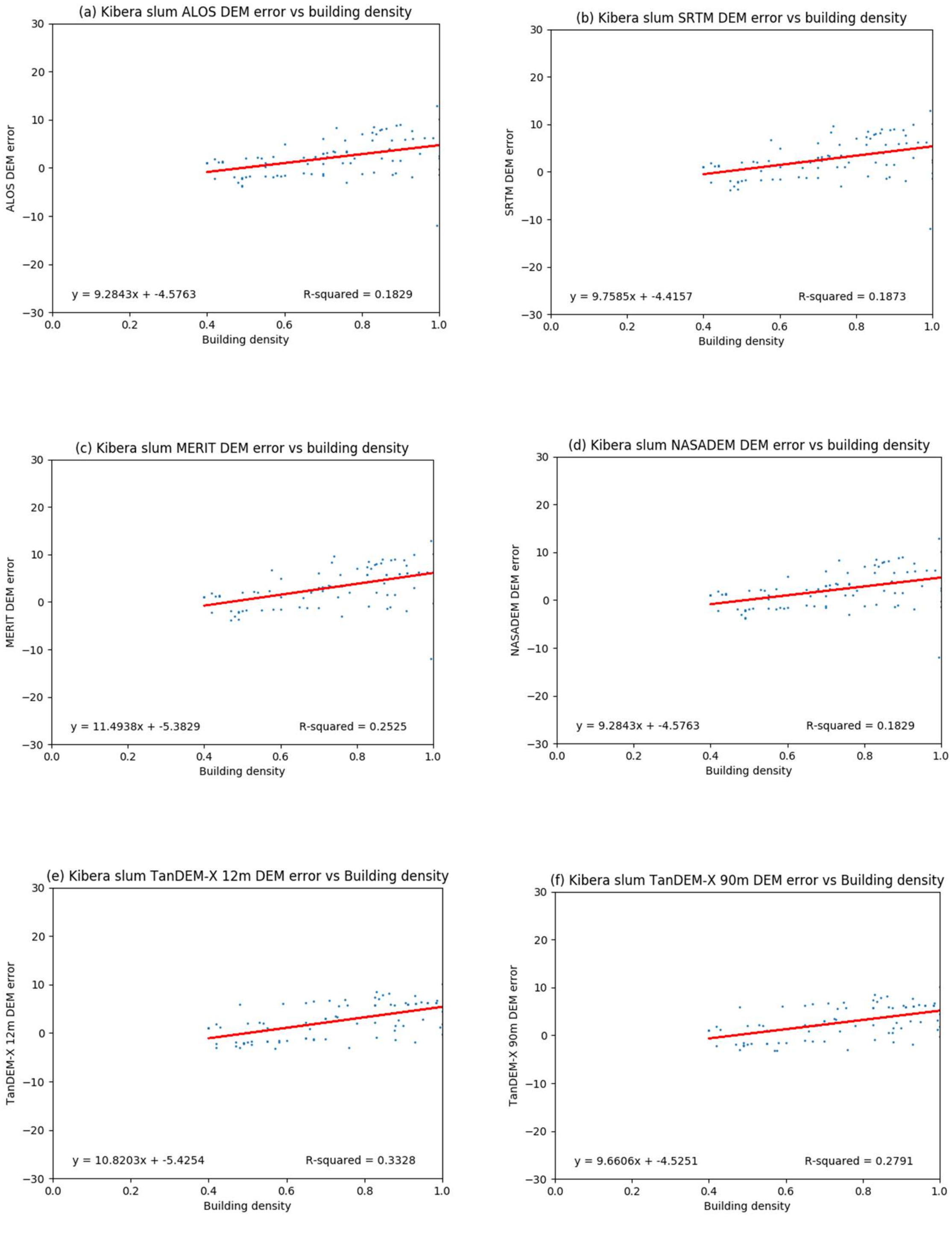

Figure 16. Scatter plots of building density with DEM error, with superimposed linear regression lines of best fit for the tested global DEMs, applied to the Kibera slum area of Nairobi city: (a) ALOS; (b) SRTM; (c) MERIT; (d) NASADEM; (e) TanDEM-X 12 m

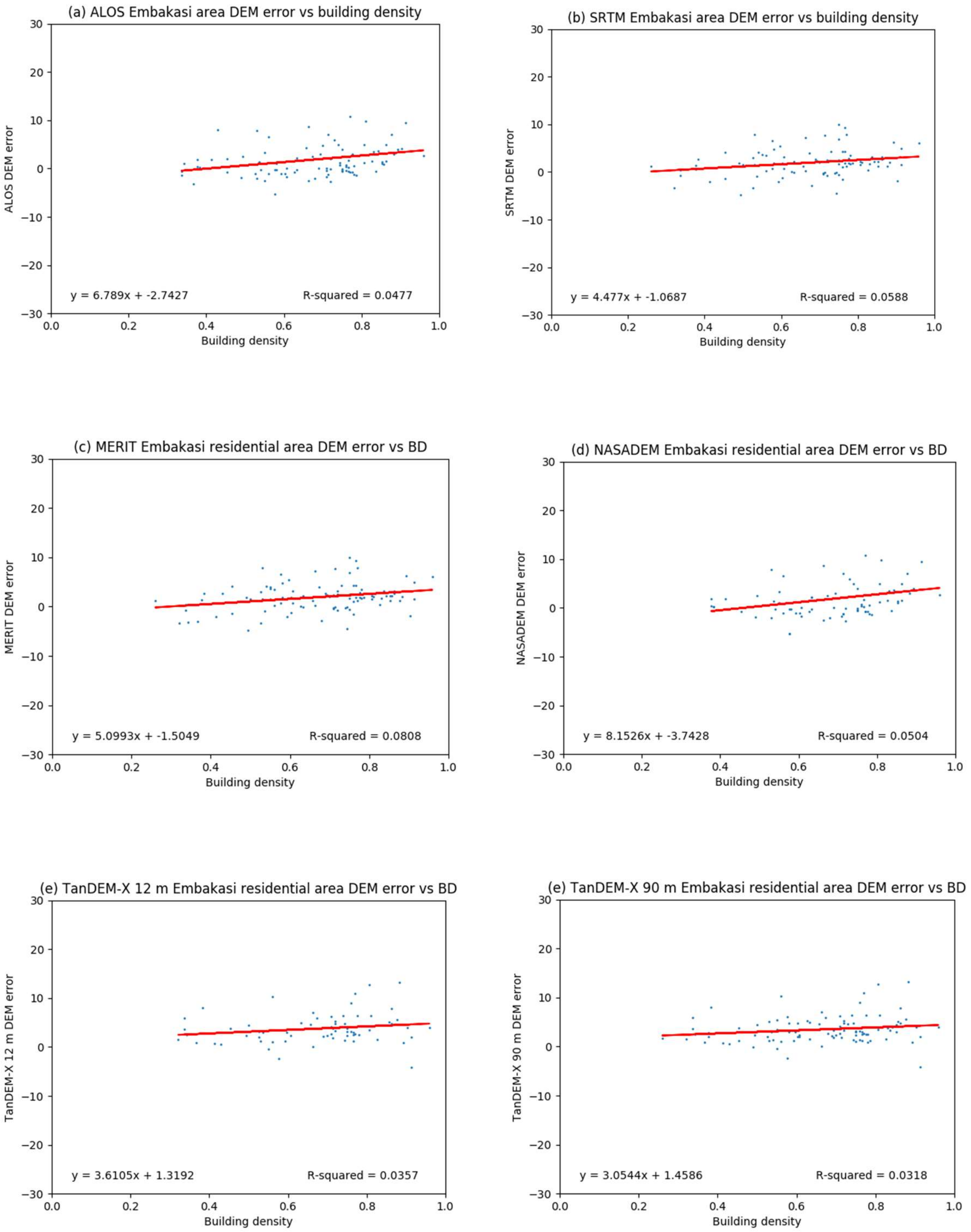

Figure 17. Scatter plots of building density with DEM error, with superimposed linear regression lines of best fit for the tested global DEMs, applied to the Embakasi residential area of Nairobi city: (a) ALOS; (b) SRTM; (c) MERIT; (d) NASADEM; (e) TanDEM-X 12 m

Table 11. p values for DEM error vs Building Density relationships for the Nairobi city, Nairobi Central Business District (CBD), Kibera slum area and Embakasi residential area.

DEM error vs Building density relationships	***P* values**			
	Nairobi Citywide	**Nairobi CBD**	**Kibera Slum**	**Embakasi Residential Area**
Reference DEM vs Building Density	0.05	0.03	1.13×10^{-5}	0.008
MERIT DEM vs Building Density	0.08	0.05	2.28×10^{-5}	0.01
SRTM DEM vs Building Density	0.09	0.05	2.28×10^{-5}	0.02
TanDEM X 12m DEM vs Building Density	0.09	0.06	3.13×10^{-5}	0.03
TanDEM X 90m DEM vs Building Density	0.11	0.08	3.58×10^{-5}	0.04
NASADEM DEM vs Building Density	0.12	0.07	2.57×10^{-5}	0.05
ALOS DEM vs Building Density	0.13	0.09	2.91×10^{-5}	0.04

5.4 Summary

Open-access global DEMs are not only useful tools for estimating flood risks, but they also provide baseline data for flood studies. Despite significant advances in developing vegetation-corrected DEMs, there is limited understanding of DEM errors that can be attributed to building heights and building density in urban areas. Current global DEMs are not corrected for building errors. Because building height data is unavailable on a global scale, this paper addresses errors due to building density biases.

In this study a methodology for building error correction is developed that can be applied to any other case study, where building density data and a local reference DEM data of vertical height accuracy higher than the global DEMs are available. In this study, quantified the building error is quantified for the city of Nairobi, Kenya for six of the most widely used global DEMs: SRTM; MERIT; ALOS; NASADEM; TanDEM-X 12 m; and TanDEM-X 90 m. The results show building error at highest building density varying between 1.25 m and 5.07 m for the DEMs used. The results show the MERIT DEM with the smallest vertical height deviation from the reference DEM, with an SD of 2.97 m, followed by TanDEM-X 12 and TanDEM-X 90 (3.03 m and 3.29 m respectively). In addition, if the RMSE metric of the errors is considered alongside mean and median values, MERIT still provides the lowest overall values and highest accuracy. A plausible explanation for its higher accuracy is that the MERIT DEM is a multiple error-reduced improved version of SRTM with tree height bias, stripe noise, absolute bias, and speckle noise removed.

By deriving a relationship between DEM error and building density the evaluated building error is corrected. It was found that there is a linear and positive, but noisy relationship between DEM error and building density. All the DEMs show a noisy relationship; with SRTM having the noisiest and TanDEM-X 12 m & 90 m DEMs the least noisy. The findings show that the removal of building density error from global DEMs resulted in the improvement of the vertical height accuracy of the global DEMs of up to 45% for MERIT and 40% for ALOS. Thus, the results show that global DEMs can be usefully corrected for building density errors in urban areas, even where specific building height data are not available.

This study also shows the results of the methodology for the Central Business District (CBD) area of Nairobi which is characterized by taller buildings and high building density. Results show the error parameters in the CBD area is between 15 to 45 % higher than those of the Nairobi city wide area for the six global DEMs. These results provided some further insights into significance of building heights contributing to errors in global DEMs. Therefore, future work is required to understand the nature of building height errors in global DEMs and how these errors can be corrected.

The additional analyses undertaken for Kibera slum and Embakasi residential areas to determine the extent of the residual building height error remaining in the corrected DEMs show a relationship that is strongest for the Kibera slum area, followed by the Embakasi residential area and lastly the Central business district area when R^2 and p values are considered. A comparison of the *p* values for all four test locations considered under this study also show similar trend of largest *p* values for the Nairobi citywide error relationships and smallest *p* values when considering the error relationships for the Kibera slum area. A comparison of the scatter plots for all four areas of Nairobi investigated in this study reflects the nature of the settlements (density) across the four areas and the specific impacts building density can have on DEM error.

6.0 CITY-SCALE MODELLING OF THE NAIROBI CATCHMENT

This section outlines the development, running and testing of five model scenarios using the HEC-HMS hydrologic model and the HEC-RAS model (v6.0.0) to simulate the rainfall and subsequent runoff of the 1st to 13th March rainfall events in Nairobi, Kenya.

S1-Baseline model uses the urban corrected DEM, 2020 land use map and March 2018 precipitation data as key input data
S2-2010LU model is developed using the same key input data as S1-Baseline model apart from using land use the 2010 land use map for the catchment
S3-CP4uplift model is developed using the 2020 land use map, the urban corrected DEM and future CP4 climate change rainfall model
S4-P25uplift model uses the 2020 land use map, the urban corrected DEM and future P25 climate change rainfall model
S5-RawDEM model is similar to the S1-Baseline model but uses a raw DEM as key input data instead of an urban corrected DEM

The 2D hydraulic model with five sets of scenarios are created in 2D and make use of the diffusive wave equation for simplification. A 6-step method detailing the procedure for the creation of the 5 models using the HEC-HMS hydrologic model and the HEC-RAS model is presented in Figure 18. The characteristics of the five sets of models are as shown in Table 12.

Table 12. Characteristics of five sets of model scenarios created in HEC-RAS 2D v6.0.0 software using the diffusive wave equation.

Model Scenarios	**Land use data**	**Rainfall data**	**DEM**
S1-Baseline	2020 LU	March 2018	Corrected DEM
S2-2000LU	2000 LU	March 2018	Corrected DEM
S3-CP4uplift	2020 LU	CP4 future climate rainfall	Corrected DEM
S4-P25uplift	2020 LU	P25 future climate rainfall	Corrected DEM
S5-RawDEM	2020 LU	March 2018	Raw DEM

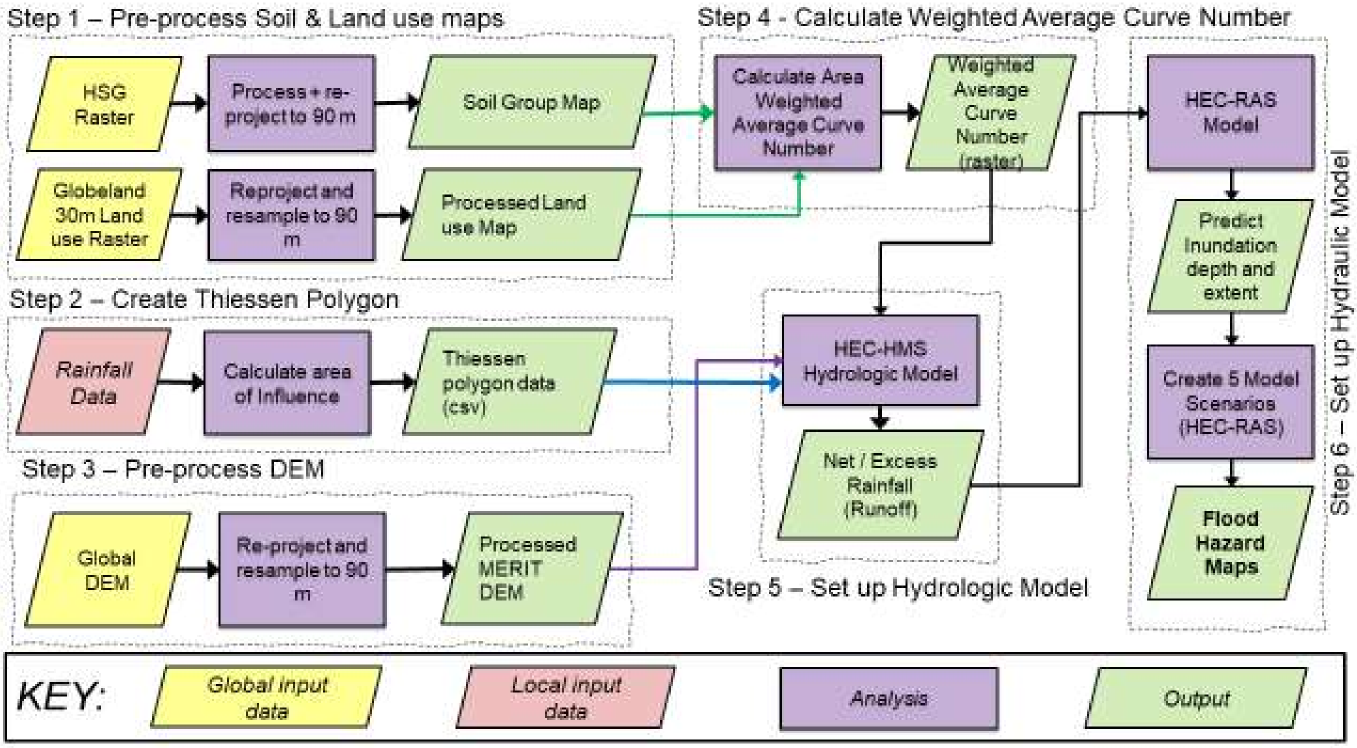

Figure 18. Six-step method flowchart of the datasets and methodology used to create the five model scenarios (S1-Baseline, S2-2000LU model, S3-CP4uplift model, S4-P25uplift model, and the S5-RawDEM model.) using HEC-HMS and HEC-RAS software.

6.1 Hydrologic Modelling System (HEC-HMS) of the Study Area

The United States (U.S.) Army Corps of Engineers' (USACE) Hydrologic Engineering Centre Hydrologic Modelling System (HEC-HMS) is a commonly used, and freely available, modelling framework that has been employed for a variety of purposes in both natural and urban systems. The HEC-HMS software includes hydrologic analysis procedures such as event infiltration, unit hydrographs, and hydrologic routing including procedures necessary for continuous simulation of evapo-transpiration, snowmelt, and soil moisture accounting. HEC-HMS deals with the basic water balance equation and the transformation of the runoff from precipitation in the HEC-HMS model is governed by landuse, soil type, evapotranspiration, and storage.

The software is used to model the flood peaks and volumes for the March 2018 rainfall events in Nairobi, Kenya in conjunction with the Hydrologic Engineering Centre River Analysis System (HEC-RAS) for the study area. The HEC-HMS model was calibrated to the 1st to 13th March 2018 runoff events primarily to generate the excess net rainfall to be applied to the HEC-RAS model. The HEC-HMS software consists of four sub-models: a basin model, meteorological model, control specifications, and time-series data. It offers the possibility to use numerous flood routing, unit hydrograph and infiltrations methods. A typical representation of watershed runoff within the HEC-HMS hydrologic model used in this study is shown in Figure 19.

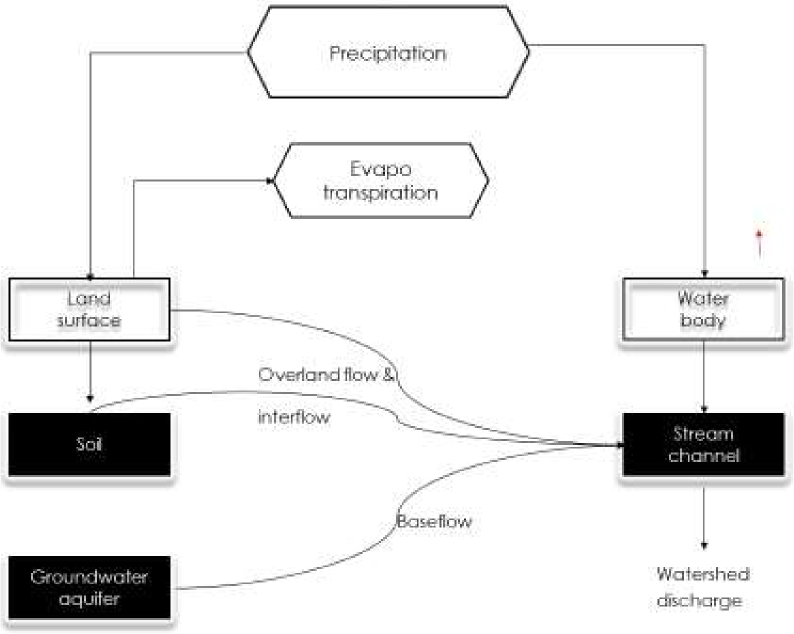

Figure 19. Typical representation of watershed runoff within the HEC-HMS hydrologic model (U.S. Army Corps of Engineering, 2016)

One of the key features of the HEC-HMS software is the ability to allow users to select among various infiltration loss parameterizations relating to the model. The Soil Conservation Service (SCS) Curve Number (CN) method was selected as the loss model in the HEC-HMS v4.8.0 and the SCS Unit Hydrograph method was chosen to transform excess precipitation into channel flow. A daily flow was selected for the 1st to 13th March storm events for the baseline model (S1-Baseline). The Muskingum-Cunge Standard Section was selected for channel routing and the SCS loss method was used to estimate the amount of precipitation, P_e, that contributed to runoff during individual storm events. Excess precipitation for the five model scenarios is calculated using precipitation for a given storm, P; an estimate for the initial abstractions, I_a; and the potential maximum retention, S. The potential maximum retention is computed using estimates of the CN assigned to the study area. P_e, P, and I_a have dimensions of inches, and CN and S are dimensionless. The empirical relationships for these terms are as described in the equations below:

$$P_e = \frac{(P - I_a)^2}{P - I_a + S}$$

Equation 11

$$I_a = (0.2)\,s$$

Equation 12

$$S = \frac{1,000}{CN} - 10$$

Equation 13

The following input parameters are required in each basin (or subbasin) for the SCS method: an estimate of I_a, CN, and the percentage of area that is impervious. Initial abstractions were calculated using the standard SCS formulation shown in Equation 12. The SCS unit hydrograph is adopted as a transform method to estimate runoff rate and the Muskingum routing method is selected to calculate the channel routing. The SCS unit hydrograph is based on a computed lag time or time of concentration (as a function of slope, hydraulic length, and basin storage. Land use and land cover modification by humans are among the most important agents of environmental change at local to global scales and have significant implications for ecosystem health, water quality, and sustainable land management (Foley et al., 2005).

The purpose of developing the HEC-HMS hydrologic model for this study is to obtain runoff (net precipitation) from the precipitation data with HEC-HMS model. The obtained runoff data is the simulated in HEC-RAS model and the output of HEC-RAS exported to QGIS software for flood plain mapping and analysis. The HEC-RAS 2D hydraulic model can simulate runoff based on channel morphology and generate flood inundation extent within the catchment. However, coupling the two models will aid in the assessment of flood inundation of the study area for the March 2018 storm events. Details of the rainfall data, terrain data, soil types and landuse data used in the HEC-HMS model is tabulated in Table 13. Key input data into the HEC-HMS hydrologic rainfall runoff model Table 13.

Table 13. Key input data into the HEC-HMS hydrologic rainfall runoff model

SN	Data	Data source
1.	3 arc second MERIT Digital elevation Model (DEM)	Multi-Error-Removed Improved-Terrain DEM (MERIT DEM)http://hydro.iis.u-tokyo.ac.jp/~yamadai/MERIT_DEM/
2.	Land use data 2020	Globeland 30m resolution landuse data. http://www.globeland30.org/
3.	Soil type Data	FAO/UNESCO Soil Map of the World. https://www.fao.org/soils-portal/data-hub/soil-maps-and-databases/faounesco-soil-map-of-the-world/en/
4.	Rainfall, Evapotranspiration data	Kenya Meteorological Services. Ngong Road. Nairobi. Kenya.

6.2 The March 2018 Rainfall Events

Over the Kenya-core region and indeed Kenya as a whole, 2018 saw the wettest March, April and May seasons over the 119-year record of the Global Precipitation Climatology Centre (GPCC) data, and the 118 years of CenTrends data (Kilavi et al., 2018). Locally in Nairobi, the capital city of Kenya, rainfall totals at the five stations exceeded the normal amounts by two to three times in March and one to two times in April (Kilavi et al., 2018). Precipitation data for the watershed was obtained from the Kenya Metrological Service for the March 2018 extreme rainfall from four rainfall-gauging stations at different locations within the watershed and shown in Table 14.

Table 14. Observed rainfall data (March 2018) at five rainfall stations in Nairobi, Kenya (Source Kenya Meteorological Service)

STATION	March Total Rainfall (mm)
Dagoretti	260.3
JIKA	216.8
Machakos	236.8
Thika	375.3

6.3 Weighted Average Curve Number

The SCS (NRCS) Curve Number is used for the quantification of infiltration loss during runoff calculation and can range from 0 (100% infiltration) to 100 (impervious, no infiltration). The overall CN of a watershed is the area-weighted average CN of each combination of soil type and land cover type. A weighted average curve number for the watershed will be required for use as input in the HEC-HMS model. Therefore, a methodology was developed for calculating area-weighted average curve number from landuse and hydrologic soil group (HSG) data as described below.

6.4 Pre-processing of Raster Data

The Globeland30 Land use data for 2020 is used as baseline land use data in the HEC-HMS and HEC-RAS models. Land use change in the catchment were analyzed based on the GlobeLand30 land use data for 2000 and 2020 downloadable from http://www.globallandcover.com/. The GlobeLand30 is a 30m resolution LULC datasets comprising 10 land cover types: cultivated land, forest, grassland, shrub land, wetland, water bodies, tundra, artificial surfaces, bare land, and permanent snow and ice (Chen et al., 2017a). In this study, the 10 land cover categories were reclassified into seven aggregate types Table 15, including cultivated land, forest, grassland, shrubland, waters, urban, and bareland.

Table 15. Landuse and Landcover (LULC) Classification

Class	Specific land cover
Cultivated	Land for agriculture such as irrigated farmland, dry farmland, and vegetable garden.
Forest	Land covered by trees such as forests, scrubland, and woodland.
Grassland	Land covered by grass such as pasturage and urban green space.
Waterbodies	Land covered by water such as river, lake and reservoir.
Wetland	Land covered by wetland plants, tidal flat, and swamp.
Urban	Land covered by artificial buildings such as residential, commercial, factories, roads, and airports.
Bareland	Land with vegetation coverage <10%, which includes sandy field, saline and alkaline land, bare rocks

The Global Hydrologic Soil Groups (HSG) cover data are 100m resolution global maps of land cover & cover changes of different areas over certain years and downloadable from https://webmap.ornl.gov/ogc/dataset.jsp?ds_id=1566 . The HYSOGs250m represents a global, gridded dataset of hydrologic soil groups (HSGs) with a resolution of approximately 250m. It is important that the Globeland30 landuse raster file has the same extent, projected coordinate reference system and resolution value as the HSG raster file so that the two files can align together to create a Curve Number raster file. Therefore, the landuse and soil group data were resampled to 30 m using raster calculator tools in QGIS.

6.5 Reclassification of Land use map

Using the Reclassify by layer tool in QGIS, the landuse raster file is reclassified to reduce landuse types to 4 and a CSV txt file for landuse class breaks is created and added to QGIS layer panel. The reason for the reclassification of the of the landuse categories is to simplify and streamline the curve number CN calculation procedure. The original landuse data for the study area in its 12 different types of land cover types will end up with 12 x 3 = 36 different combinations for CN assignment when combined with HSG soil types (1, 2, & 3).

6.6 Combination of Land use and HSG soil group raster files

The final step involved the combination of the two raster files described above using GDAL Raster calculator of QGIS to create a Curve Number (CN) raster file. A simple logic equation expression is created for the CN calculation. Finally, using Zonal statistics tool of QGIS, a watershed boundary shapefile was loaded and parameters count, sum and mean are selected for statistics to calculate and use Curve Number (CN). Three new fields are added to the watershed boundary shapefile, where and the value under the column of Mean is the area-weighted average CN (Mean) for the watershed area is 69.898 and 82.122 in 2000 and 2020 respectively.

6.7 Net / excess rainfall values from HEC-HMS

Figure 20 shows the watershed, sub-basins and reach of the study area from the HEC-HMS model and Table 16Table 19 shows the net model output flow results from the HEC HMS model following model runs for the five model scenarios (S1-Baseline, S2-2010LU, S3-CP4uplift, S4-P25uplift & S5-RawDEM). Consequently, the net rainfall data output from the HEC HMS model were used for the development of the rain on grid model in HEC-RAS.

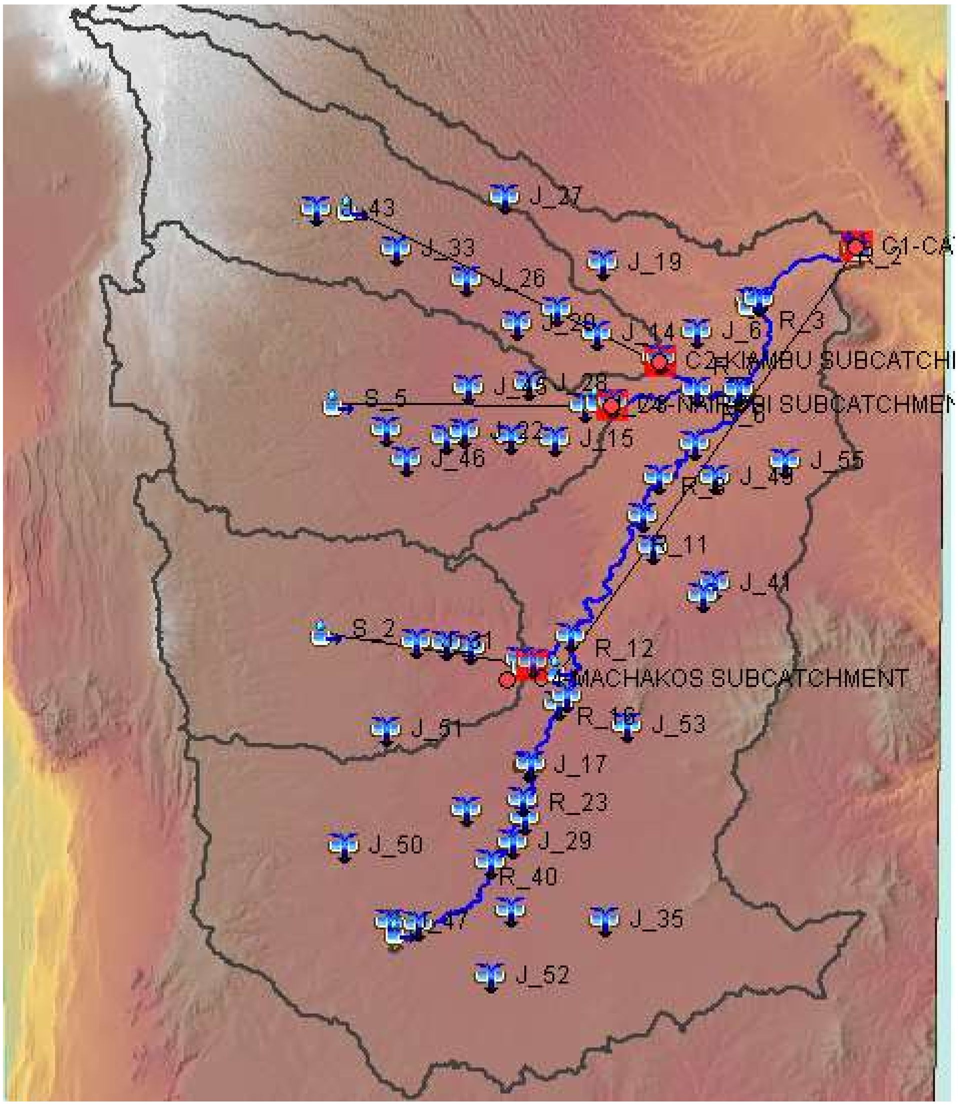

Figure 20. A screenshot from the HEC-HMS hydrologic model showing the sub-basins and reach of the Nairobi catchment.

Table 16. HEC HMS net model output flow result.

Date	Net Daily Rainfall Derived from the HEC-HMS Model (mm)				
	S1-Baseline	**S2-2000LU**	**S3-CP4uplift**	**S4-P25uplift**	**S5-RawDEM**
01/03/2018	0.51	0.32	1.11	1.56	0.51
02/03/2018	3.43	1.73	6.33	8.24	3.43
03/03/2018	56.76	38.15	91.7	113.86	56.76
04/03/2018	14.73	11.57	23.47	29.03	14.73
05/03/2018	8.37	5.79	13.33	16.48	8.37
06/03/2018	17.85	13.07	28.41	35.13	17.85

6.8 HEC-RAS 2D Hydraulic Model Computational Setting

The hydraulic model is set up to simulate a 13-day period to replicate the extreme flood events of 1st to 13th March 2018 and therefore the rain-on-grid model will be run in HEC-RAS using the 2D unsteady diffusion wave equation set and will run for a duration of 13 days to better capture the processes happening in the catchment for the extreme flood events of March 2018. The simulation time Window was set from 00:00am 1st March 2018 to 23:59pm. 13th March 2018. The computational and advanced time step will be varied based on keeping the Courant value between 0.75 and 2 in order to keep the value as close to 1 as possible and generate reliable results. The computational settings used in the HEC-RAS model simulation are summarized in Figure 24 & Figure 25 respectively. The flowchart for the five-step method flowchart of the datasets and methodology used to create the five model scenarios (S1-Baseline, S2-2000LU model, S3-CP4uplift model, S4-P25uplift model, and the S5-RawDEM model.) using the software is shown in Figure 21.

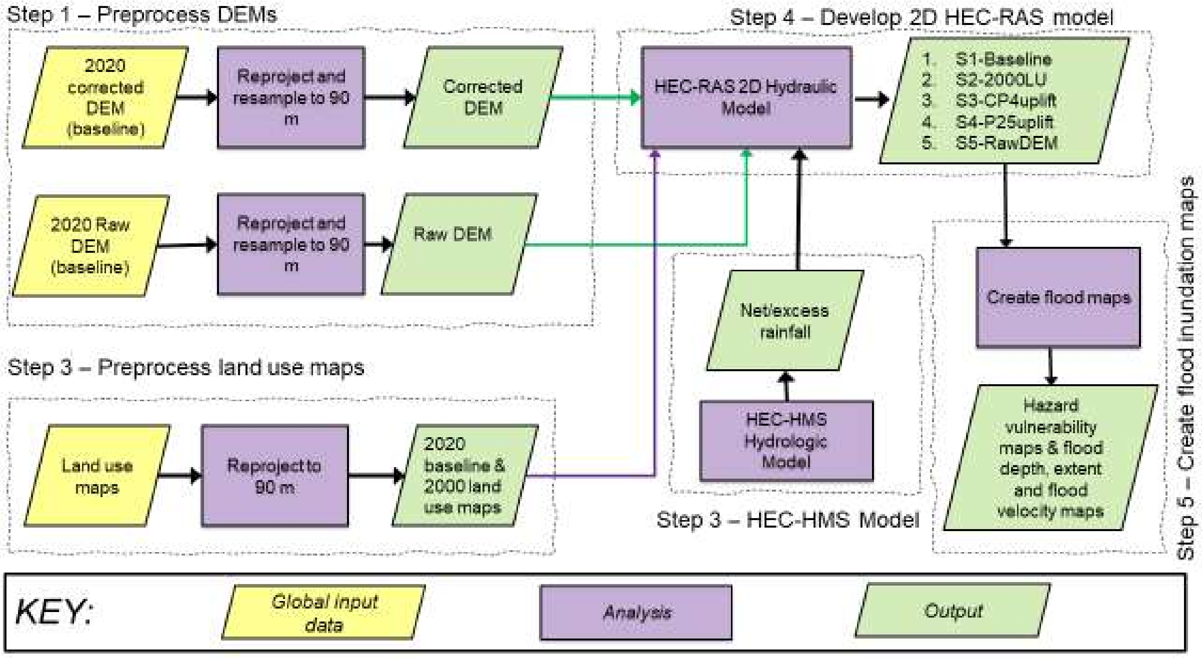

Figure 21. Five-step method flowchart of the datasets and methodology used to create the five model scenarios (S1-Baseline, S2-2000LU model, S3-CP4uplift model, S4-P25uplift model, and the S5-RawDEM model.) using the software.

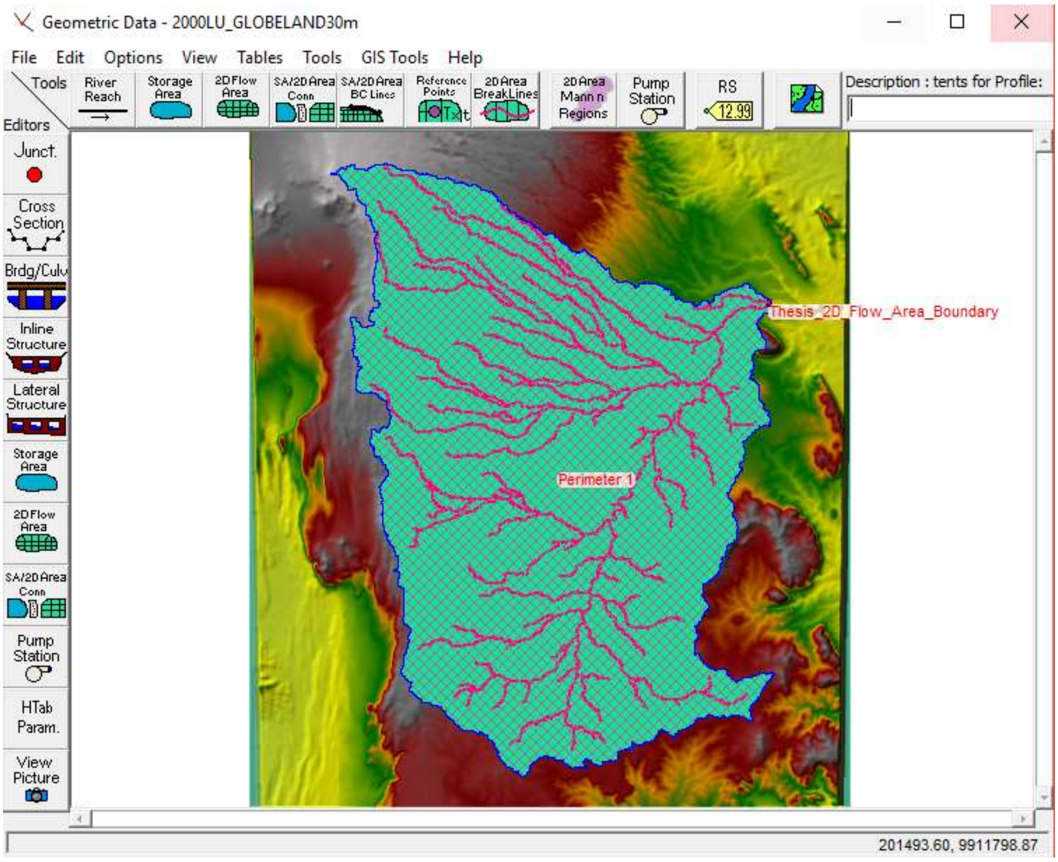

Figure 22. A screenshot from the HEC-RAS model showing the set-up of the 2D flow area boundary used for the five model scenarios.

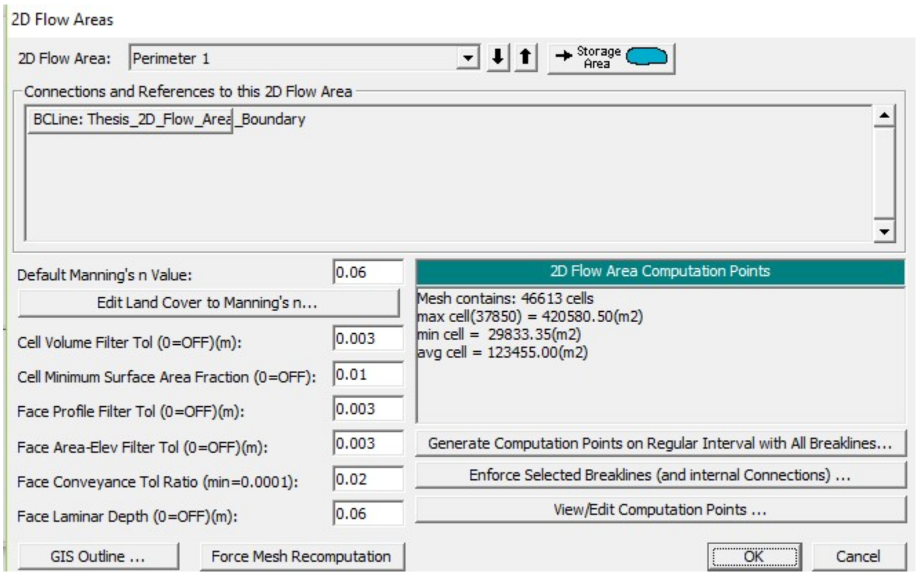

2D Flow Area: Perimeter 1

BCLine: Thesis_2D_Flow_Area_Boundary

Default Manning's n Value: 0.06

Cell Volume Filter Tol (0=OFF)(m): 0.003

Cell Minimum Surface Area Fraction (0=OFF): 0.01

Face Profile Filter Tol (0=OFF)(m): 0.003

Face Area-Elev Filter Tol (0=OFF)(m): 0.003

Face Conveyance Tol Ratio (min=0.0001): 0.02

Face Laminar Depth (0=OFF)(m): 0.06

```
Mesh contains: 46613 cells
max cell(37850) = 420580.50(m2)
min cell =  29833.35(m2)
avg cell = 123455.00(m2)
```

Figure 23. 2D flow area computational points created within the HEC-RAS model.

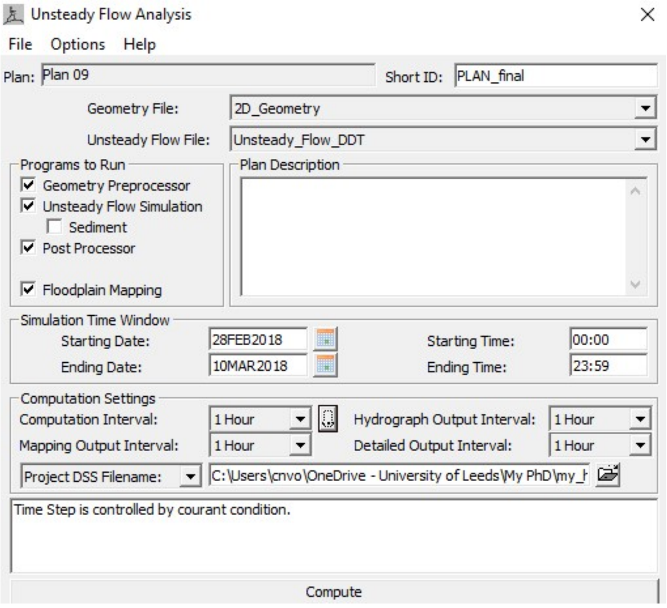

Plan: Plan 09
Short ID: PLAN_final
Geometry File: 2D_Geometry
Unsteady Flow File: Unsteady_Flow_DDT

Programs to Run
☑ Geometry Preprocessor
☑ Unsteady Flow Simulation
☐ Sediment
☑ Post Processor
☑ Floodplain Mapping

Plan Description

Simulation Time Window
Starting Date: 28FEB2018
Ending Date: 10MAR2018
Starting Time: 00:00
Ending Time: 23:59

Computation Settings
Computation Interval: 1 Hour
Hydrograph Output Interval: 1 Hour
Mapping Output Interval: 1 Hour
Detailed Output Interval: 1 Hour
Project DSS Filename: C:\Users\cnvo\OneDrive - University of Leeds\My PhD\my_

Time Step is controlled by courant condition.

Figure 24. Computational settings used in the HEC-RAS 2D hydraulic simulation model.

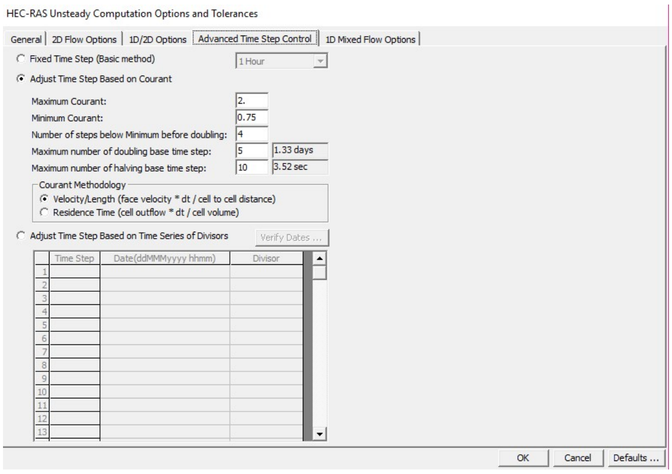

○ Fixed Time Step (Basic method) 1 Hour
● Adjust Time Step Based on Courant

Maximum Courant: 2.
Minimum Courant: 0.75
Number of steps below Minimum before doubling: 4
Maximum number of doubling base time step: 5 1.33 days
Maximum number of halving base time step: 10 3.52 sec

Courant Methodology
● Velocity/Length (face velocity * dt / cell to cell distance)
○ Residence Time (cell outflow * dt / cell volume)

○ Adjust Time Step Based on Time Series of Divisors

Figure 25. Advance time step settings used in the HEC-RAS 2D hydraulic simulation model.

6.9 Watershed and Stream Network Delineation

The hydraulic modelling was performed in HEC-RAS after delineating the catchment basin model using various plugins in QGIS environment. Flow direction and accumulation rasters were derived in QGIS environment using the GRASS GIS tool r.watershed tool. The tool allows the calculation of several parameters to derive the flow accumulation and direction rasters. The r.watershed plugin tool was used to define the main river outlet and delineate the watershed. With the catchment delineated, a raster layer was produced and the final steps involved the conversion of raster layer to a vector file using the r.t.vect plugin tool in QGIS to generate the river catchments of the study area as shown in Figure 26. A screenshot from QGIS software environment showing the Strahler order of each stream segment, sub-watershed draining into each stream segment (reach). This tool produces a vector network and shapefile from the stream raster grid. The flow direction grid was used to connect flow paths along the stream raster. The sub-watershed draining to each stream segment (reach) is also delineated and labelled with the value identifier that corresponds to the WSNO (watershed number) attribute in the Stream Reach shapefile. The tool orders the stream network according to the Strahler ordering system as shown in Figure 27. Delineated Watershed and Stream Network of Study Area.

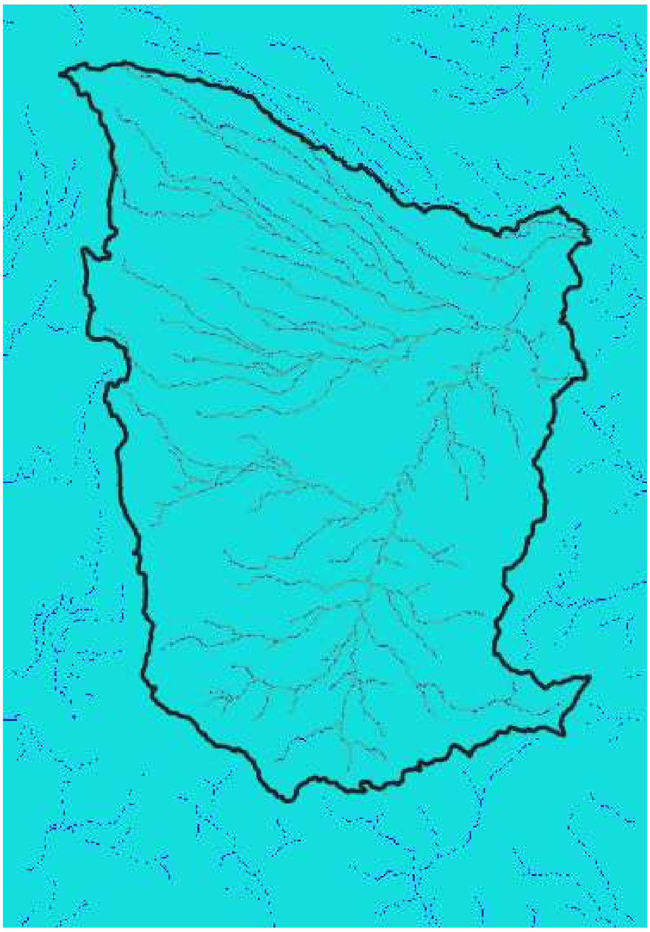

Figure 26. A screenshot from QGIS software environment showing the Strahler order of each stream segment, sub-watershed draining into each stream segment (reach).

Streams that don't have any other streams draining in to them are order 1. When two stream reaches of different order join, the order of the downstream reach is the order of the highest incoming reach. When two reaches of equal order join the downstream reach order is increased by 1. When more than two reaches join, the downstream reach order is calculated as the maximum of the highest incoming reach order or the second highest incoming, reach order + 1. This generalizes the common definition to cases where more than two reaches join at a point.

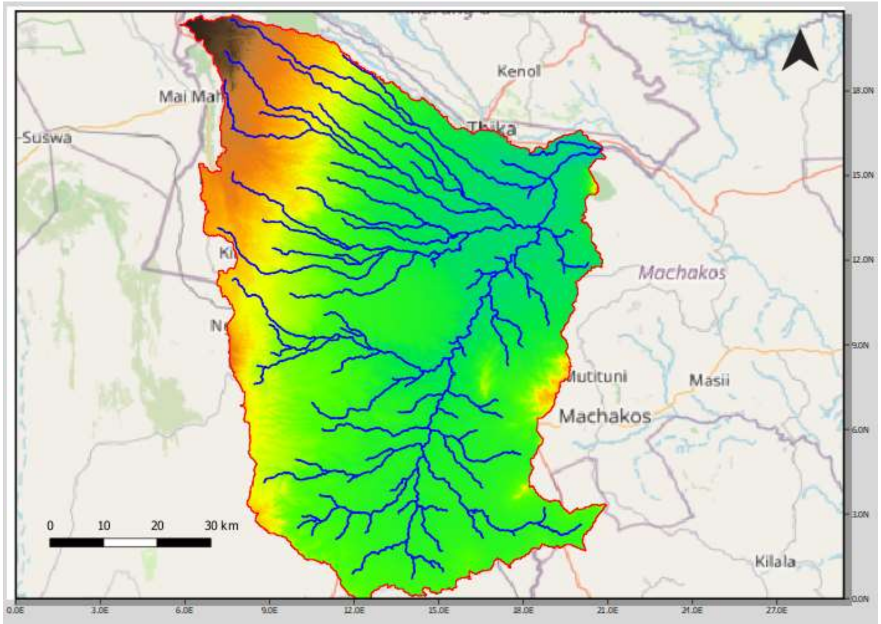

Figure 27. Delineated Watershed and Stream Network of Study Area

Manning’s n (Roughness Coefficient) for HEC-RAS 2D Modelling

The HEC-RAS 2D modelling software used for the study has manning’s n values (Roughness Coefficient) for 2D flow area that are associated with land cover types to account for energy friction losses of overland flow and/or channel flow. Certain factors such as, overland surface type and texture, pervious or impervious areas, 2D flow depth impact on the manning’s n values for 2D hydraulic flood modelling. The HEC-RAS 2D Manual provides an estimate of manning’s n value for each NLCD (land cover) and they are summarized in Table 17 below.

Table 17. Example Manning's n values for various NLCD Land Cover Types.

NLCD Value	Manning'sn Value range	Normal Manning's n value	Description
11	0.025 -0.05	0.035	**Open Water-** areas of open water, generally with lessthan 25% cover of vegetation or soil. This is for natural streams on mild to moderate slopes.
12	n/a	n/a	**Perennial Ice/Snow-** areas characterized by a perennial cover of ice and/or snow, generally greaterthan 25% of total cover.
21	0.03 - 0.05	0.040	**Developed, Open Space-** areas with a mixture of some constructed materials, but mostly vegetation in the form of lawn grasses. Impervious surfaces accountfor less than 20% of total cover. These areas most commonly include large-lot single-family housing units, parks, golf courses, and vegetation planted in developed settings for recreation, erosion control, or aesthetic purposes.
22	0.06 - 0.12	0.100	**Developed, Low Intensity-** areas with a mixture ofconstructed materials and vegetation. Impervious surfaces account for 20% to 49% percent of total cover. These areas most commonly include single-family housing units.
23	0.08 - 0.16	0.080	**Developed, Medium Intensity** -areas with a mixtureof constructed materials and vegetation. Impervious surfaces account for 50% to 79% of the total cover. These areas most commonly include single-family housing units.
24	0.12 - 0.20	0.150	**Developed High Intensity-highly** developed areaswhere people reside or work in high numbers. Examples include apartment complexes, row housesand commercial/industrial. Impervious surfaces account for 80% to 100% of the total cover.
31	0.023 - 0.030	0.025	**Barren Land (Rock/Sand/Clay)** - areas of bedrock, desert pavement, scarps, talus, slides, volcanic material, glacial debris, sand dunes, strip mines, gravelpits and other accumulations of earthen material. Generally, vegetation accounts for less than 15% of total cover.
41	0.10 - 0.20	0.160	**Deciduous Forest-** areas dominated by trees generallygreater than 5 meters tall, and greater than 20% of totalvegetation

NLCD Value	Manning's n Value range	Normal Manning's n value	Description
			cover. More than 75% of the tree species shed foliage simultaneously in response to seasonal change.
42	0.08 - 0.16	0.160	**Evergreen Forest-** areas dominated by trees generally greater than 5 meters tall, and greater than 20% of total vegetation cover. More than 75% of the tree species maintain their leaves all year. Canopy is never without green foliage.
43	0.08 - 0.20	0.160	**Mixed Forest-** areas dominated by trees generally greater than 5 meters tall, and greater than 20% of total vegetation cover. Neither deciduous nor evergreen species are greater than 75% of total tree cover.
51	0.025 - 0.05	0.040	**Dwarf Scrub-** Alaska only areas dominated by shrubs less than 20 centimetres tall with shrub canopy typically greater than 20% of total vegetation. This type is often co-associated with grasses, sedges, herbs, and non-vascular vegetation.
52	0.07 - 0.16	0.100	**Shrub/Scrub-** areas dominated by shrubs; less than 5 meters tall with shrub canopy typically greater than 20% of total vegetation. This class includes true shrubs, young trees in an early successional stage or trees stunted from environmental conditions.
71	0.025 - 0.50	0.035	**Grassland/Herbaceous-** areas dominated by graminoid or herbaceous vegetation, generally greater than 80% of total vegetation. These areas are not subject to intensive management such as tilling but can be utilized for grazing.
72	0.025 - 0.50	0.040	**Sedge/Herbaceous-** Alaska only areas dominated by sedges and forbs, generally greater than 80% of total vegetation. This type can occur with significant other grasses or other grass like plants, and includes sedge tundra, and sedge tussock tundra.
73	n/a	n/a	**Lichens-** Alaska only areas dominated by fruticose or foliose lichens generally greater than 80% of total vegetation.
74	n/a	n/a	**Moss-** Alaska only areas dominated by mosses, generally greater than 80% of total vegetation.

NLCD Value	Manning'sn Value range	Normal Manning's n value	Description
81	0.025 - 0.50	0.030	**Pasture/Hay-areas** of grasses, legumes, or grass- legume mixtures planted for livestock grazing or theproduction of seed or hay crops, typically on a perennial cycle. Pasture/hay vegetation accounts for greater than 20% of total vegetation.
82	0.020 - 0.15	0.035	**Cultivated Crops** -areas used for the production of annual crops, such as corn, soybeans, vegetables, tobacco, and cotton, and also perennial woody crops such as orchards and vineyards. Crop vegetation accounts for greater than 20% of total vegetation. This class also includes all land being actively tilled.
90	0.045 - 0.015	0.120	**Woody Wetlands-** areas where forest or shrubland vegetation accounts for greater than 20% of vegetative cover and the soil or substrate is periodically saturatedwith or covered with water.
95	0.05 - 0.085	0.070	**Emergent Herbaceous Wetlands-** Areas where perennial herbaceous vegetation accounts for greater than 80% of vegetative cover and the soil or substrateis periodically saturated with or covered with water.

Once imported into the HEC-RAS software, the land covers were assigned a Manning's value based on their respective land categories. The different land cover used and their corresponding Manning's coefficients are in line with the National Land Cover Database (Jin et al., 2019). The land cover types for the landcover maps are shown in Figure 28.

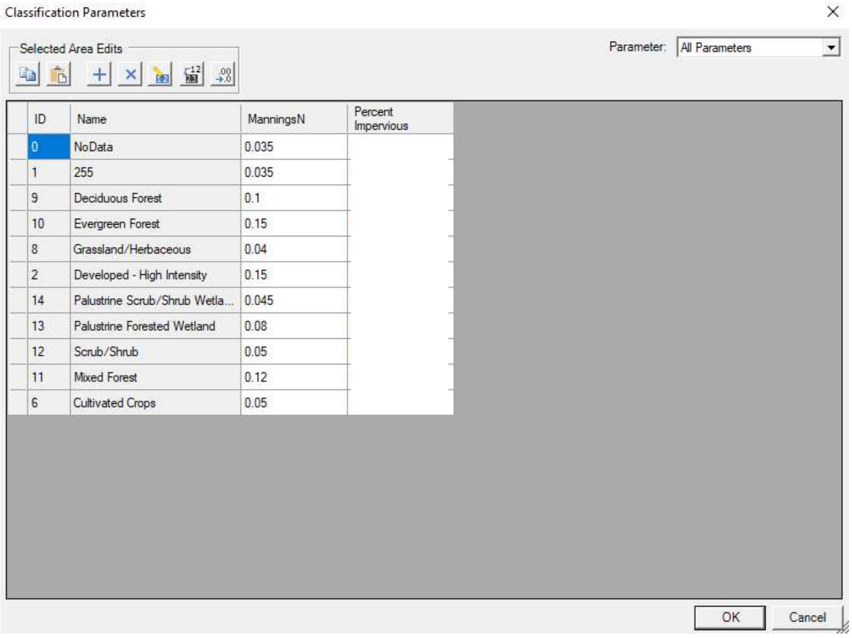

Parameter: All Parameters

ID	Name	ManningsN	Percent Impervious
0	NoData	0.035	
1	255	0.035	
9	Deciduous Forest	0.1	
10	Evergreen Forest	0.15	
8	Grassland/Herbaceous	0.04	
2	Developed - High Intensity	0.15	
14	Palustrine Scrub/Shrub Wetla...	0.045	
13	Palustrine Forested Wetland	0.08	
12	Scrub/Shrub	0.05	
11	Mixed Forest	0.12	
6	Cultivated Crops	0.05	

Figure 28. A screenshot from the HEC-RAS hydraulic model software of the land cover data types, Manning's roughness coefficient values data for the 2008 & 2018 land maps for the study area and their respective Manning's value.

Once the Land Cover/Manning's n layer was developed within the HEC-RAS model, the next step is to associate the Landcover/Manning's data with a specific Geometry data that will only be applied to that specific Geometry data set, Figure 29.

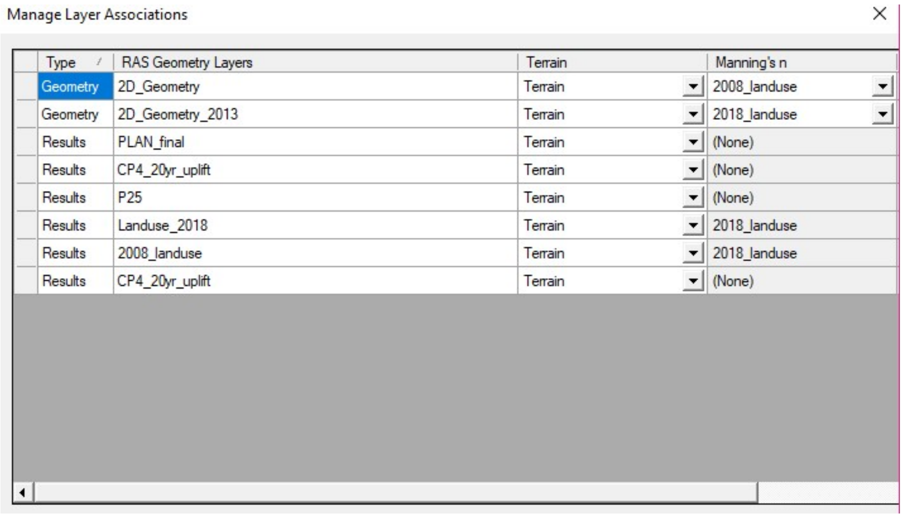

Type	RAS Geometry Layers	Terrain	Manning's n
Geometry	2D_Geometry	Terrain	2008_landuse
Geometry	2D_Geometry_2013	Terrain	2018_landuse
Results	PLAN_final	Terrain	(None)
Results	CP4_20yr_uplift	Terrain	(None)
Results	P25	Terrain	(None)
Results	Landuse_2018	Terrain	2018_landuse
Results	2008_landuse	Terrain	2018_landuse
Results	CP4_20yr_uplift	Terrain	(None)

Figure 29. A screenshot from the HEC-RAS 2D hydraulic model of the Manage Layer Association showing the association of Land Cover/Manning's n layer with a specific Geometry data set.

6.10 Flood Hazard Assessment

Flow depth and velocity typically are the flow base data used when assessing flood hazard. In order to quantify the hydraulic output from the HEC-RAS model, the combined flood hazard curves of flow depth and velocity of the study area are taken from the Australian Rainfall and Runoff (Ball et al., 2019b). The hazard curves are incorporated into the HEC-RAS 2D hydraulic model for five modelling scenarios under (1). 2020 baseline landuse conditions: **S1-Baseline**, (2) 2000 historical landuse conditions: **S2-2020LU** (3). Future 20yr return period rainfall with uplift factor: **S3-CP4uplift**, and (4) Future 20yr return period rainfall with uplift factor: **S4-P25uplift**, at a fixed profile time of 3rd March 2018 05:00 when flowrate is at its maximum. The vulnerability classifications are calculated by multiplying the depth (d) of flow and velocity (v) of flow.

The raster calculator script below (Figure 31) is used as input in the HEC-RAS model and matches the APR flood hazard mapping which draws from (Smith et al., 2014) as referenced in Australian Rainfall and Runoff guidelines (Ball et al., 2019a). Each section is then assigned a certain limit, as shown in Table 18 adapted from (Smith et al., 2014). The process of quantifying flood hazard involved the interpretation of the output/flood behavior information generated by the HEC-RAS 2D model directly into the flood hazard classification index Figure 30, adapted from (Smith et al., 2014). This involved combining the mapped depth (D) and velocity (V) information from the HEC-RAS model into a velocity-depth product (D x V) and categorizing this product value using the hazard vulnerability curves.

The combined hazard curves – vulnerability thresholds classification limits has been applied in this research to describe the flood behavior of the study site. This chapter describes the process of flood hazard quantification of the study area by, first, quantifying the defined flood event using the HEC-RAS model. Second, quantify the flood hazard by using a combination of flood depth and flood velocity. The hazard vulnerability curve adapted from (Smith et al., 2014) is applied to quantify the flood hazard to people, buildings and infrastructure. The safety of people on flood path or flooded streets is of major concern in urban storm water design and floodplain management (R. J. Cox et al., 2010). The safety of people can be compromised when exposed to flows, which exceed their ability to remain standing and/or traverse a waterway. The current Australian Rainfall and Runoff (ARR) guidelines (Smith et al., 2014) stipulate that “to prevent pedestrians being swept along streets and other drainage paths during major storm events, the product of velocities (V) and depths (D) in streets and major flow paths generally should not exceed D.V = 0.4 m2 /s”. For example, when considering the safety of driving a vehicle during a flood event, the hazard values above the D x V thresholds for vehicle stability based on the hazard vulnerability curve will indicate a potential hazard, similar to potential hazard to people during a flood event. It is possible that maximum hazard value during a flood event may not occur at the peak flow rate or peak flood level, but on some combination of D x V (Smith et al., 2014).

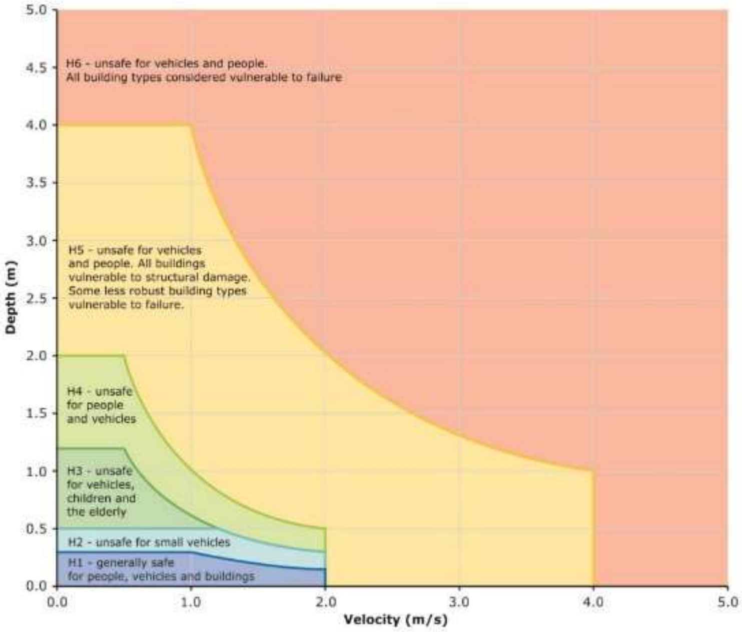

Figure 30. Combined flood hazard curve developed by (Smith et al., 2014).

```
‘——————————————————————————-
‘ rasscript for Flood Hazard mapping based on
‘ WRL Technical Report 2014/07 Flood Hazard
‘ by G P Smith, E K Davey and R J Cox
‘ UNSW Water Research Laboratory
‘ https://knowledge.aidr.org.au/media/2334/wrl-flood-hazard-techinical-report-september-2014.pdf
‘ As cited in ARR 2019 Book 6: Flood Hydraulics Chapter 7: Safety Design Criteria
‘ http://book.arr.org.au.s3-website-ap-southeast-2.amazonaws.com/
‘ Figure 5-5 and Table 5-2
‘ Requirements: Terrain, Depth, ‘d’ and Velocity, ‘v’
‘——————————————————————————-
If d = NoData OrElse v = NoData Then
Output = NoData
ElseIf d > 4 Or v > 4 Or d*v > 4 Then
Output = 6 ‘H6 unsafe for people, vehicles & all buildings
ElseIf d > 2 Or v>2 Or d*v>1 Then
Output = 5 ‘H5 unsafe for people, vehicles & some buildings
ElseIf d > 1.2 Or d * v > 0.6 Then
Output = 4 ‘H4 unsafe for people & vehicle
ElseIf d > 0.5 Then
Output = 3 ‘H3 unsafe for vehicle and vulnerable people
ElseIf d > 0.3 Or d * v > 0.3 Then
Output = 2 ‘H2 unsafe for small vehicles
Else
Output = 1 ‘H1 generally safe for people, vehicles, & buildings
End If
```

Figure 31. The Australian Rainfall and Runoff guidelines raster calculator script (Smith et al., 2014), 2014) used for the calculation of flood hazard mapping in the HEC-RAS model.

The combined flood hazard curves presented in Figure 30 shows the hazard thresholds that relate to the vulnerability of people living in the catchments of the study area when interacting with floodwaters. The combined curves (Smith et al., 2014) are divided into hazard classifications that relate to specific vulnerability thresholds as described in Table 18.

Table 18. Combined hazard curves – vulnerability threshold classification limits.

Hazard Vulnerability Classification	Description
Hl	Generally safe for vehicles, people and buildings.
H2	Unsafe for small vehicles.
H3	Unsafe for vehicles children and the elderly.
H4	Unsafe for vehicles and people.
H5	Unsafe for vehicles and people. All buildings vulnerable to structural damage. Some less robust buildings subject to failure.
H6	Unsafe for vehicles and people. All building types considered vulnerable to failure.

7.0 SCENARIO ANALYSIS

This chapter describes the scenario analysis of the five model scenarios developed in the HEC-HMS and HEC-RAS 2 D hydraulic models in this study: a baseline model (S1-Baseline) for the extreme rainfall event for 1st to 13th of March 2018 with 2020 landuse; the 2000 landuse model (S2-2000LU) with 2000 landuse; the CP4 future 20yr return period uplift model (S3-CP4uplift with 2020 landuse; the P25 future 20yr return period uplift model (S4-P25uplift) with 2020 landuse and (S5-RawDEM) model with 2020 land use data. The rainfall hydrographs used in the five sets of model scenarios developed in this study for the March 2018 rainfall events is shown in Figure 32. The area under the hyetograph for the S1-Baseline mode and S5-RawDEM The hydrograph for the S1-Baseline and S5-Raw DEM model is combined in Figure 32. Analysis will be undertaken for the five model scenarios to investigate the impact of landuse change and climate change on flooding over the overall catchment area (C1-Combined) and sub-catchments Kiambu (C2-Kiambu), Nairobi CBD (C3-Nairobi) and Machakos (C4-Machakos) sub-catchment areas shown in Figure 33, Figure 34, Figure 35 & Figure 36 respectively.

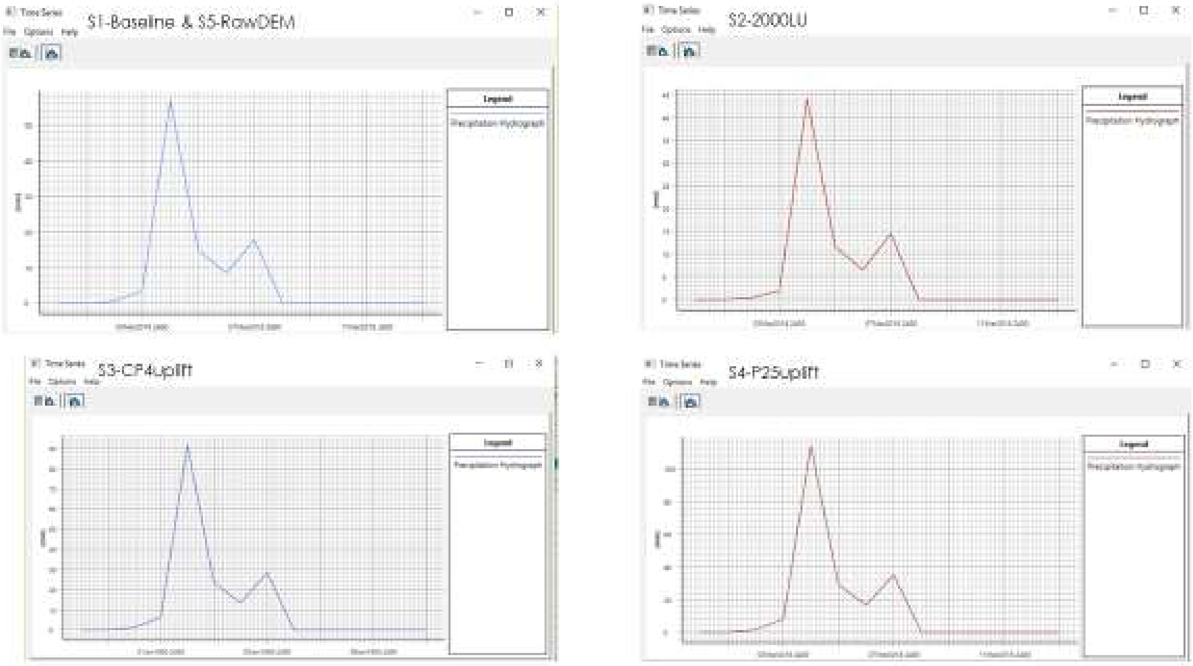

Figure 32. Rainfall hydrographs for the five sets of models (S1-Baseline, S2-2000LU, S3-CP4uplift, S4-P25uplift and S5-RawDEM) developed in this study for the 1st to 13th March rainfall evens of 2018.

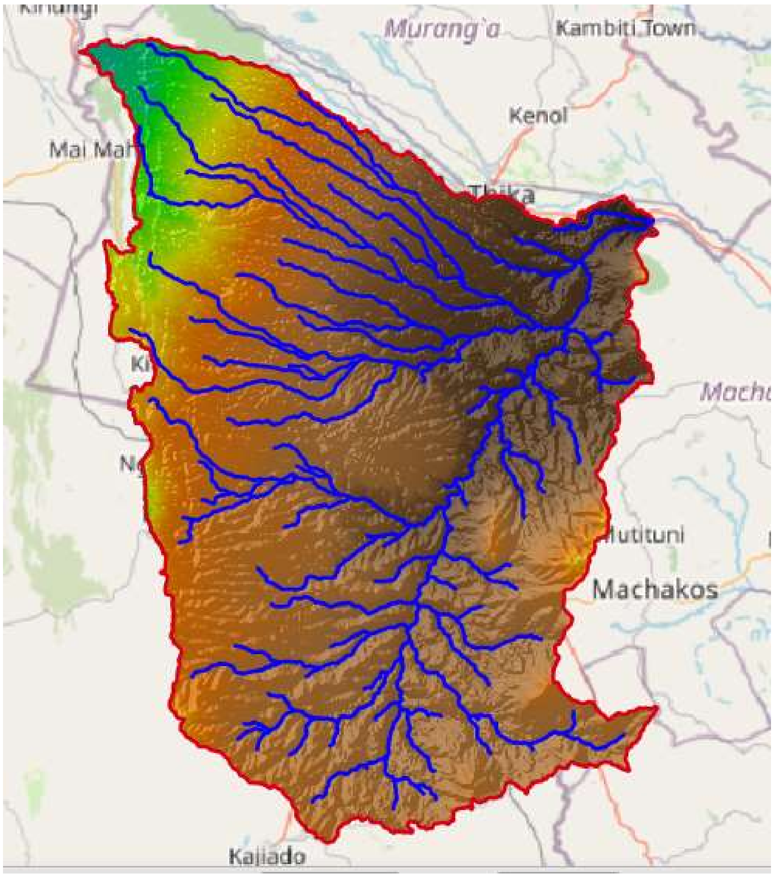

Figure 33. A screenshot from QGIS software of the overall catchment area (C1) used in the model

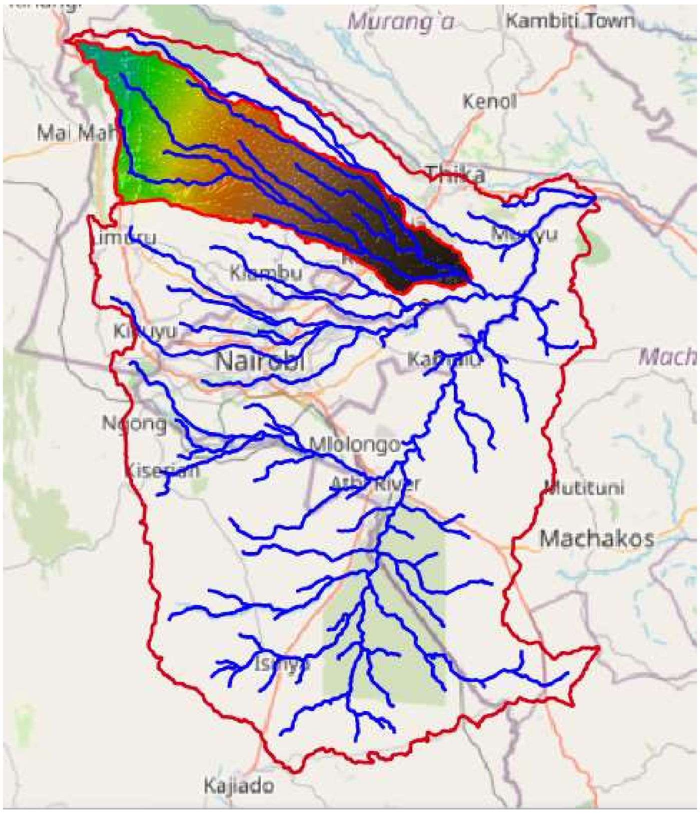

Figure 34. A screenshot from QGIS software of the Kiambu sub-catchment area (C2) used in the model.

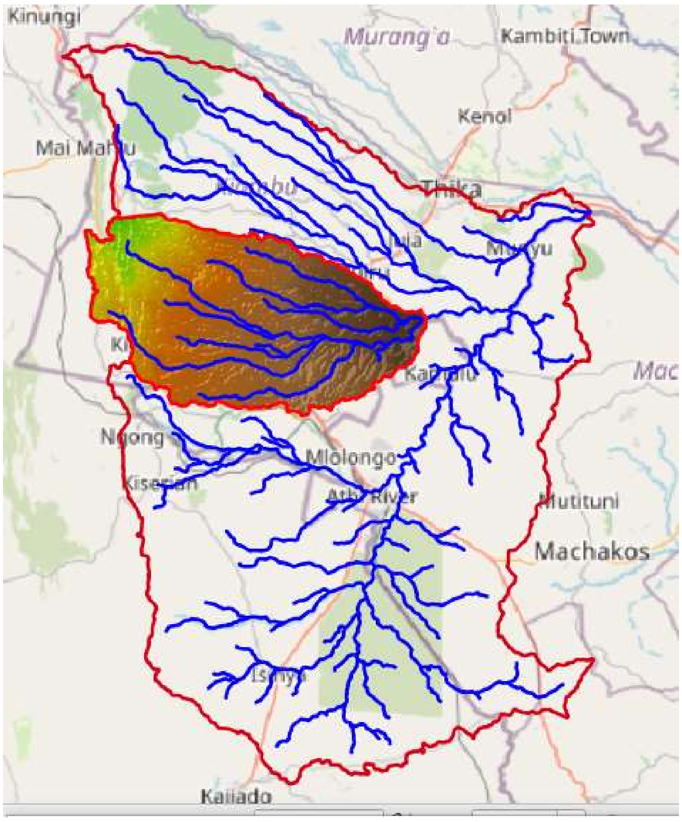

Figure 35. A screenshot from QGIS software of the Nairobi district sub-catchment area (C3) used in the model.

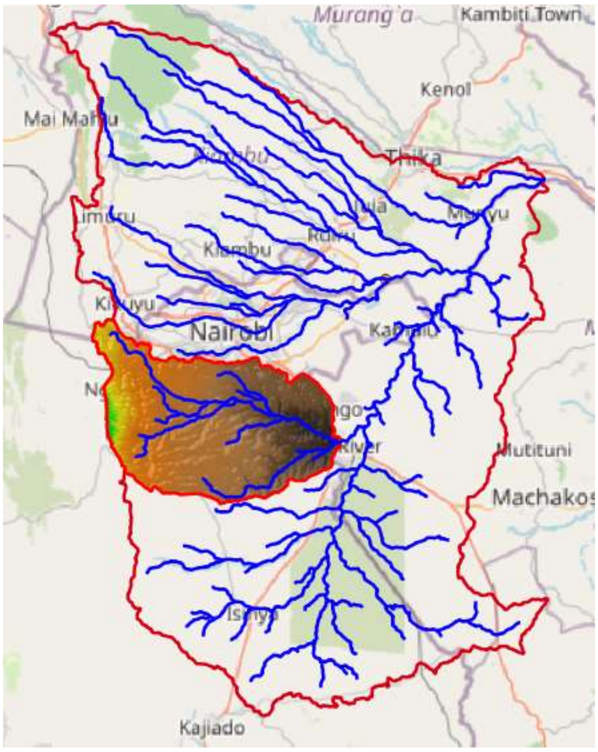

Figure 36. A screenshot from the QGIS software of the Machakos sub-catchment area (C4) used in the model.

7.1 Land use change and Climate change impact scenario analysis

In performing the unsteady flow analysis for the four different model scenarios in this study, the RAS Mapper within the HEC-RAS software application was used to build various type of inundation maps (Depth(max), Velocity(max), Water Surface Elevation, WSE(max), D*V(max)) and visualize HEC-RAS software application results in a map-based format (Figure 37). Flow hydrographs at the outlet sections of the catchments C1, C2, C3 and C4 draining into the River Athi are plotted below in Figure 38, Figure 39, Figure 40, and showing flow in (m^3/s) plotted against the time of simulation. The hydrographs for S1-Baseline, S2-2000LU, S3-CP4uplift and S4-P25uplift generally follow similar pattern for C1, C2, C3 and C4. Peak flows of 5,200 m^3/s, 600 m3/s, 600 m3/s and 1,100 m3/s were reached on 5th March 2018 for the S1-Baseline, S2-2000LU, S3-CP4uplift and S4-P25uplift respectively. The maximum flood depth and velocities for the model results for S1-Baseline, S2-2000LU, S3-CP4uplift and S4-P25uplift are shown in Figure 42, Figure 43, Figure 44, and Figure 45. There are two distinctive peak flows on 5th and 8th March corresponding to the rainfall data input for the HECRAS model. The S3-CP4uplift and S4-P25uplift hydrographs show significantly higher peak flows than S1-Baseline and S2-2000LU suggesting that the impact of climate change is more pronounced than change in landuse across C1, C2, C3 and C4 catchments.

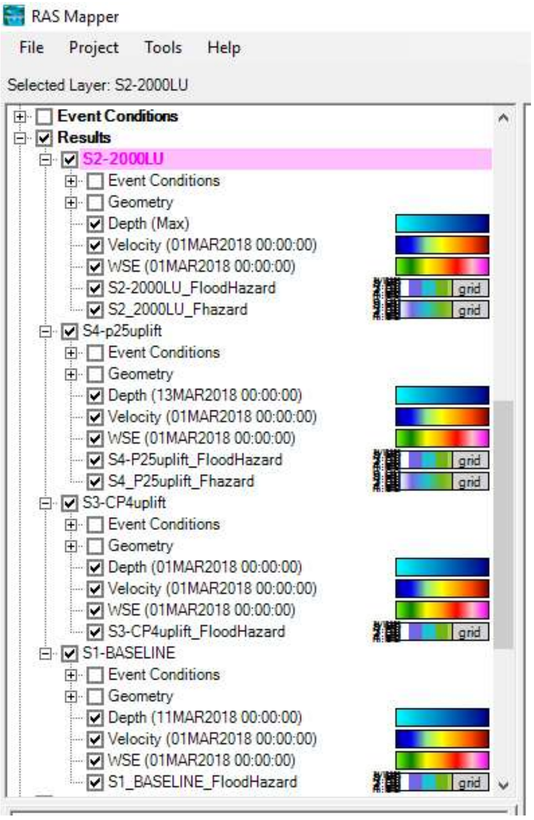

Selected Layer: S2-2000LU

- ☐ Event Conditions
- ☑ Results
  - ☑ S2-2000LU
    - ☐ Event Conditions
    - ☐ Geometry
    - ☑ Depth (Max)
    - ☑ Velocity (01MAR2018 00:00:00)
    - ☑ WSE (01MAR2018 00:00:00)
    - ☑ S2-2000LU_FloodHazard
    - ☑ S2_2000LU_Fhazard
  - ☑ S4-p25uplift
    - ☐ Event Conditions
    - ☐ Geometry
    - ☑ Depth (13MAR2018 00:00:00)
    - ☑ Velocity (01MAR2018 00:00:00)
    - ☑ WSE (01MAR2018 00:00:00)
    - ☑ S4-P25uplift_FloodHazard
    - ☑ S4_P25uplift_Fhazard
  - ☑ S3-CP4uplift
    - ☐ Event Conditions
    - ☐ Geometry
    - ☑ Depth (01MAR2018 00:00:00)
    - ☑ Velocity (01MAR2018 00:00:00)
    - ☑ WSE (01MAR2018 00:00:00)
    - ☑ S3-CP4uplift_FloodHazard
  - ☑ S1-BASELINE
    - ☐ Event Conditions
    - ☐ Geometry
    - ☑ Depth (11MAR2018 00:00:00)
    - ☑ Velocity (01MAR2018 00:00:00)
    - ☑ WSE (01MAR2018 00:00:00)
    - ☑ S1_BASELINE_FloodHazard

*Figure 37. A screenshot showing the results of the various type of inundation maps (Depth(max), Velocity(max), Water Surface Elevation, WSE(max), D*V(max), and Flood Hazard Maps) generated using the RAS Mapper within the HEC-RAS software application.*

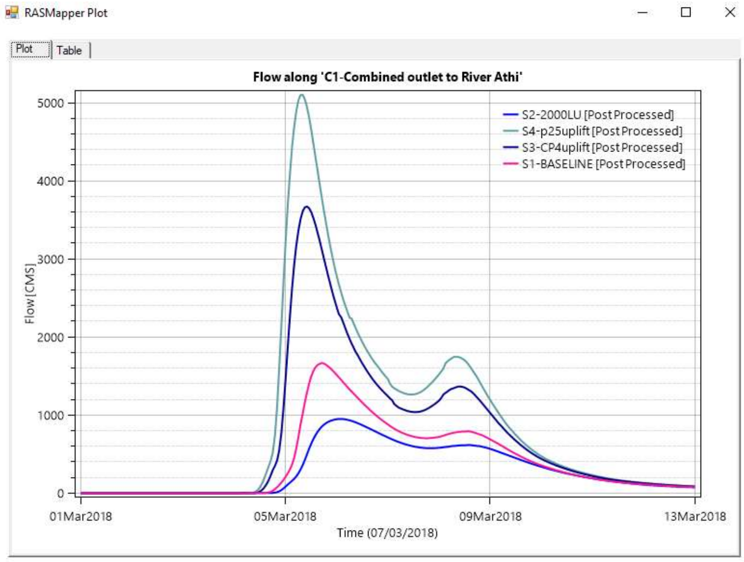

Figure 38. A screenshot from the HECRAS model of flow hydrograph for C1 outlet to River Athi.

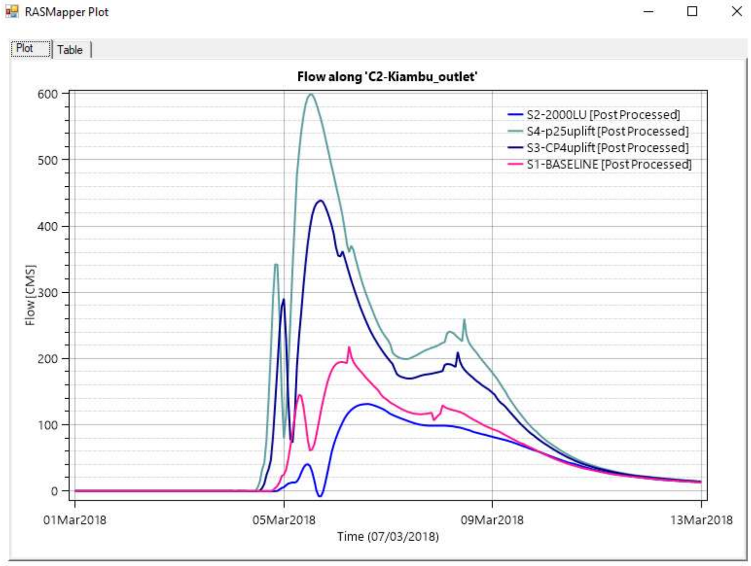

Figure 39. A screenshot from the HECRAS model of flow hydrograph for C2-Kiambu outlet to River Athi.

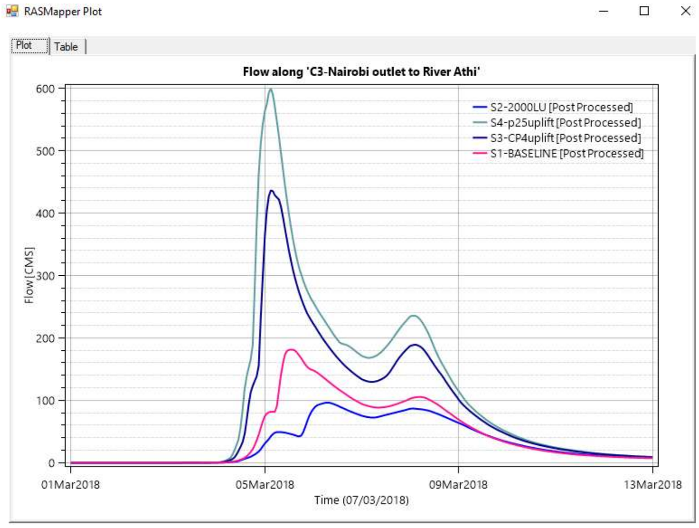

Figure 40. A screenshot from the HECRAS model of flow hydrograph for C3-Nairobi outlet to River Athi.

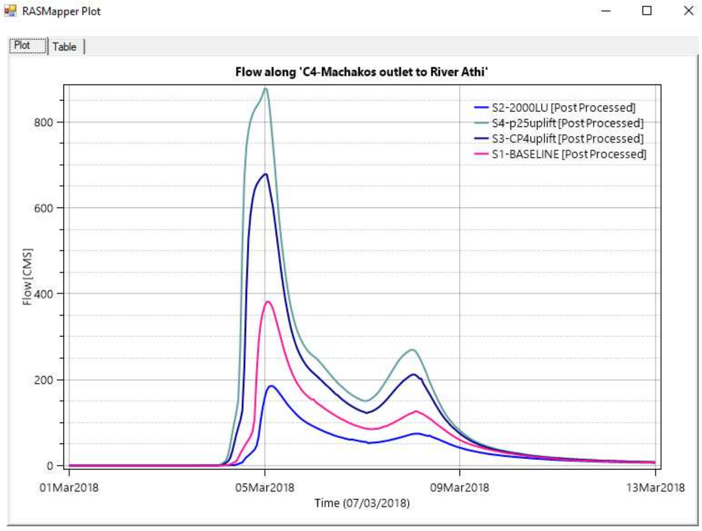

Figure 41. A screenshot from the HECRAS model of flow hydrograph for C4-Machakos outlet to River Athi.

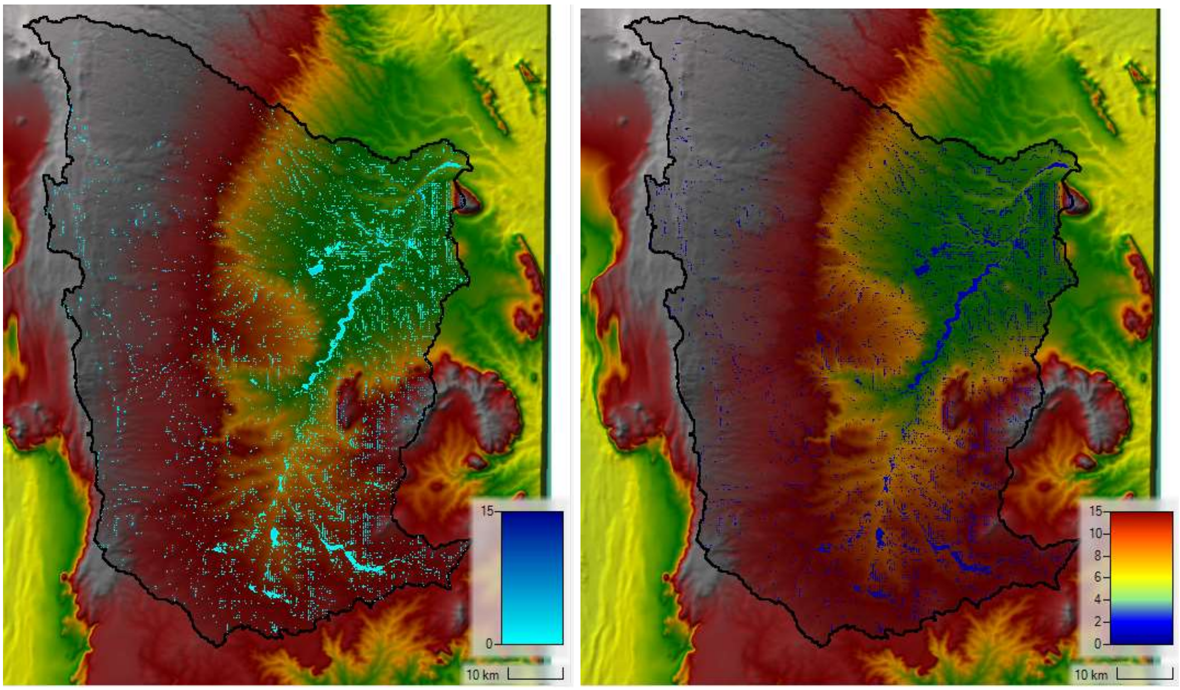

Figure 42. A screenshot from the HECRAS model of maximum flow depth (left) and velocity (right) for S1-Baseline over C1 catchment.

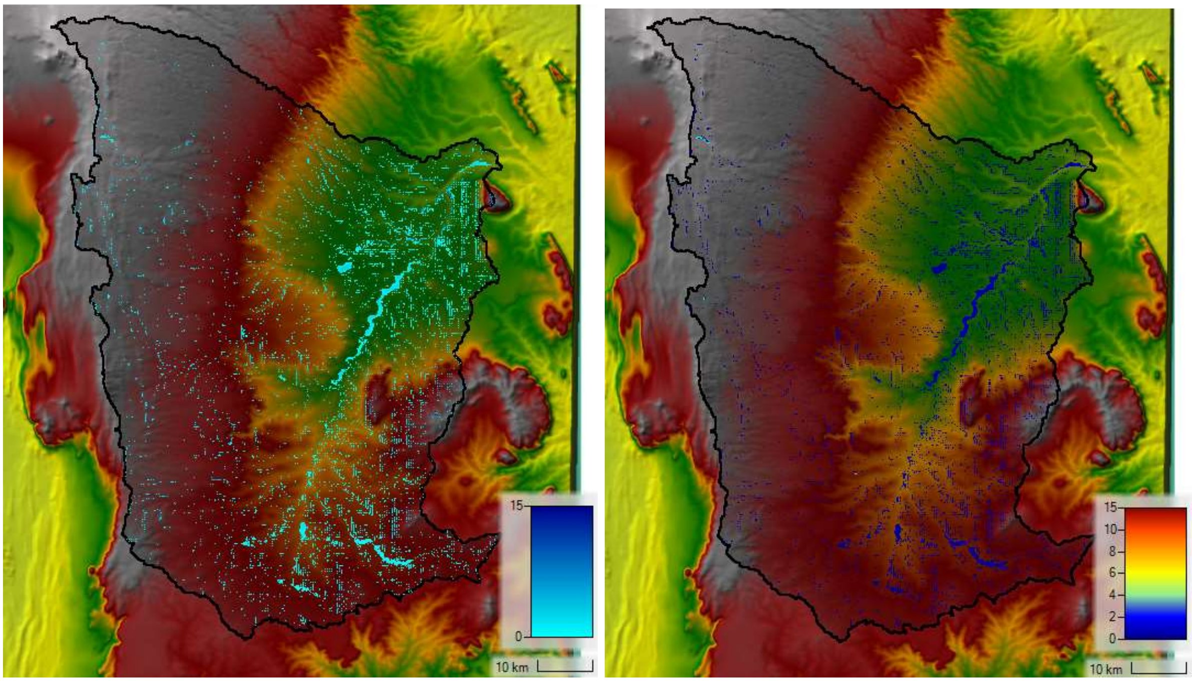

Figure 43. A screenshot from the HECRAS model of maximum flow depth (left) and velocity (right) for S2-2000LU over C1 catchment.

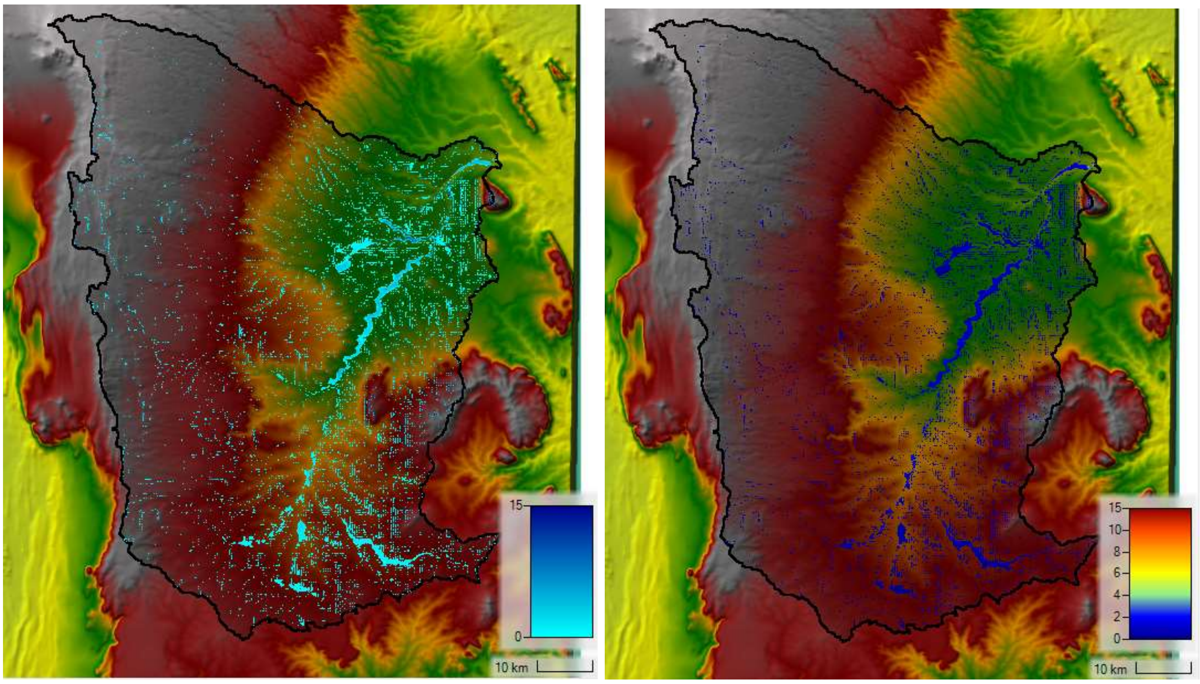

Figure 44. A screenshot from the HECRAS model of maximum flow depth (left) and velocity (right) for S3-CP4uplift over C1 catchment.

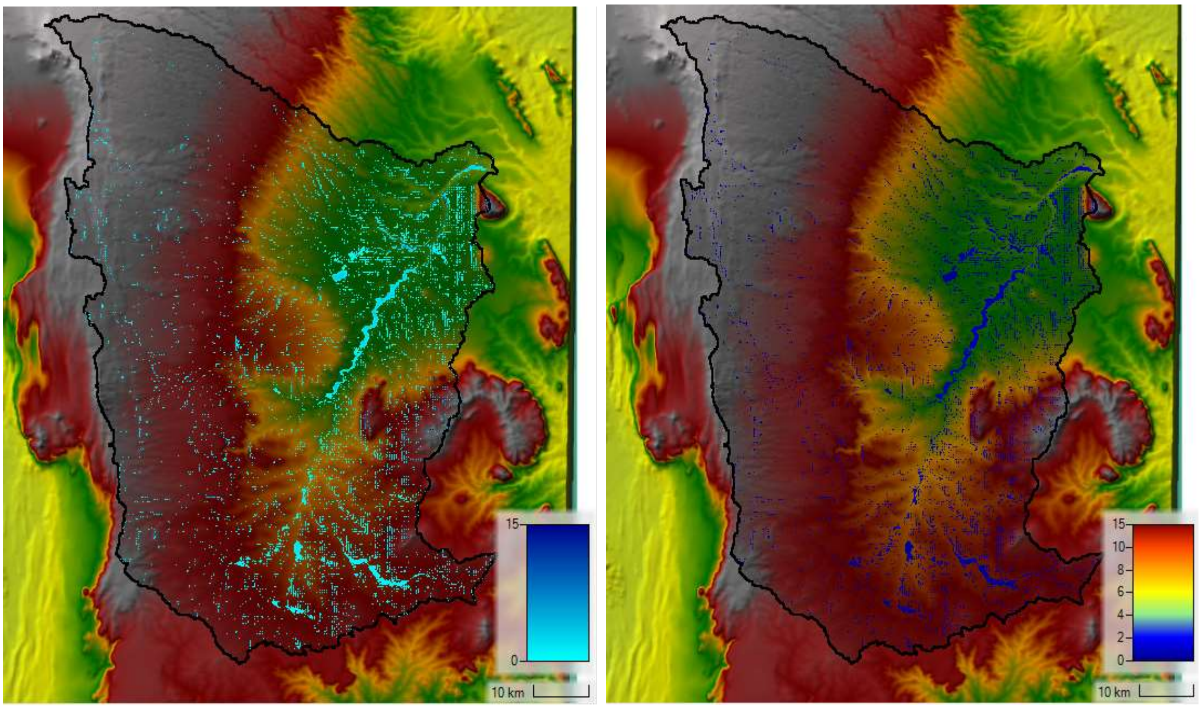

Figure 45. A screenshot from the HECRAS model of maximum flow depth (left) and velocity (right) for S4-P25uplift over C1 catchment.

7.2 Urban Land Use Transition

The landuse for 2000, 2020, and change in landuse between 2000 and 2020 for the catchments C1, C2, C3 and C4 are shown in Figure 46, Figure 47, Figure 48, and Figure 48 respectively. The transition matrix showing Landuse and landcover (LULC) change in C1, C2, C3 and C4 between 2000 and 2020 are also shown in Table 19, Table 20, Table 21, and Table 22 respectively. The change in landuse across C1 change revealed there's increase/decrease of 4.46%, 0.77%, -3.64%, 0.12%, -0.03%, 0.41%, and -1.98% in cultivated land, forest, grassland, shrubland, waterbodies, urban area, and bareland respectively between 2000 and 2020. The increase in cultivated land by 4.46% from 32.5% in 2000 to 36.9% in 2020 was due to direct result of grassland and bareland converted to cultivated land in 2020. The most predominant landuse change class across C1, C2, C3, and C4 is cultivated land. The trend of increase in cultivated land in witnessed in C1 in 2020 is similar for C3 and C4 sub-catchments, except for C2 sub-catchment where there is a small decrease (-0.12%) in cultivated land between 2000 and 2020. The increase in cultivated land area across C1, C3, and C4 is undoubtedly a contributing factor to the peaks witnessed in the hydrographs, especially with C4 where there was a significant increase (7.59%) in cultivated land area between 2000 and 2020.

A comparison of landuse change in forested area across C1, C2, C3 and C4 revealed a percentage increase of 0.77%, 1.09% across C1, C3 and C4 with the exception of C2 which unsurprisingly being predominantly an urban area witnessed a decrease of 0.7% in forested area between 2000 and 2020. between S1-Baseline and S2-2000LU reveal the impact of change in landuse on the hydrograph between 2000 and 2020. A comparison of changes in urban landuse classification across C1, C2, C3, C4 revealed a percentage increase of 0.41%, 0.003%, 1%, and 0.44 respectively. The significant change in urban landuse classification witnessed across C3 is unsurprising considering the urban nature of the sub-catchment, Nairobi city. The increase in peak flow as seen in the flow hydrograph for C3 and shown in Figure 40 can be attributed to the change in urban land use between 2000 and 2020.

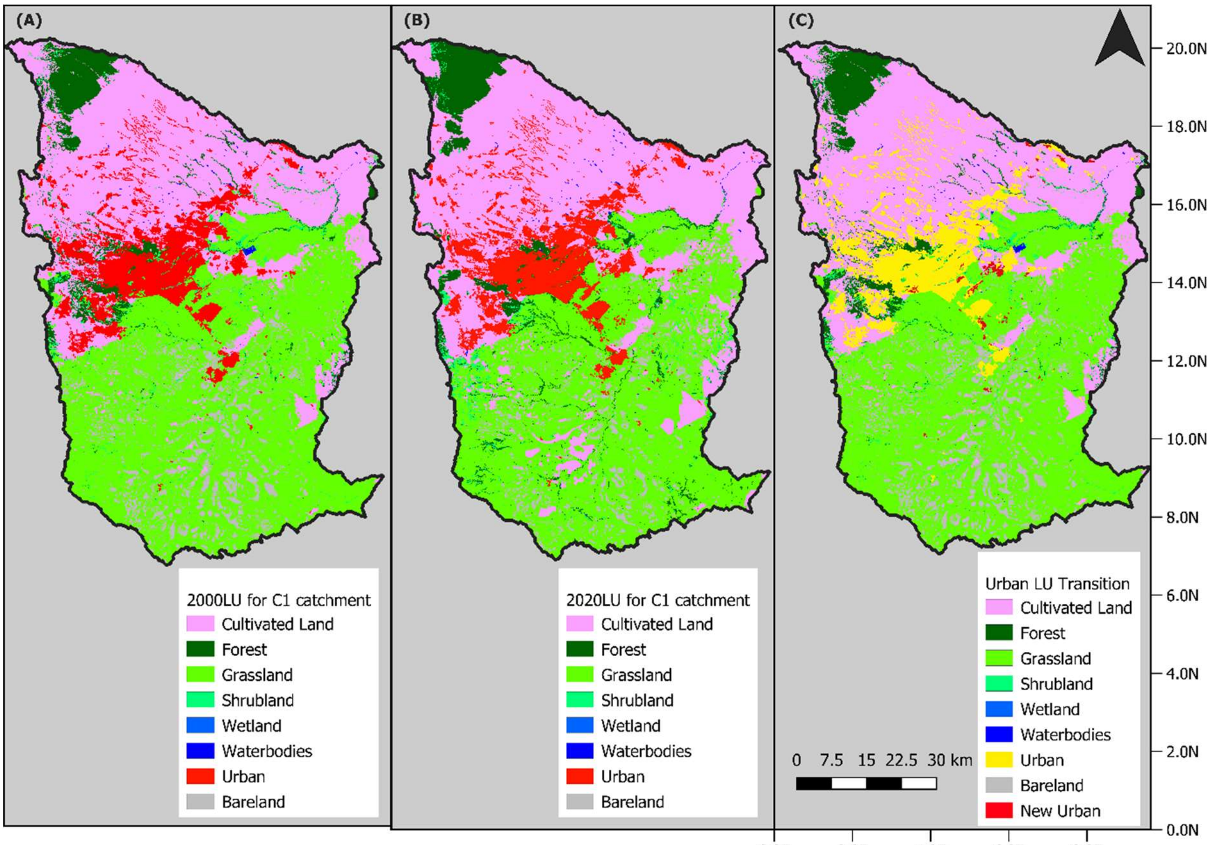

Figure 46. Year 2000 land use map for C1 catchment, (B) Year 2020 landuse map for C1 catchment, (C) Urban area transition landuse map for C1 catchment between 2000 and 2020.

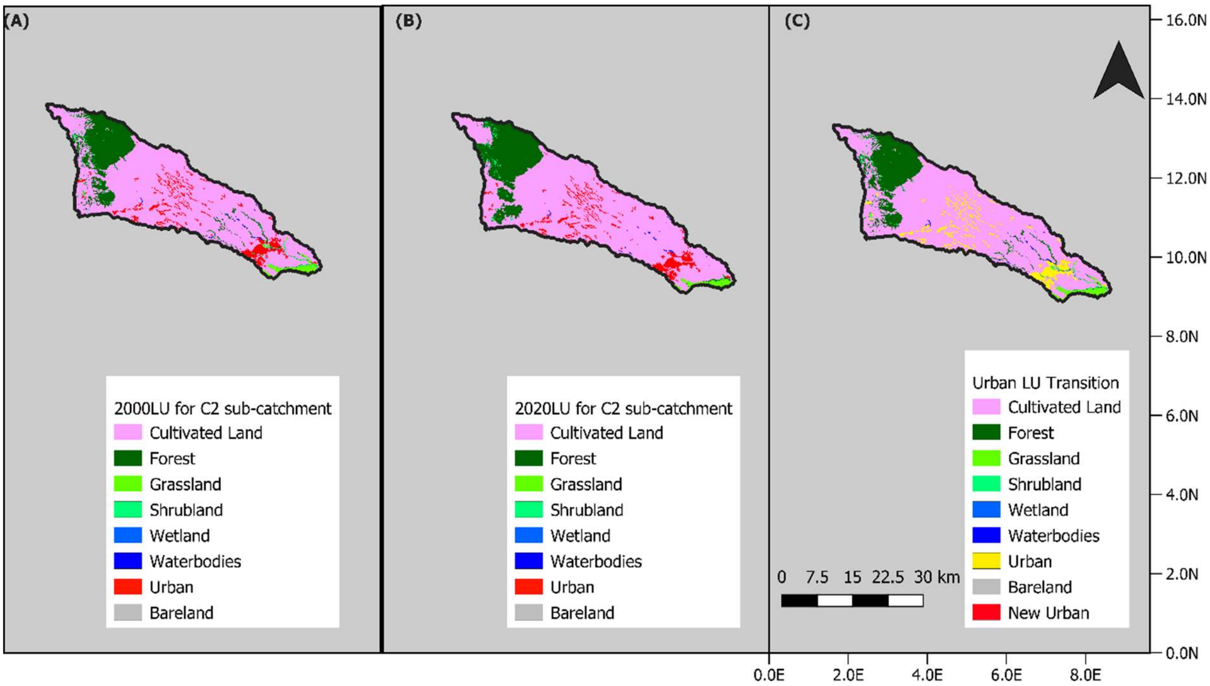

Figure 47. Year 2000 landuse map for C2 sub-catchment, (B) Year 2020 landuse map for C2 sub-catchment, (C) Urban area transition landuse map for C2 sub-catchment between 2000 and 2020.

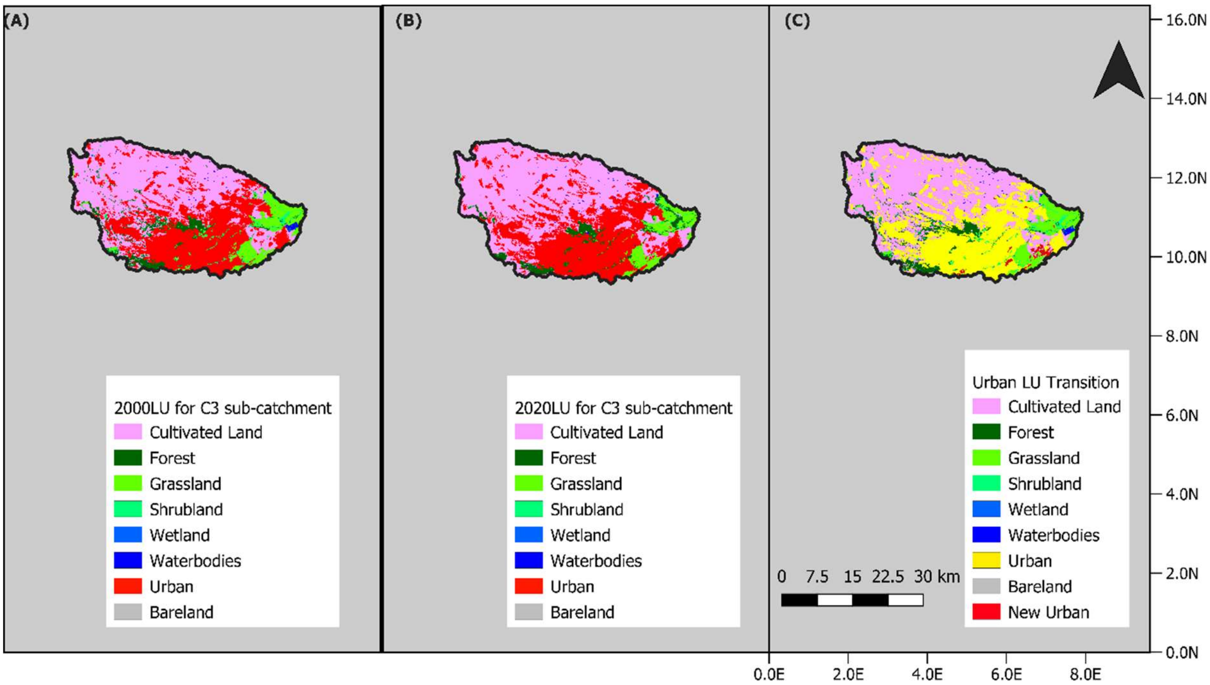

Figure 48. Year 2000 landuse map for C3 sub-catchment, (B) Year 2020 landuse map for C3 sub-catchment, (C) Urban area transition landuse map for C3 sub-catchment between 2000 and 2020.

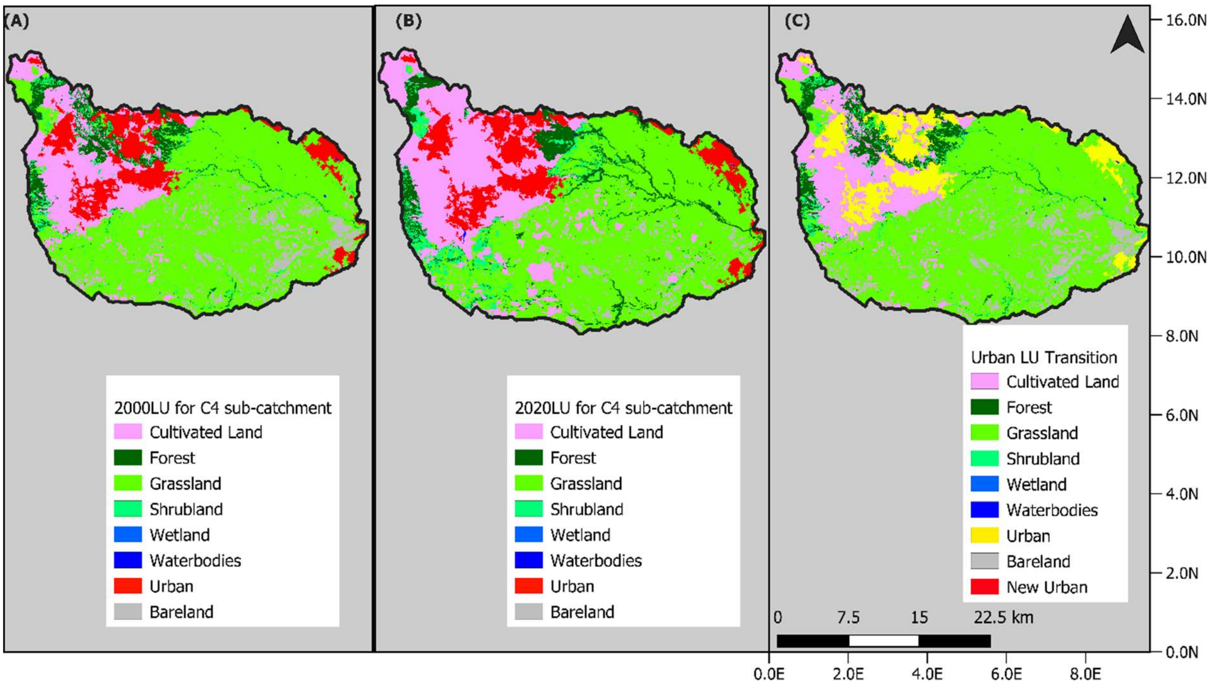

Figure 49. (A) Year 2000 landuse map for C4 sub-catchment, (B) Year 2020 landuse map for C4 sub-catchment, (C) Urban area transition landuse map for C4 sub-catchment between 2000 and 2020.

Table 19. Transition matrix showing Landuse and landcover (LULC) change in C1-Combined catchment between 2000 & 2020.

Ref	**Landuse Classification**	**C1 - Catchment 2000 Landuse**				**C1 - Catchment 2020 Landuse**				**Percent % Change in Landuse between 2000 & 2020**	**Percent % Change between 2000 & 2020**
		Pixel Count	**Area (m^2)**	**Area (km^2)**	**%**	**Pixel Count**	**Area (m^2)**	**Area (km^2)**	**Percent (%)**		
10	Cultivated Land	2077188	1869469200	1869.5	32.5%	2362535	2126281500	2126.3	36.9%	256812300	4.461%
20	Forest	326416	293774400	293.8	5.1%	375462	337915800	337.9	5.9%	44141400	0.767%
30	Grassland	2844691	2560221900	2560.2	44.5%	2612309	2351078100	2351.1	40.9%	-209143800	-3.637%
40	Shrubland	101113	91001700	91.0	1.6%	102138	91924200	91.9	1.6%	922500	0.016%
60	Waterbodies	12181	10962900	11.0	0.2%	10148	9133200	9.1	0.2%	-1829700	-0.032%
80	Urban	615598	554038200	554.0	9.6%	641692	577522800	577.5	10.0%	23484600	0.408%
90	bareland	416546	374891400	374.9	6.5%	289834	260850600	260.9	4.5%	-114040800	-1.982%
Total		6393733	5,754,359,700.00	5754.4	100.0%	6394118	5754706200	5754.7	100.0%		

Table 20. Transition matrix showing Landuse and landcover (LULC) change in C2-Kiambu sub-catchment between 2000 & 2020.

Ref.	**Landuse Classification**	**C2 - Kiambu sub-catchment 2000 Landuse**				**C2 - Kiambu sub-catchment 2020 Landuse**				**Percent % Change in Landuse between 2000 & 2020**	**Percent % Change between 2000 & 2020**
		Pixel Count	**Area (m^2)**	**Area (km^2)**	**Percent Change (%)**	**Pixel Count**	**Area (m^2)**	**Area (km^2)**	**Percent Change (%)**		
10	Cultivated Land	662062	595855800	595.9	74.1%	660953	594857700	594.9	74.0%	-998100	-0.118%
20	Forest	142833	128549700	128.5	16.0%	153261	137934900	137.9	17.2%	9385200	1.168%
30	Grassland	20039	18035100	18.0	2.2%	14789	13310100	13.3	1.7%	-4725000	-0.587%
40	Shrubland	9697	8727300	8.7	1.1%	5953	5357700	5.4	0.7%	-3369600	-0.419%
60	Waterbodies	2064	1857600	1.9	0.2%	2029	1826100	1.8	0.2%	-31500	-0.004%
80	Urban	56495	50845500	50.8	6.3%	56518	50866200	50.9	6.3%	20700	0.003%
90	bareland	399	359100	0.4	0.0%	18	16200	0.0	0.0%	-342900	-0.043%
Total		893589	804,230,100.00	804.2	100.0%	893521	804168900	804.2	100.0%		

Table 21. Transition matrix showing Landuse and landcover (LULC) change in C3-Nairobi sub-catchment between 2000 & 2020.

Ref	**Landuse Classification**	**C3 - Nairobi sub-catchment 2000 Landuse**				**C3 - Nairobi sub-catchment 2020 Landuse**				**Percent % Change in Landuse between 2000 & 2020**	**Percent % Change between 2000 & 2020**
		Pixel Count	**Area (m^2)**	**Area (km^2)**	**Percent % Change**	**Pixel Count**	**Area (m^2)**	**Area (km^2)**	**Percent % Change**		
10	Cultivated Land	545274	490746600	490.7	48.3%	581740	523566000	523.6	51.5%	32819400	3.2%
20	Forest	57823	52040700	52.0	5.1%	50100	45090000	45.1	4.4%	-6950700	-0.7%
30	Grassland	87688	78919200	78.9	7.8%	69884	62895600	62.9	6.2%	-16023600	-1.6%
40	Shrubland	23992	21592800	21.6	2.1%	5835	5251500	5.3	0.5%	-16341300	-1.6%
60	Waterbodies	5966	5369400	5.4	0.5%	3110	2799000	2.8	0.3%	-2570400	-0.3%
80	Urban	406067	365460300	365.5	36.0%	416954	375258600	375.3	36.9%	9798300	1.0%
90	bareland	1988	1789200	1.8	0.2%	1136	1022400	1.0	0.1%	-766800	-0.1%
Total		1128798	1,015,918,200.00	1015.9	100.0%	1128759	1015883100	1015.9	100.0%		

Table 22.Transition matrix showing Landuse and landcover (LULC) change in C4-Machakos sub-catchment between 2000 & 2020.

Ref	**Landuse Classification**	**C4 - Machakos sub-catchment 2000 Landuse**				**C4 - Machakos sub-catchment 2020 Landuse**				**Percent % Change in Landuse between 2000 & 2020**	**Percent % Change between 2000 & 2020**
		Pixel Count	Area (m^2)	Area (km^2)	Percent (%)	Pixel Count	Area (m^2)	Area (km^2)	Percent (%)		
10	Cultivated Land	122992	110692800	110.7	15.3%	183988	165589200	165.6	22.9%	54896400	7.585%
20	Forest	44915	40423500	40.4	5.6%	53677	48309300	48.3	6.7%	7885800	1.090%
30	Grassland	462740	416466000	416.5	57.5%	410984	369885600	369.9	51.1%	-46580400	-6.428%
40	Shrubland	25551	22995900	23.0	3.2%	37502	33751800	33.8	4.7%	10755900	1.486%
60	Waterbodies	390	351000	0.4	0.0%	550	495000	0.5	0.1%	144000	0.020%
80	Urban	88638	79774200	79.8	11.0%	92173	82955700	83.0	11.5%	3181500	0.441%
90	bareland	59179	53261100	53.3	7.4%	25441	22896900	22.9	3.2%	-30364200	-4.194%
Total		804405	723,964,500.00	724.0	100.0%	804315	723883500	723.9	100.0%		

7.3 Hazard Vulnerability Classification of Land Use Change and Climate Change

Fundamental to the estimation of flood hazard due to the impact of climate change and land use change in this study is the estimation of flood depth, flood velocity, and depth and velocity in combination. The calculation of flood hazard raster layers for the five model scenarios is undertaken in the HEC-RAS model by using the raster calculator script described in Figure 31. The procedure for the calculation of flood hazard raster layers in the HEC-RAS model is shown in Figure 50 and the flow path for simulated flood extent for the S3-CP4 model is shown in Figure 51.

Figure 52 shows the hazard vulnerability maps for the S1-Baseline, S2-2000LU, S3-CP4uplift and S4-P25uplift models for the catchments C1, C2, C3 and C4 respectively. The RawDEM model is not included in the flood hazard vulnerability classification analysis. The flood hazard vulnerability raster layers are calculated in the HEC-RAS model by adding the hazard vulnerability curves (Smith et al., 2014) described in Figure 30 onto the results of the four model scenarios namely S1-Baseline, S2-2000LU, S3-CP4uplift and S4-P25uplift. The purpose of using the flood hazard vulnerability classification in this study is to make an assessment of the vulnerability of people, buildings and infrastructure within the catchment to flood hazard by identifying specific flood parameters that can be measured consistently for the March 2018 flood events and to benchmark these parameters against certain thresholds (Smith et al., 2014).

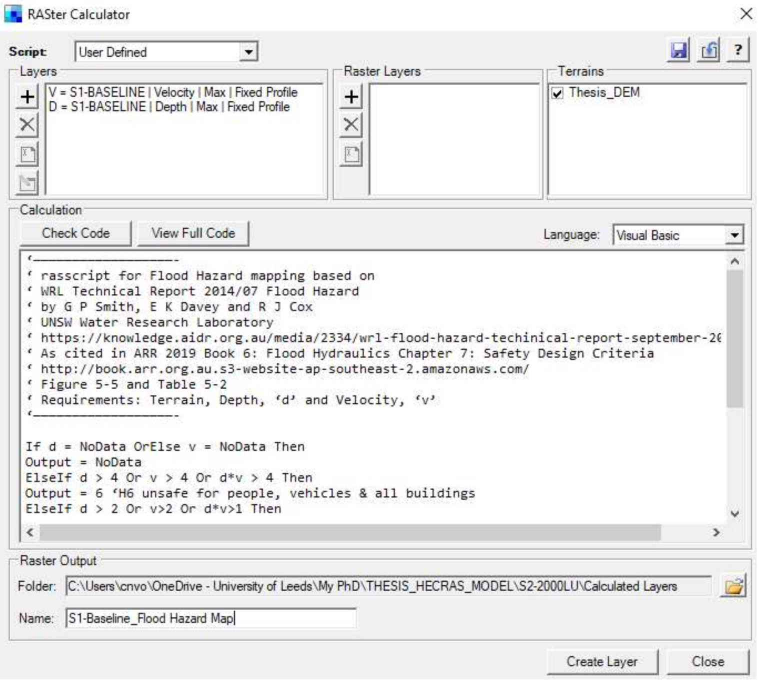

Script: User Defined

V = S1-BASELINE | Velocity | Max | Fixed Profile
D = S1-BASELINE | Depth | Max | Fixed Profile

☑ Thesis_DEM

Language: Visual Basic

```
‘-------------------
‘ rasscript for Flood Hazard mapping based on
‘ WRL Technical Report 2014/07 Flood Hazard
‘ by G P Smith, E K Davey and R J Cox
‘ UNSW Water Research Laboratory
‘ https://knowledge.aidr.org.au/media/2334/wrl-flood-hazard-techinical-report-september-2
‘ As cited in ARR 2019 Book 6: Flood Hydraulics Chapter 7: Safety Design Criteria
‘ http://book.arr.org.au.s3-website-ap-southeast-2.amazonaws.com/
‘ Figure 5-5 and Table 5-2
‘ Requirements: Terrain, Depth, ‘d’ and Velocity, ‘v’
‘-------------------

If d = NoData OrElse v = NoData Then
Output = NoData
ElseIf d > 4 Or v > 4 Or d*v > 4 Then
Output = 6 ‘H6 unsafe for people, vehicles & all buildings
ElseIf d > 2 Or v>2 Or d*v>1 Then
```

Folder: C:\Users\cnvo\OneDrive - University of Leeds\My PhD\THESIS_HECRAS_MODEL\S2-2000LU\Calculated Layers

Name: S1-Baseline_Flood Hazard Map

Figure 50. A screenshot from the HEC-RAS model showing the generation of calculated flood hazard raster layers for the five model scenarios by adding the hazard curves onto the results.

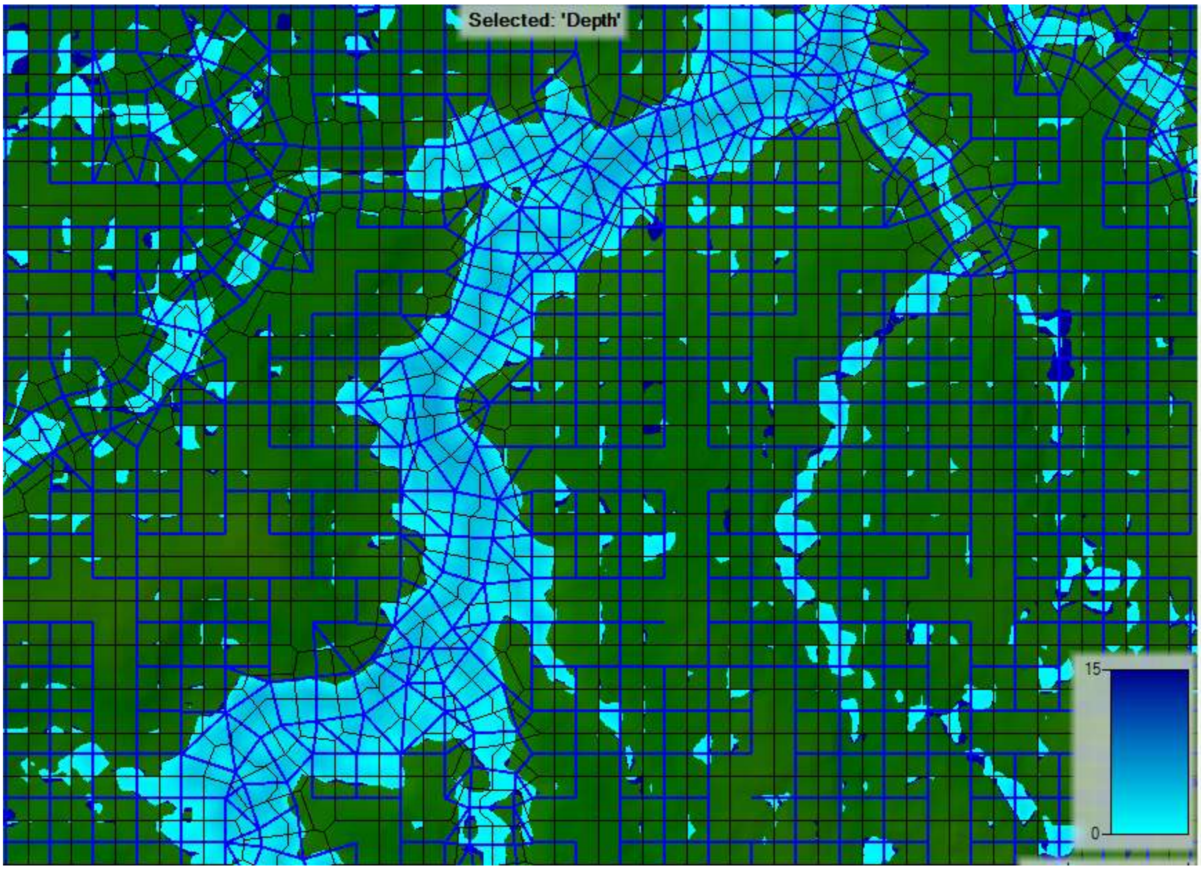

Figure 51. Cell to cell flow paths of simulated floods for the S3-CP4 model.

The results show the overall impacts of land use change and climate change over the study area under the S1-Baseline, S2-2000LU, S3-CP4uplift and S4-P25uplift model scenarios. The results show how the set hazard thresholds that relate to the vulnerability of the catchment and sub-catchments when interacting with floodwaters. Interrogation of the four sets of flood models results to determine flood hazard as the product of flood depth (D) multiplied by flood velocity (V) (Smith et al., 2014), showed that the peak flood hazard (D.V) corresponded with the maximum inundation of the study area at the peak of the flood hydrographs. Analysis of the mapped hazard value (D x V) for a range of the four model scenarios (S1-Baseline, S2-2000LU, S3-CP4uplift and S4-P25uplift) showed the magnitude of predicted flood hazard level varied significantly under future climate change rainfall of the CP4 and P25 climate models Figure 54.

The calculated flood hazard vulnerability maps in Figure 52 for the S1-Baseline, S2-2000LU, S3-CP4uplift and S4-P25uplift models show H6 the most hazardous area to people, infrastructure and vehicles in the catchment and is shown in pink zone in the plots. The vast majority of the rest of the catchment where flooding occurs has been calculated to have hazard vulnerability classification of H5, which is represented by the yellow zone in the plots. Zones 5 and Zones 6 are considered the most hazardous vulnerability zones i.e. unsafe for vehicles and people (Smith et al., 2014). The remaining hazard vulnerability represented by H1, H2, H3, and H4, (purple, cyan, green and yellow) in the plots are at less risk to severe damage and destruction. For the purposes of assessing hazard vulnerability to people, infrastructure and vehicles in the catchment due to flooding, C3 sub-catchment has been selected for the analysis due to the urbanized nature of the catchment, i.e. central business district of Nairobi city.

Table 23, Table 24, Table 25 and Table 26 show the results of the analysis of the hazard vulnerability maps Figure 52 imported into the QGIS software for further analysis. The results show that when calculating and comparing the areas of each hazard vulnerability classification for the S1-Baseline with S3-CP4uplift and S4-P25uplift models across the C3 sub-catchment, the two most severe hazard levels, H5 and H6, have increased in area over the baseline model by +6.2% and +1.6%, and +9.5% and +2.5% respectively (Table 23, Table 24, & Table 26). When comparing the change in hazard area between models, the result show the combined hazard area (H1 to H6) for the S3-CP4uplift and S4-P25uplift models increased by +16 and +22% respectively under the S1-Baseline model. The sharp increase in the hazard vulnerability category is attributed to the higher velocity and higher depth of the flood water that's due to climate change and land use change applied to the S3-CP4uplift and S4-P25uplift models.

Total hazard area for the vulnerability classification for H1, H2, H3, & H4 increased by +1%, +0.3%, +3.2 and +3.3% respectively for the S3-CP4uplift model and +1.8%, +0.5%, +3.2% and +4.5% respectively for the S4-P25uplift models (Table 23 and Table 24). The total hazard vulnerability area increased by 14.2 km^2 from 90.6 km^2 to 104.8 km^2 in the S3-CP4uplift model and by 19.9 km^2 from 90.6 km^2 to 110.5 km^2 in the S4-P25uplift model (Table 23, Table 24 and Table 26). A similar comparison of the results between the S1-Baseline model and the S2-2000LU model show the two most severe hazard levels, H5 and H6 increased in area +1.7% & +0.2% (Table 25 & Table 26) in the C3 Nairobi sub-catchment. The total hazard area for the vulnerability classification for H1, H2, H3, & H4 increased by +0.1%, +0.8%, +0.5% and +0.5% respectively. The total hazard vulnerability area increased by 3.2 km^2 from 87.4 km to 90.6 km between 2000 and 2020, Table 25 & Table 26.
The results show that climate change is a bigger pluvial flood hazard threat than change in urban landuse.

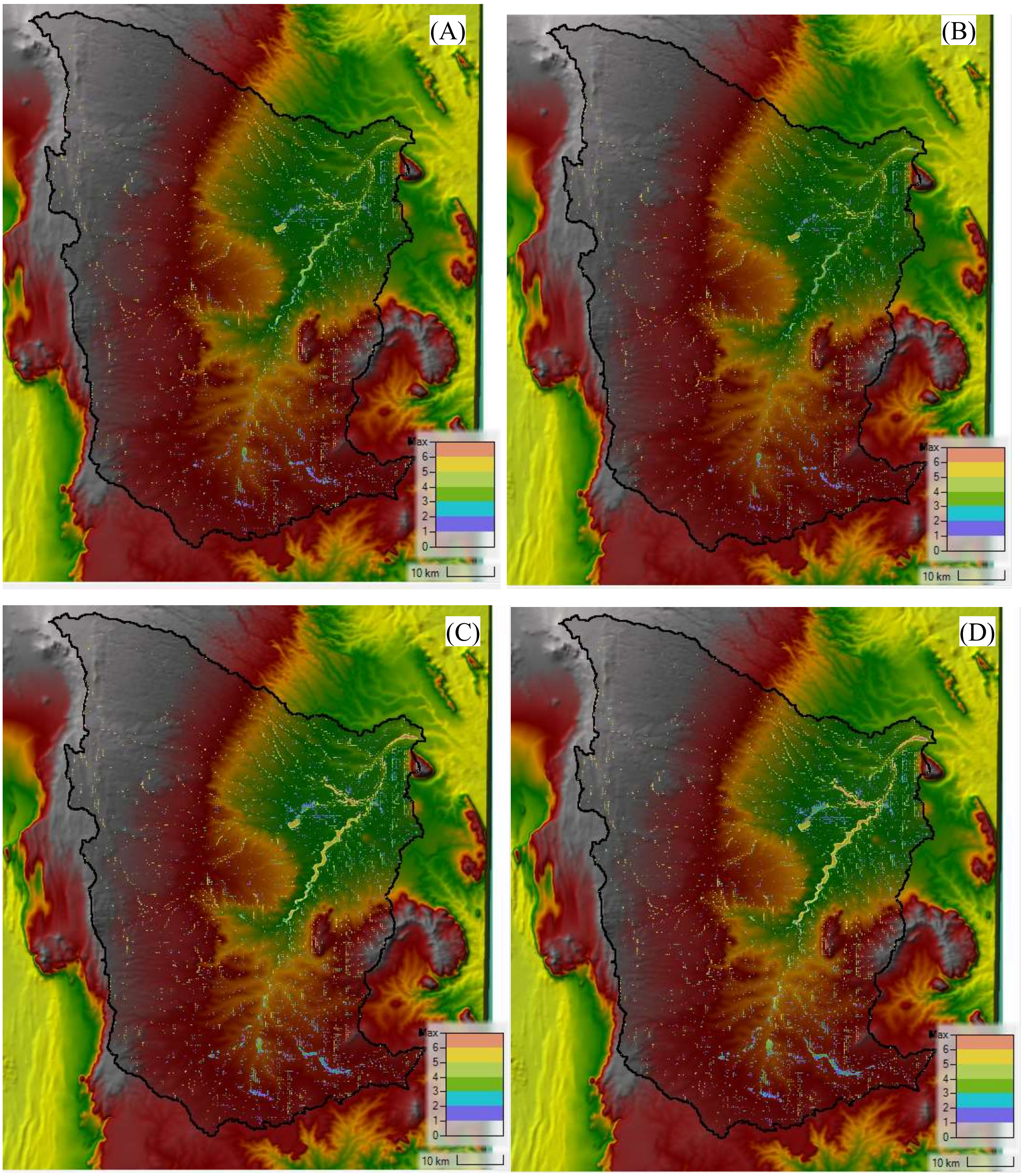

Figure 52. A screenshot from the HECRAS model of the flood hazard category map for A: S1-Baseline; B: S2-2000LU; S3-C: CP4uplift; and D: S4-P25uplift over C1 catchment.

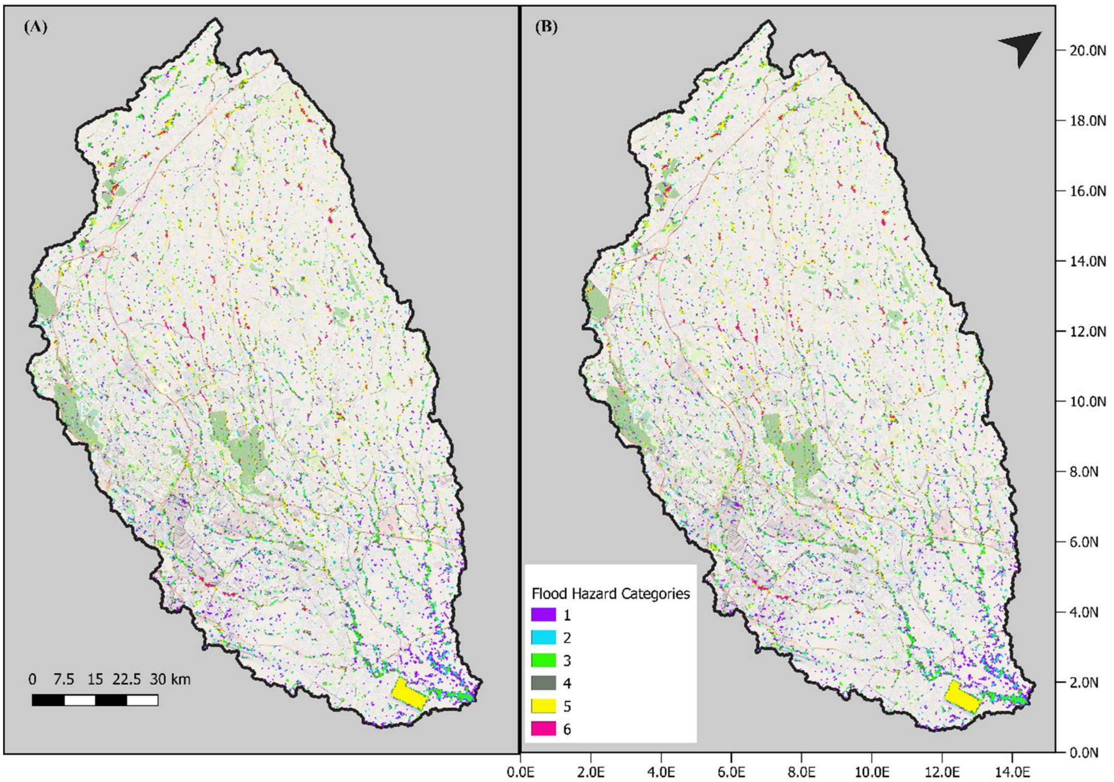

Figure 53. (A) Flood Hazard Category map for S1_Baseline and (B) Flood Hazard Category map for S2-200LU for C3 Nairobi sub-catchment area processed within the QGIS software.

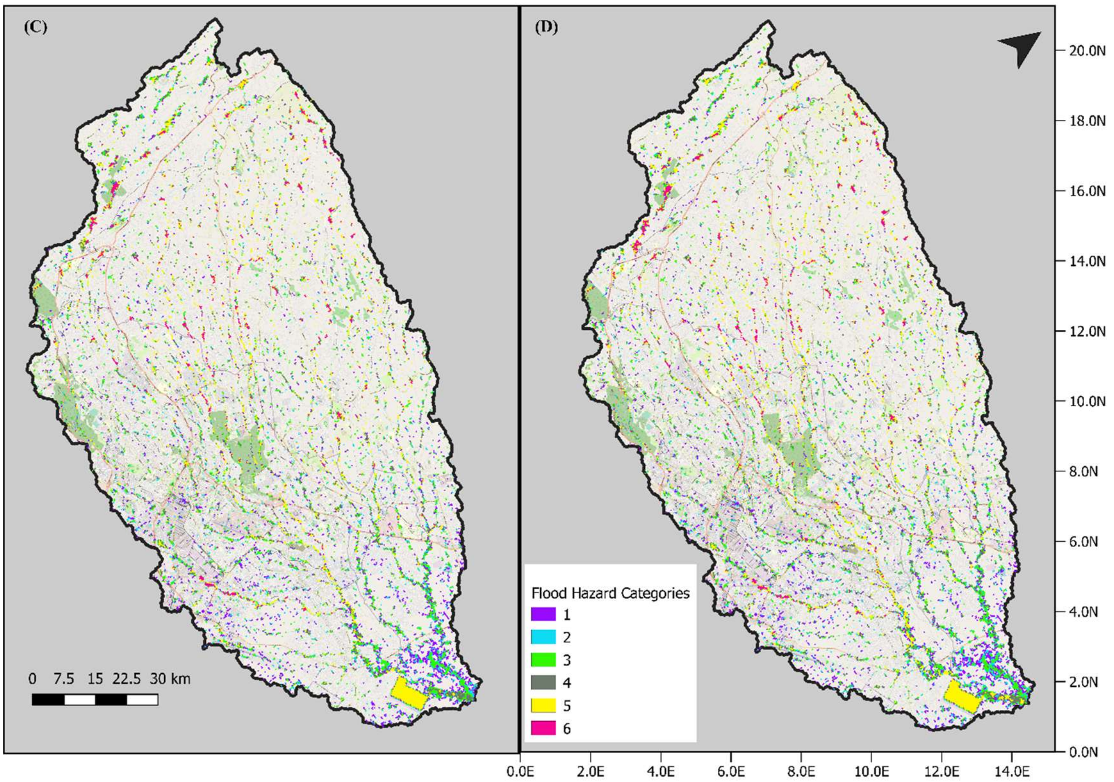

Figure 54. (C) Flood Hazard Category map for S3_CP4uplift and (D) Flood Hazard Category map for S4-P25uplift for C3 Nairobi sub-catchment area processed within the QGIS software.

Table 23. Areas of each hazard vulnerability classification for S4-P25uplift model for C3: Nairobi sub-catchment area.

Hazard Category	**S4-P25uplift Model for Nairobi sub-catchment**				
	Pixel Count	**Hazard Area (m^2)**	**Hazard Area (km^2)**	**% of Area Occupied**	**% Change from Baseline**
H1	2660	22707128.11	22.7	25.0%	1.8%
H2	1478	12616968.18	12.6	13.9%	0.5%
H3	3150	26890020.14	26.9	29.7%	3.2%
H4	2029	17320587.57	17.3	19.1%	4.5%
H5	2881	24593697.78	24.6	27.1%	9.5%
H6	752	6419458.775	6.4	7.1%	2.5%
Total	12950	110,547,860.56	110.5	122.0%	22.0%

Table 24. Areas of each hazard vulnerability classification for S3-CP4uplift model for C3: Nairobi sub-catchment area.

Hazard Category	**S3-CP4uplift Model for Nairobi sub-catchment**				
	Pixel Count	**Hazard Area (m^2)**	**Hazard Area (km^2)**	**% of Area Occupied**	**% Change from Baseline**
H1	2573	21964451.37	22.0	24.2%	1.0%
H2	1466	12514530.01	12.5	13.8%	0.3%
H3	3148	26872947.11	26.9	29.6%	3.2%
H4	1906	16270596.31	16.3	17.9%	3.3%
H5	2534	21631527.31	21.6	23.9%	6.2%
H6	651	5557270.828	5.6	6.1%	1.6%
Total	12278	104,811,322.93	104.8	115.6%	15.6%

Table 25. Areas of each hazard vulnerability classification for S2-2000LU model for C3: Nairobi sub-catchment area.

Hazard Category	**S2-2000LU Model for Nairobi sub-catchment**				
	Pixel Count	**Hazard Area (m^2)**	**Hazard Area (km^2)**	**% of Area Occupied**	**% Change from Baseline**
H1	2461	21008361.76	21.0	23.2%	-0.1%
H2	1346	11490148.29	11.5	12.7%	-0.8%
H3	2760	23560779.55	23.6	26.0%	-0.5%
H4	1504	12838917.55	12.8	14.2%	-0.5%
H5	1697	14486464.82	14.5	16.0%	-1.7%
H6	466	3978015.677	4.0	4.4%	-0.2%
Total	10234	87,362,687.64	87.4	96.4%	-3.6%

Table 26. Areas of each hazard vulnerability classification for S1-Baseline model for C3: Nairobi sub-catchment area.

Hazard Category	S1-Baseline Model for Nairobi sub-catchment				
	Pixel Count	Hazard Area (m^2)	Hazard Area (km^2)	% of Area Occupied	% Change from 2000LU
H1	2468	21068117.36	21.1	23.2%	0.1%
H2	1430	12207215.49	12.2	13.5%	0.8%
H3	2809	23979068.75	24.0	26.5%	0.5%
H4	1552	13248670.24	13.2	14.6%	0.5%
H5	1874	15997427.85	16.0	17.6%	1.7%
H6	486	4148745.964	4.1	4.6%	0.2%
Total	10619	90,649,245.66	90.6	100.0%	3.6%

The S5-RawDEM model uses the raw, uncorrected DEM as key input data and a was undertaken to compare the flood inundation maps from the S1-Baseline model and the S5-RawDEM model with actual flood height data obtained from three flooding hotspot sites across Nairobi. The result of the comparison of the two models with site data is shown in Table 54. The results show the S5-RawDEM model underestimates flood height level at the flooding hotspot sites by between 56% to 58% compared to 25% to 33% for the S1-Baseline model with corrected DEM. to the . It is clear from the results that the urban correction of global DEMs can have some impacts on the accuracy of urban flood models in estimating flood heights.

7.4 CREATION OF ADDITIONAL SIX MODEL SIMULATION SCENARIOS USING URBAN CORRECTED GLOBAL AND LOCAL DEMs.

In order to analyse the effect of DEMs on the model outputs and therefore, try to isolate the effect of building density errors, additional simulations were run in the HEC-HMS and HEC-RAS 2 D hydrological and hydraulic models using the remaining five urban corrected global DEMs as key input data including the use of the reference DEM. Six more sets of model scenarios are developed using the five urban corrected global DEMs and the local JICA reference DEM (SRTM DEM, ALOS DEM, NASA DEM, TanDEM-X 12m, TanDEM-X 90m DEM, and the JICA Reference DEM). Additional details of the simulated scenarios are reported below.

JICA Reference DEM Model

S1_ Ref-Baseline model uses the urban corrected NASADEM DEM, 2020 land use map and March 2018 precipitation data as key input data

S2_ Ref-2010LU model is developed using the same key input data as S1-Baseline model apart from using land use the 2010 land use map for the catchment

S3_ Ref-CP4uplift model is developed using the 2020 land use map, the urban corrected DEM and future CP4 climate change rainfall model

S4_ Ref model uses the 2020 land use map, the urban corrected DEM and future P25 climate change rainfall model

S5_ TanDEM-X 90m-RawDEM model is similar to the S1-Baseline model but uses a raw DEM as key input data instead of an urban corrected DEM.

SRTM DEM Model.

S1_SRTM-Baseline model uses the urban corrected SRTM DEM, 2020 land use map and March 2018 precipitation data as key input data

S2_SRTM-2010LU model is developed using the same key input data as S1-Baseline model apart from using land use the 2010 land use map for the catchment

S3_SRTM-CP4uplift model is developed using the 2020 land use map, the urban corrected DEM and future CP4 climate change rainfall model

S4_SRTM-P25uplift model uses the 2020 land use map, the urban corrected DEM and future P25 climate change rainfall model

S5_SRTM-RawDEM model is similar to the S1-Baseline model but uses a raw DEM as key input data instead of an urban corrected DEM.

ALOS DEM Model

S1_ALOS-Baseline model uses the urban corrected ALOS DEM, 2020 land use map and March 2018 precipitation data as key input data

S2_ALOS-2010LU model is developed using the same key input data as S1-Baseline model apart from using land use the 2010 land use map for the catchment

S3_ALOS-CP4uplift model is developed using the 2020 land use map, the urban corrected DEM and future CP4 climate change rainfall model

S4_ALOS-P25uplift model uses the 2020 land use map, the urban corrected DEM and future P25 climate change rainfall model

S5_ALOS-RawDEM model is similar to the S1-Baseline model but uses a raw DEM as key input data instead of an urban corrected DEM.

NASA DEM Model

S1_NASA-Baseline model uses the urban corrected NASADEM DEM, 2020 land use map and March 2018 precipitation data as key input data

S2_ NASA-2010LU model is developed using the same key input data as S1-Baseline model apart from using land use the 2010 land use map for the catchment

S3_ NASA-CP4uplift model is developed using the 2020 land use map, the urban corrected DEM and future CP4 climate change rainfall model

S4_ NASA-P25uplift model uses the 2020 land use map, the urban corrected DEM and future P25 climate change rainfall model

S5_ NASA-RawDEM model is similar to the S1-Baseline model but uses a raw DEM as key input data instead of an urban corrected DEM.

TanDEM-X 12m DEM Model

S1_ TM12-Baseline model uses the urban corrected TanDEM-X 12m DEM, 2020 land use map and March 2018 precipitation data as key input data

S2_ TM12-2010LU model is developed using the same key input data as S1-Baseline model apart from using land use the 2010 land use map for the catchment

S3_ TM12-CP4uplift model is developed using the 2020 land use map, the urban corrected DEM and future CP4 climate change rainfall model

S4_ TM12-P25uplift model uses the 2020 land use map, the urban corrected DEM and future P25 climate change rainfall model

S5_ TM12-RawDEM model is similar to the S1-Baseline model but uses a raw DEM as key input data instead of an urban corrected DEM.

TanDEM-X 90m DEM Model

S1_ TM90-Baseline model uses the urban corrected TanDEM-X 90m DEM, 2020 land use map and March 2018 precipitation data as key input data

S2_ TM90-2010LU model is developed using the same key input data as S1-Baseline model apart from using land use the 2010 land use map for the catchment

S3_ TM90-CP4uplift model is developed using the 2020 land use map, the urban corrected DEM and future CP4 climate change rainfall model

S4_ TM90-P25uplift model uses the 2020 land use map, the urban corrected DEM and future P25 climate change rainfall model

S5_ TM90-RawDEM model is similar to the S1-Baseline model but uses a raw DEM as key input data instead of an urban corrected DEM.

Table 27 To Table 53 show the results of the hazard vulnerability classifications for the models using the remainder five urban corrected global DEMs and a local Reference DEM (SRTM DEM, ALOS DEM, NASA DEM, TanDEM-X 12m, TanDEM-X 90m DEM, and the JICA Reference DEM) for the Nairobi sub-catchment. Similar to the results obtained from the model using the MERIT urban corrected DEM as key input data, the results obtained from the six models show H6 the most hazardous area to people, infrastructure and vehicles in the catchment and is shown in pink zone in the tables. The vast majority of the rest of the catchment where flooding occurs has been calculated to have hazard vulnerability classification of H5, which is represented by the yellow zone in the plots. Zones 5 and Zones 6 are considered the most hazardous vulnerability zones i.e. unsafe for vehicles and people (Smith et al., 2014). The remaining hazard vulnerability represented by H1, H2, H3, and H4, (purple, cyan, green and yellow) in the table are at less risk to severe damage and destruction.

When comparing the results of hazard vulnerability classifications for all seven models comprising the Reference model, MERIT, SRTM, NASADEM, ALOS, TanDEM x 12m, TanDEM x 90m (Table 27 To Table 53), the Reference/truth DEM have the highest values for the hazard vulnerability classifications across all board of H1 to H6 in terms of total area exposed to pluvial flooding. Topography has been identified as a key critical dataset for flood modelling accuracy and for estimating flood extent (Horritt and Bates, 2001) and many models of flood extent rely on DEMs in order to simulate paths of water flow, flood extent and depth. Therefore, the better performance of the local reference DEM in capturing flood hazards more profoundly than the global DEMs can be attributed to the better resolution of the reference DEM. For example, in Table 51, when considering the extent of the areas covered by the hazard vulnerability classifications for the H1 to H6 across all seven models (S4-P25uplift), the reference DEM is MERIT DEM model is next to the Reference DEM model, followed by the SRTM model, the TanDEM-X 12m, TanDEM-X 90m, NASADEM model and the ALOS DEM model in that order.

When observing the results of the seven models and comparing the results with actual flood height data obtained from the flooding hotspots, the Reference DEM model showed the best performance (Table 52). The MERIT, SRTM and TanDEM X 12m models show the better performance compared to the TanDEM X 90m, NASADEM, and the ALOS model. From all models, the Reference DEM model shows the most realistic results Table 52 when compared to the site survey data.

There are multiple studies of the influence of surface topography of digital elevation models—DEMs on the outcome of hydrodynamic modelling when DEMs are used as key input data (Horritt and Bates, 2001, Casas et al., 2006, Sanders, 2007a, Saksena and Merwade, 2015, Savage et al., 2015, Thomas Steven Savage et al., 2016, Acharya et al., 2018, Garrote, 2022). The central narrative of one of the main conclusions typical to these studies is the positive relationship between higher spatial resolutions and more accurate flooding predictions.

The validation of the global DEMs and the Reference DEM using site survey data for the three flooding hotspots sites aligns with the conclusions reached in these studies. Also, the use of the urban corrected DEMs and the Reference DEMS in the hydrodynamic models appears to be essential for urban flooding assessments where the effect on buildings is less evident.

Table 27. Hazard vulnerability classification for the S4-P25uplift JICA Reference model for C3: Nairobi catchment area.

Hazard Category	**S4Ref-P25uplift Model for Nairobi sub-catchment**				
	Pixel Count	**Hazard Area (m^2)**	**Hazard Area (km^2)**	**% of Area Occupied**	**% Change from Baseline**
H1	2740	24984674	25.0	24.4%	1.7%
H2	1498	13964363	14.0	13.3%	-0.2%
H3	3176	31863537	31.9	28.3%	1.9%
H4	2048	18173351	18.2	18.2%	3.2%
H5	2995	23176387	23.2	26.7%	9.1%
H6	830	7698632	7.7	7.4%	2.6%

Table 28. Hazard vulnerability classification for the S3-CP4uplift JICA Reference model for C3: Nairobi catchment area.

Hazard Category	**S3Ref-CP4uplift Model for Nairobi sub-catchment**				
	Pixel Count	**Hazard Area (m^2)**	**Hazard Area (km^2)**	**% of Area Occupied**	**% Change from Baseline**
H1	2722	22362813	22.4	24.2%	1.5%
H2	1577	12961797	13.0	14.0%	0.5%
H3	3245	26107406	26.1	28.9%	2.5%
H4	2046	16883637	16.9	18.2%	3.2%
H5	2578	23887734	23.9	23.0%	5.4%
H6	721	5787454	5.8	6.4%	1.6%

Table 29. Hazard vulnerability classification for the S2-2000LU JICA Reference model for C3: Nairobi catchment area.

Hazard Category	S2Ref-2000LU Model for Nairobi sub-catchment				
	Pixel Count	Hazard Area (m^2)	Hazard Area (km^2)	% of Area Occupied	% Change from Baseline
H1	2462	21343445	21.3	21.9%	-0.8%
H2	1365	11767107	11.8	12.2%	-1.4%
H3	2788	23877871	23.9	24.8%	-1.6%
H4	1523	12906782	12.9	13.6%	-1.4%
H5	1728	14861575	14.9	15.4%	-2.2%
H6	478	4327131	4.3	4.3%	-0.5%

Table 30. Hazard vulnerability classification for the S1-Baseline JICA Reference model for C3: Nairobi catchment area.

Hazard Category	S1Ref-Baseline Model for Nairobi sub-catchment				
	Pixel Count	Hazard Area (m^2)	Hazard Area (km^2)	% of Area Occupied	% Change from 2000LU
H1	2548	21437459	21.4	22.7%	0.8%
H2	1521	12790339	12.8	13.5%	1.4%
H3	2965	25399036	25.4	26.4%	1.6%
H4	1684	13264658	13.3	15.0%	1.4%
H5	1974	16723743	16.7	17.6%	2.2%
H6	538	4484948	4.5	4.8%	0.5%

Table 31. Hazard vulnerability classification for the S4-P25uplift SRTM model for C3: Nairobi sub-catchment area.

Hazard Category	S4_SRTM-P25uplift Model for Nairobi sub-catchment				
	Pixel Count	Hazard Area (m^2)	Hazard Area (km^2)	% of Area Occupied	% Change from Baseline
H1	2556	20148963	20.1	24.7%	0.7%
H2	1456	10981266	11.0	14.1%	1.1%
H3	2998	24360614	24.4	29.0%	2.8%
H4	1980	16773355	16.8	19.2%	4.1%
H5	2567	21815856	21.8	24.8%	7.8%
H6	688	5877911	5.9	6.7%	2.1%

Table 32. Hazard vulnerability classification for the S3-CP4uplift SRTM model for C3: Nairobi catchment area.

Hazard Category	S3_SRTM-CP4uplift Model for Nairobi sub-catchment				
	Pixel Count	Hazard Area (m^2)	Hazard Area (km^2)	% of Area Occupied	% Change from Baseline
H1	2498	21964451	22.0	24.2%	0.1%
H2	1455	12514530	12.5	14.1%	1.1%
H3	2987	26872947	26.9	28.9%	2.7%
H4	1789	16270596	16.3	17.3%	2.3%
H5	2284	21631527	21.6	22.1%	5.0%
H6	624	5557271	5.6	6.0%	1.5%

Table 33. Hazard vulnerability classification for the S2-2000LU SRTM model for C3: Nairobi catchment area.

Hazard Category	S2_SRTM-2000LU Model for Nairobi sub-catchment				
	Pixel Count	Hazard Area (m^2)	Hazard Area (km^2)	% of Area Occupied	% Change from Baseline
H1	2414	21008362	21.0	23.4%	-0.7%
H2	1298	11490148	11.5	12.6%	-0.4%
H3	2556	23560780	23.6	24.7%	-1.5%
H4	1467	12838918	12.8	14.2%	-0.8%
H5	1567	14486465	14.5	15.2%	-1.9%
H6	434	3978016	4.0	4.2%	-0.4%

Table 34. Hazard vulnerability classification for the S1-Baseline SRTM model for C3: Nairobi catchment area.

Hazard Category	S1_SRTM-Baseline Model for Nairobi sub-catchment				
	Pixel Count	Hazard Area (m^2)	Hazard Area (km^2)	% of Area Occupied	% Change from 2000LU
H1	2488	21068117	21.1	24.1%	0.7%
H2	1344	12207215	12.2	13.0%	0.4%
H3	2709	23979069	24.0	26.2%	1.5%
H4	1552	13248670	13.2	15.0%	0.8%
H5	1764	15997428	16.0	17.1%	1.9%
H6	474	4148746	4.1	4.6%	0.4%

Table 35. Hazard vulnerability classification for the S4-P25uplift TM12 model for C3: Nairobi sub-catchment area.

Hazard Category	S4_TM12-P25uplift Model for Nairobi sub-catchment				
	Pixel Count	Hazard Area (m^2)	Hazard Area (km^2)	% of Area Occupied	% Change from Baseline
H1	2422	19836252	19.8	23.9%	0.0%
H2	1388	12886473	12.9	13.7%	0.7%
H3	2698	22885599	22.9	26.6%	0.1%
H4	1876	16394774	16.4	18.5%	3.6%
H5	2482	20736363	20.7	24.5%	7.2%
H6	672	5773635	5.8	6.6%	2.3%

Table 36. Hazard vulnerability classification for the S3-CP4uplift TM12 model for C3: Nairobi sub-catchment area.

Hazard Category	S3_TM12-CP4uplift Model for Nairobi sub-catchment				
	Pixel Count	Hazard Area (m^2)	Hazard Area (km^2)	% of Area Occupied	% Change from Baseline
H1	2496	20282813	20.3	24.6%	0.7%
H2	1389	12161797	12.2	13.7%	0.7%
H3	2747	25374036	25.4	27.1%	0.6%
H4	1711	16218994	16.2	16.9%	2.0%
H5	2223	21394566	21.4	21.9%	4.6%
H6	588	5413463	5.4	5.8%	1.5%

Table 37. Hazard vulnerability classification for the S2-2000LU TM12 model for C3: Nairobi sub-catchment area.

Hazard Category	S2_TM12-2000LU Model for Nairobi sub-catchment				
	Pixel Count	Hazard Area (m^2)	Hazard Area (km^2)	% of Area Occupied	% Change from Baseline
H1	2409	20034435	20.0	23.8%	-0.1%
H2	1277	10267107	10.3	12.6%	-0.4%
H3	2545	22477871	22.5	25.1%	-1.4%
H4	1433	11806782	11.8	14.1%	-0.8%
H5	1555	13161575	13.2	15.4%	-2.0%
H6	428	3227131	3.2	4.2%	-0.1%

Table 38. Hazard vulnerability classification for the S1-Baseline TM12 model for C3: Nairobi sub-catchment area.

Hazard Category	S1_TM12-Baseline Model for Nairobi sub-catchment				
	Pixel Count	Hazard Area (m^2)	Hazard Area (km^2)	% of Area Occupied	% Change from 2000LU
H1	2422	20637459	20.6	23.9%	0.1%
H2	1318	11490339	11.5	13.0%	0.4%
H3	2689	22499036	22.5	26.5%	1.4%
H4	1511	12384658	12.4	14.9%	0.8%
H5	1755	14923743	14.9	17.3%	2.0%
H6	435	3894948	3.9	4.3%	0.1%

Table 39. Hazard vulnerability classification for the S4-P25uplift TM90 model for C3: Nairobi sub-catchment area.

Hazard Category	S4_TM90-P25uplift Model for Nairobi sub-catchment				
	Pixel Count	Hazard Area (m^2)	Hazard Area (km^2)	% of Area Occupied	% Change from Baseline
H1	2411	19774492	19.8	24.0%	0.0%
H2	1361	12674926	12.7	13.5%	0.5%
H3	2697	22730975	22.7	26.8%	0.2%
H4	1858	15903672	15.9	18.5%	3.5%
H5	2446	20548892	20.5	24.3%	7.2%
H6	668	5479075	5.5	6.6%	2.4%

Table 40. Hazard vulnerability classification for the S3-CP4uplift TM90 model for C3: Nairobi sub-catchment area.

Hazard Category	S3_TM90-CP4uplift Model for Nairobi sub-catchment				
	Pixel Count	Hazard Area (m^2)	Hazard Area (km^2)	% of Area Occupied	% Change from Baseline
H1	2477	20282810	20.3	24.6%	0.6%
H2	1363	12161768	12.2	13.5%	0.5%
H3	2721	25374021	25.4	27.0%	0.4%
H4	1700	16218998	16.2	16.9%	1.9%
H5	2213	21394532	21.4	22.0%	4.9%
H6	568	5413443	5.4	5.6%	1.4%

Table 41. Hazard vulnerability classification for the S2-2000LU TM90 model for C3: Nairobi sub-catchment area.

Hazard Category	S2_TM90-2000LU Model for Nairobi sub-catchment				
	Pixel Count	Hazard Area (m^2)	Hazard Area (km^2)	% of Area Occupied	% Change from Baseline
H1	2388	20034422	20.0	23.7%	-0.2%
H2	1258	10267101	10.3	12.5%	-0.5%
H3	2527	22477834	22.5	25.1%	-1.5%
H4	1412	11806740	11.8	14.0%	-1.0%
H5	1525	13161545	13.2	15.2%	-2.0%
H6	415	3227121	3.2	4.1%	-0.1%

Table 42. Hazard vulnerability classification for the S1-Baseline TM90 model for C3: Nairobi sub-catchment area.

Hazard Category	S1_TM90-Baseline Model for Nairobi sub-catchment				
	Pixel Count	Hazard Area (m^2)	Hazard Area (km^2)	% of Area Occupied	% Change from 2000LU
H1	2412	20637438	20.6	24.0%	0.2%
H2	1310	11490328	11.5	13.0%	0.5%
H3	2678	22499014	22.5	26.6%	1.5%
H4	1510	12384639	12.4	15.0%	1.0%
H5	1723	14923720	14.9	17.1%	2.0%
H6	430	3894934	3.9	4.3%	0.1%

Table 43. Hazard vulnerability classification for the S4-P25uplift NASADEM model for C3: Nairobi sub-catchment area.

Hazard Category	S4_NASA-P25uplift Model for Nairobi sub-catchment				
	Pixel Count	Hazard Area (m^2)	Hazard Area (km^2)	% of Area Occupied	% Change from Baseline
H1	2423	19697463	19.7	24.2%	0.1%
H2	1342	12234567	12.2	13.4%	0.4%
H3	2678	21686437	21.7	26.8%	0.3%
H4	1724	15848965	15.8	17.2%	2.1%
H5	2348	20336564	20.3	23.5%	6.4%
H6	660	5373565	5.4	6.6%	2.3%

Table 44. Hazard vulnerability classification for the S3-CP4uplift NASADEM model for C3: Nairobi sub-catchment area.

Hazard Category	S3_NASA-CP4uplift Model for Nairobi sub-catchment				
	Pixel Count	Hazard Area (m^2)	Hazard Area (km^2)	% of Area Occupied	% Change from Baseline
H1	2455	19798021	19.8	24.5%	0.5%
H2	1342	11864832	11.9	13.4%	0.4%
H3	2687	24848494	24.8	26.9%	0.4%
H4	1689	15774946	15.8	16.9%	1.8%
H5	2200	20464664	20.5	22.0%	4.9%
H6	555	5046646	5.0	5.5%	1.3%

Table 45. Hazard vulnerability classification for the S2-2000LU NASADEM model for C3: Nairobi sub-catchment area.

Hazard Category	S2_NASA-2000LU Model for Nairobi sub-catchment				
	Pixel Count	Hazard Area (m^2)	Hazard Area (km^2)	% of Area Occupied	% Change from Baseline
H1	2382	18953006	19.0	23.8%	-0.3%
H2	1250	10017533	10.0	12.5%	-0.5%
H3	2511	22181109	22.2	25.1%	-1.4%
H4	1389	11397128	11.4	13.9%	-1.2%
H5	1512	12987444	13.0	15.1%	-2.0%
H6	400	3029288	3.0	4.0%	-0.3%

Table 46. Hazard vulnerability classification for the S1-Baseline NASADEM model for C3: Nairobi sub-catchment area.

Hazard Category	S1_NASA-Baseline Model for Nairobi sub-catchment				
	Pixel Count	Hazard Area (m^2)	Hazard Area (km^2)	% of Area Occupied	% Change from 2000LU
H1	2408	20209433	20.2	24.1%	0.3%
H2	1298	11108454	11.1	13.0%	0.5%
H3	2647	22073993	22.1	26.5%	1.4%
H4	1509	12048921	12.0	15.1%	1.2%
H5	1711	14633220	14.6	17.1%	2.0%
H6	428	3584774	3.6	4.3%	0.3%

Table 47. Hazard vulnerability classification for the S4-P25uplift ALOS model for C3: Nairobi sub-catchment area.

Hazard Category	S4_ALOS-P25uplift Model for Nairobi sub-catchment				
	Pixel Count	Hazard Area (m^2)	Hazard Area (km^2)	% of Area Occupied	% Change from Baseline
H1	2419	19409822	19.4	24.4%	0.2%
H2	1311	11993558	12.0	13.2%	0.4%
H3	2655	21609476	21.6	26.8%	0.3%
H4	1699	15438764	15.4	17.1%	2.0%
H5	2128	20029877	20.0	21.5%	4.3%
H6	577	5293618	5.3	5.8%	1.6%

Table 48. Hazard vulnerability classification for the S3-CP4uplift ALOS model for C3: Nairobi sub-catchment area.

Hazard Category	S3_ALOS-CP4uplift Model for Nairobi sub-catchment				
	Pixel Count	Hazard Area (m^2)	Hazard Area (km^2)	% of Area Occupied	% Change from Baseline
H1	2437	19406874	19.4	24.6%	0.4%
H2	1323	11690016	11.7	13.4%	0.6%
H3	2687	24630013	24.6	27.1%	0.7%
H4	1656	15511986	15.5	16.7%	1.6%
H5	2198	20310347	20.3	22.2%	5.0%
H6	543	4908725	4.9	5.5%	1.2%

Table 49. Hazard vulnerability classification for the S2-2000LU ALOS model for C3: Nairobi sub-catchment area.

Hazard Category	S2_NASA-2000LU Model for Nairobi sub-catchment				
	Pixel Count	Hazard Area (m^2)	Hazard Area (km^2)	% of Area Occupied	% Change from Baseline
H1	2344	18788339	18.8	23.7%	-0.5%
H2	1238	9817533	9.8	12.5%	-0.3%
H3	2489	21811733	21.8	25.1%	-1.3%
H4	1365	11022890	11.0	13.8%	-1.3%
H5	1501	12108832	12.1	15.2%	-2.0%
H6	389	2887336	2.9	3.9%	-0.3%

Table 50. Hazard vulnerability classification for the S1-Baseline ALOS model for C3: Nairobi sub-catchment area.

Hazard Category	S1_NASA-Baseline Model for Nairobi sub-catchment				
	Pixel Count	Hazard Area (m^2)	Hazard Area (km^2)	% of Area Occupied	% Change from 2000LU
H1	2398	19688742	19.7	24.2%	0.5%
H2	1267	10883681	10.9	12.8%	0.3%
H3	2622	21833980	21.8	26.5%	1.3%
H4	1498	11894462	11.9	15.1%	1.3%
H5	1700	14299036	14.3	17.2%	2.0%
H6	422	3187822	3.2	4.3%	0.3%

Table 51. Comparison of the Hazard vulnerability classifications (H1 to H6) for all seven DEMs for the S4-P25uplift model for the Nairobi sub-catchment area – (all values in square km)

Hazard Category	Reference DEM Model	MERIT DEM Model (m^2)	SRTM DEM Model (km^2)	TanDEM 12 DEM Model	TanDEM 90 DEM Model	NASADEM DEM Model	ALOS DEM MODEL
H1	25.0	22.7	20.1	19.8	19.8	19.7	19.4
H2	14.0	12.6	11.0	12.9	12.9	12.2	12.0
H3	31.9	26.9	24.4	22.9	22.9	21.7	21.6
H4	18.2	17.3	16.8	16.4	16.4	15.8	15.4
H5	23.2	24.6	21.8	20.7	20.7	20.3	20.0
H6	7.7	6.4	5.9	5.8	5.8	5.4	5.3

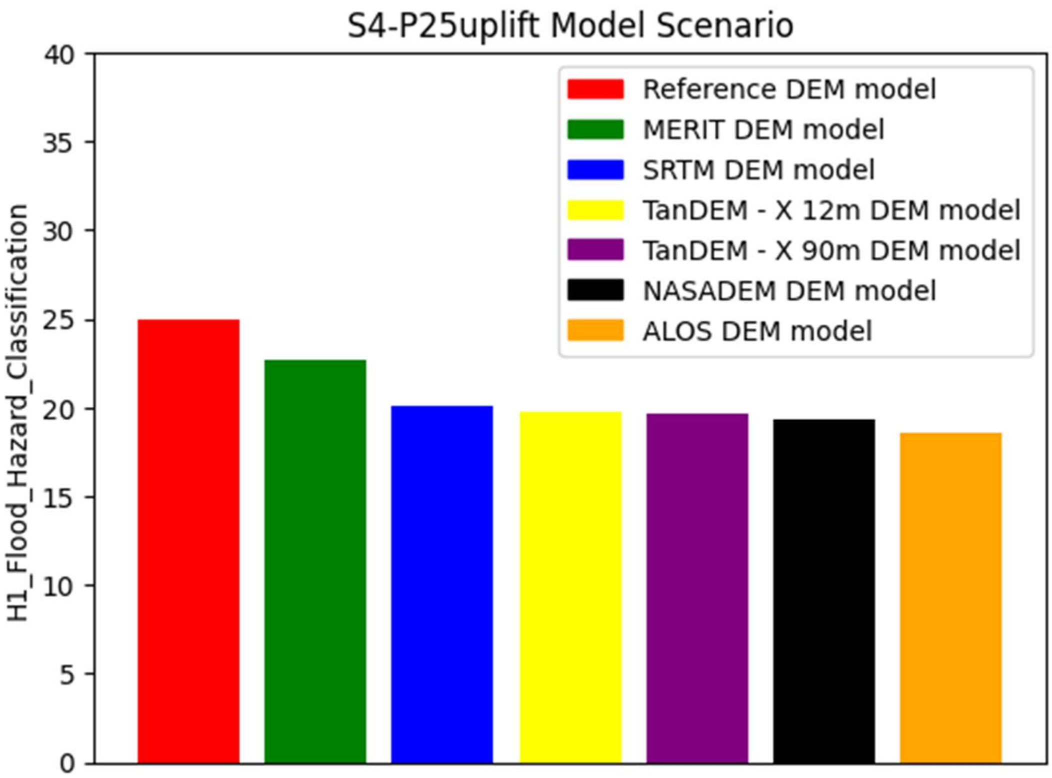

Figure 55. Comparison of Flood Hazard Vulnerability Classification (H1) for seven DEMs under the S4-P25uplift Model Scenario

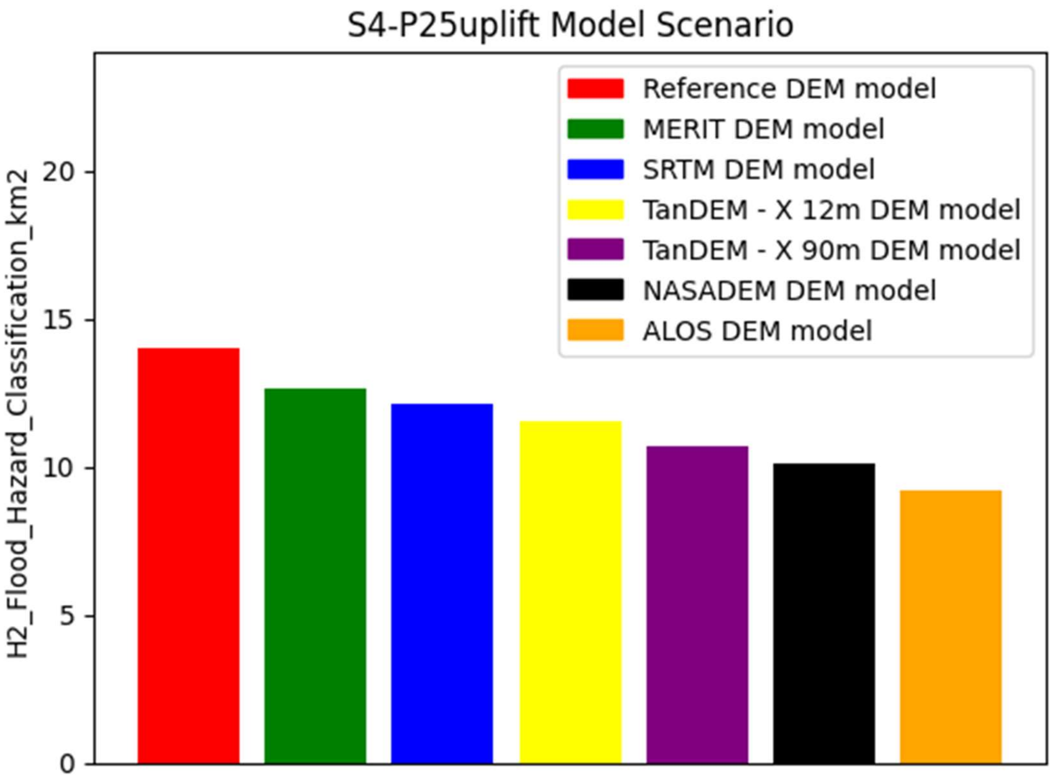

Figure 56. Comparison of Flood Hazard Vulnerability Classification (H2) for seven DEMs under the S4-P25uplift Model Scenario

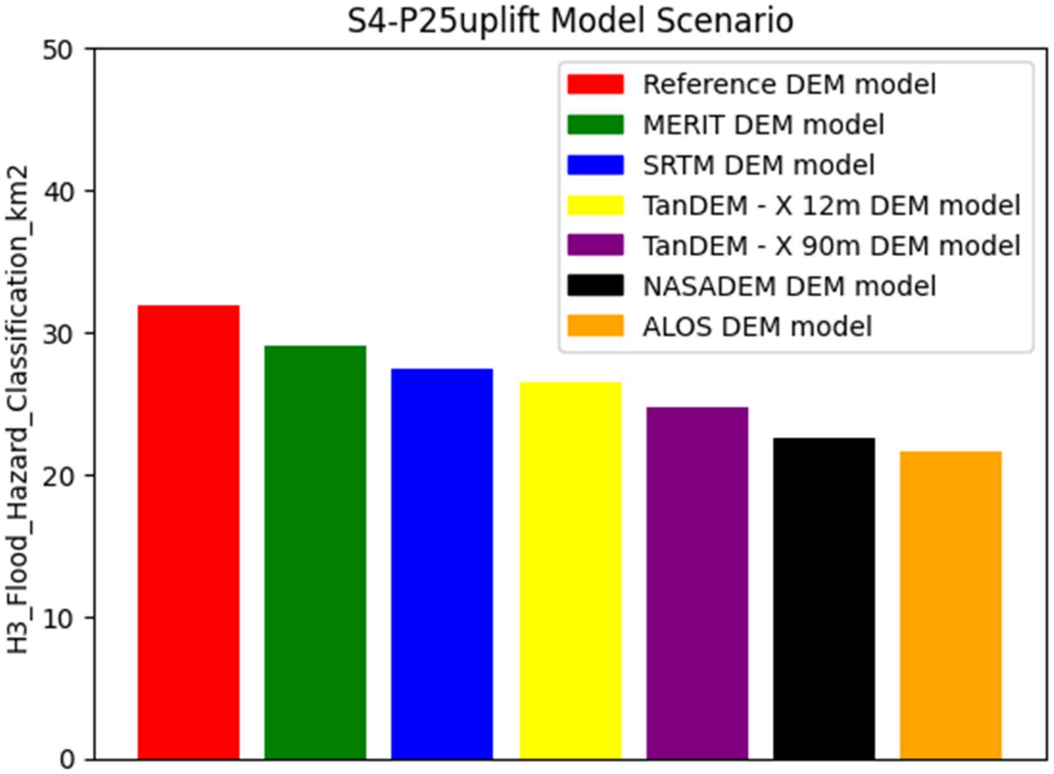

Figure 57. Comparison of Flood Hazard Vulnerability Classification (H3) for seven DEMs under the S4-P25uplift Model Scenario

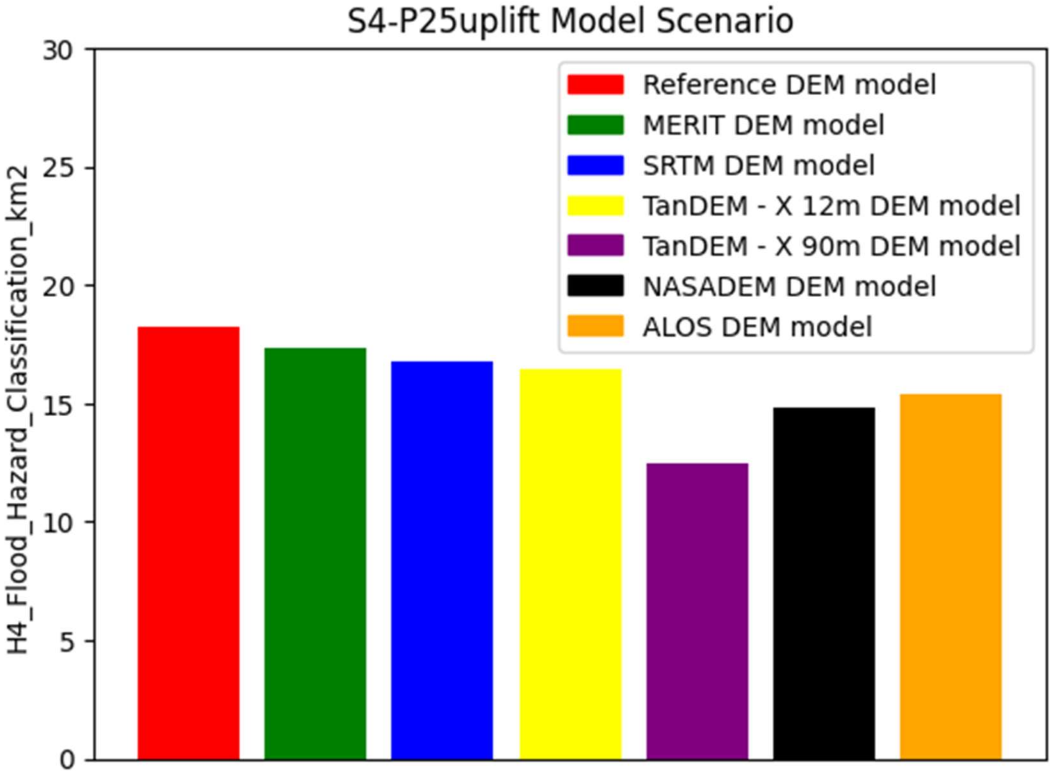

Figure 58. Comparison of Flood Hazard Vulnerability Classification (H4) for seven DEMs under the S4-P25uplift Model Scenario

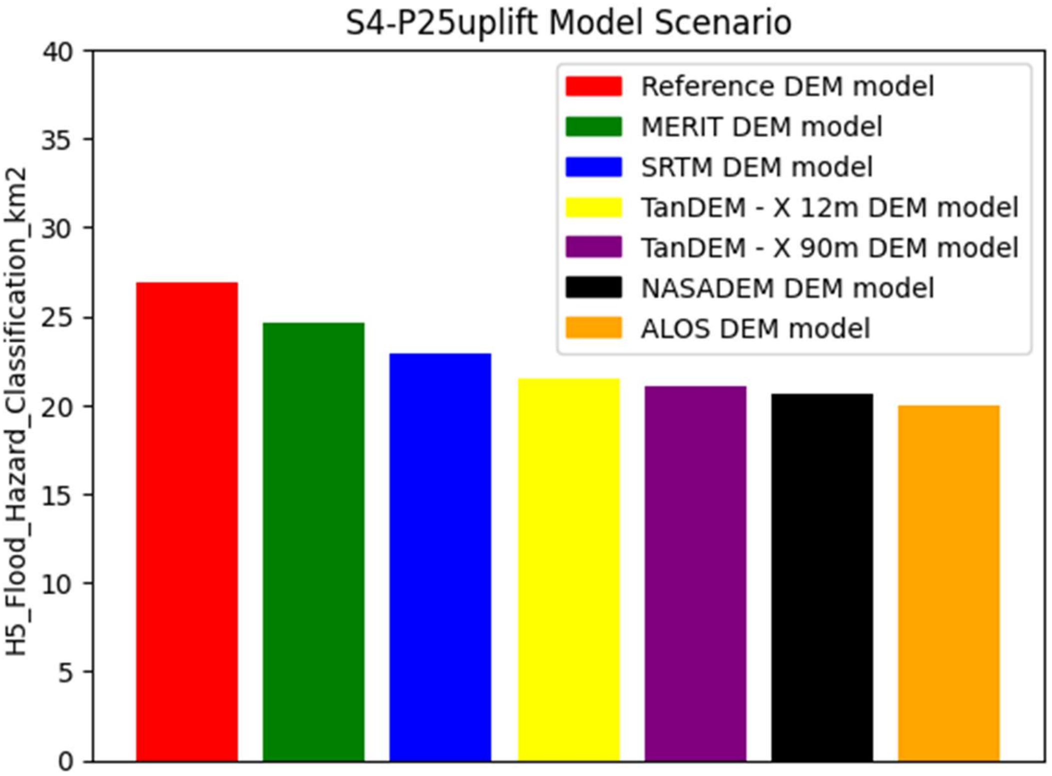

Figure 59. Comparison of Flood Hazard Vulnerability Classification (H5) for seven DEMs under the S4-P25uplift Model Scenario

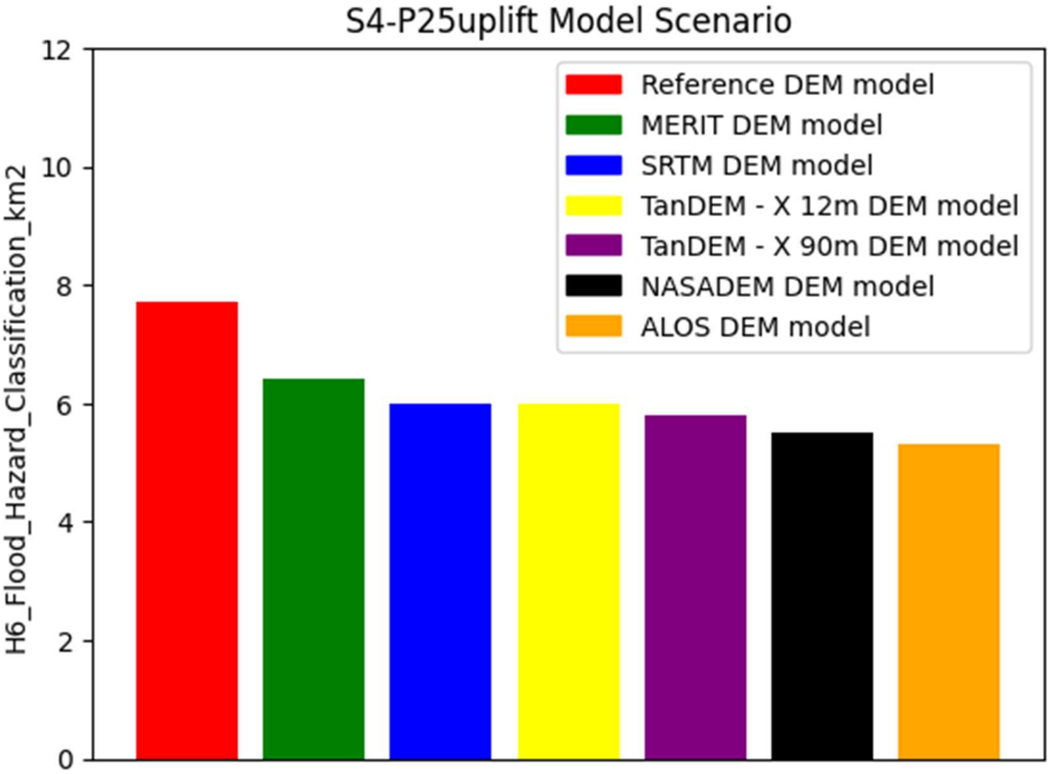

Figure 60.Comparison of Flood Hazard Vulnerability Classification (H6) for seven DEMs under the S4-P25uplift Model Scenario

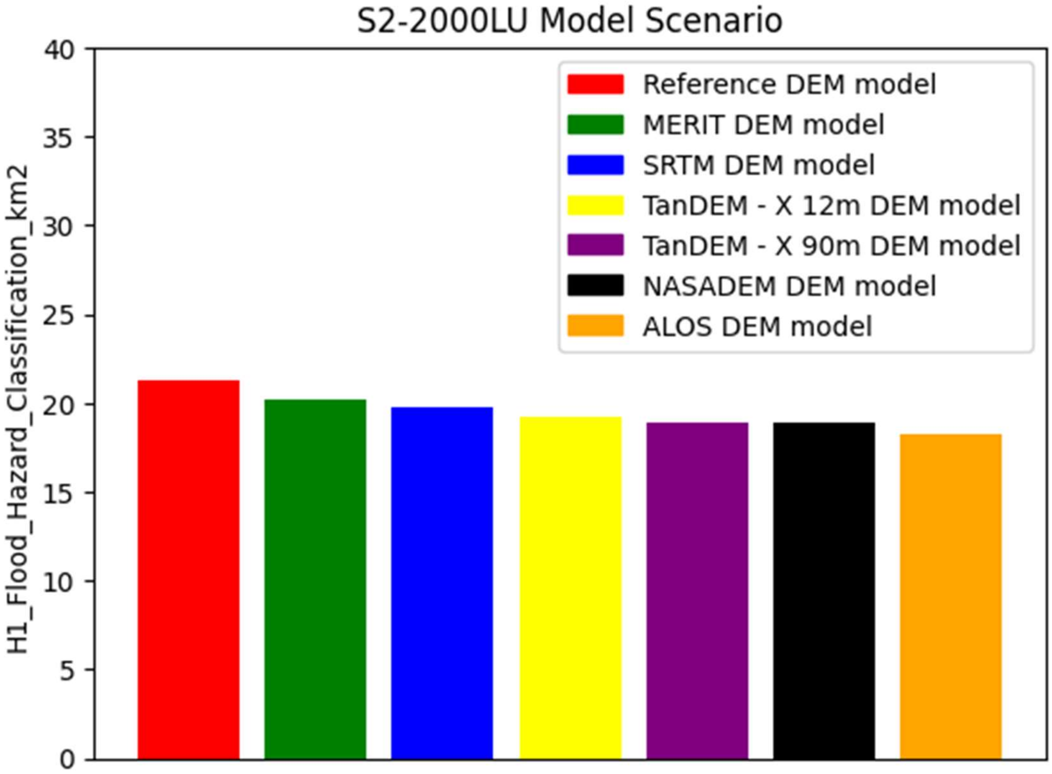

Figure 61. Comparison of Flood Hazard Vulnerability Classification (H1) for seven DEMs under the S2-2000LU Model Scenario

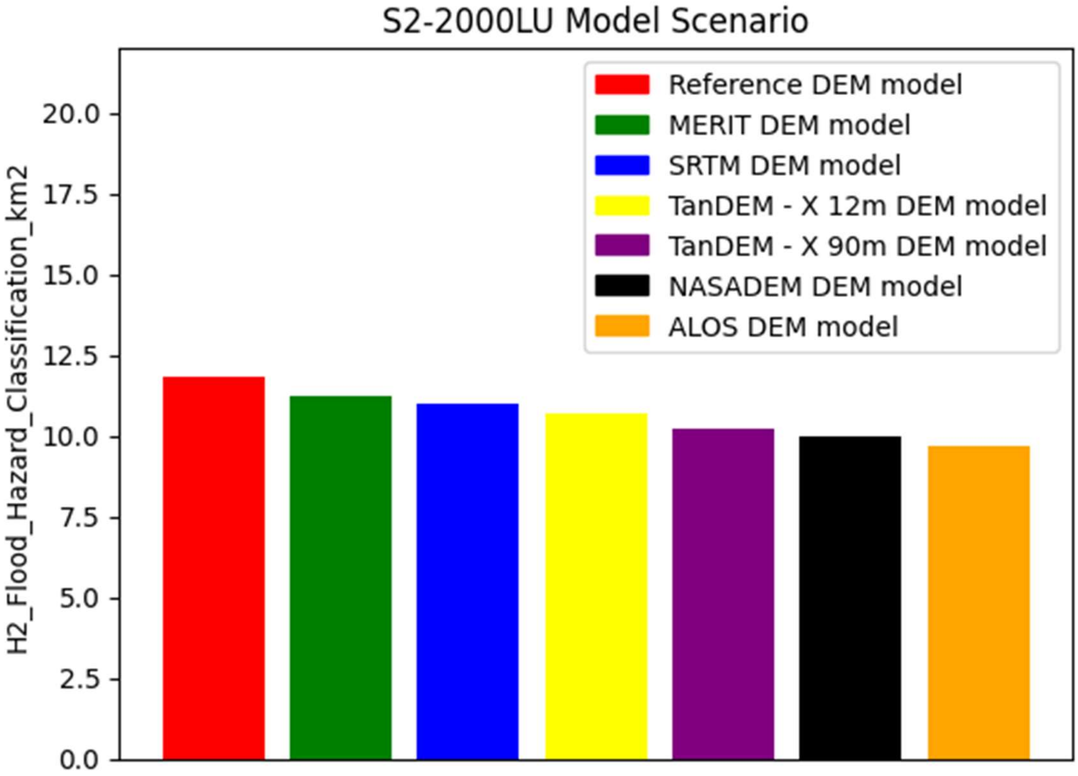

Figure 62. Comparison of Flood Hazard Vulnerability Classification (H2) for seven DEMs under the S2-2000LU Model Scenario

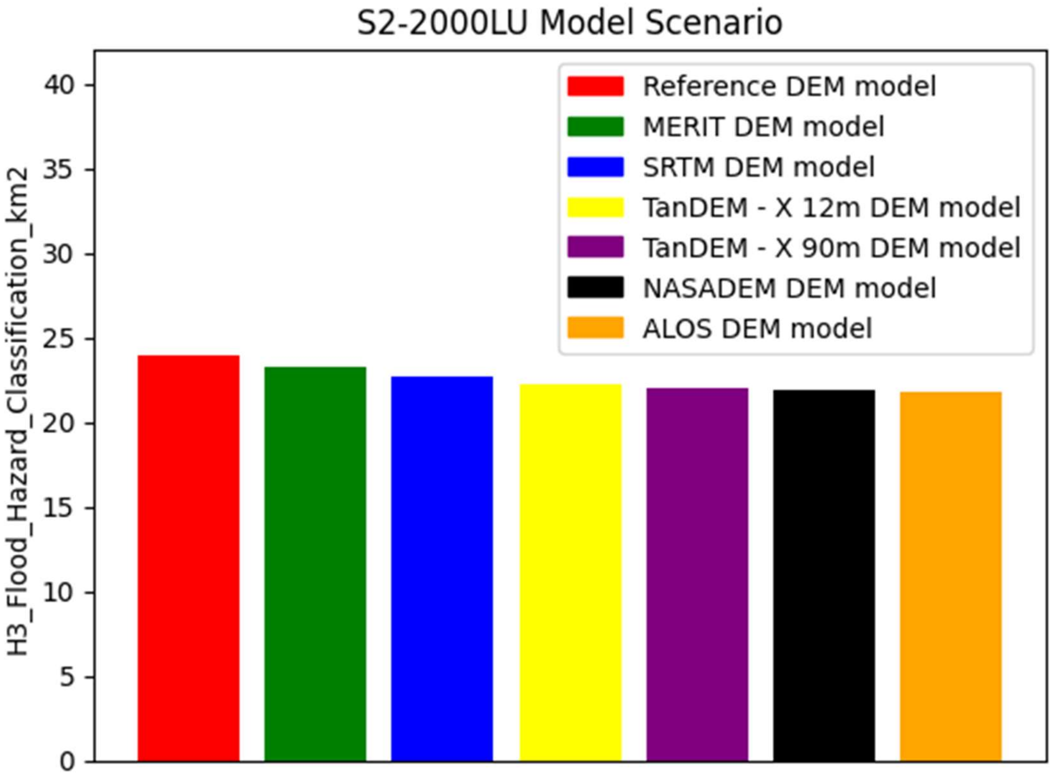

Figure 63. Comparison of Flood Hazard Vulnerability Classification (H3) for seven DEMs under the S2-2000LU Model Scenario

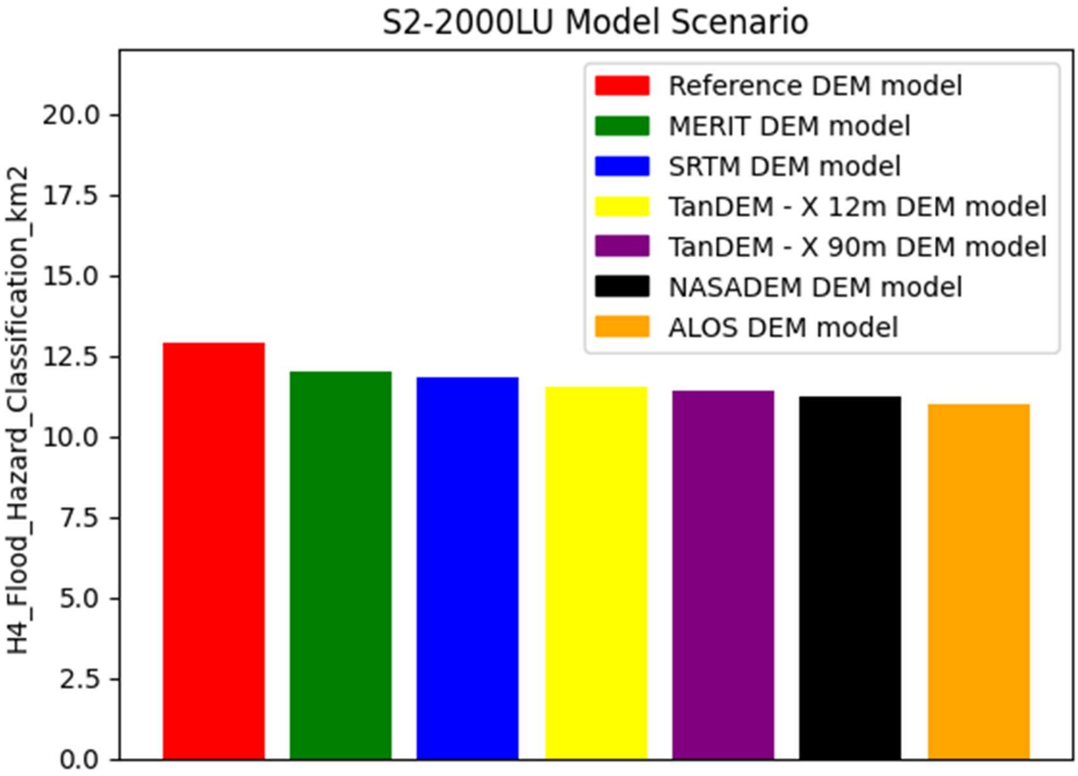

Figure 64. Comparison of Flood Hazard Vulnerability Classification (H4) for seven DEMs under the S2-2000LU Model Scenario

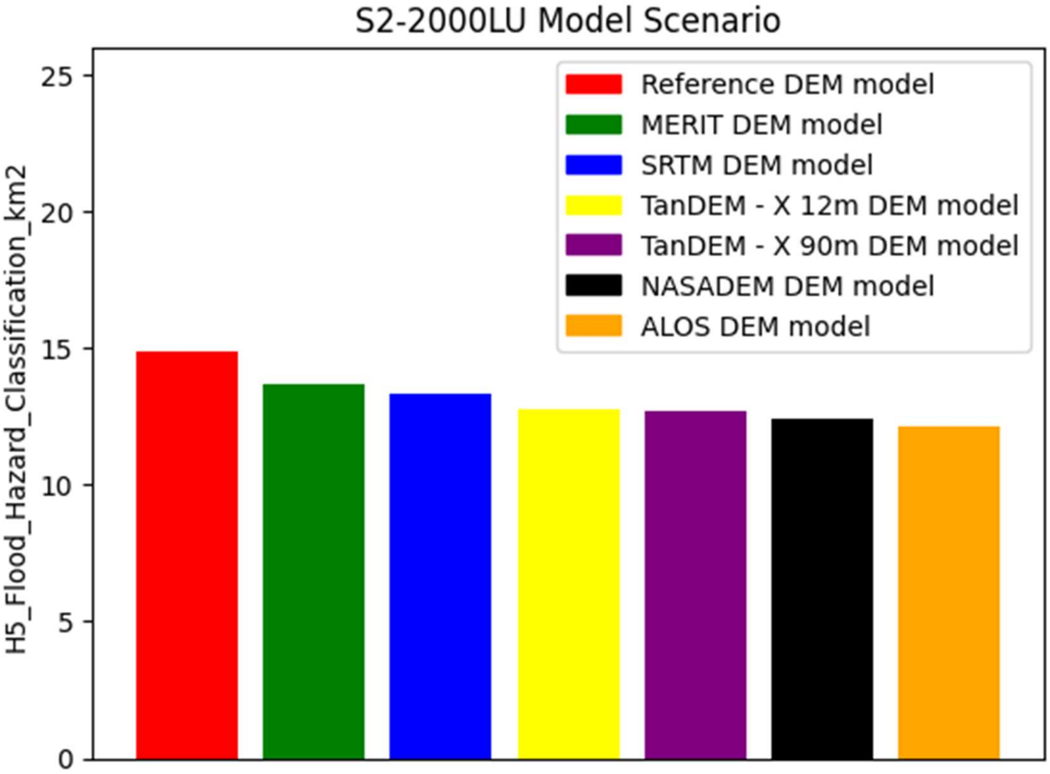

Figure 65. Comparison of Flood Hazard Vulnerability Classification (H5) for seven DEMs under the S2-2000LU Model Scenario

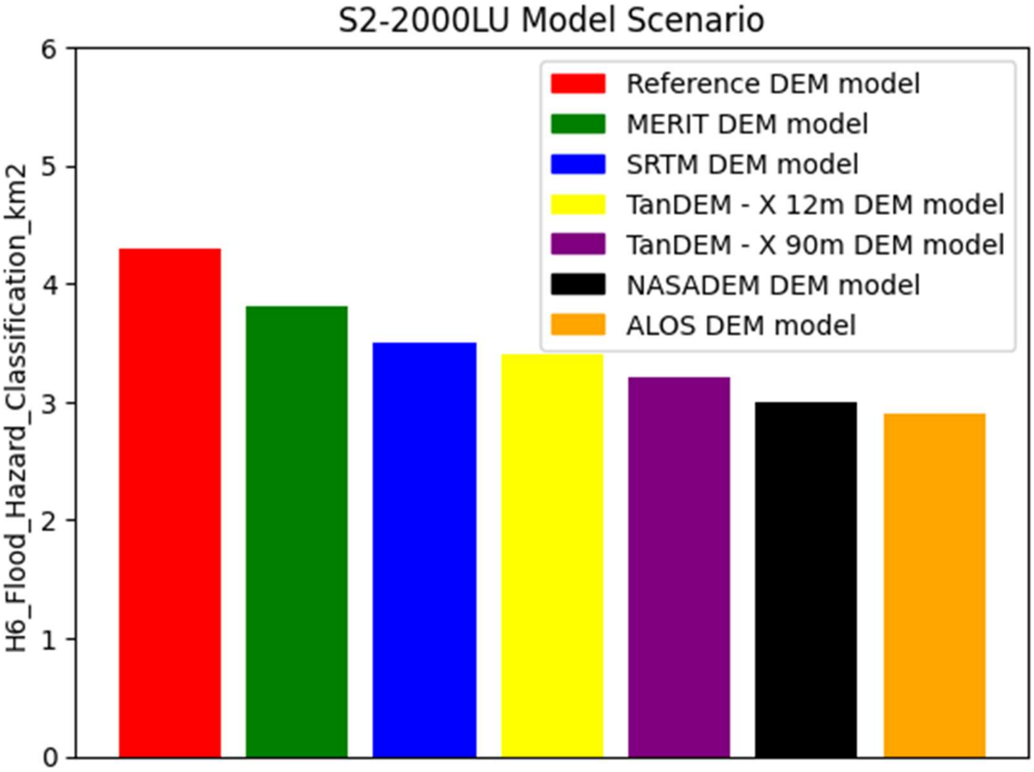

Figure 66. Comparison of Flood Hazard Vulnerability Classification (H6) for seven DEMs under the S2-2000LU Model Scenario

Table 52. Model Validation: Comparison of site survey data across three flooding hotspots areas of Nairobi with model results of the seven DEM models

Flooding Hotspots	Site Survey Flood Depth (m)	Reference DEM model	MERIT DEM model	SRTM DEM model	TanDEM-X 12m DEM model	TanDEM-X 90m DEM model	NASADEM DEM model	ALOS DEM model
Westgate Shopping Mall	1.58	1.71	1.99	2.15	2.32	2.45	2.58	2.77
Thika Super Highway and Industrial Area	1.39	1.52	1.86	2.08	1.79	2.17	2.31	2.52
Lindi Area, Kibera	1.78	2.01	2.38	2.55	2.3	2.57	2.68	2.81

7.5 Model Validation

The validation of the model was undertaken using actual field data collected across various flooding hotspots located within the catchment, during a one-week field trip to Nairobi, Kenya. The main purpose of the model validation was to assess the accuracy and reliability of the five model scenarios developed in this study by comparing simulated flood water levels with site data collected from flooding hotspots across Nairobi, Kenya.

The March 2018 rainfall across Kenya and parts of East Africa caused serious devastation to lives and properties. Approximately three hundred thousand people were displaced across Kenya by the flooding events that ravaged through the country (OCHA, 10th May, 2018). At the peak of the rains in March 2018 the flooding has caused widespread damage across Kenya, particularly several counties in the capital city, Nairobi, Kenya. There were approximately 150 deaths resulting directly from the flooding and a further 310,000 displaced across 40 counties in Kenya. The flooding event resulted in the destruction of public infrastructure such as bus terminals, hospitals, shopping malls, schools, police stations and government offices across Nairobi (UNICEF, 15th June, 2018). The flooding events provide reliable field data suitable for the validation of the five sets of 2D hydraulic models developed in this study.

The three sites for flood inundation analysis were selected from areas where major flood damages have occurred in in the past and which are listed as flood prone areas by the Kenya Meteorological Service. The field trip to collect flood height data at the flooding hotspots was undertaken between 20th to 28th July 2018. Photo images of the topographical survey are shown in Figure 68, Figure 69, Figure 70, Figure 71, and Figure 72. The timing of the field trip Nairobi was specifically arranged to coincide with the immediate aftermath the national & international recovery efforts to address the devastation caused by the historic flooding events in Kenya, March 2018. Figure 67 shows the three flooding hotspots: (1). Westgate Shopping Mall, Westlands, Nairobi. (2). Lindi Area, Kibera. (3).

Thika Super Highway and Industrial Area, Nairobi where site survey was undertaken to collect flood height/depth data.

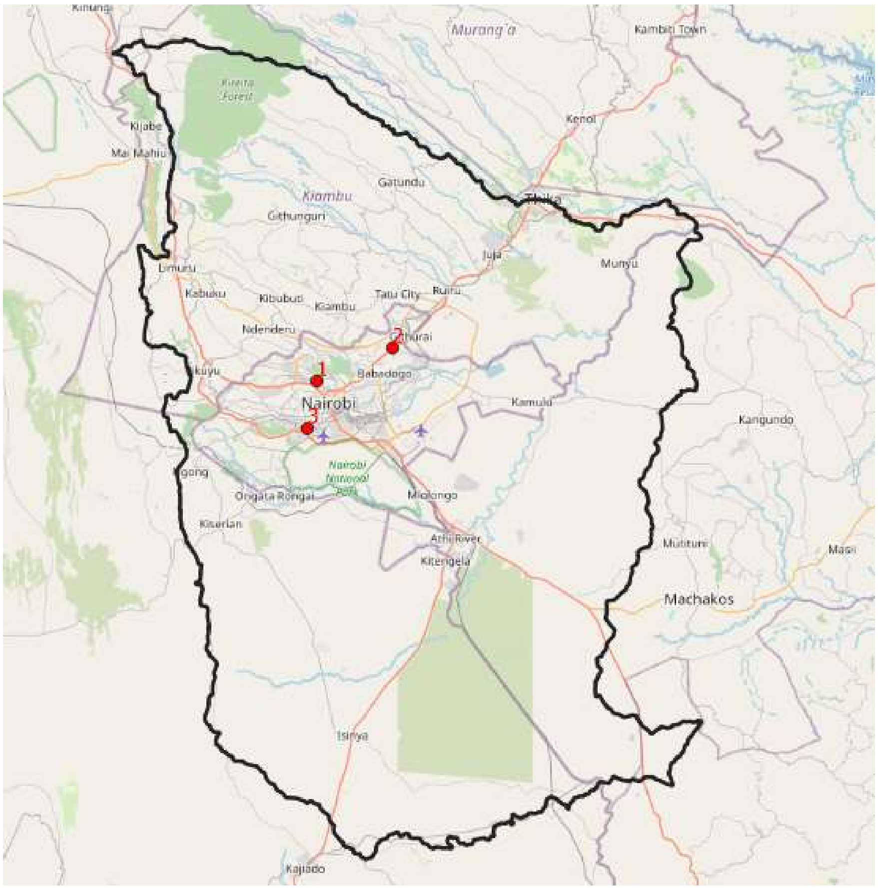

Figure 67. A screenshot from the QGIS software showing locations of three flooding hotspots in (1). Westgate Shopping Mall, Westlands, Nairobi. (2). Lindi Area, Kibera. (3). Thika Super Highway and Industrial Area in Nairobi where model validation data were collected between 20th and 27th July 2018.

7.6 Survey errors

There is potential for errors in the surveying process of the flooding hotspots that could include instrumental errors associated with faulty equipment due to age and lack of regular maintenance of survey equipment provided and operated by local surveyor in Nairobi. It was impossible to travel with survey equipment from the United Kingdom to Nairobi during the fieldwork exercise. The survey was undertaken at historic flooding hotspots sites where 'flood marks' have been left on walls, buildings and other surface features. There is potential for the introduction of gross error in the measurement from the survey instrument, human error associated with observing, taking or recording reading at flooding hotspot sites, and difficulty in identifying the exact level/locations etc.

Readings are taking at six locations of each of the three flooding hotspots site spanning an area of 10m^2 to 15m^2 in other to mitigate the impacts of these errors and uncertainties associated with the survey. Therefore, there is a high level of confidence in the accuracy of the survey results and any errors introduced could have been very negligible and have little significance on the overall accuracy of the survey results. The order of error is estimated at approximately 1cm.

Loose tripod shoes will always result in unstable set-ups of the survey equipment impacting on the accuracy of survey results. Therefore, it was ensured the tripod has no loose fixings that could cause twisting and movement of the tripod head.

Figure 68. Offloading of survey equipment (researcher) from car on arrival at the Westgate Shopping Mall flooding hotpot site to undertake topographic survey – 27th March 2018.

Figure 69. A hired local surveyor (Stanley Kimani) of the Kenya National Survey authority, Nairobi, with highly technical surveying knowledge providing support during the survey exercise.

Figure 70. Setting up of the survey equipment by the survey team at one of the survey sites.

Figure 71. Survey in progress at the Westgate Shopping Mall flooding hotspot showing a breach of the shopping mall fence line during the March 2018 flooding event to allow the passage of floodwater – brick rubble can be seen visible behind the gaping hole in fence wall in the background.

Figure 72. Measurement of flood historic flood depth levels at flooding hotspot site.

Sample data relating to the March 2018 flooding event were taken/recorded within 30m radius of the locations shown in Figure 67 across each site. The choice of the flooding hotspots were dictated by (1) the urban nature of the Westgate Shopping Mall located at the Central Business District in Nairobi. (2). the densely populated informal urban settlement of Kibera and (3) the industrial nature of the Thika area. A comparison of the of the average flood depths at the three flooding hotspots with the values represented in the baseline model, S1-Baseline is presented in Table 53. The results show acceptable level of accuracy in comparison with actual site survey data across the representative three flooding hotspot sites.

Table 53. Model Validation: Comparison of site survey data across three flooding hotspots areas of Nairobi with model results

Ref	Survey Flooding Hotspots	Coordinates (decimal)	Site Survey Elevation (mAOD)	Site Survey Flood Depth (m)	DEM Elevation (mAOD)	S1-Baseline Flood Depth (m)
1	Westgate Shopping Mall	-1.257, 36.803	1701.8	1.58	1702.5	1.99
2	Thika Super Highway and Industrial Area	-1.257, 36.895	1600.6	1.39	1601.8	1.86
3	Lindi Area, Kibera	-1.314, 36.792	1713.5	1.78	1715.0	2.38

8.0 SYNTHESIS OF RESEARCH FINDINGS

Accurate flood prediction using hydrodynamic models that rely on use of free, global datasets are crucial for making decisions to reduce urban pluvial flood hazard at city scale level. Climate change and land use change are some of the factors affecting urban pluvial flood hazard in rapidly developing cities most at risk areas from flooding but have not been modelled extensively. Building density in urban areas has been shown to contribute to vertical height accuracy of global DEMs and influential on flood predictions. This thesis has applied hydrodynamic models to assess the impact of climate change and land use change on urban pluvial flood hazard predictions. The major scientific findings from this thesis are: 1) when considering model application, data available, computational resources, and time available, it is possible to develop a hydrodynamic model that achieves a trade-off between model complexity and resolution of the input datasets. 2) A city-scale hydrodynamic model of the Nairobi catchment built using freely available, global data shows a good level of skill in urban flood predictions with topography a major control on predicted flood extent and flood depth; 3) Removal of building density error from global DEMs resulted in the improvement of the vertical height accuracy of global DEMs; 4) The use of corrected urban global DEM as key input data in the hydrodynamic flood models resulted in a more accurate flood predictions; 5) Land use change contributed to increases in urban pluvial flood hazard; 6) Climate change has a significant influence in increasing urban pluvial flood hazard.

8.1 Work on Urban Correction of Global DEM and Impacts on Urban Flood Modelling.

Global DEMs used in flood models are representations of physical ground surface and the spatial resolution of a DEM refers to the area of land being represented by single regular or irregular grid, with the value of each grid element representing the height of the ground at the corresponding datum (Vaze et al., 2010). There are many open access global scale DEMs such as the Shuttle Radar Topography Mission (SRTM), and its derivatives, the Multi-Error-Removed Improved-Terrain DEM (MERIT DEM) and NASA DEM (NASADEM), as well as Advanced Spaceborne Thermal Emission and Reflection Radiometer (ASTER) DEM and TerraSAR-X add-on for Digital Elevation Measurement (TanDEM-X 90m) etc. The global coverage of these DEMs makes them highly suitable for use in scientific applications where they are used extensively in flood models and have been critical in facilitating important flood studies, particularly in data-sparse areas, where local data is often difficult to access or unavailable (Hawker et al., 2018).

Chen and Hill (Chen and Hill, 2007) investigated the influence of DEM resolution on flood hazard modelling in urban areas and found that both vertical height error and spatial resolution of DEMs can impact on flood inundation depth and extent in urban flood modelling. Although, spaceborne DEMs provide fundamental input to many geoscience studies, they suffer from non-negligible height errors (Yamazaki et al., 2017). Sources of error in spaceborne DEMs include: (i) incomplete spatial sampling; (ii) measurement errors, such as positional inaccuracy, data entry errors; and (iii) processing errors such as computational numerical errors, interpolation errors, and classification and generalisation errors (Burrough, 1986). Global DEMs suffer from many different types of errors, some of which are significant at local scales; for example, (Rodríguez et al., 2006) reported a global mean and standard vertical height error of 8.2 ± 0.7 and 6.9 ± 0.5 m for SRTM X- and C-band data, respectively.

(Muthusamy et al., 2021) investigated impact of DEM resolution on urban flood modelling outputs using DEMs with different grid resolutions. The results show that there is a 30% increase in flood extent and a 150% increase in mean flood depth when the resolution of DEM reduces from a 1 m grid to a 50 m grid. There is a number of published work on the correction of errors in global DEMs, especially vegetation errors. (Falorni et al., 2005, Bhang et al., 2007, Dong et al., 2015, Gallant et al., 2012, Baugh et al., 2013, O'Loughlin et al., 2016, Chen et al., 2018). Also, there are many previous studies focused on the assessment of the vertical height accuracy of DEMs by comparing elevation values of DEMs to that of a reference local DEM having a higher vertical accuracy. A more accurate reference DEM such as the Light Detection and Ranging (LiDAR) is required in order to make an assessment of the vertical accuracy of global DEMs (Dong et al., 2015, Wessel et al., 2018, Acharya et al., 2018).

Although many studies (Robinson et al., 2014, Yamazaki et al., 2012, Yamazaki et al., 2017) have developed new vegetation-corrected DEMs, by either editing or adjusting existing global DEMs. However, despite significant advances in developing vegetation-corrected DEMs, there is limited understanding of DEM errors that can be attributed to building heights and building density in urban areas. Local DEMs that are based on airborne light detection and ranging (LiDAR) are preferential over open access, global DEMs due of their superior vertical accuracy, horizontal resolution, and ability to distinguish between ‘bare earth’ from built structures and vegetation (Yamazaki et al., 2017). However, (LiDAR) DEMs (<10 m horizontal resolution) are only available for a very small percentage of Earth's land surface (~0.005%), and data acquisition is often expensive (Hawker et al., 2018).

Topography plays an important role in the accuracy of flood inundation maps (Saksena, 2015). Therefore, in order to investigate the impact of the urban correction of global DEMs on flooding within an urban context (C3 sub-catchment), a fifth model was created in the HEC-RAS model environment that uses raw MERIT DEM and titled S5-RawDEM. The objective is to demonstrate how the building errors in global DEMs can impact negatively on accuracy of urban flood models that use them as key input data. The S5-RawDEM model is similar to the S1-Baseline model except for the variation in the input DEM data i.e. corrected MERIT DEM and uncorrected/Raw MERIT DEM for the S1-Baseline model and S5-RawDEM model respectively. The hazard vulnerability classification map for the S5-RawDEM model is shown in Figure 73. A comparison of the hydrograph for the S1-Baseline model and the S5-RawDEM model is also shown in Figure 74.

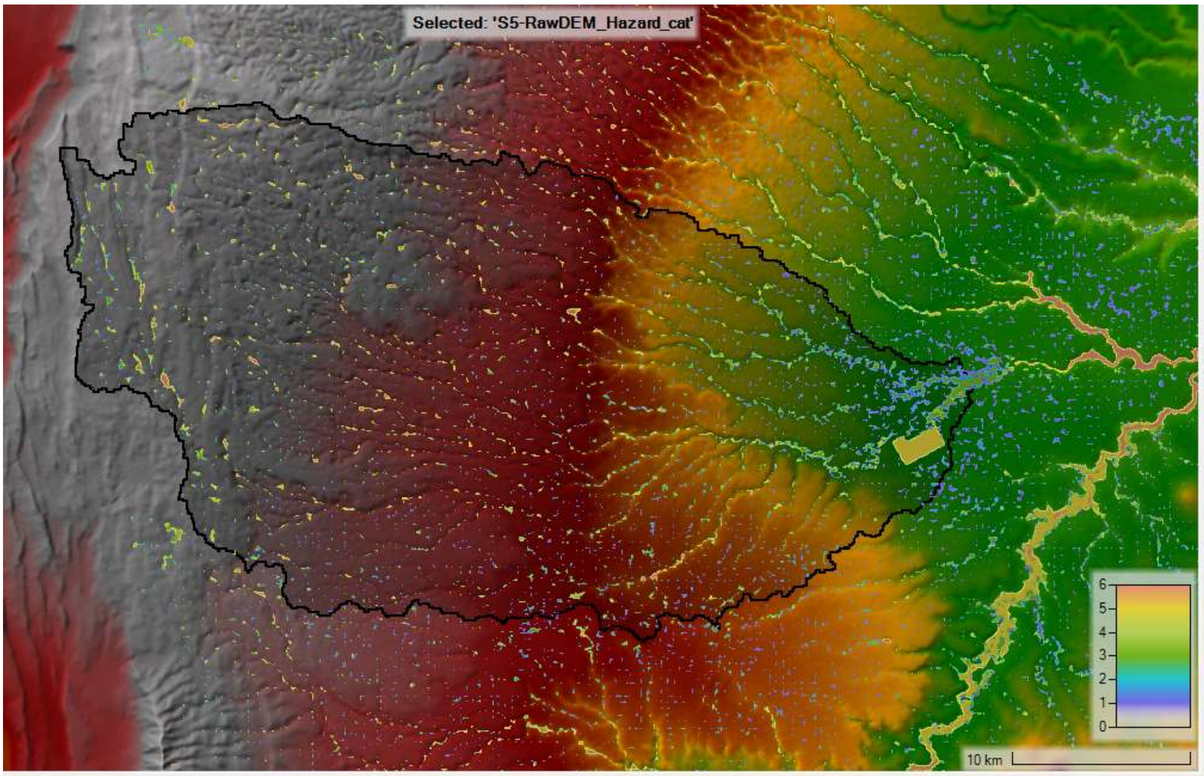

Figure 73. A screenshot from the HEC-RAS model showing hazard vulnerability classification map for the S5-RawDEM model that used raw DEM data instead of the corrected MERIT DEM.

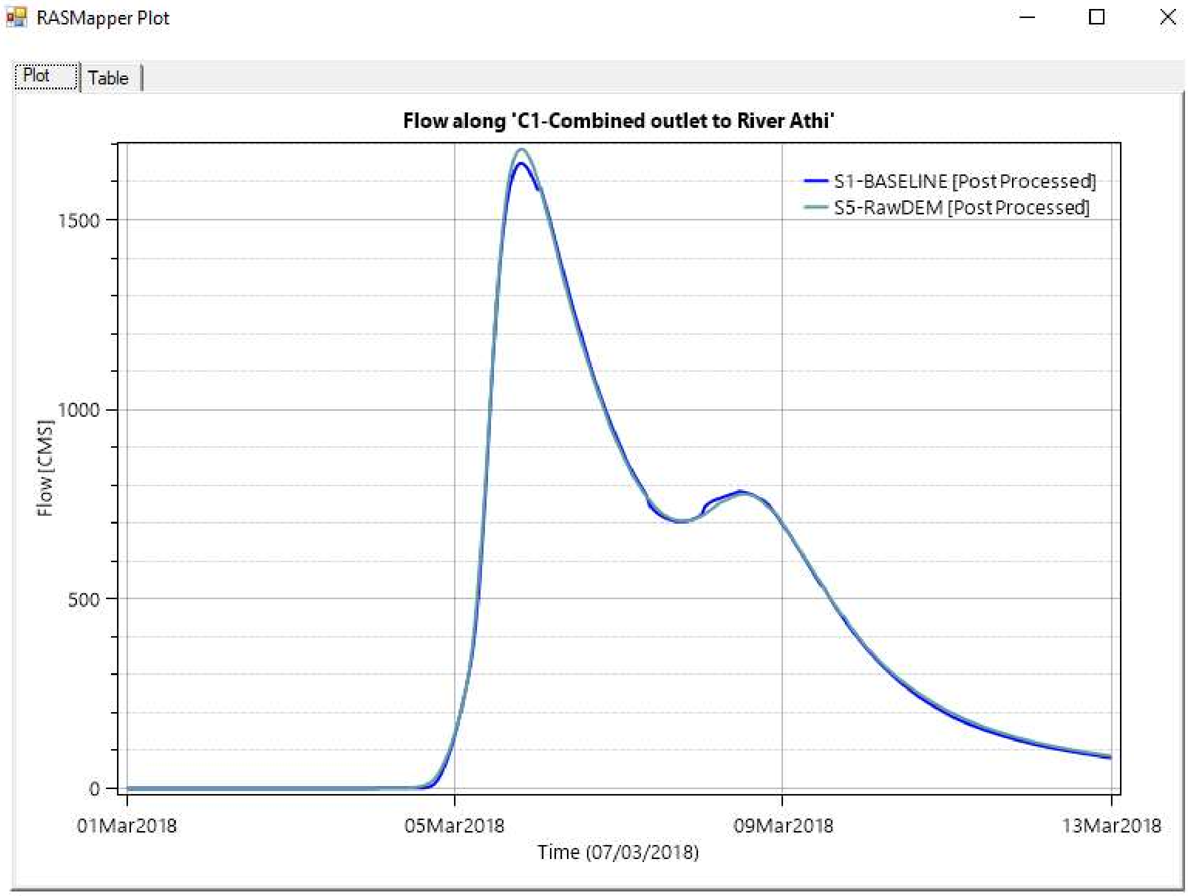

Figure 74. Cmparison of the flow hydrograph for the S1-Baseline model and S5-RawDEM model.

The flood hazard category map for the S1-Baseline model using the corrected MERIT DEM as key model input data compared to the flood hazard category map for S5-RawDEM model that uses the Raw MERIT DEM is shown in Figure 75. A comparison of flood depth levels between the S1-Baseline and S5-Baseline models with actual survey data at flooding hotspot sites is presented in Figure 45. Figure 76 illustrates the difference between the Hazard Vulnerability Classification of the S1-Baseline model and the S5-RawDEM model for the Nairobi C3 sub-catchment. The results show that there’s a similarity in the volume of water in the two models and very similar level of runoff including both models achieving peak flowrate of 1,649 m^3 1,685 m^3 for S1-Baseline and S5-RawDEM respectively, near about the same time (19:25 hrs) on March the 5th 2018 Figure 74.

In Figure 76, a comparison of the hazard vulnerability classification for the two models is shown. The hazard vulnerability classification for the S5-RawDEM is slightly higher than the S1-Baseline model across all the six hazard measurement thresholds, H1 to H6, due to the different flow paths internally in the uncorrected DEM fused into the S5-RawDEM and leading to these errors. A comparison of the flood depths for the S1-Baseline Model and S5-RawDEM model with measurements taken from across the three validation flooding hotspot sites show (Table 54) that the S5-RawDEM has a higher margin of deviation from the site reference data in comparison to the S1-Baseline model. The result show the S5-RawDEM model overestimating flood height by 18% to 23% more than the S1-Baseline model when compared to the reference site data collected at the flooding hotspot sites. From the results, it is evident that the s1-Baseline model is more accurate that the S5-RawDEM model predominantly due to the building error inherent in the raw DEM used as input data in the S5-RawDEM model.

The results obtained that show the S5-RawDEM model overestimating flood inundation depth more than the S1-Baseline is in agreement with previous studies such as (Ogania et al., 2019) that found digital elevation model with higher vertical accuracy generates more accurate flood hazard maps whilst DEMs with less vertical height accuracy over-predicts the flood hazard. The results of comparing the S1-Baseline model and the S5-RawDEM model with site data show that the S5-RawDEM model is less accurate by over predicting flood inundation depths across the three flooding hotspot sites where site data have been collected. The over prediction of the flood inundation depths by the S1-RawDEM model over the S1-Baseline model is evident in the comparison of hazard vulnerability classification for the two model.

The result of the hazard vulnerability classification of the S1-Baseline and the S5-RawDEM show the S5-RawDEM with slightly higher values across the H1 to H6 classification categories, Figure 76. The result of the model validation show that even though a comparison of the hazard vulnerability classification of the S1-Baseline model and S5-RawDEM model show slightly higher values across all hazard categories (H1 to H6), the model validation Table 54 show that the difference is important for model fit to reality. The hazard vulnerability classification maps comparing S1-Baseline and S5-RawDEM is shown in Figure 75.

Table 54. Comparison of flood height levels between the S1-Baseline and S5-RawDEM models with actual survey data at flooding hotspot sites.

Ref	Survey Flooding Hotspots	Coordinates (decimal)	Survey Elevation (mAOD)	Survey Flood Height (m)	S1-Baseline (mAOD)	S1-Baseline Flood Height (m)	S5-RawDEM (mAOD)	S5-RawDEM Flood Height (m)
1	Westgate Shopping Mall	-1.257, 36.803	1701.8	1.58	1702.5	1.99	1703.4	2.35
2	Thika Super Highway and Industrial Area	-1.257, 36.895	1600.6	1.39	1601.8	1.86	1602.9	2.23
3	Lindi Area, Kibera	-1.314, 36.792	1713.5	1.78	1715.0	2.38	1715.8	2.95

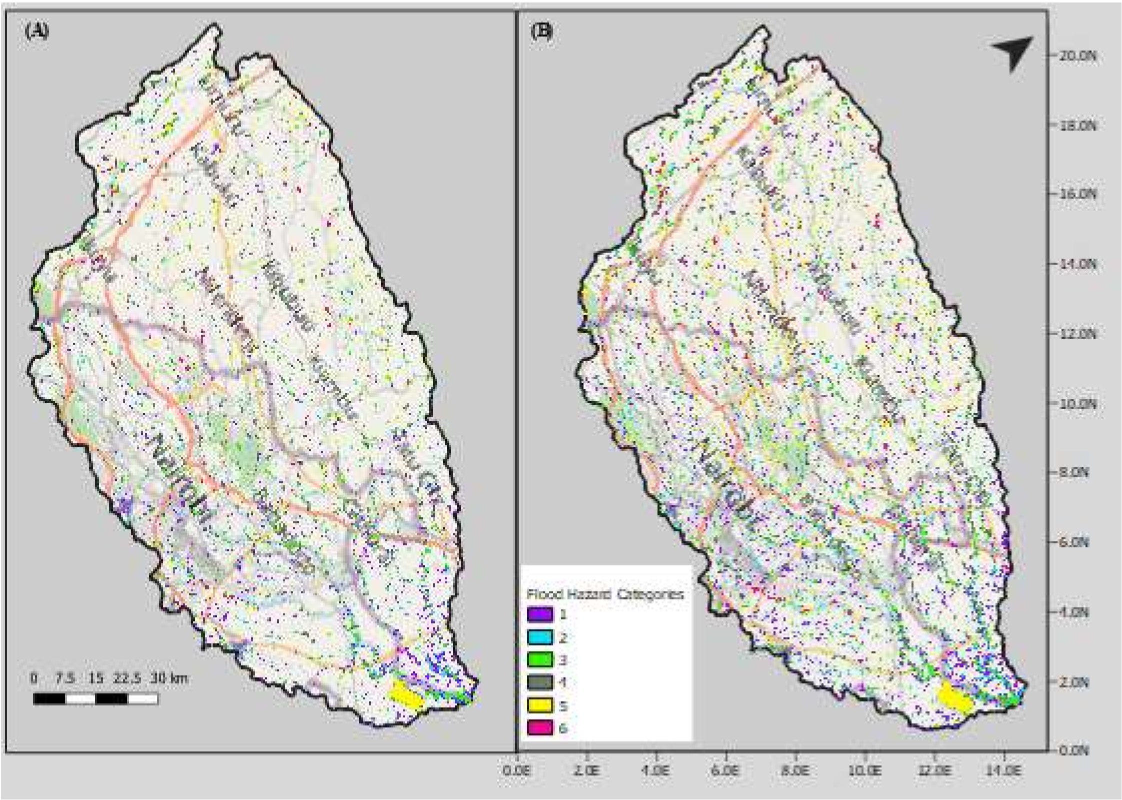

Figure 75. (A) Flood Hazard Category map for the S1-Baseline and (B) Flood Hazard Category map for S5-RawDEM models for C3 Nairobi sub-catchment area.

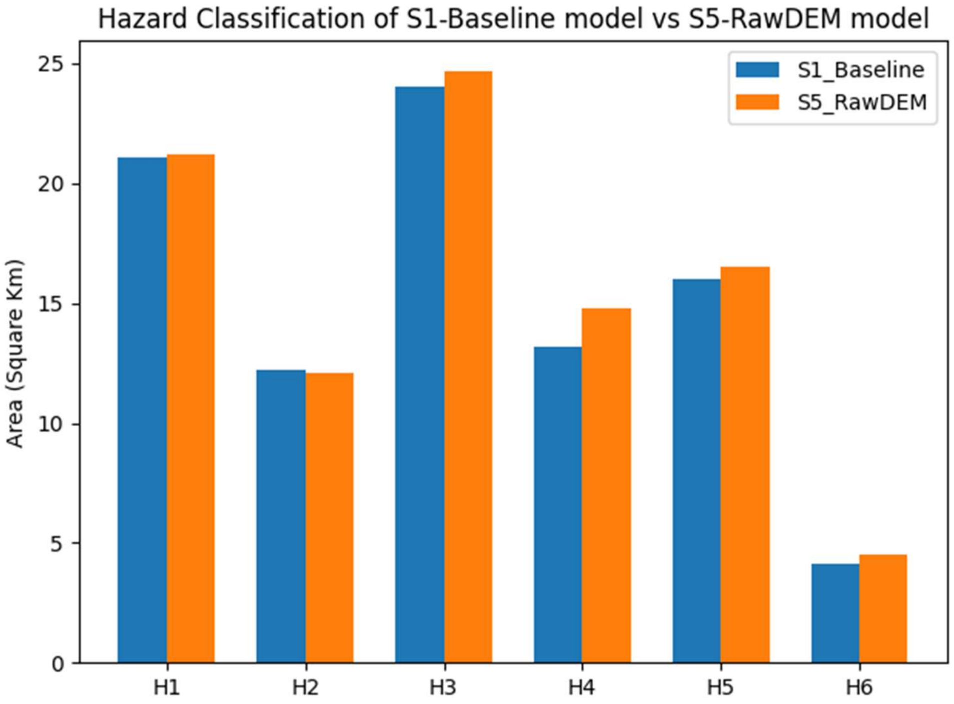

Figure 76. Comparison of Hazard Vulnerability Classification between S1-Baseline model and S5-RawDEM model for the Nairobi C3 sub-catchment.

8.2 Impacts of Land use change on Pluvial Flooding.

Climate change and urbanization pose significant threats for flooding and water quality in urban areas (Miller and Hutchins, 2017). Various researches have highlighted how rapid urbanization processes have influenced flood behaviour and contributed to flooding (Braud et al., 2013, Chen et al., 2017b, Donald Houston, 2011, Miller and Hutchins, 2017, Sanyal et al., 2014, Suriya and Mudgal, 2012). They found that physical growth of urban areas, amongst others characterized by the increase of impervious surfaces lead to the decrease in infiltration rate thus to an increase of overland flow. Removing vegetation and soil, grading the land surface, and constructing drainage networks increase runoff to streams from rainfall and snowmelt. As a result, the peak discharge, volume, and frequency of floods increase in nearby streams. Roads and buildings constructed in flood-prone areas are exposed to increased flood hazards, including inundation and erosion, as new development continues. Floodplains can alter the capacity of a channel to convey water and can increase the height of the water surface corresponding to a given discharge. In particular, structures that encroach on the floodplain, such as bridges, can increase upstream flooding by narrowing the width of the channel and increasing the channel’s resistance to flow. As a result, the water is at a higher stage as it flows past the obstruction, creating a backwater that will inundate a larger area upstream.

(Suriya and Mudgal, 2012) found that the rapid increase in population and the change in land use pattern between 1976 and 2005 are the major reasons for occurrence of flooding at the Thirusoolam sub watershed. The land use pattern of the Thirusoolam was classified into a built-up area and the results reflect that the increase in impervious area has altered the water cycle and obstructed natural runoff, which in turn led to flood risks to inhabitants. Similarly, (Konrad, 2003) found, generally, urbanization increases the size and frequency of floods and expose communities to increasing flood hazards. Urbanisation affects hydrological processes, often detrimentally and the growth of urban population, combined with an increase of extreme rainfall events due to climate change call for a better understanding and representation of urban floods (Courty et al., 2018). One of the key aims of this study is to assess the impact of urbanization, changes in land use, land cover on pluvial flooding at a city-scale.

Using the Storm water Management Model (SWMM), (Zhou et al., 2019), whilst taking into account the role of urban drainage system, found that urbanization led to an increase in annual surface runoff by 208 to 413% and annual flood volumes increases within a range of 194 to 942% whilst extension in size of the urban area resulted in increasing surface runoff from 208% to up to 413%. The flow hydrograph for the S1-Baseline model and the S2-2000LU model is shown in Figure 77. Figure 78, illustrates the change in hazard vulnerability classification under the S1-Baseline model and S2-2000LU land use scenarios at 2000 and 2020 in the Nairobi, C3 sub-catchment. The result show a percentage increase (hazard area) of 0.1%, 0.8%, 0.5%, 0.5%, 1.7%, and 0.2% in hazard area in H1, H2, H3, H4, H5, and H6 respectively. The results show the changes in land use over a period of 20 years, are significant enough to increase flood hazard vulnerability of the Nairobi sub-catchment. The result show that a total volume of 112,148,000 m^3 runoff was induced as a result of the changes in land use that occurred in the catchment between 2000 and 2020. The change in flood volume and surface runoff due to land use change within the sub-catchment equates to a 36% increase in flood extent between 2000 and 2020.

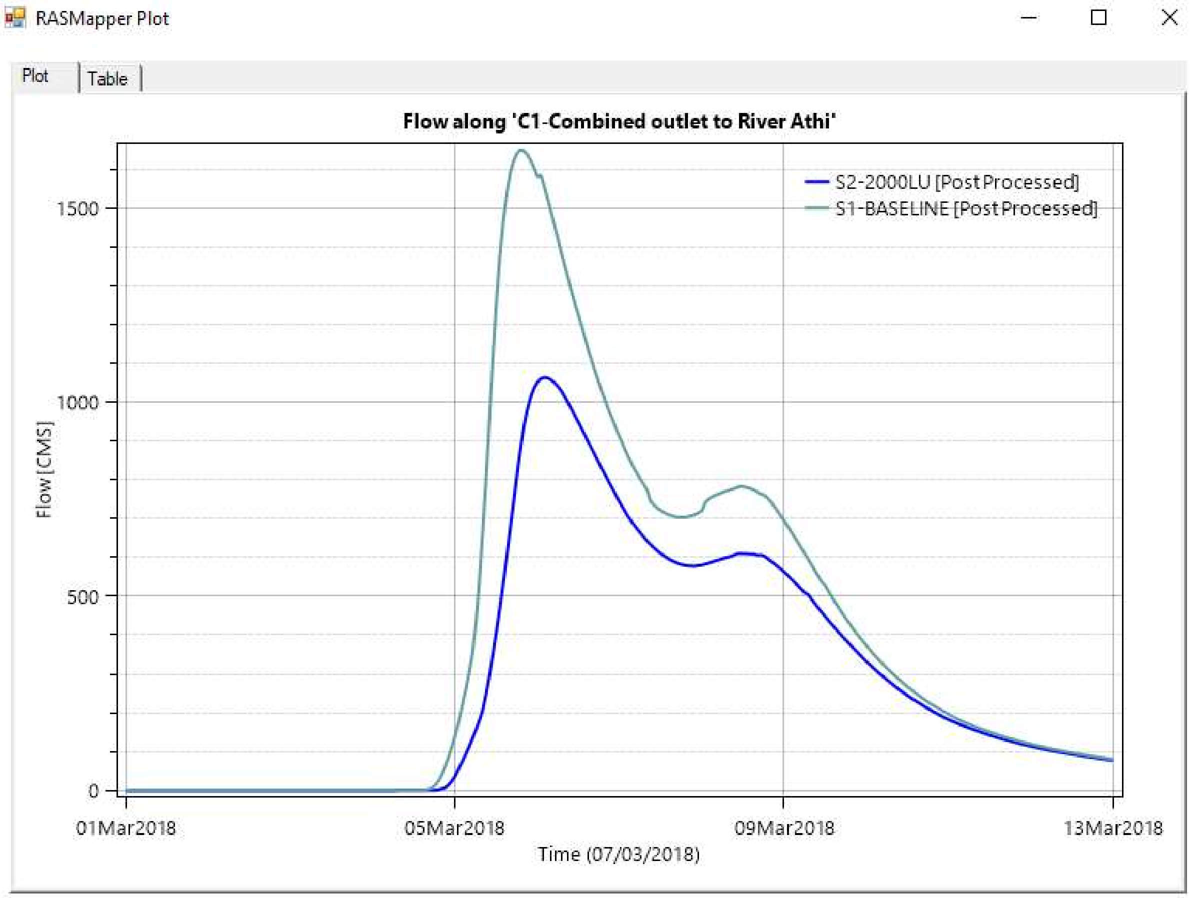

Figure 77. A screenshot from the HEC-RAS software showing comparison of flood hydrographs for the S1-Baseline model and the S2-2000LU model.

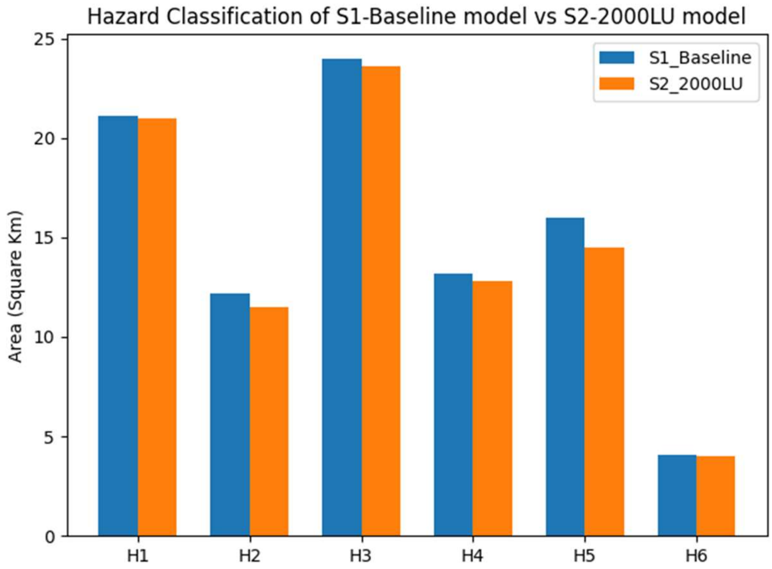

Figure 78. Comparison of Hazard Vulnerability Classification between S1-Baseline model and S2-2000LU model for the Nairobi C3 sub-catchment.

A comparison of the six hazard vulnerability classification for the S1-Baseline model with the S3-CP4uplift and S4-P25uplift climate models is shown in Figure 88, Figure 89, Figure 90, Figure 91, Figure 92, and Figure 93.

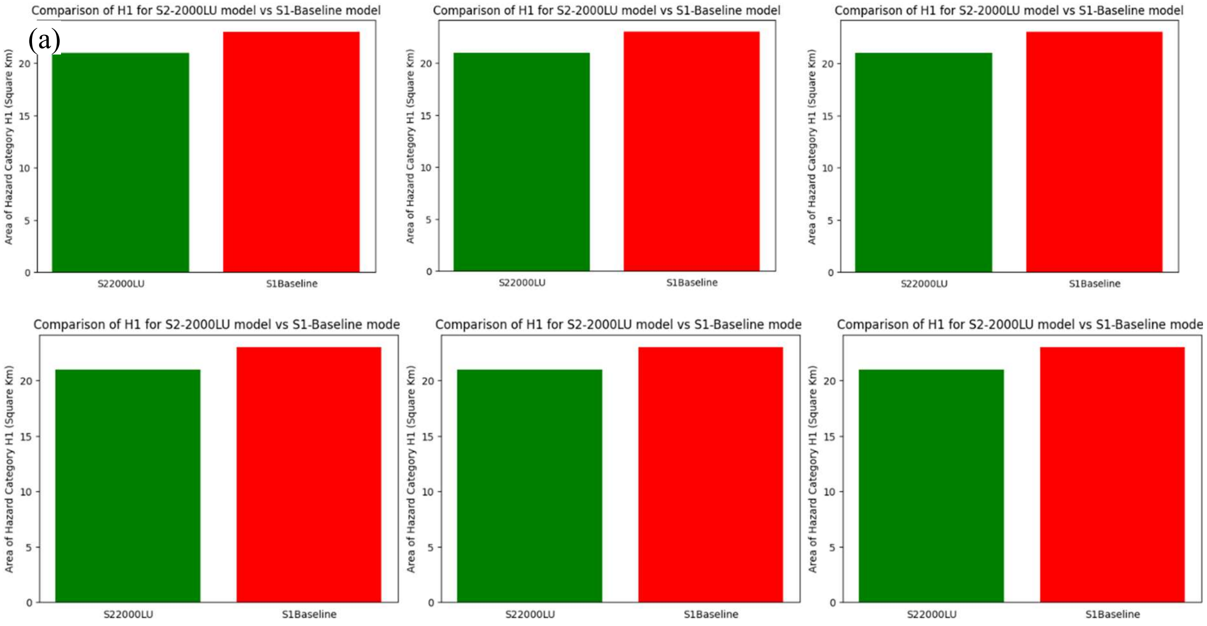

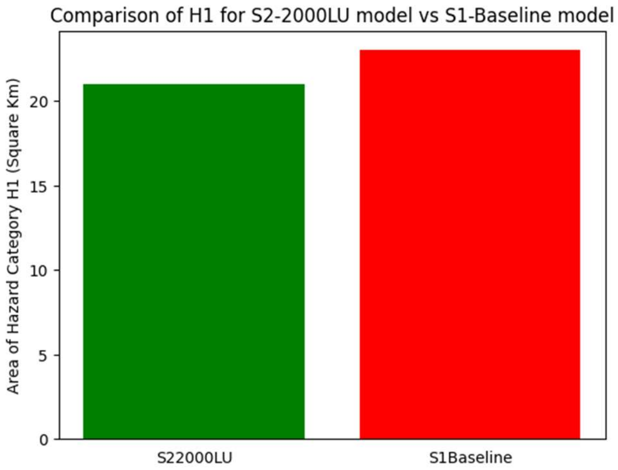

Figure 79. Comparison of Hazard Vulnerability Classification, H1 for the S2-2000LU model and the S1-Baseline model.

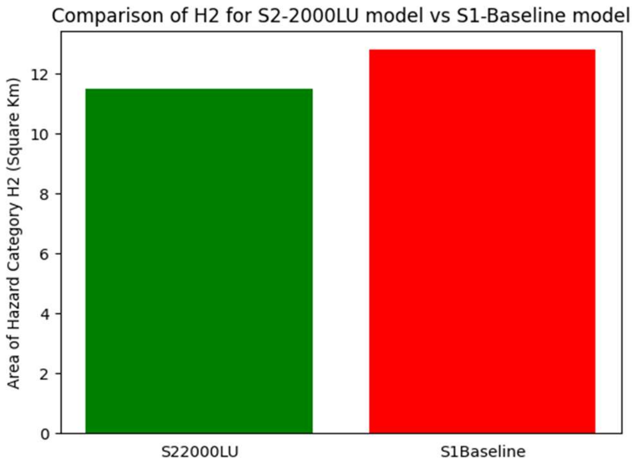

Figure 80. Comparison of Hazard Vulnerability Classification, H2 for the S2-2000LU model and the S1-Baseline model.

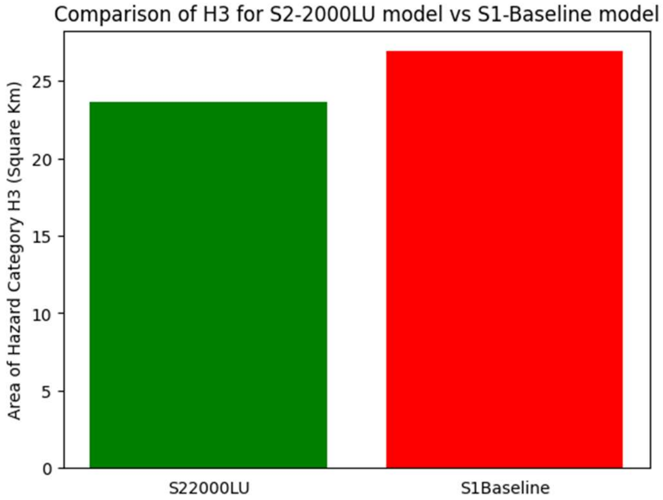

Figure 81. Comparison of Hazard Vulnerability Classification, H3 for the S2-2000LU model and the S1-Baseline model.

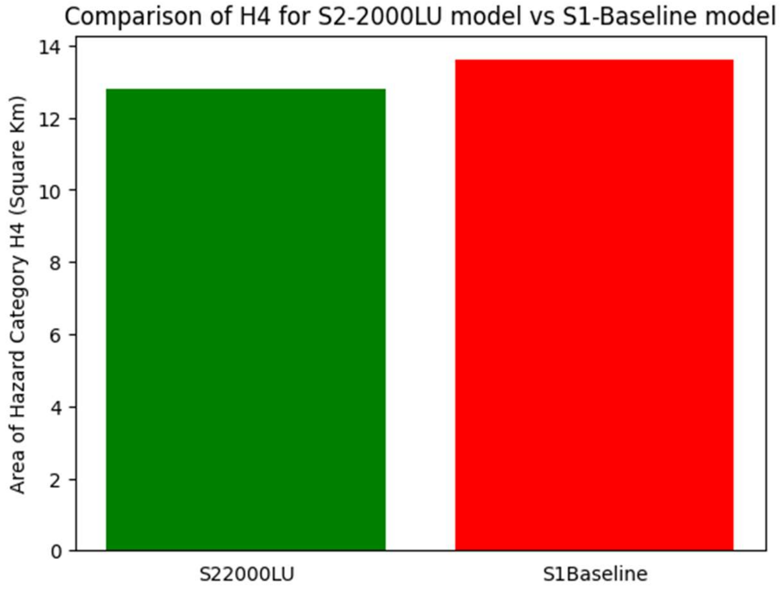

Figure 82. Comparison of Hazard Vulnerability Classification, H4 for the S2-2000LU model and the S1-Baseline model.

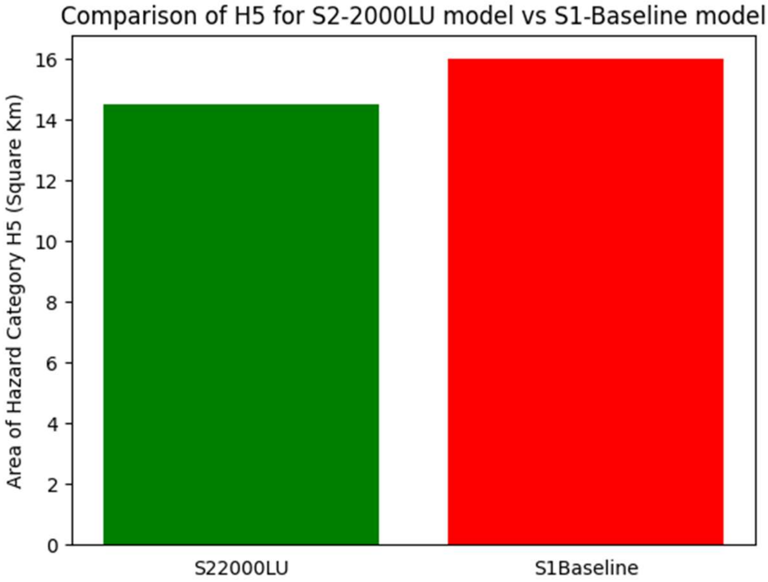

Figure 83. Comparison of Hazard Vulnerability Classification, H5 for the S2-2000LU model and the S1-Baseline model.

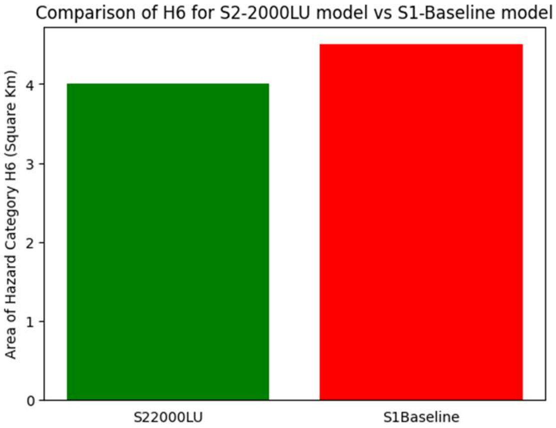

Figure 84. Comparison of Hazard Vulnerability Classification, H6 for the S2-2000LU model and the S1-Baseline model.

8.3 Impacts of climate change on urban pluvial flooding

Climate models are primary tools used to estimate how climate might change in future. Rainfall is one of the most important variables to assess in a changing climate, is not adequately simulated in present climate models. For Africa, the ranges of available climate models largely disagree in the direction of projected changes (i.e. whether getting wetter or drier). Global and regional climate models cannot simulate local-scale processes such as convection due to their relatively large grid cells (coarse resolution), typically several tens of kilometre across. Projections of climate change over Africa are highly uncertain, therefore, (Rowell et al., 2016) addressed this uncertainty by ranking models according to their historical climate performance and disregard those with least skill. The inability of global and regional models to accurately capture local-level processes results in biases in key outcomes such as temperature and rainfall compared to observations that increase uncertainty in future climate projections from these models. This study found that when the more capable models are selected by an overall performance measure, projection uncertainty is not reduced because these models are typically spread across the full range of projections. Further research must develop an expert judgement approach that will discriminate models using an in-depth understanding of the mechanisms that drive the errors and uncertainty in projected changes over Africa. Many of the most important impacts of climate change on society can typically be found on the micro- and meso-scale. For example, water supply management demand for reliable climate projections on the scale of single river catchments are in most cases much smaller than the resolution of modern Global Climate Models (GCMs). All processes which have smaller spatial scales than those resolved in the GCMs cannot be represented explicitly.

As improvements in technology and data sharing allow researchers to set up novel experiments to overcome the problem of large grid cells, scientists have developed very high-resolution climate models with grid cells that are a few kilometres wide, rather than tens of kilometres. They are known as “convection-permitting” models because they can simulate larger convective storms without the need of parameterisation schemes. They have been shown to improve the representation of dynamics such as the influence of mountains and statistical properties of convection and heavy rainfall, and hence have the potential to better represent changes in convection and local storms in future projections. The rainfall uplift factors used in the study are for the end of century data (RCP85). For CORDEX, the historical period was 1989 - 1999, the future period 2089 - 2099. For CP4A and P25 the historical period is 1997 - 2006, the future period is 2097 - 2106.

Changes to the timing and magnitude (depth) of rainfall events as a result of climate change are predicted to significantly alter the flooding experienced in many urban areas of the world (Ashley et al., 2005a, Wheater and Evans, 2009, Hunt and Watkiss, 2011, Arnell et al., 2015). Global warming have been found to be responsible for increases in frequency and intensity of extreme rainfall (IPCC, 2014, IPCC, 2007). The number of quantitative assessment studies of the impact of climate change on urban drainage remains, however, rather limited (Willems et al., 2012a). It has been found that future changes in rainfall intensities and frequencies will render most large urban areas vulnerable to extreme rainfall and pluvial flooding due to lack of resilience in existing drainage infrastructure (Willems et al., 2012b). (Veijalainen et al., 2010) found increase precipitation resulted in growing floods in major central lakes and their outflow rivers in Finland.

The frequency and severity of the Combined Sewer Overflow (CSO) discharges are strongly influenced by climatic factors governing the occurrence of urban storm water runoff, particularly the amount and intensity of the rainfall. Modelling studies undertaken by (Abdellatif et al., 2014) found that urbanisation and increasing rainfall intensity will increase drainage overflow volumes, resulting significant uplift (10% and 20%) to the 0.5% AEP event and more frequent and severe pluvial flooding. (Ashley et al., 2005a), found that due to the effects of climate change, flood risks may be increased by a factor of almost 30 times.

A comparison of the flood hydrographs for the S1-Baseline model, S3-CP4uplift model and the S4-P25uplift model is shown in Figure 85. The result show that climate change rainfall used in the S3-CP4uplift model and the S4-P25uplift model has a significant effect on flood extent and flood depth. There is a sharp increase in peak flowrates peak flowrates to up to 55% when comparing S1-Baseline model to the S3-CP4uplift model. Similarly, when comparing the S1-Baseline model with the S4-P25 model, the increase in peak flowrate is more pronounced with a sharp increase in peak flowrate of up to 67%. Figure 86 and Figure 87 show the change in Hazard Vulnerability Classification when the S1-Baseline model is compared to the S3-CP4uplift model and the S4-P25uplift model respectively. The results show the climate change models (S3-CP4uplift and S4-P25uplift) have higher hazard vulnerability thresholds when compared to the S1-Baseline model. The result show that climate change will create severe impacts resulting in more flooding in urban areas. The results show the S4-P25uplift climate change model with higher hazard levels and an indication that the extent and scale of the flood forecasting in urban areas will depend on the climate model simulation considered and used in the hydraulic flood model. A comparison of the six hazard vulnerability classification for the S1-Baseline model with the S3-CP4uplift and S4-P25uplift climate models is shown in Figure 88, Figure 89, Figure 90, Figure 91, Figure 92, and Figure 93,

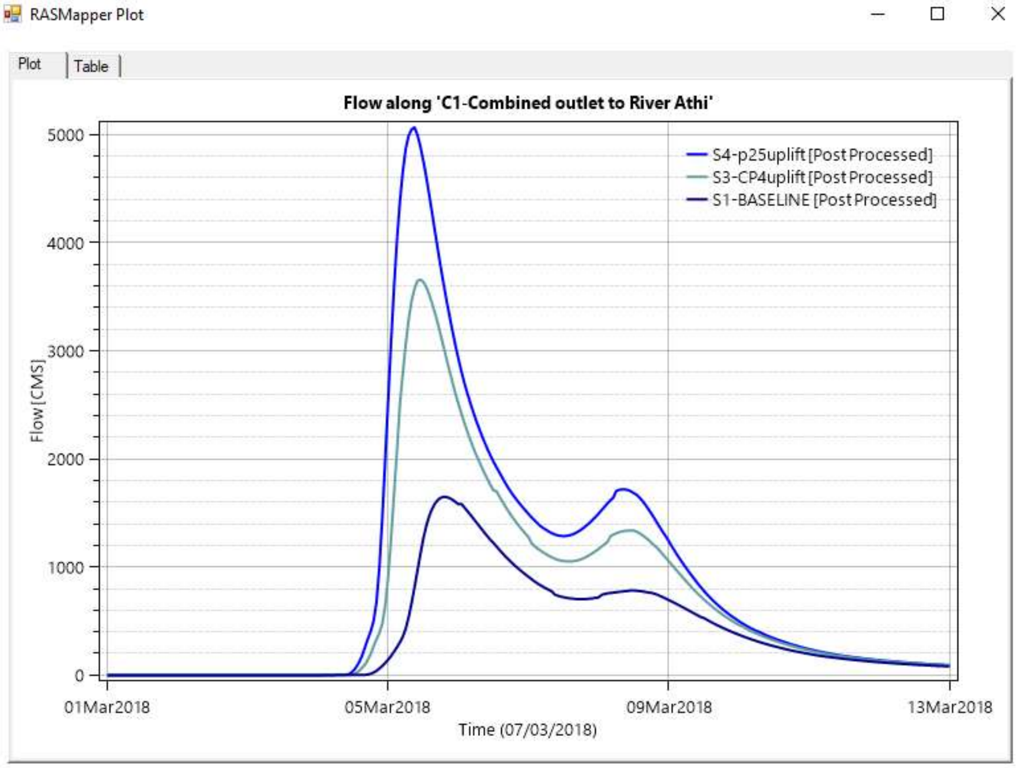

Figure 85. A screenshot from the HEC-RAS software showing comparison of flood hydrographs for the S1-Baseline model, S3-CP4uplift model and the S4-P25uplift model.

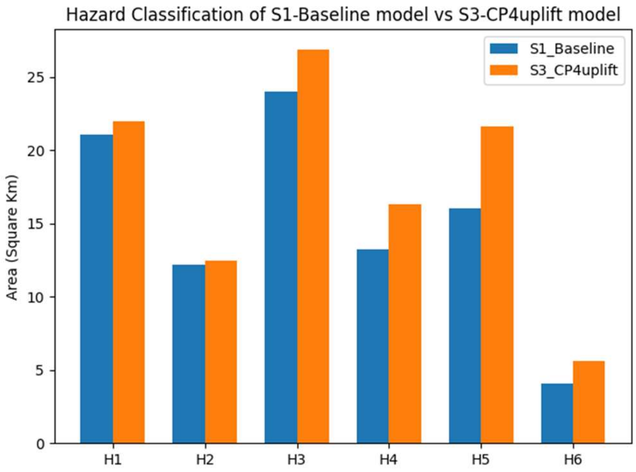

Figure 86. Comparison of Hazard Vulnerability Classification between S1-Baseline model and S3-CP4uplift model for the Nairobi C3 sub-catchment.

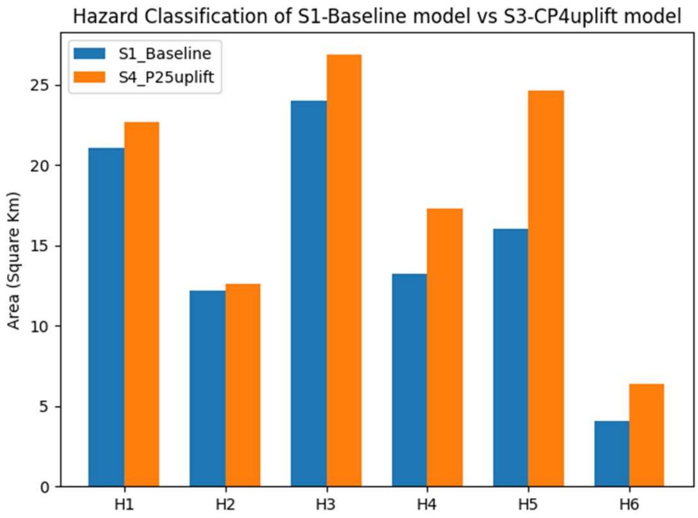

Figure 87. Comparison of Hazard Vulnerability Classification between S1-Baseline model and S4-P25uplift model for the Nairobi C3 sub-catchment.

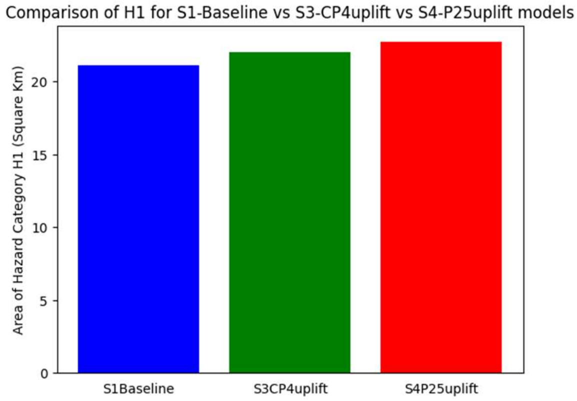

Figure 88. Comparison of Hazard Vulnerability Classification, H1 for S1-Baseline model vs S3-CP4uplift model vs S4-P25uplift model.

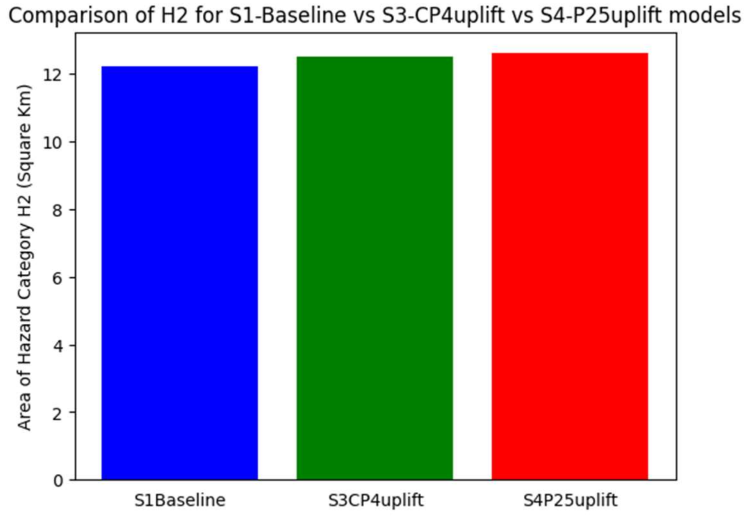

Figure 89. Comparison of Hazard Vulnerability Classification, H2 for S1-Baseline model vs S3-CP4uplift model vs S4-P25uplift model.

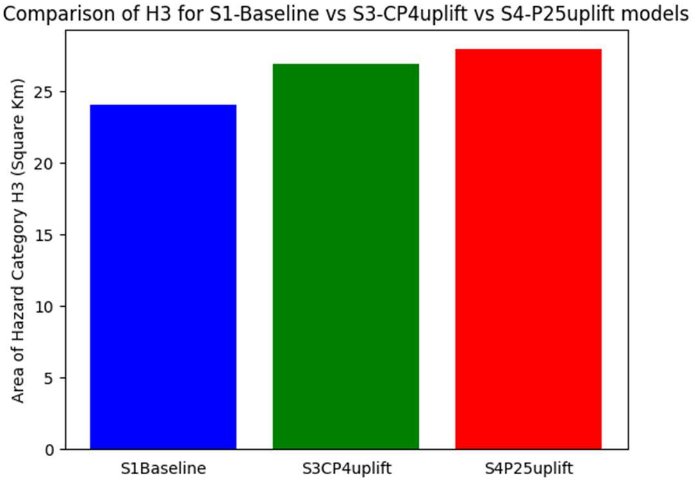

Figure 90. Comparison of Hazard Vulnerability Classification, H3 for S1-Baseline model vs S3-CP4uplift model vs S4-P25uplift model.

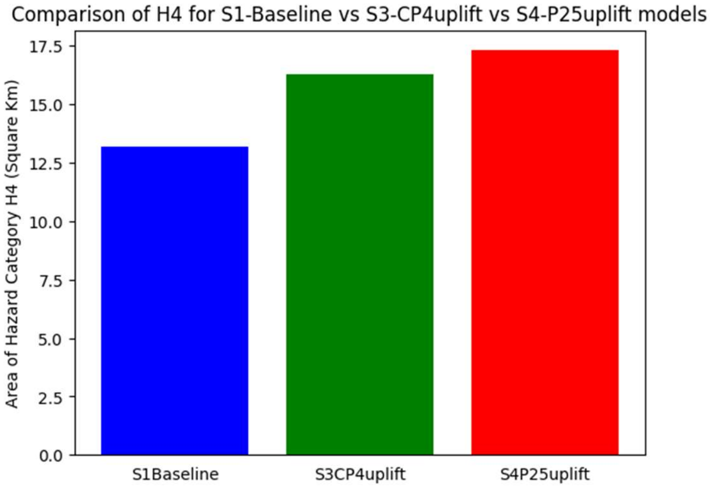

Figure 91. Comparison of Hazard Vulnerability Classification, H4 for S1-Baseline model vs S3-CP4uplift model vs S4-P25uplift model.

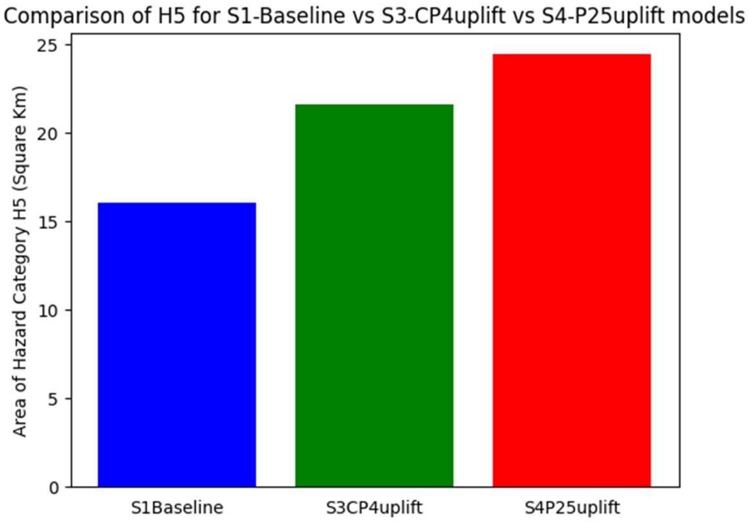

Figure 92. Comparison of Hazard Vulnerability Classification, H5 for S1-Baseline model vs S3-CP4uplift model vs S4-P25uplift model.

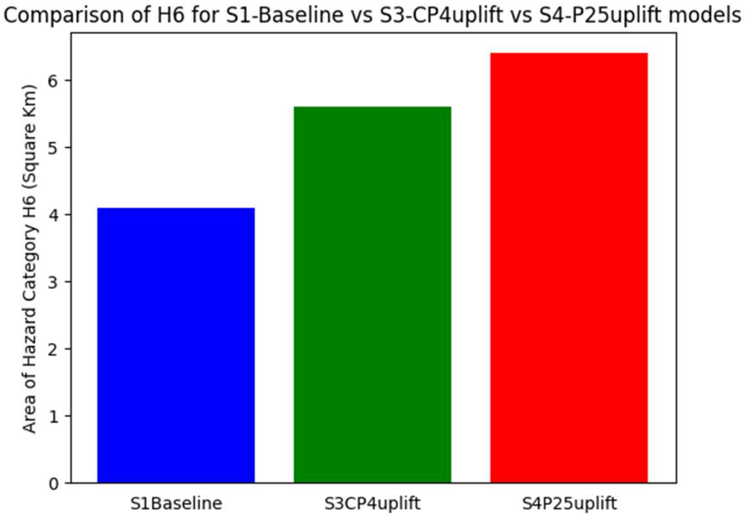

Figure 93. Comparison of Hazard Vulnerability Classification, H6 for S1-Baseline model vs S3-CP4uplift model vs S4-P25uplift model.

8.4 Discussion of study in the context of wider literature

Digital Elevation Models (DEMs) are used for a wide range of applications, including hydrology and water resources, geology and geomorphology, civil engineering projects, vegetation survey, glaciology, volcanology and modelling natural hazards such as flooding, landslides and coastal inundation (Bamber, 1994). (Carabajal and Harding, 2005) validated the SRTM DEM using ICESat, a satellite laser altimeter, and discovered that the errors in SRTM increased with increasing tree cover. This was because the C-band radar used by SRTM could not fully penetrate the vegetation canopy to the ground. (Berry et al., 2007) utilised satellite radar altimeters to validate the SRTM DEM and supports the findings of (Carabajal and Harding, 2005).

(O'Loughlin et al., 2016) developed the first global 'Bare-Earth' Digital Elevation Model (DEM) based on the Shuttle Radar Topography Mission (SRTM) for all landmasses between 60N and 54S. The new 'Bare-Earth' SRTM DEM combines multiple remote sensing datasets, including point-ground elevations from NASA's laser altimeter ICESat, a database of percentage of tree cover from the MODIS satellite as a proxy for penetration depth of SRTM and a global vegetation height map in order to remove the vegetation artefacts present in the original SRTM DEM. The final 'Bare-Earth' SRTM product showed global improvements greater than 10 m in the bias over the original SRTM DEM in vegetated areas compared with ground elevations determined from ICESat data with a significant reduction in the root mean square error from over 14 m to 6 m globally.

(Zhao et al., 2018) used a linear regression based method to estimate the original SRTM DEM error and therefore corrected the SRTM DEM data. The results showed that the original SRTM DEM data is around 6 m higher than the actual land surfaces on average across all vegetation types. (Yamazaki et al., 2017) Introduced a high-accuracy global DEM at 3″ resolution (~90 m at the equator) by eliminating major error components from existing DEMs. The study separated absolute bias, stripe noise, speckle noise, and tree height bias of the original SRTM DEM by using multiple satellite data sets and filtering techniques to create the Multi-Error-Removed Improved-Terrain DEM (MERIT). After the error removal, land areas mapped with ±2 m or better vertical accuracy were increased from 39% to 58%. Significant improvements were found in flat regions where height errors larger than topography variability, and landscapes such as river networks and hill-valley structures, became clearly represented. The newly developed MERIT DEM has enhanced many geoscience applications which are terrain dependent.

The previous studies dealt only with vegetation biases and do not develop methodologies for the correction or removal of biases due to built structures in urban areas. Despite recent advances in developing vegetation corrected DEMs, the effect of building height errors in DEMs in urban areas are still poorly understood, and their correction remains a challenge. This study presents the first urban corrected global DEM using building density data, locally for Nairobi, Kenya. By comparing six global DEMs (SRTM, MERIT, AW3DD30, NASADEM, TanDEM-X 12 m, and TanDEM-X 90 m DEM) with a local reference DEM for the study area, a relationship is established between building density, derived from urban footprint map of the study area, and DEM error.

The results reveal a linear relationship between building density and DEM error for SRTM; MERIT; AW3DD30; NASADEM; TanDEM X 12 m and TanDEM X 90 m, which have building errors of 2.2 m, 5.0 m, 1.2 m, 4.5 m, 3.0 m and 3.3 m, respectively. A building density raster was created for the global DEMs using the building density – DEM error relationships, and then subtracted from the original DEMs to create a new urban-corrected DEM for the study area. A comparison of error statistics of the global DEMs, before and after urban correction, reveal an important improvement in the mean average error (MAE), root mean square error (RMSE), and standard deviation (SD) of the corrected DEMs. In urban flood modelling, there are often significant negative impacts of overestimating actual ground surfaces due to building density errors inherent in global DEMs. Therefore, the work on urban DEM correction will enable the development of more accurate flood models in urban areas and provide a template to scale up the methodology described in this study for global application.

Climate change and urbanization pose significant threats for flooding and water quality in urban areas (Miller and Hutchins, 2017). Changes to the timing and magnitude (depth) of rainfall events as a result of climate change are predicted to significantly alter the flooding experienced in many urban areas of the world and without suitable mitigation lead to increased future flood risk and associated damages (Wheater and Evans, 2009). Previous studies (Ashley et al., 2005a, Arnbjerg-Nielsen et al., 2013, Jung et al., 2014, Yazdanfar and Sharma, 2015, Miller and Hutchins, 2017, Yang et al., 2021) have investigated the impacts of urban developments on hydrological runoff and urban flood volumes in major cities, and compared the impacts of urbanization with the effects induced by climate change. (Zhou et al., 2019) found that urbanization led to an increase in annual surface runoff by 208 to 413% and by comparing the impacts of urbanization and climate change on urban runoff and flood volumes, highlighted the importance for re-assessment of current and future urban drainage in coping with the changing urban floods induced by local and large-scale changes.

(Liu et al., 2022) found in general, that urbanization contributed greater to the nonstationarity of extreme precipitation than climate change in the majority of the study area whilst (Ashley et al., 2005b) found that flood risks in urban areas due to climate change and urbanization may increase by a factor of almost 30 times and that traditional engineering measures alone are unlikely to be able to provide protection against loss of lives, properties and infrastructure. (Rangari et al., 2019) using similar HEC-RAS 2D hydraulic model used in this study, identified 17% of total study area to be liable to foods out of which 9% area are classified as high risk, with 52% area showing as medium risk and remaining 35% area falling under low risk of flooding. In this study, a comparison of the flood hydrographs for the S1-Baseline model, S3-CP4uplift model and the S4-P25uplift model is shown in Figure 85. The result show that climate change rainfall used in the S3-CP4uplift model and the S4-P25uplift model has a significant effect on flood extent and flood depth.
When comparing the S1-Baseline model with the S4-P25 model, the increase in peak flowrate is more pronounced with a sharp increase in peak flowrate of up to 67%. Figure 86 and Figure 87 show the change in Hazard Vulnerability Classification when the S1-Baseline model is compared to the S3-CP4uplift model and the S4-P25uplift model respectively. The results show the climate change models (S3-CP4uplift and S4-P25uplift) have higher hazard vulnerability thresholds when compared to the S1-Baseline model. The result show that climate change will create severe impacts resulting in more flooding in urban areas. The results show the S4-P25uplift climate change model with higher hazard levels and an indication that the extent and scale of the flood forecasting in urban areas will depend on the climate model simulation considered and used in the hydraulic flood model. A comparison of the six hazard vulnerability classification for the S1-Baseline model with the S3-CP4uplift and S4-P25uplift climate models is shown in Figure 88, Figure 89, Figure 90, Figure 91, Figure 92, and Figure 93,

A review of current literatures and studies has shown there is a large body of literature on the impacts of climate change on flooding and water quality but that specific literature on urban areas and urban impacts is less well covered, and specifically that the combined pressures are less researched. A vast number of numerical models have evolved over the past few years which are capable of simulating urban flooding; with the majority of these models available on commercial basis only, rigorous and require extensive dataset, high computational efficiency etc to run and generate precise, accurate and reliable results. This thesis has subsequently enhanced our understanding of the value of free global hydrological and hydraulic models developed at city-scale to model the impacts of climate change and land use change on urban pluvial flood hazard in data-sparse context of rapidly developing cities where availability of high-quality data for urban flood studies are a rarity.

The study has shown that it is possible to leverage the opportunities provided by the growing availability of free, global datasets to develop urban flood models. Traditional urban flood models rely on the use of high-quality datasets as key input data and require computers with high computational efficiency to run detailed flood inundation models. A trade-off is achieved between complexity and resolution by the use of simplified 2D hydraulic flood models that use global dataset as key input data.

8.5 Summary

Global DEMS are extensively used for flood modelling and both vertical height error and spatial resolution of DEMs can impact on flood inundation depth and extent, especially in urban areas (Chen and Hill, 2007). However, in chapter 4 of this study, I identified there is a major limitation to using these datasets in urban areas. I set out to correct these errors by developing a methodology for building error correction that can be applied to any other case study, where building density data and a local reference DEM data of vertical height accuracy higher than the global DEMs are available.

I quantified the building error for the city of Nairobi, Kenya for six of the most widely used global DEMs: SRTM; MERIT; ALOS; NASADEM; TanDEM-X 12 m; and TanDEM-X 90 m. The results show building error at highest building density varying between 1.25 m and 5.07 m for the DEMs used. I found the MERIT DEM with the smallest vertical height deviation from the reference DEM, with an SD of 2.97 m, followed by TanDEM-X 12 and TanDEM-X 90 (3.03 m and 3.29 m respectively). In chapter 5, I ran two specific (S1-Baseline and S5-RawDEM) model scenarios to understand the implications of DEM correction for flood modelling. The results show that there's a similarity in the volume of water in the two models and very similar level of runoff including both models achieving peak flowrate of 1,649 m3 1,685 m3 for S1-Baseline and S5-RawDEM respectively, near about the same time (19:25 hrs) on March the 5th 2018 Figure 74.

I compared the hazard vulnerability classification for the two models and found the hazard vulnerability classification for the S5-RawDEM to be slightly higher than the S1-Baseline model across all the six hazard measurement thresholds, H1 to H6, due to the different flow paths internally in the uncorrected DEM fused into the S5-RawDEM and leading to these errors. By comparing the flood heights at flooding hotspots sites in Nairobi, Kenya for the S1-Baseline Model and S5-RawDEM, I found that the S5-RawDEM has a higher margin of deviation than the S1-Baseline model when both models are compared to the survey reference data. The results show that the S5-RawDEM model is slightly less accurate by over-predicting the flood extent and flood depth, hence, the flood vulnerability classification. While these are meaningful reductions in error, they do not necessarily translate to better flood modelling.

In order assess the impact of climate change and land use change on pluvial flood hazard in urban areas using global datasets, in Chapter 6, I created and processed five modelling scenarios using the HEC-HMS hydrologic and HEC-RAS 2D hydraulic models: a baseline model (S1-Baseline), 2000LU model, S3-CP4uplift model, S4-P25uplift model, and the S5-RawDEM model. The five sets of models are created in 2D and make use of the diffusive wave equation of the HEC-RAS model for simplification. The results of the models show a lot of promises by justifying the hypothesis that urban flood models built at city-scale level using free global datasets have a good level of skill and proficient enough to accurately estimate urban flood inundation depth and extent in rapidly developing cities characterised by sparsity of data. A comparison of the results of the five sets of with flood height data taken from actual flooding hotspots sites across Nairobi, show that the models have a good level of accuracy that can be relied upon for urban flood modelling.

I quantified the impact of land use change and climate change on urban pluvial flood hazard by using hazard vulnerability curve and classification factors adapted from (Smith et al., 2014). A hazard vulnerability factor of between H1 and H6 is used in the assessment by, first, quantifying the defined flood event using the HEC-RAS model. Second, quantify the flood hazard by using a combination of flood depth and flood velocity to quantify the flood hazard to people, buildings and infrastructure etc. The result show that climate change rainfall data used in the S3-CP4uplift model and the S4-P25uplift model have a significant effect on flood extent, flood depth and velocity. There is a sharp increase in peak flowrates peak flowrates to up to 55% when comparing S1-Baseline model to the S3-CP4uplift model and up to 67% increase when comparing the S1-Baseline model with the S4-P25 climate model. When comparing the change in hazard vulnerability classification of the S1-Baseline model with the S3-CP4uplift and S4-P25uplift climate models, the results show the climate change models (S3-CP4uplift and S4-P25uplift) have significantly higher hazard vulnerability thresholds than the S1-Baseline model.

9.0 CONCLUSIONS AND RECOMMENDATIONS

City-scale hydrodynamic models that can effectively utilise limited data and have an appropriate computation time that allows for simulations of the impacts of land use change and climate change on urban pluvial flooding are needed to improve our understanding of the flood hazard in data-sparse area in rapidly developing cities, which are often the most at-risk areas. To this end, this thesis aims to assess the skill of a hydrodynamic model built at the city-scale scale for a large city catchment, before investigating the impact of climate change, land use change and urban corrected DEM on flood predictions and how the hazard vulnerability relating to the impacts of these factors can be quantified. The following section will summarise the conclusions from each results chapter that addresses each objective in turn. The key conclusions and implications from this research are as follows:

The five models (S1-Baseline; S2-2000SU; S3-CP4uplift; S4-P25uplift; S5-RawDEM) were verified by visually and qualitatively analysing topographic survey data collected from historic flood hotspots sites in Nairobi, Kenya. It was determined that the HEC-RAS 2D models created within this study is sufficiently accurate at representing realistic conditions of flood extent under extreme weather events and can be a useful tool in predicting the location and severity of future flooding events.

Sophisticated full SWE-based models require high-quality data for representing urban features, such as buildings and a computational cost that is significant. Full 2D shallow water models are considered not feasible for calculations in very large-scale catchments with fine resolution grids because of the simulation time required. Simplified SWE-based models such as the diffusive wave equation (diffuse solver) of the HEC-RAS model used in this study, are less computationally expensive compared to full 2D shallow water equation models because of the simplification or omission of certain hydraulic processes. This study has shown that it is possible to undertake city-scale urban flood modelling by using simplified SWE models (diffusive wave equation) that require coarse global datasets whilst achieving a balance of computational efficiency and accuracy.

Open-access global DEMs are not only useful datasets for estimating flood risks, but they also provide baseline data for flood studies. Despite significant advances in developing vegetation corrected DEMs, there is still a limited understanding of DEM errors that can be attributed to building heights and building density in urban areas. Current global DEMs are not corrected for building errors. Because building height data is unavailable on a global scale, this paper addresses errors due to building density biases. As part of this research, a methodology for building error correction in urban DEMs was developed and applied to the case study city. The building error for the city of Nairobi, Kenya was quantified for six of the most widely used global DEMs: SRTM; MERIT; ALOS;

NASADEM; TanDEM-X 12 m; and TanDEM-X 90 m. The results show building error at highest building density varying between 1.25 m and 5.07 m for the DEMs used. The results showed the MERIT DEM with the smallest vertical height deviation from the reference DEM, with an SD of 2.97 m, followed by TanDEM-X 12 and TanDEM-X 90 (3.03 m and 3.29 m respectively). In addition, if the RMSE metric of the errors is considered alongside mean and median values, MERIT still provides the lowest overall values and highest accuracy. A plausible explanation for its higher accuracy is that the MERIT DEM is a multiple error-reduced improved version of SRTM with tree height bias, stripe noise, absolute bias, and speckle noise removed.

By deriving a relationship between DEM error and building density, the building error associated with the global DEMs were evaluated and corrected. It was found that there is a linear and positive, but noisy relationship between DEM error and building density. All the DEMs show a noisy relationship; with SRTM having the noisiest and TanDEM-X 12 m & 90 m DEMs the least noisy. The findings show that the removal of building density error from global DEMs resulted in the improvement of the vertical height accuracy of the global DEMs of up to 45% for MERIT and 40% for ALOS. Thus, the results show that global DEMs can be usefully corrected for building density errors in urban areas, even where specific building height data are not available. The results of the work on the urban correction of global DEMs for the Central Business District (CBD) area of Nairobi, which is characterized by taller buildings and high building density show the error parameters in the CBD area is between 15 to 45 % higher than those of the Nairobi city wide area for the six global DEMs. These results provided some further insights into significance of building heights contributing to errors in global DEMs. Therefore, future work is required to understand the nature of building height errors in global DEMs and how these errors can be corrected.

The results of comparing the flood inundation maps for S1-Baseline model that uses a corrected version of the MERIT DEM with the S5-RawDEM model with the “raw” DEM as input data show that the hydraulic modelling outputs obtained from urban corrected global DEMs using the approach described extensively in Chapter 4 of this Thesis have a higher vertical accuracy than the latter, Table 53. It is evident that the accuracy of flood inundation maps can be improved modestly by using urban corrected DEMs over raw DEMs as key input data when conducting both hydrological and hydraulic modelling. Therefore, by using the approach developed for urban correction of global DEMs in this study, it is possible to obtain more accurate flood maps from less accurate global topographic data in areas where LiDAR or any other form of accurate topography information is not available.

Land use change due to urbanisation and climate change were found to be contribute significantly to surface water runoff and exacerbate urban flooding. However, it is found that climate change, rather than land use change is a bigger threat to urban flooding. Specifically, the effects induced by climate change under the CP4 and P25 climate rainfall models are much higher than the effects induced by land use change due to urbanisation in Nairobi from 2000 to 20020. Therefore, it is found that changes caused by current and future changes in rainfall intensities and frequencies are most likely to render most large urban areas vulnerable to extreme rainfall and pluvial flooding due to lack of resilience in existing drainage infrastructure and flood mitigation system. Assessment of land use changes alone cannot fully account for hydrological and hydraulic alterations in the urban context and it is important for policy makers and people with responsibilities for managing urban flood risks to consider adaptation and mitigation strategies that considers increasing threat of urban flooding emanating from increased runoff from climate change rainfall.The HEC-HMS and HEC-RAS models were found to be capable of resolving to predict flood effects coupled with the QGIS for hydrologic risk management

Finally, one of the key findings of this study is that in the context of conducting urban flood modelling in data sparse regions in rapidly developing cities across the world, it is possible to leverage on the opportunities provided by the growing availability of free, global datasets to develop urban flood models. Most urban flood models rely on the use of high quality datasets as key input data and require computers with high computational efficiency to run flood inundation models.
Most importantly, this research demonstrated that it is possible to achieve the right balance between computational efficiency and accuracy by the use of simplified urban flood models that use global dataset as key input data.

9.1 Reflection of study objectives

There is lack of adequate research focused on the impact of building density on the vertical accuracy of global DEMs and how these errors can be assessed and corrected especially for urban areas. This research managed to address this research gap by deriving a methodology for correcting building errors in freely available global DEMs with Nairobi, Kenya as a case study and that can be applied to any other case study anywhere in the world where building density data and local reference DEM data are available. To derive urban corrected DEMs with global datasets using Nairobi as a test city, raster data for six global DEMs were pre-processed, resampled and DEM error for six global DEMs were calculated using QGIS raster algebra tools to determine the vertical accuracy for the six global DEMs followed by the creation DEM error versus building density relationships. The error relationships were applied to the original global DEMs for Nairobi to correct the DEMs for building density errors.

This research managed to identify global datasets especially remote sensing-based sources for: climate change rainfall, digital elevation model (DEM), and urban land use etc. global datasets required to build a city scale hydrodynamic models for assessing the impact of climate change and urbanization on urban pluvial flooding. In order to build and run the appropriate city scale numerical hydrological and hydraulic models used in this study, the research identified physical processes that are required that are required in building a hydrodynamic model including model set up, calibration, appropriate application scale, computational speed, analysis of model outputs and validation of model results.

At the end of this study, a city scale hydrodynamic model that assesses the impacts of climate change and land use change (urbanization) on urban pluvial flooding was developed using Nairobi, Kenya as a test location. The extent of the model built involved the creation of five sets of model scenarios for the urban corrected MERIT DEM including model representations for urban corrected SRTM, TanDEM X 12m and 90m DEMs, the NASADEM DEM, ALOS DEM and the local JICA reference DEM. Validation of the models was undertaken by comparing results from the models with historical flooding observations at three flooding hotspots site across Nairobi. The results of the validation show urban flood models that uses global DEMs as key input data can be a useful, accurate and reliable tool for modelling the impacts of climate change and land use change on urban pluvial flooding at a city scale setting.

9.2 Summary

The key summary from this research are as follows:

- Identification of global datasets and hydraulic models that could be used for city scale modelling of pluvial flood hazard in data scarce areas using global datasets
- Derivation of urban corrected DEMs with global datasets using Nairobi as a test city
- Building and testing a city scale urban pluvial flood model with global datasets using Nairobi as a test city

9.3 Research contribution to science and literature

The key contribution of this research to science, current state of knowledge and its implications on the current state of knowledge in the field of urban flood studies are set out in the following subsections.

9.4 Computational efficiency of 2D city-scale hydraulic flood models that use global datasets as key input data.

The results show that in the context of conducting urban flood modelling in data sparse regions in rapidly developing cities across the world, it is possible to leverage the opportunities provided by the growing availability of free, global datasets to develop urban flood models. Most urban flood models rely on the use of high quality datasets as key input data and require computers with high computational efficiency to run flood inundation models. Most importantly, this research demonstrated that it is possible to achieve the right balance between computational efficiency and model accuracy by the use of coarse, free global datasets as key input data for use in simplified urban flood models.

The results of the flood inundation depths of the five sets of hydraulic models show a lot of promises for the future of urban flood modelling in data sparse contexts that rely on the use of free, global datasets of coarse resolution. The results show that the five sets of models (S1-Baseline; S2-2000SU; S3-CP4uplift; S4-P25uplift; S5-RawDEM) developed in this study are computationally efficient and highly accurate when compared with measured data. The results show that the (S1-Baseline; S2-2000SU; S3-CP4uplift; S4-P25uplift; S5-RawDEM). The validation of the results of the 2D hydraulic models show the flood inundation depths and flood extent at the selected flooding hotspots are comparable with real life flooding scenarios experienced across the sites. The results of this study show that city planners with responsibilities for managing urban flood risk can focus particularly on the full exploitation of the benefits of urban flood models that use free, global data sets.

9.5 Urban correction of global DEMs

Urban flood models that use ground height surface models such as Digital Elevation Models (DEMs) for prediction of flood inundation rely on the accuracy of the DEMs for predicting flood events, extent and depth. Global DEMs have a significant influence on the outcome of flood modelling and the higher the vertical accuracy of the DEM, the better are the results of the flood model. Local DEMs that are based on airborne light detection and ranging (LiDAR) are preferential over open access, global DEMs due of their superior vertical accuracy, horizontal resolution, and ability to distinguish between 'bare earth' from built structures and vegetation.

Global DEMs suffer from many different types of errors, some of which are significant at local scales; for example, (Rodríguez et al., 2006) reported a global mean and standard vertical height error of 8.2 ± 0.7 and 6.9 ± 0.5 m for SRTM X- and C-band data, respectively. There is a number of published work on the correction of errors in global DEMs, especially vegetation errors. (Falorni et al., 2005, Bhang et al., 2007, Dong et al., 2015, Gallant et al., 2012, Baugh et al., 2013, O'Loughlin et al., 2016, Chen et al., 2018). Although many studies (Robinson et al., 2014, Yamazaki et al., 2012, Yamazaki et al., 2017) have developed new vegetation-corrected DEMs, by either editing or adjusting existing global DEMs. However, despite significant advances in developing vegetation-corrected DEMs, there is limited understanding of DEM errors that can be attributed to building heights and building density in urban areas. This study created the first urban corrected global DEM using building density data, locally for Nairobi, Kenya. The work on urban DEM correction would allow more accurate flood models in urban areas and provide a template to scale up the methodology described in this thesis for global application. The work on urban correction of global DEMs using building density data for Nairobi, Kenya is published in the Earth Science Informatics Journal (Olajubu et al., 2021).

9.6 Contribution to thinking around urban flood projections using future climate change precipitation dataset

The results of the models on the impacts of urbanization and climate change on pluvial flooding is found to be consistent with science (literatures) on future pluvial flooding across the globe. This study will provide medium-high confidence of evidence that urban pluvial flooding is set to increase and worsen due to the effects of climate change and rapid urbanisation. There is overall lack of globally focussed research into the combined pressures of rapid urbanisation and climate change. For example, while localised flood risk assessments are carried out there is a lack of suitable climate model precipitation outputs and consideration of uncertainty.

Climate change and urbanization pose significant threats for flooding and water quality in urban areas (Miller and Hutchins, 2017). City planners and engineers from time to time seek up to date information on planning and designing new hydraulic-conveyance and flood water control facilities to prepare for and respond to floods. Historical hydrologic and hydraulic data for the catchment can be a good starting point for developing models that can predict the behavior of urban runoff under different scenarios. However, with the current limitations of inadequate credible, future climate change precipitation data, developers of urban flood models are increasingly faced with developing reliable urban flood models that take into account the change that has not yet taking place with the catchment. There is lack of city-scale assessments of the negative impacts of climate change and urbanization on pluvial flooding in rapidly developing cities across the globe. The findings of this research, specifically, results of the CP4 and P25 future climate models will provide city planners and officials ability to strategically plan flood mitigation measure and design effective flood management system that takes into account the impact of future climate change and urbanization/land use change.

9.7 Quantification of Vulnerability of People and Built Environment to Urban Flood Hazard

The use of the Hazard Vulnerability Classification adapted from (Smith et al., 2014) for use in this study has shown that, open access derived urban models can be a useful tool in identifying urban flood hazards that have the potentials of leading to loss of life, injury and economic loss caused by future flood events that's due to climate change and land use change. This study has shown how the degree of hazard varies with the severity of flooding and how flood hazard in urban areas is affected by flood behaviour i.e. flood extent, depth, velocity, topography. This study will be useful in providing vital information on the scale, and the drivers (climate change and land use change) for urban flood hazard to people, vehicles, buildings and the built environment. This work would influence decisions in urban flood risk management and aid in devising mitigation measures that may be considered at city-scale level to manage the risk.

9.8 Study Limitations and Recommendations for Future Research

The HEC-RAS 2D hydraulic model used in this study adopts the use of use of the diffusive wave approximation approach in undertaken flood inundation modelling by use of coarse, free global datasets. Consideration should be given to undertaking further research into the use of high quality local datasets if datasets become available in the future at city-scale level. The developments of such models with high quality data will create and provided opportunities to compare and contrast the level of accuracy of the two different sets of models.

Nairobi, similar to other rapidly developing cities of the world faces challenges in relation to solid waste management. Increasing urbanization, rural-urban migration, rising standards of living and rapid development associated with population growth have resulted in increased solid waste generation. The city produces more solid waste than its collection and disposal systems can handle. Approximately a third of the city's waste is collected. The city's only official dumpsite Dandora is at overcapacity. The majority of waste is dumped in illegal dumpsites Nairobi produces approximately 2,475 tonnes of waste each day. While 95% of Nairobi's waste is potentially reusable, only 5% of waste is recycled. Moreover, only 33 per cent of waste produced is collected for disposal at Nairobi's only official dumpsite, Dandora. The rest is dumped illegally in dumpsites, is left next to houses, or burned. Improperly disposed of waste is often collected by both natural and engineered storm water drainage systems resulting in blockages compounding the problems of frequent urban flooding witnessed in the city. Waste production and waste management in Nairobi is a severe challenge by international standards according to available data (ULA, 2021).

When compared to cities of similar population size, Nairobi generates 50% more than Addis Ababa and 30% more than Dar es Salaam. The city generates more waste than its income levels would suggest, and its production per day per capita is expected to grow by nearly 70% by 2030 (ULA, 2021). The scope of this research is limited to the city scale modelling of factors of land use change and climate change on urban pluvial flooding in rapidly developing cities. However, given the prevalent nature of problems of poor solid waste management in majority of rapidly developing cities in the world and how the significant role they play in exacerbating urban flooding by blocking both natural and engineered drainage network systems, it is recommended that future research be conducted into adding the factor of poor solid waste management into the 2D hydraulic modelling developed in this study.

The work on urban correction of global DEMs described in Chapter 4 of this study is currently limited to the use of building density data and global DEMs. Building height data are currently unavailable at global scale level and it is anticipated that once building height data becomes globally available, the urban correction of global DEMs can be extended to the use of not only building density data but equally building height data.

The scope of this research is limited to the use of recent and historic land use datasets to develop the land use change models. The results of the simulation are very promising in simulating the impact of past land use change on urban flooding at city-scale level. However, the development of urban flood models that use projected/future land use change models at city-scale similar to the future climate change rainfall model used in this study would be beneficial for future research.

Flood hazard assessment is a key input to the understanding of flood risk. This study is limited to the city-scale modelling of factors affecting urban pluvial flood hazard by focusing on the assessment of the sources of potential harm of urban pluvial floods to people and the built environment. It is recommended that future study on urban pluvial flooding focus on the flood risks that come from exposing people, communities and the built environment to that hazard.

10.0 REFERENCES

ABDELLATIF, M., ATHERTON, W. & ALKHADDAR, R. 2014. Assessing combined sewer overflows with long lead time for better surface water management. *Environmental Technology,* 35**,** 568-580.

ACHARYA, T., YANG, I. & LEE, D. 2018. Comparative analysis of digital elevation models between AW3D30, SRTM30 and airborne LiDAR: A case of chuncheon, South Korea. *Journal of the Korean Society of Surveying Geodesy Photogrammetry and Cartography,* 36**,** 17-24.

AERTS, J. C. J. H., BOTZEN, W. J. W., EMANUEL, K., LIN, N., DE MOEL, H. & MICHEL-KERJAN, E. O. 2014. Evaluating Flood Resilience Strategies for Coastal Megacities. *Science,* 344**,** 473-475.

ALGANCI, U., BESOL, B. & SERTEL, E. 2018. Accuracy Assessment of Different Digital Surface Models. *ISPRS - International Archives of the Photogrammetry, Remote Sensing and Spatial Information Sciences,* 7.

AMNESTY-INTERNATIONAL 2019. Kenya: The Unseen Majority: Nairobi's Two Million Slum-Dwellers. *Amnesty International Publications: London, UK***,** 3.

APEL, H., ARONICA, G. T., KREIBICH, H. & THIEKEN, A. H. 2009. Flood risk analyses—how detailed do we need to be? *Natural Hazards,* 49**,** 79-98.

ARNBJERG-NIELSEN, K., WILLEMS, P., OLSSON, J., BEECHAM, S., PATHIRANA, A., BÜLOW GREGERSEN, I., MADSEN, H. & NGUYEN, V.-T.-V. 2013. Impacts of climate change on rainfall extremes and urban drainage systems: a review. *Water Science and Technology,* 68**,** 16-28.

ARNELL, N. W., HALLIDAY, S. J., BATTARBEE, R. W., SKEFFINGTON, R. A. & WADE, A. J. 2015. The implications of climate change for the water environment in England. *Progress in Physical Geography: Earth and Environment,* 39**,** 93-120.

ASHLEY, R., BALMFORTH, D., SAUL, A. & BLANSKBY, J. 2005a. Flooding in the future--predicting climate change, risks and responses in urban areas. *Water science and technology : a journal of the International Association on Water Pollution Research,* 52 5**,** 265-73.

ASHLEY, R. M., BALMFORTH, D. J., SAUL, A. J. & BLANSKBY, J. D. 2005b. Flooding in the future – predicting climate change, risks and responses in urban areas. *Water Science and Technology,* 52**,** 265-273.

BALL, J., BABISTER, M., NATHAN, R., WEEKS, W., WEINMANN, E., RETALLICK, M. & TESTONI, I. 2019a. Australian Rainfall and Runoff: A Guide to Flood Estimation 2019.

BALL, J., BABISTER, M., NATHAN, R., WEEKS, W., WEINMANN, E., RETALLICK, M. & TESTONI, I. 2019b. *Australian Rainfall and Runoff: A Guide to Flood Estimation, Commonwealth of Australia*.

BAMBER, J. L. 1994. A digital elevation model of the Antarctic ice sheet derived from ERS-1 altimeter data and comparison with terrestrial measurements. *Annals of Glaciology,* 20**,** 48-54.

BATES, P. D., HORRITT, M. S. & FEWTRELL, T. J. 2010. A simple inertial formulation of the shallow water equations for efficient two-dimensional flood inundation modelling. *Journal of Hydrology,* 387**,** 33-45.

BAUGH, C. A., BATES, P. D., SCHUMANN, G. & TRIGG, M. A. 2013. SRTM vegetation removal and hydrodynamic modeling accuracy. *Water Resources Research,* 49**,** 5276-5289.

BERRY, P. A. M., GARLICK, J. D. & SMITH, R. G. 2007. Near-global validation of the SRTM DEM using satellite radar altimetry. *Remote Sensing of Environment,* 106**,** 17-27.

BHANG, K. J., SCHWARTZ, F. W. & BRAUN, A. 2007. Verification of the Vertical Error in C-Band SRTM DEM Using ICESat and Landsat-7, Otter Tail County, MN. *IEEE Transactions on Geoscience and Remote Sensing,* 45**,** 36-44.

BORNEMANN, F. J., ROWELL, D. P., EVANS, B., LAPWORTH, D. J., LWIZA, K., MACDONALD, D. M. J., MARSHAM, J. H., TESFAYE, K., ASCOTT, M. J. & WAY, C. 2019. Future changes and uncertainty in decision-relevant measures of East African climate. *Climatic Change,* 156**,** 365-384.

BRAUD, I., BREIL, P., THOLLET, F., LAGOUY, M., BRANGER, F., JACQUEMINET, C., KERMADI, S. & MICHEL, K. 2013. Evidence of the impact of urbanization on the hydrological regime of a medium-sized periurban catchment in France. *Journal of Hydrology,* 485**,** 5-23.

BUCKLEY, S. M., AGRAM, P.S., J. E. BELZ, R. E. CRIPPEN, E. M. GURROLA, S., HENSLEY, M. K., M. LAVALLE, J. M. MARTIN, M. NEUMANN, Q. D. NGUYEN, & P. A. ROSEN, J. G. S., M. SIMARD, W. W. TUNG 2020. Nasadem Userguide Version 1.

BURROUGH, P. A. 1986. *Principles of geographical information systems for land resources assessment,* Oxford, Clarendon.

CAGLAR, B., BECEK, K., MEKIK, C. & OZENDI, M. 2018. On the vertical accuracy of the ALOS world 3D-30m digital elevation model. *Remote Sensing Letters,* 9**,** 607-615.

CARABAJAL, C. C. & HARDING, D. J. 2005. ICESat validation of SRTM C-band digital elevation models. *Geophysical Research Letters,* 32.

CASAS, A., BENITO, G., THORNDYCRAFT, V. R. & RICO, M. 2006. The topographic data source of digital terrain models as a key element in the accuracy of hydraulic flood modelling. *Earth Surface Processes and Landforms,* 31**,** 444-456.

CHEN, H., LIANG, Q., LIU, Y. & XIE, S. 2018. Hydraulic correction method (HCM) to enhance the efficiency of SRTM DEM in flood modeling. *Journal of Hydrology,* 559**,** 56-70.

CHEN, J., CAO, X., PENG, S. & REN, H. 2017a. Analysis and Applications of GlobeLand30: A Review. *ISPRS International Journal of Geo-Information,* 6**,** 230.

CHEN, J. & HILL, A. 2007. MODELING URBAN FLOOD HAZARD: JUST HOW MUCH DOES DEM RESOLUTION MATTER? *Applied Geography* 30**,** 8.

CHEN, J., THELLER, L., GITAU, M. W., ENGEL, B. A. & HARBOR, J. M. 2017b. Urbanization impacts on surface runoff of the contiguous United States. *Journal of Environmental Management,* 187**,** 470-481.

CHINI, M., PELICH, R., HOSTACHE, R., MATGEN, P. & LOPEZ-MARTINEZ, C. 2018. Towards a 20 m Global Building Map from Sentinel-1 SAR Data. *Remote Sensing,* 10**,** 1833.

CHOWDHURY, M. A. H. & AKTER, A. 2021. City scale urban flood modelling and mapping. *Proceedings of the Institution of Civil Engineers - Water Management,* 0**,** 1-18.

CHOY, A. 2018. Better forecast, better preparedness – investing in improved weather services. *World Bank Blog* [Online].

CHRISTENSEN, J. H., HEWITSON, B., BUSUIOC, A., CHEN, A., GAO, X., HELD, I., JONES, R., KOLLI, R. K., KWON, W.-T., LAPRISE, R., MAGAÑA RUEDA, V., MEARNS, L., MENÉNDEZ, C. G., RÄISÄNEN, J., RINKE, A., SARR, A. & WHETTON, P. 2007. Regional Climate Projections. In: Climate Change 2007: The Physical Science Basis. Contribution of Working Group I to the Fourth Assessment Report of the Intergovernmental Panel on Climate Change [Solomon, S., D. Qin, M. Manning, Z. Chen, M. Marquis, K.B. Averyt, M. Tignor and H.L. Miller (eds.)]. Cambridge, United Kingdom & New York, NY, USA.: .

COLLINS, M. R., KNUTTI, R., ARBLASTER, J., DUFRESNE, J.-L., FICHEFET, T., FRIEDLINGSTEIN, T., GAO, X., GUTOWSKI, W. J., JOHNS, T., KRINNER, G., SHONGWE, M., TEBALDI, C., WEAVER, A. J. & WEHNER, M. 2013. Long-term climate change: Projections, commitments and irreversibility. *In: Climate Change 2013: The Physical Science Basis. Contribution of Working Group I to the Fifth Assessment Report of the Intergovernmental Panel on Climate Change.* . Stocker TF, Qin D, Plattner G-K et al. (eds). .

COOK, K. H. & VIZY, E. K. 2013. Projected Changes in East African Rainy Seasons. *Journal of Climate* 26**,** 5931-5948.

COSTABILE, P., COSTANZO, C., FERRARO, D., MACCHIONE, F. & PETACCIA, G. 2020. Performances of the New HEC-RAS Version 5 for 2-D Hydrodynamic-Based Rainfall-Runoff Simulations at Basin Scale: Comparison with a State-of-the Art Model. *Water,* 12**,** 2326.

COURTY, L. G., RICO-RAMIREZ, M. Á. & PEDROZO-ACUÑA, A. 2018. The Significance of the Spatial Variability of Rainfall on the Numerical Simulation of Urban Floods. *Water,* 10**,** 207.

CRIPPEN, R., BUCKLEY, S., AGRAM, P., BELZ, E., GURROLA, E., HENSLEY, S., KOBRICK, M., LAVALLE, M., MARTIN, J., NEUMANN, M., NGUYEN, Q., ROSEN, P., SHIMADA,

J., SIMARD, M. & TUNG, W. 2016. NASADEM GLOBAL ELEVATION MODEL: METHODS AND PROGRESS. *ISPRS - International Archives of the Photogrammetry, Remote Sensing and Spatial Information Sciences,* XLI-B4**,** 125-128.

DAWSON, R. J., SPEIGHT, L., HALL, J. W., DJORDJEVIC, S., SAVIC, D. & LEANDRO, J. 2008. Attribution of flood risk in urban areas. *Journal of Hydroinformatics,* 10**,** 275-288.

DI BALDASSARRE, G. 2012a. . *Floods in a Changing Climate: Inundation Modelling,* Cambridge, Cambridge University Press.

DOMENEGHETTI, A. 2016. On the use of SRTM and altimetry data for flood modeling in data-sparse regions. *Water Resources Research,* 52**,** 2901-2918.

DONALD HOUSTON, A. W., DAVID BASSETT, ALISTAIR GEDDES, ANDREW HOOLACHAN AND MARION MCMILLAN 2011. Pluvial (rain-related) flooding in urban areas: the invisible hazard.

DONG, Y., CHANG, H.-C., CHEN, W., ZHANG, K. & FENG, R. 2015. Accuracy assessment of GDEM, SRTM, and DLR-SRTM in Northeastern China. *Geocarto International,* 30**,** 779-792.

DOTTORI, F., SALAMON, P., BIANCHI, A., ALFIERI, L., HIRPA, F. A. & FEYEN, L. 2016. Development and evaluation of a framework for global flood hazard mapping. *Advances in Water Resources,* 94**,** 87-102.

DUNNING, C. M., BLACK, E., AND ALLAN, R. P. 2018. Later Wet Seasons with More Intense Rainfall over Africa under Future Climate Change. . *Journal of Climate* 31 9719-9738.

FALORNI, G., TELES, V., VIVONI, E. R., BRAS, R. L. & AMARATUNGA, K. S. 2005. Analysis and characterization of the vertical accuracy of digital elevation models from the Shuttle Radar Topography Mission. *Journal of Geophysical Research: Earth Surface,* 110.

FARR, T. G., ROSEN, P. A., CARO, E., CRIPPEN, R., DUREN, R., HENSLEY, S., KOBRICK, M., PALLER, M., RODRIGUEZ, E., ROTH, L., SEAL, D., SHAFFER, S., SHIMADA, J., UMLAND, J., WERNER, M., OSKIN, M., BURBANK, D. & ALSDORF, D. 2007. The Shuttle Radar Topography Mission. *Reviews of Geophysics,* 45.

FINNEY, D. L., MARSHAM, J. H., ROWELL, D. P., KENDON, E. J., TUCKER, S. O., STRATTON, R. A. & JACKSON, L. S. 2020. Effects of Explicit Convection on Future Projections of Mesoscale Circulations, Rainfall, and Rainfall Extremes over Eastern Africa. *Journal of Climate,* 33**,** 2701.

FOLEY, J. A., DEFRIES, R., ASNER, G. P., BARFORD, C., BONAN, G., CARPENTER, S. R., CHAPIN, F. S., COE, M. T., DAILY, G. C., GIBBS, H. K., HELKOWSKI, J. H., HOLLOWAY, T., HOWARD, E. A., KUCHARIK, C. J., MONFREDA, C., PATZ, J. A., PRENTICE, I. C., RAMANKUTTY, N. & SNYDER, P. K. 2005. Global Consequences of Land Use. *Science,* 309**,** 570-574.

GALLANT, J. C., READ, A. M. & DOWLING, T. I. 2012. Removal of Tree Offsets from Srtm and Other Digital Surface Models. *ISPRS - International Archives of the Photogrammetry, Remote Sensing and Spatial Information Sciences,* XXXIX-B4**,** 275-280.

GARROTE, J. 2022. Free Global DEMs and Flood Modelling—A Comparison Analysis for the January 2015 Flooding Event in Mocuba City (Mozambique). *Water,* 14**,** 176.

GIANNINI, A., LYON, B., SEAGER, R. & VIGAUD, N. 2018. Dynamical and Thermodynamic Elements of Modeled Climate Change at the East African Margin of Convection. *Geophysical Research Letters,* 45**,** 992-1000.

GUO, K., GUAN, M. & YU, D. 2021. Urban surface water flood modelling – a comprehensive review of current models and future challenges. *Hydrol. Earth Syst. Sci.,* 25**,** 2843-2860.

GUTENSON, J. L., FOLLUM, M. L., SNOW, A. D. & WAHL, M. D. 2017. Large-Scale Flood Inundation Modeling in Data Sparse Environments using TanDEM-X Terrain Data. *Open Water Journal,* 4

HAWKER, L., BATES, P., NEAL, J. & ROUGIER, J. 2018. Perspectives on Digital Elevation Model (DEM) Simulation for Flood Modeling in the Absence of a High-Accuracy Open Access Global DEM. *Frontiers in Earth Science,* 6.

HAWKER, L., NEAL, J. & BATES, P. 2019. Accuracy assessment of the TanDEM-X 90 Digital Elevation Model for selected floodplain sites. *Remote Sensing of Environment,* 232**,** 111319.

HENDERSON, J. V., VENABLES, A. J., REGAN, T. & SAMSONOV, I. 2016. Building functional cities. *Science,* 352**,** 946-947.

HIRT, C. 2018. Artefact detection in global digital elevation models (DEMs): The Maximum Slope Approach and its application for complete screening of the SRTM v4.1 and MERIT DEMs. *Remote Sensing of Environment,* 207**,** 27-41.

HORRITT, M. S. & BATES, P. D. 2001. Effects of spatial resolution on a raster based model of flood flow. *Journal of Hydrology,* 253**,** 239-249.

HOUSTON, D., WERRITY, A., BASSETT, D. 2011. Pluvial (rain-related) Flooding in Urban Areas: the invisible Hazard. . *Joseph Rowntree Foundation*

HUNT, A. & WATKISS, P. 2011. Climate change impacts and adaptation in cities: a review of the literature. *Climatic Change,* 104**,** 13-49.

HUNTER, N. M., BATES, P. D., NEELZ, S., PENDER, G., VILLANUEVA, I., WRIGHT, N. G., LIANG, D., FALCONER, R. A., LIN, B., WALLER, S., CROSSLEY, A. J. & MASON, D. C. 2008. Benchmarking 2D hydraulic models for urban flooding. *Proceedings of the Institution of Civil Engineers - Water Management,* 161**,** 13-30.

IPCC 2007. Climate Change 2007: Synthesis Report. Contribution of Working Groups I, II and III to the Fourth Assessment Report of the Intergovernmental Panel on Climate Change

IPCC 2014. Climate Change 2014: Synthesis Report.

IPCC 2014a. Climate Change 2014: Impacts, Adaptation, and Vulnerability. Part A: Global and Sectoral Aspects. Contribution of Working Group II to the Fifth Assessment Report of the Intergovernmental Panel on Climate Change. *In:* [FIELD, C. B., V.R. BARROS, D.J. DOKKEN, K.J. MACH, M.D. MASTRANDREA, T.E. BILIR, M. CHATTERJEE, K.L. EBI, Y.O. ESTRADA, R.C. GENOVA, B. GIRMA, E.S. KISSEL, A.N. LEVY, S. MACCRACKEN, P.R. MASTRANDREA, AND L.L. WHITE (EDS.)]. (ed.).

JAMALI, B., LÖWE, R., BACH, P. M., URICH, C., ARNBJERG-NIELSEN, K. & DELETIC, A. 2018. A rapid urban flood inundation and damage assessment model. *Journal of Hydrology,* 564**,** 1085-1098.

JIN, S., HOMER, C., YANG, L., DANIELSON, P., DEWITZ, J., LI, C., ZHU, Z., XIAN, G. & HOWARD, D. 2019. Overall Methodology Design for the United States National Land Cover Database 2016 Products. *Remote Sensing,* 11**,** 2971.

JUNG, M., KIM, H., MALLARI, K. J. B., PAK, G. & YOON, J. 2014. Analysis of effects of climate change on runoff in an urban drainage system: a case study from Seoul, Korea. *Water Science and Technology,* 71**,** 653-660.

KAIHUA, G., MINGFU, G. & DAPENG, Y. 2021. *Urban surface water flood modelling – a comprehensive review of current models and future challenges*.

KENDON, E. J., STRATTON, R. A., TUCKER, S., MARSHAM, J. H., BERTHOU, S., ROWELL, D. P. & SENIOR, C. A. 2019. Enhanced future changes in wet and dry extremes over Africa at convection-permitting scale. *Nature Communications,* 10**,** 1794.

KENT, C., CHADWICK, R. & ROWELL, D. P. 2015. Understanding Uncertainties in Future Projections of Seasonal Tropical Precipitation. *J. Climate,* 28**,** 4390-4413.

KHADKA, D. & PATHAK, D. 2016. Climate change projection for the marsyangdi river basin, Nepal using statistical downscaling of GCM and its implications in geodisasters. *Geoenvironmental Disasters,* 3**,** 15.

KILAVI, M., MACLEOD, D., AMBANI, M., ROBBINS, J., DANKERS, R., GRAHAM, R., TITLEY, H., SALIH, A. & TODD, M. 2018. Extreme rainfall and flooding over central Kenya including Nairobi City during the long-rains Season 2018: causes, predictability, and potential for early warning and actions. *Atmosphere,* 9**,** Article: 472.

KIM, D. E., LIONG, S.-Y., GOURBESVILLE, P., ANDRES, L. & LIU, J. 2020. Simple-Yet-Effective SRTM DEM Improvement Scheme for Dense Urban Cities Using ANN and Remote Sensing Data: Application to Flood Modeling. *Water,* 12**,** 816.

KLONNER, C., BARRON, C., NEIS, P. & HÖFLE, B. 2015. Updating digital elevation models via change detection and fusion of human and remote sensor data in urban environments. *International Journal of Digital Earth,* 8**,** 153-171.

KNBS 2019. 2019 Kenya Population and Housing Census *Kenya National Bureau of Statistics,* Volume I.

KOLECKA, N. & KOZAK, J. 2014. Assessment of the Accuracy of SRTM C- and X-Band High Mountain Elevation Data: a Case Study of the Polish Tatra Mountains. *Pure and Applied Geophysics,* 171**,** 897-912.

KOMI, K., NEAL, J., TRIGG, M. A. & DIEKKRÜGER, B. 2017. Modelling of flood hazard extent in data sparse areas: a case study of the Oti River basin, West Africa. *Journal of Hydrology: Regional Studies,* 10**,** 122-132.

KONRAD, C. P. 2003. Effects of Urban Development on Floods. U.S. Geological Survey-Water Resources.

KRIEGER, G., MOREIRA, A., FIEDLER, H., HAJNSEK, I., WERNER, M., YOUNIS, M. & ZINK, M. 2007. TanDEM-X: A Satellite Formation for High-Resolution SAR Interferometry. *IEEE Transactions on Geoscience and Remote Sensing,* 45**,** 3317-3341.

KUNDZEWICZ, Z. W., KANAE, S., SENEVIRATNE, S. I., HANDMER, J., NICHOLLS, N., PEDUZZI, P., MECHLER, R., BOUWER, L. M., ARNELL, N., MACH, K., MUIR-WOOD, R., BRAKENRIDGE, G. R., KRON, W., BENITO, G., HONDA, Y., TAKAHASHI, K. & SHERSTYUKOV, B. 2014. Flood risk and climate change: global and regional perspectives. *Hydrological Sciences Journal,* 59**,** 1-28.

LEFSKY, M. A. 2010. A global forest canopy height map from the Moderate Resolution Imaging Spectroradiometer and the Geoscience Laser Altimeter System. *Geophysical Research Letters,* 37.

LI, C.-J., CHAI, Y.-Q., YANG, L.-S. & LI, H.-R. 2016. Spatio-temporal distribution of flood disasters and analysis of influencing factors in Africa. *Natural Hazards,* 82**,** 721-731.

LI, X., COOPER, J. R. & PLATER, A. J. 2021. Quantifying erosion hazards and economic damage to critical infrastructure in river catchments: Impact of a warming climate. *Climate Risk Management,* 32**,** 100287.

LIU, H., ZOU, L., XIA, J., CHEN, T. & WANG, F. 2022. Impact assessment of climate change and urbanization on the nonstationarity of extreme precipitation: A case study in an urban agglomeration in the middle reaches of the Yangtze river. *Sustainable Cities and Society,* 85**,** 104038.

MARTHA, T. R., KERLE, N., JETTEN, V., VAN WESTEN, C. J. & KUMAR, K. V. 2010. Characterising spectral, spatial and morphometric properties of landslides for semi-automatic detection using object-oriented methods. *Geomorphology,* 116**,** 24-36.

MASON, D. C., TRIGG, M., GARCIA-PINTADO, J., CLOKE, H. L., NEAL, J. C. & BATES, P. D. 2016. Improving the TanDEM-X Digital Elevation Model for flood modelling using flood extents from Synthetic Aperture Radar images. *Remote Sensing of Environment,* 173**,** 15-28.

MAUNE, D. F. & NAYEGANDHI, A. 2017. Digital Elevation Model Technologies and Applications: The DEM Users Manual
3rd Edition**,** 655.

MILLER, J. D. & HUTCHINS, M. 2017. The impacts of urbanisation and climate change on urban flooding and urban water quality: A review of the evidence concerning the United Kingdom. *Journal of Hydrology: Regional Studies,* 12**,** 345-362.

MIRZA, M. M. Q. 2011. Climate change, flooding in South Asia and implications. *Regional Environmental Change,* 11**,** 95-107.

MOORE, I. D., GRAYSON, R. B. & LADSON, A. R. 1991. Digital terrain modelling: A review of hydrological, geomorphological, and biological applications. *Hydrological Processes,* 5**,** 3-30.

MURRAY, V. & EBI, K. L. 2012. IPCC Special Report on Managing the Risks of Extreme Events and Disasters to Advance Climate Change Adaptation (SREX). *Journal of Epidemiology and Community Health,* 66**,** 759.

MUTHUSAMY, M., CASADO, M. R., BUTLER, D. & LEINSTER, P. 2021. Understanding the effects of Digital Elevation Model resolution in urban fluvial flood modelling. *Journal of Hydrology,* 596**,** 126088.

NICHOLSON, S. E. 2017. Climate and climatic variability of rainfall over eastern Africa. *Reviews of Geophysics,* 55**,** 590-635.

NIPPON, K. 2014. The project on Integrated Urban Development Master Plan for the City of Nairobi in the Republic of Kenya. *Final Report,* Part 1**,** 692.

NKWUNONWO, U. C., WHITWORTH, M. & BAILY, B. 2020. A review of the current status of flood modelling for urban flood risk management in the developing countries. *Scientific African,* 7**,** e00269.

O'LOUGHLIN, F. E., PAIVA, R. C. D., DURAND, M., ALSDORF, D. E. & BATES, P. D. 2016. A multi-sensor approach towards a global vegetation corrected SRTM DEM product. *Remote Sensing of Environment,* 182**,** 49-59.

OCHA 10th May, 2018. OCHA Flash Update #5: Floods in Kenya UN Office for the Coordination of Humanitarian Affairs.

OGANIA, J. L., PUNO, G., ALIVIO, M. B. T. & TAYLARAN, J. M. G. 2019. Effect of digital elevation model's resolution in producing flood hazard maps. *Global Journal of Environmental Science and Management,* 5**,** 95-106.

OLAJUBU, V., TRIGG, M. A., BERRETTA, C., SLEIGH, A., CHINI, M., MATGEN, P., MOJERE, S. & MULLIGAN, J. 2021. Urban correction of global DEMs using building density for Nairobi, Kenya. *Earth Science Informatics,* 14**,** 1383-1398.

ONGOMA, V., CHEN, H. & GAO, C. 2018. Projected changes in mean rainfall and temperature over East Africa based on CMIP5 models. *International Journal of Climatology,* 38**,** 1375-1392.

OSIMA, S., INDASI, V. S., ZAROUG, M., ENDRIS, H. S., GUDOSHAVA, M., MISIANI, H. O., NIMUSIIMA, A., ANYAH, R. O., OTIENO, G., OGWANG, B. A., JAIN, S., KONDOWE, A. L., MWANGI, E., LENNARD, C., NIKULIN, G. & DOSIO, A. 2018. Projected climate over the Greater Horn of Africa under 1.5 °C and 2 °C global warming. *Environmental Research Letters,* 13**,** 065004.

OTIENO, G., MUTEMI, J., OPIJAH, F., OGALLO, L. & OMONDI, H. 2018. The Impact of Cumulus Parameterization on Rainfall Simulations over East Africa. *Atmospheric and Climate Sciences* 8

PITT, M. 2008. Lessons from the 2007 Floods.

R. J. COX, T. D. SHAND & BLACKA, M. J. 2010. Australian Rainfall and Runoff Revision Project 10: Appropriate Safety Criteria for People The University of south Wales. Water Research Laboratory.

RANGARI, V. A., UMAMAHESH, N. V. & BHATT, C. M. 2019. Assessment of inundation risk in urban floods using HEC RAS 2D. *Modeling Earth Systems and Environment,* 5**,** 1839 - 1851.

RAYBURG, S., THOMS, M. & NEAVE, M. 2009. A comparison of digital elevation models generated from different data sources. *Geomorphology,* 106**,** 261-270.

ROBINSON, N., REGETZ, J. & GURALNICK, R. P. 2014. EarthEnv-DEM90: A nearly-global, void-free, multi-scale smoothed, 90m digital elevation model from fused ASTER and SRTM data. *ISPRS Journal of Photogrammetry and Remote Sensing,* 87**,** 57.

RODRÍGUEZ, E., MORRIS, C. S. & BELZ, J. E. 2006. A Global Assessment of the SRTM Performance. *Photogrammetric Engineering & Remote Sensing,* 72**,** 249-260.

ROSSI, C., FRITZ, T., EINEDER, M., ERTEN, E., ZHU, X. X. & GERNHARDT, S. 2012. Towards AN Urban dem Generation with Satellite SAR Interferometry. *ISPRS - International Archives of the Photogrammetry, Remote Sensing and Spatial Information Sciences,* 39B7**,** 73.

ROWELL, D. P., SENIOR, C. A., VELLINGA, M. & GRAHAM, R. J. 2016. Can climate projection uncertainty be constrained over Africa using metrics of contemporary performance? *Climatic Change,* 134**,** 621-633.

SAKSENA, S. 2015. *Investigating the Role of DEM Resolution and Accuracy on Flood Inundation Mapping*.

SAKSENA, S. & MERWADE, V. 2015. Incorporating the effect of DEM resolution and accuracy for improved flood inundation mapping. *Journal of Hydrology,* 530**,** 180-194.

SAMPSON, C. C., BATES, P. D., NEAL, J. C. & HORRITT, M. S. 2013. An automated routing methodology to enable direct rainfall in high resolution shallow water models. *Hydrological Processes,* 27**,** 467-476.

SANDERS, B. F. 2007a. Evaluation of on-line DEMs for flood inundation modeling. *Advances in Water Resources,* 30**,** 1831-1843.

SANDERS, B. F. 2007b. Evaluation of on-line DEMs for flood inundation modeling. *Advances in water resources,* 2007 v.30 no.8**,** pp. 1831-1843.

SANYAL, J., CARBONNEAU, P. & DENSMORE, A. L. 2013. Hydraulic routing of extreme floods in a large ungauged river and the estimation of associated uncertainties: a case study of the Damodar River, India. *Natural Hazards,* 66**,** 1153-1177.

SANYAL, J., DENSMORE, A. L. & CARBONNEAU, P. 2014. Analysing the effect of land-use/cover changes at sub-catchment levels on downstream flood peaks: A semi-distributed modelling approach with sparse data. *CATENA,* 118**,** 28-40.

SAVAGE, J., BATES, P., FREER, J., NEAL, J. & ARONICA, G. 2015. When does spatial resolution become spurious in probabilistic flood inundation predictions? *Hydrological Processes,* 30**,** n/a-n/a.

SCHMID, C. 2015. 14 Patterns and Pathways of Global Urbanization: Towards Comparative Analysis Implosions /Explosions. *In:* BRENNER, N. (ed.). JOVIS Verlag GmbH.

SHONGWE, M., E., OLDENBORGH, G., HURK, B. & AALST, M. 2011a. Projected Changes in Mean and Extreme Precipitation in Africa under Global Warming. Part II: East Africa. *Journal of Climate* 24**,** 3718-3733.

SHONGWE, M. E., VAN OLDENBORGH, G. J., VAN DEN HURK, B. & VAN AALST, M. 2011b. Projected Changes in Mean and Extreme Precipitation in Africa under Global Warming. Part II: East Africa. *Journal of Climate*
24**,** 3718-3733.

SIMARD, M., PINTO, N., FISHER, J. B. & BACCINI, A. 2011. Mapping forest canopy height globally with spaceborne lidar. *Journal of Geophysical Research: Biogeosciences,* 116.

SLIUZAS, R. V., FLACKE, J., AND JETTEN, V.G. Modelling urbanization and flooding in Kampala, Uganda. 14th N-AERUS / GISDECO conference 12-14 September 2013 2013 Enschede, Netherlands. 16 p.-.

SMITH, G. P., DAVEY, E. K. & COX, R. J. 2014. Flood Hazard UNSW Australia Water Research Laboratory Technical Report

STEPHENS, E. M., BATES, P. D., FREER, J. E. & MASON, D. C. 2012. The impact of uncertainty in satellite data on the assessment of flood inundation models. *Journal of Hydrology,* 414-415**,** 162-173.

STEPHENS, G. L., L'ECUYER, T., FORBES, R., GETTELMEN, A., GOLAZ, J.-C., BODAS-SALCEDO, A., SUZUKI, K., GABRIEL, P. & HAYNES, J. 2010. Dreary state of precipitation in global models. *Journal of Geophysical Research: Atmospheres,* 115.

STRATTON, R. A., SENIOR, C. A., VOSPER, S. B., FOLWELL, S. S., BOUTLE, I. A., EARNSHAW, P. D., KENDON, E., LOCK, A. P., MALCOLM, A., MANNERS, J., MORCRETTE, C. J., SHORT, C., STIRLING, A. J., TAYLOR, C. M., TUCKER, S., WEBSTER, S. & WILKINSON, J. M. 2018. A Pan-African Convection-Permitting Regional Climate Simulation with the Met Office Unified Model: CP4-Africa *Journal of Climate,* 31**,** 3485-3508.

SURIYA, S. & MUDGAL, B. V. 2012. Impact of urbanization on flooding: The Thirusoolam sub watershed – A case study. *Journal of Hydrology,* 412-413**,** 210-219.

TADONO, T., NAGAI, H., ISHIDA, H., ODA, F., NAITO, S., MINAKAWA, K. & IWAMOTO, H. 2016. GENERATION OF THE 30 M-MESH GLOBAL DIGITAL SURFACE MODEL BY ALOS PRISM. *ISPRS - International Archives of the Photogrammetry, Remote Sensing and Spatial Information Sciences,* XLI-B4**,** 157-162.

TAKAKU, J., TADONO, T., TSUTSUI, K. & ICHIKAWA, M. 2016. Validation of "AW3D" Global Dsm Generated from Alos Prism. *ISPRS Annals of Photogrammetry, Remote Sensing and Spatial Information Sciences,* III4**,** 25.

THIERY, W., DAVIN, E. L., SENEVIRATNE, S. I., BEDKA, K., LHERMITTE, S. & VAN LIPZIG, N. P. M. 2016. Hazardous thunderstorm intensification over Lake Victoria. *Nature communications,* 7**,** 12786-12786.

THOMAS STEVEN SAVAGE, J., PIANOSI, F., BATES, P., FREER, J. & WAGENER, T. 2016. Quantifying the importance of spatial resolution and other factors through global sensitivity analysis of a flood inundation model. *Water Resources Research,* 52**,** 9146-9163.

TIECKE, T., LIU, X., ZHANG, A., GROS, A., LI, N., YETMAN, G., KILIC, T., MURRAY, S., BLANKESPOOR, B., PRYDZ, E. & DANG, H.-A. 2017. Mapping the world population one building at a time.

TRIGG, M. A., BIRCH, C. E., NEAL, J. C., BATES, P. D., SMITH, A., SAMPSON, C. C., YAMAZAKI, D., HIRABAYASHI, Y., PAPPENBERGER, F., DUTRA, E., WARD, P. J., WINSEMIUS, H. C., SALAMON, P., DOTTORI, F., RUDARI, R., KAPPES, M. S., SIMPSON, A. L., HADZILACOS, G. & FEWTRELL, T. J. 2016. The credibility challenge for global fluvial flood risk analysis. *Environmental Research Letters,* 11**,** 094014.

U.S. ARMY CORPS OF ENGINEERING, U. S. A. C. O. E. 2016. HEC-RAS 5.0 Hydraulic Reference Manual.: U.S. Army Corps of Engineers, Institute for Water Resources, Hydrologic Engineering Center, Davis, CA, USA. .

ULA, C. 2021. Nairobi Solid Waste Management & Storm Water Drainage and Flooding Urban Links Africa (ULA).

UN-DESA 2018. Population Division (2018) World urbanization prospects: the 2018 revision.

UN 2019. World Urbanization Prospects: The 2018 Revision New York: United Nations. *Department of Economic and Social Affairs*

UNICEF 15th June, 2018. Kenya Floods Response Update. *Situation Report.*

VAKA, D. S., KUMAR, V., RAO, Y. S. & DEO, R. Comparison of Various DEMs for Height Accuracy Assessment Over Different Terrains of India. IGARSS 2019 - 2019 IEEE International Geoscience and Remote Sensing Symposium, 28 July-2 Aug. 2019 2019. 1998-2001.

VAZE, J., TENG, J. & SPENCER, G. 2010. Impact of DEM accuracy and resolution on topographic indices. *Environmental Modelling & Software,* 25**,** 1086-1098.

VEIJALAINEN, N., LOTSARI, E., ALHO, P., VEHVILÄINEN, B. & KÄYHKÖ, J. 2010. National scale assessment of climate change impacts on flooding in Finland. *Journal of Hydrology,* 391**,** 333-350.

VOJTEK, M., PETROSELLI, A., VOJTEKOVÁ, J. & ASGHARINIA, S. 2019. Flood inundation mapping in small and ungauged basins: sensitivity analysis using the EBA4SUB and HEC-RAS modeling approach. *Hydrology Research,* 50**,** 1002-1019.

WAINWRIGHT, C. M., FINNEY, D. L., KILAVI, M., BLACK, E. & MARSHAM, J. H. 2021. Extreme rainfall in East Africa, October 2019–January 2020 and context under future climate change. *Weather,* 76**,** 26-31.

WANG, W., YANG, X. & YAO, T. 2012. Evaluation of ASTER GDEM and SRTM and their suitability in hydraulic modelling of a glacial lake outburst flood in southeast Tibet. *Hydrological Processes,* 26**,** 213-225.

WANG, Y., CHEN, A. S., FU, G., DJORDJEVIĆ, S., ZHANG, C. & SAVIĆ, D. A. 2018. An integrated framework for high-resolution urban flood modelling considering multiple information sources and urban features. *Environmental Modelling & Software,* 107**,** 85-95.

WESSEL, B., HUBER, M., WOHLFART, C., MARSCHALK, U., KOSMANN, D. & ROTH, A. 2018. Accuracy assessment of the global TanDEM-X Digital Elevation Model with GPS data. *ISPRS Journal of Photogrammetry and Remote Sensing,* 139**,** 171-182.

WHEATER, H. & EVANS, E. 2009. Land use, water management and future flood risk. *Land Use Policy,* 26**,** S251-S264.

WILLEMS, P., ARNBJERG-NIELSEN, K., OLSSON, J. & NGUYEN, V.-T.-V. 2012a. Climate change impact assessment on urban rainfall extremes and urban drainage: Methods and shortcomings. *Atmospheric Research,* 103**,** 106-118.

WILLEMS, P., OLSSON, J., ARNBJERG-NIELSEN, K., BEECHAM, S., PATHIRANA, A., GREGERSEN, I. B., MADSEN, H. & NGUYEN, V.-T.-V. 2012b. *Impacts of Climate Change on Rainfall Extremes and Urban Drainage Systems*, IWA Publishing.

WU, X., WANG, Z., GUO, S., LAI, C. & CHEN, X. 2018. A simplified approach for flood modeling in urban environments. *Hydrology Research,* 49**,** 1804-1816.

XIA, X., LIANG, Q., MING, X. & HOU, J. 2017. An efficient and stable hydrodynamic model with novel source term discretization schemes for overland flow and flood simulations. *Water Resources Research,* 53**,** 3730-3759.

YAMAZAKI, D., BAUGH, C. A., BATES, P. D., KANAE, S., ALSDORF, D. E. & OKI, T. 2012. Adjustment of a spaceborne DEM for use in floodplain hydrodynamic modeling. *Journal of Hydrology,* 436-437**,** 81-91.

YAMAZAKI, D., IKESHIMA, D., TAWATARI, R., YAMAGUCHI, T., O'LOUGHLIN, F., NEAL, J. C., SAMPSON, C. C., KANAE, S. & BATES, P. D. 2017. A high-accuracy map of global terrain elevations. *Geophysical Research Letters,* 44**,** 5844-5853.

YAN, K., DI BALDASSARRE, G., SOLOMATINE, D. P. & SCHUMANN, G. J.-P. 2015. A review of low-cost space-borne data for flood modelling: topography, flood extent and water level. *Hydrological Processes,* 29**,** 3368-3387.

YANG, Q., ZHENG, X., JIN, L., LEI, X., SHAO, B. & CHEN, Y. 2021. Research Progress of Urban Floods under Climate Change and Urbanization: A Scientometric Analysis. *Buildings,* 11**,** 628.

YANG, W., SEAGER, R., CANE, M. & LYON, B. 2014. The East African Long Rains in Observations and Models. *Journal of Climate,* 27**,** 7185-7202.

YAZDANFAR, Z. & SHARMA, A. 2015. Urban drainage system planning and design – challenges with climate change and urbanization: a review. *Water Science and Technology,* 72**,** 165-179.

YU, D., YIN, J. & LIU, M. 2016. Validating city-scale surface water flood modelling using crowd-sourced data. *Environmental Research Letters,* 11**,** 124011.

ZAITCHIK, B. F. 2017. Madden-Julian Oscillation impacts on tropical African precipitation. *Atmospheric Research,* 184**,** 88-102.

ZHAO, X., SU, Y., HU, T., CHEN, L., GAO, S., WANG, R., JIN, S. & GUO, Q. 2018. A global corrected SRTM DEM product for vegetated areas. *Remote Sensing Letters,* 9**,** 393-402.

ZHOU, Q., LENG, G., SU, J. & REN, Y. 2019. Comparison of urbanization and climate change impacts on urban flood volumes: Importance of urban planning and drainage adaptation. *Science of The Total Environment,* 658**,** 24-33.

ZHOU, Q., MIKKELSEN, P. S., HALSNÆS, K. & ARNBJERG-NIELSEN, K. 2012. Framework for economic pluvial flood risk assessment considering climate change effects and adaptation benefits. *Journal of Hydrology,* 414-415**,** 539-549.

ZINK, M., MOREIRA, A., BACHMANN, M., BRÄUTIGAM, B., FRITZ, T., HAJNSEK, I., KRIEGER, G. & WESSEL, B. TanDEM-X mission status: The complete new topography of the Earth. 2016 IEEE International Geoscience and Remote Sensing Symposium (IGARSS), 10-15 July 2016 2016. 317-320.

11.0 LIST OF APPENDICES

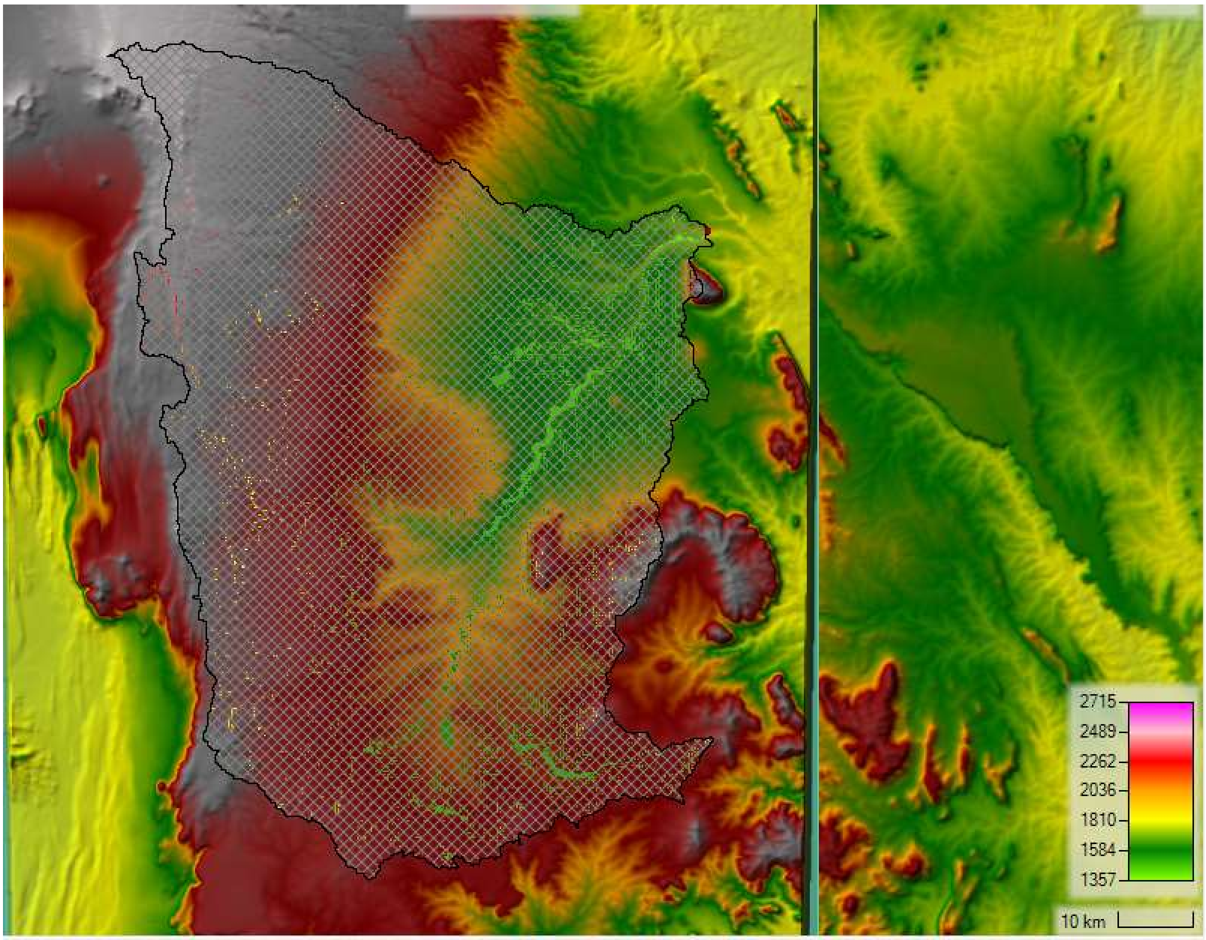

Figure 94. A screenshot from HEC-RAS software showing Water Surface Elevation Map (WSE) for the S1-Baseline model.

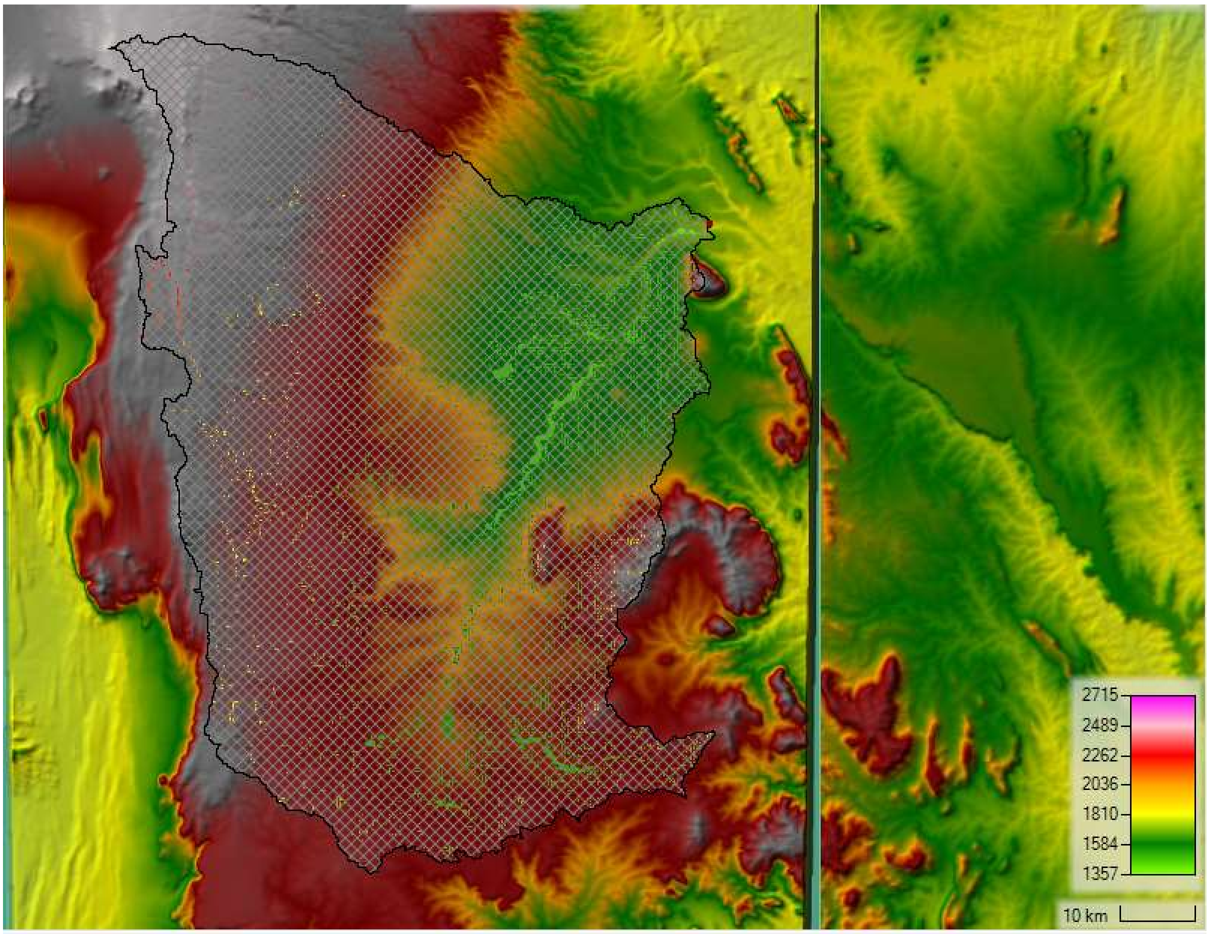

Figure 95. A screenshot from HEC-RAS software showing Water Surface Elevation Map (WSE) for the S2-2000LU model.

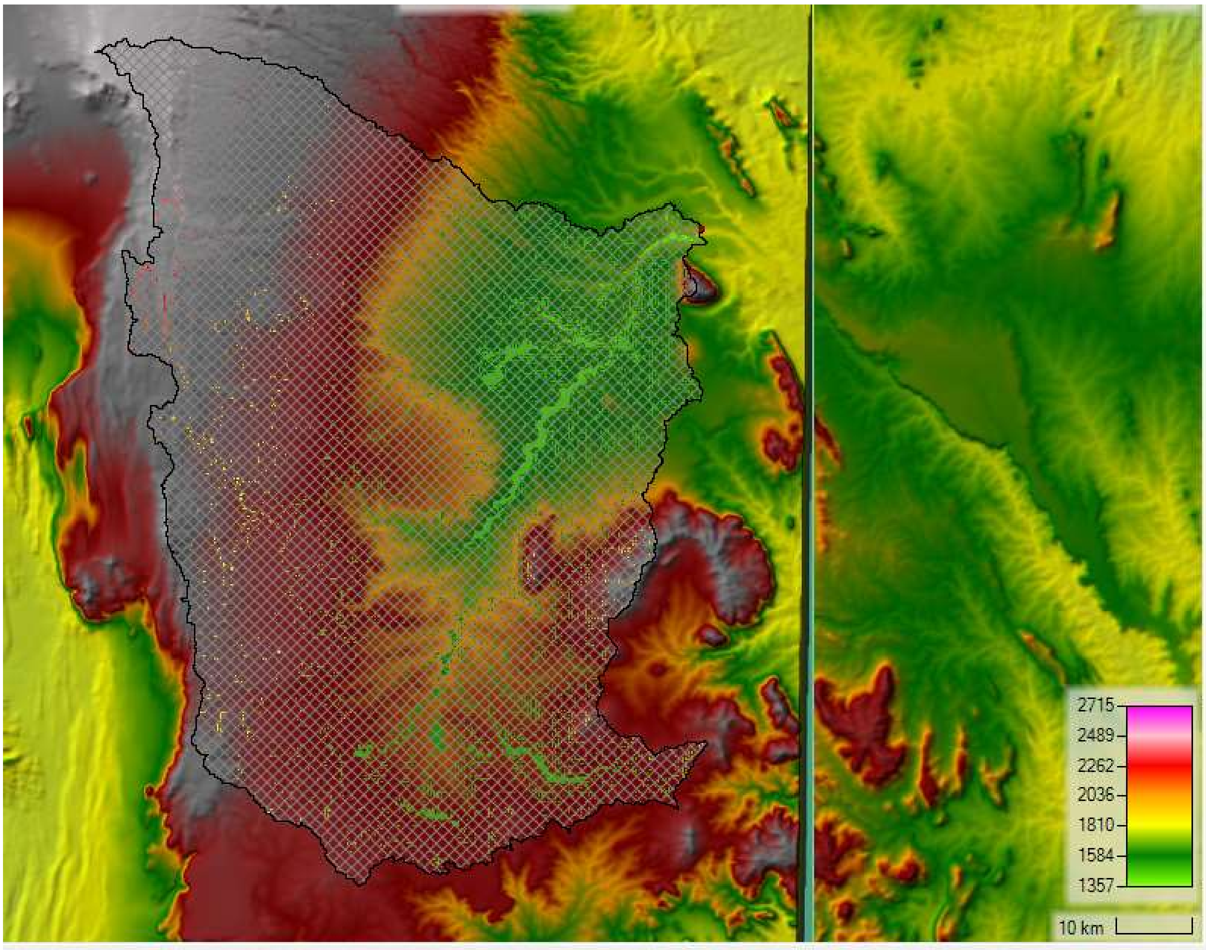

Figure 96. A screenshot from HEC-RAS software showing Water Surface Elevation Map (WSE) for the S3-CP4uplift model.

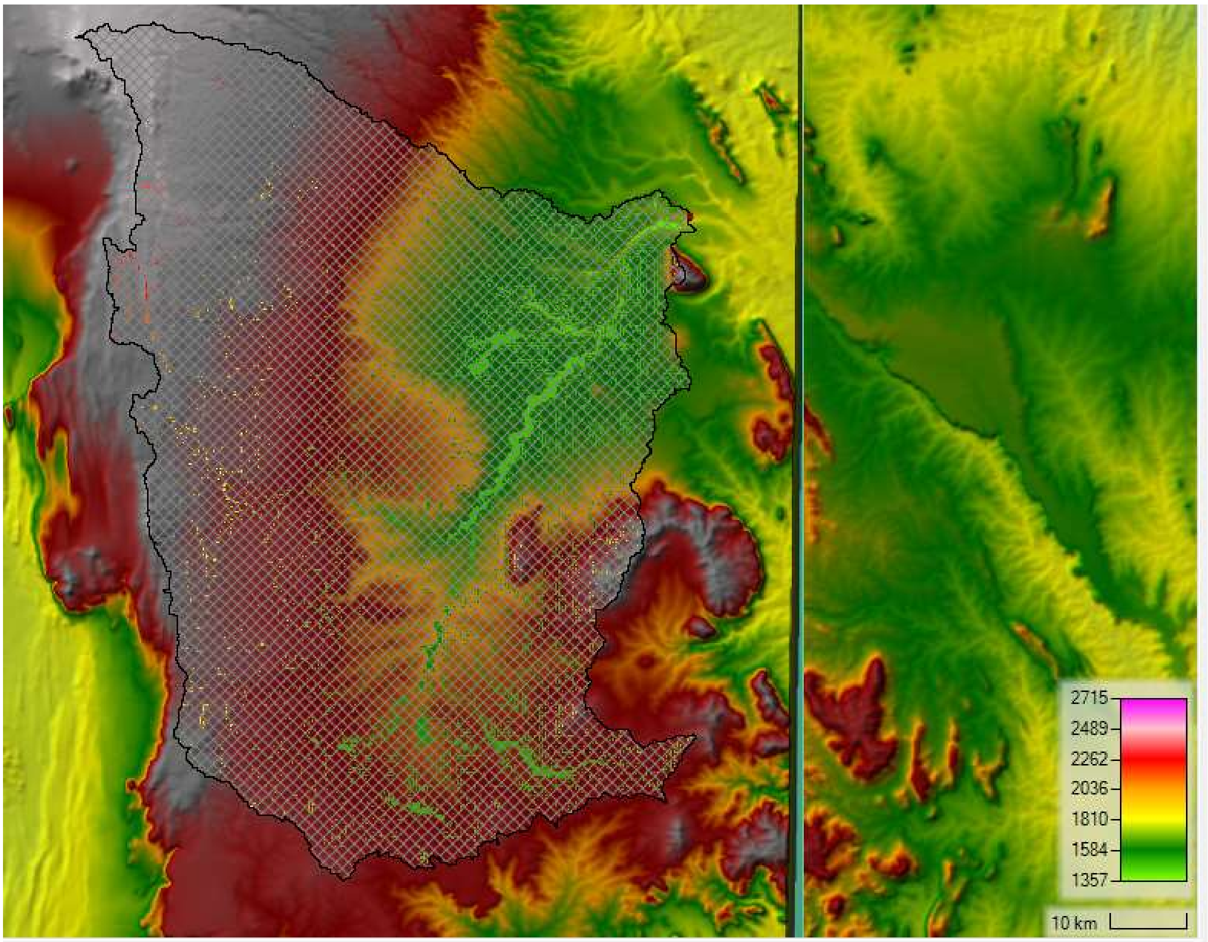

Figure 97. A screenshot from HEC-RAS software showing Water Surface Elevation Map (WSE) for the S4-P25uplift model.

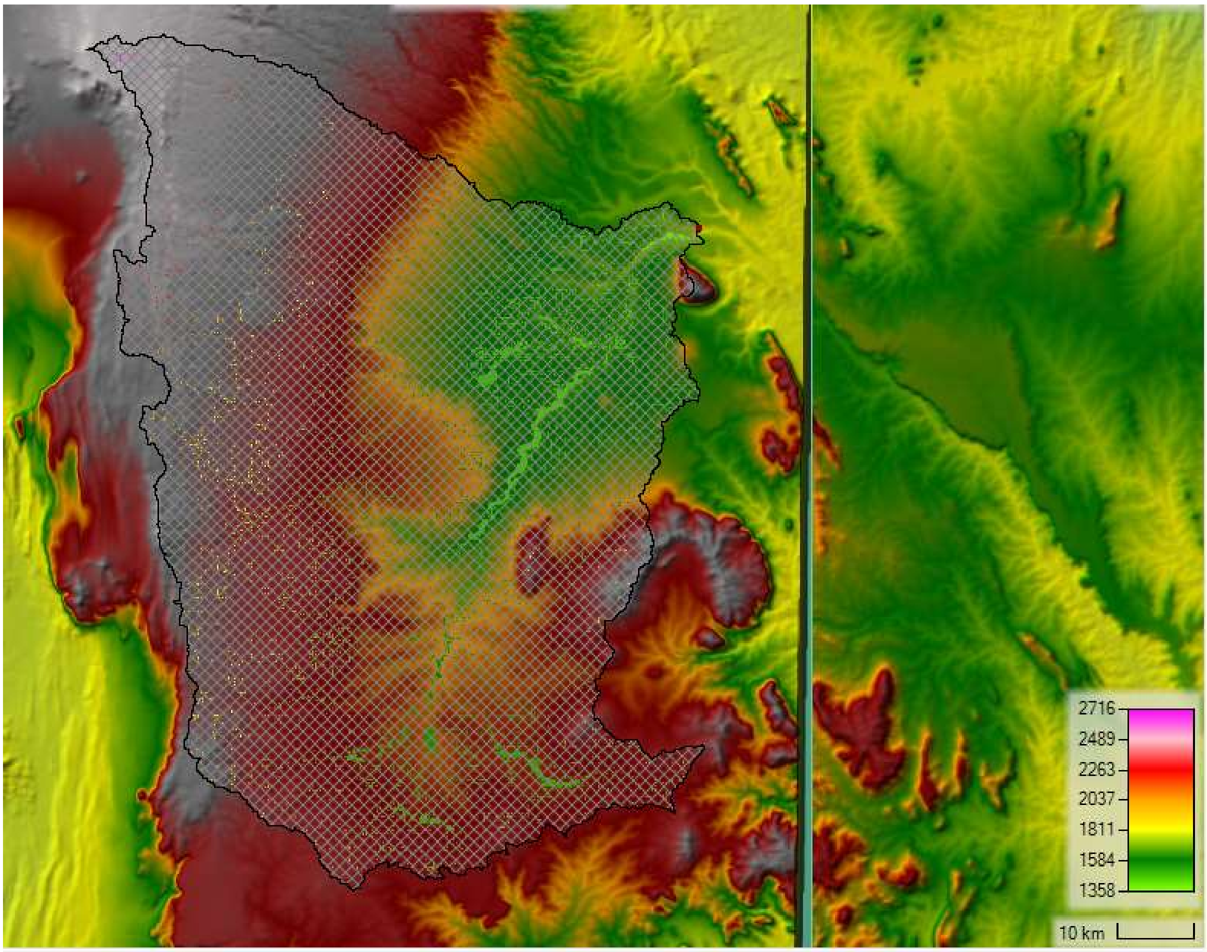

Figure 98. A screenshot from HEC-RAS software showing Water Surface Elevation Map (WSE) for the S5-RawDEM model.

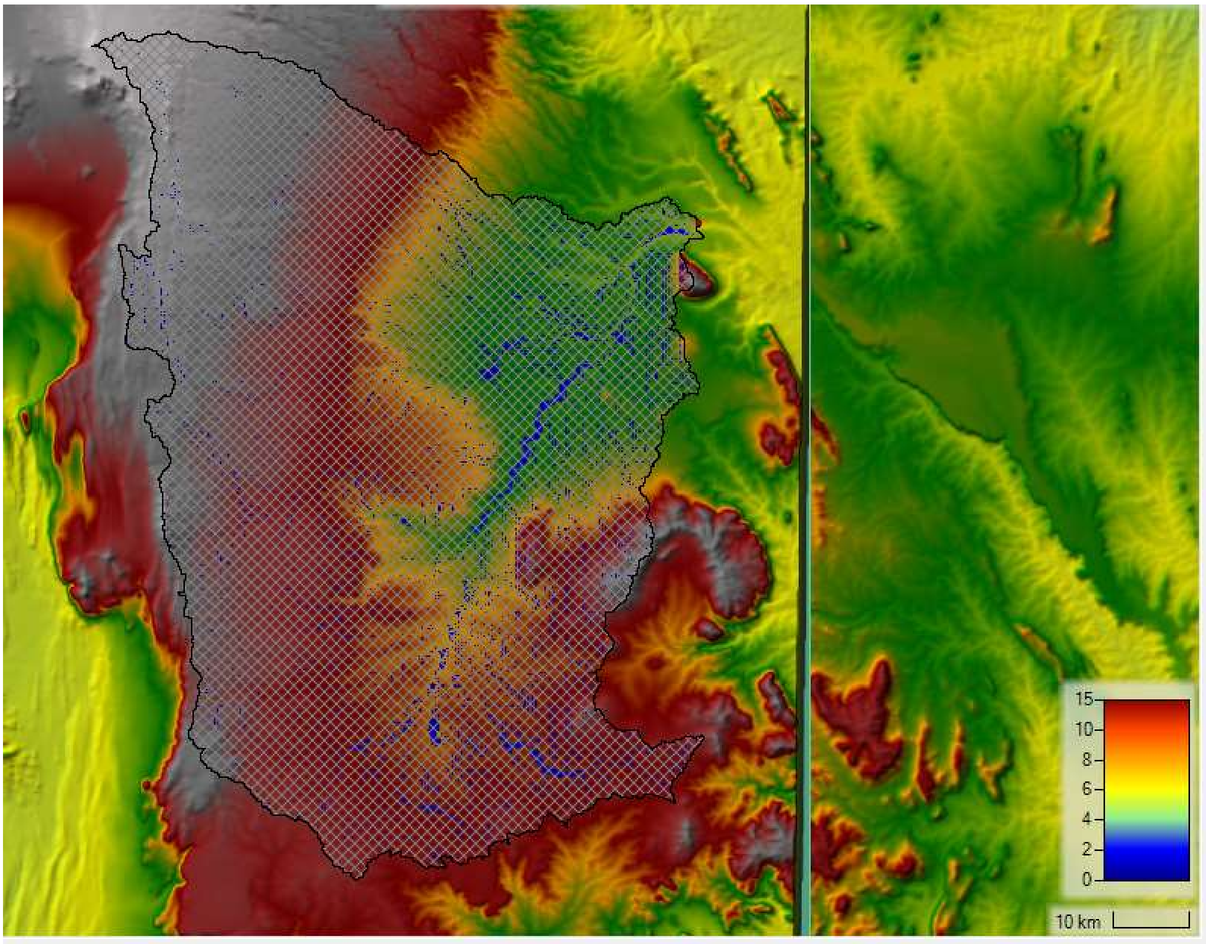

Figure 99. A screenshot from HEC-RAS software showing flood depth for the S1-Baseline model.

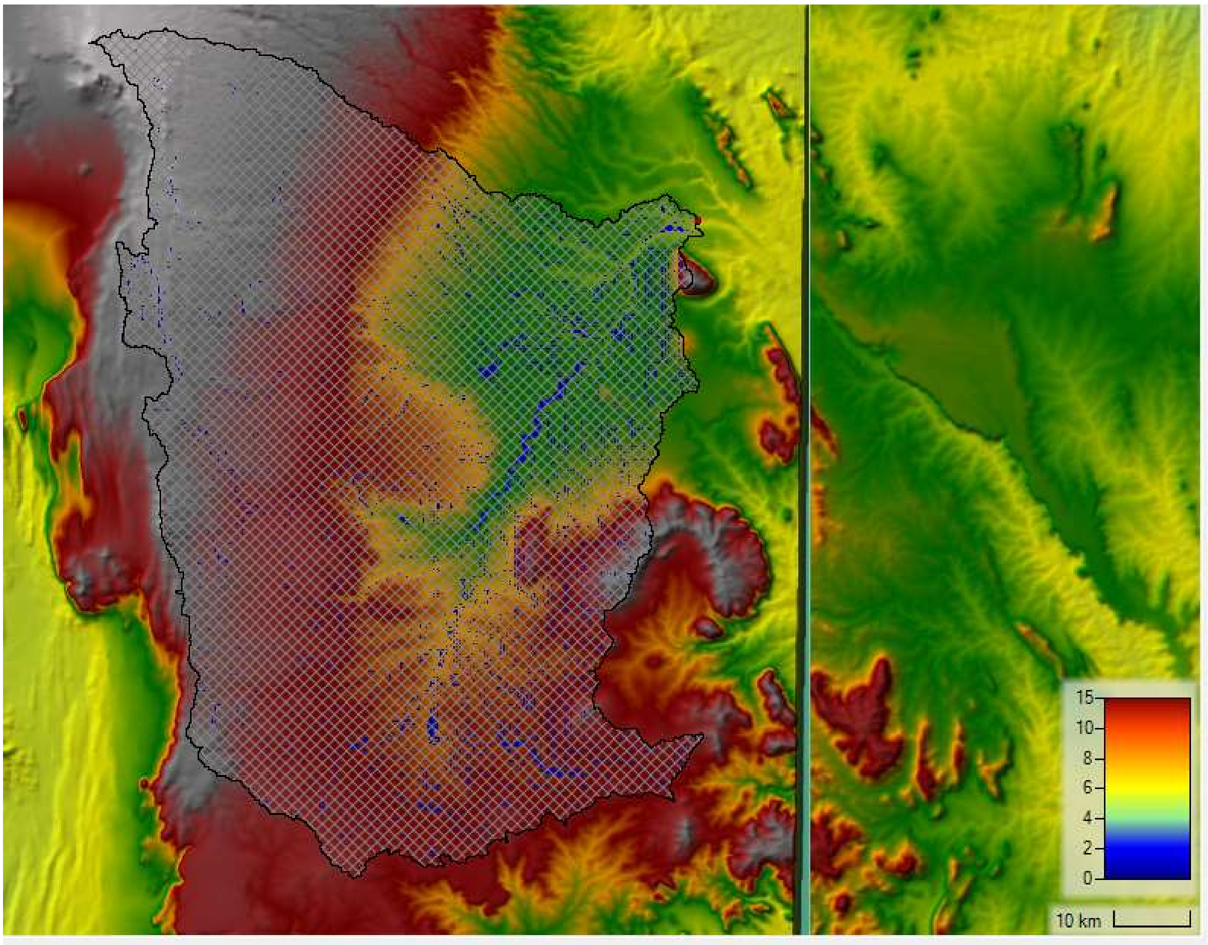

Figure 100. A screenshot from HEC-RAS software showing flood depth for the S2-2000LU model.

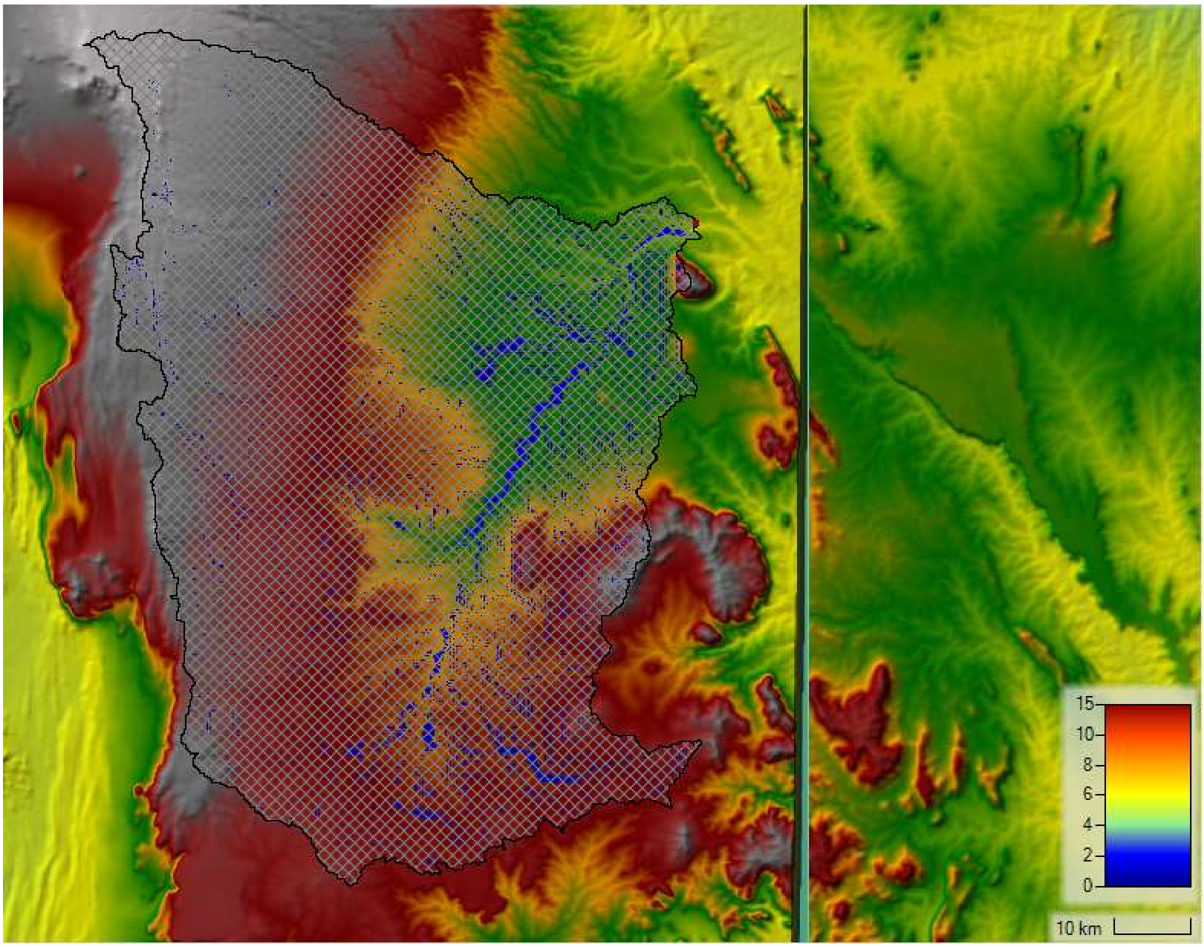

Figure 101. A screenshot from HEC-RAS software showing flood depth for the S3-CP4uplift model.

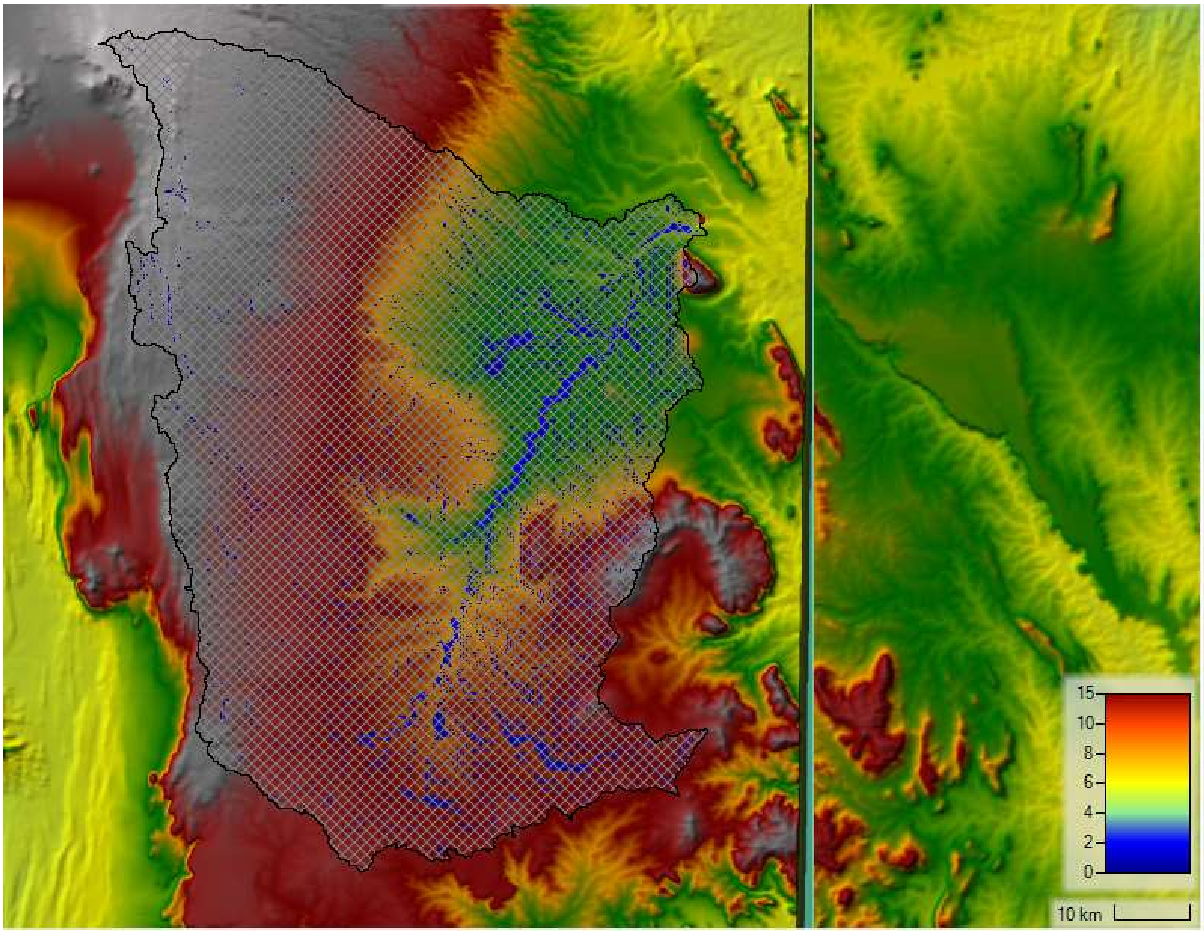

Figure 102. A screenshot from HEC-RAS software showing flood depth for the S4-P25uplift model.

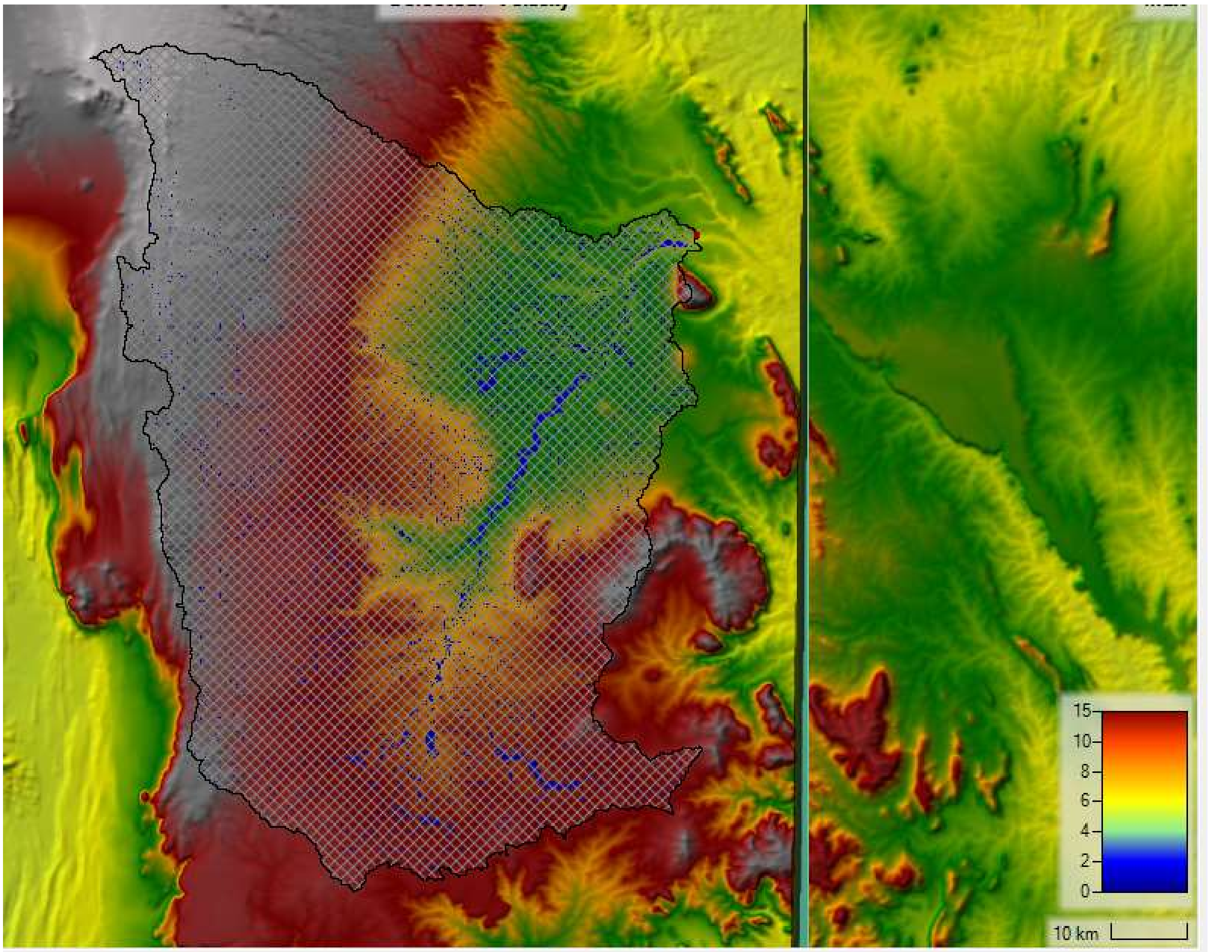

Figure 103. A screenshot from HEC-RAS software showing flood depth for the S5-RawDEM model.

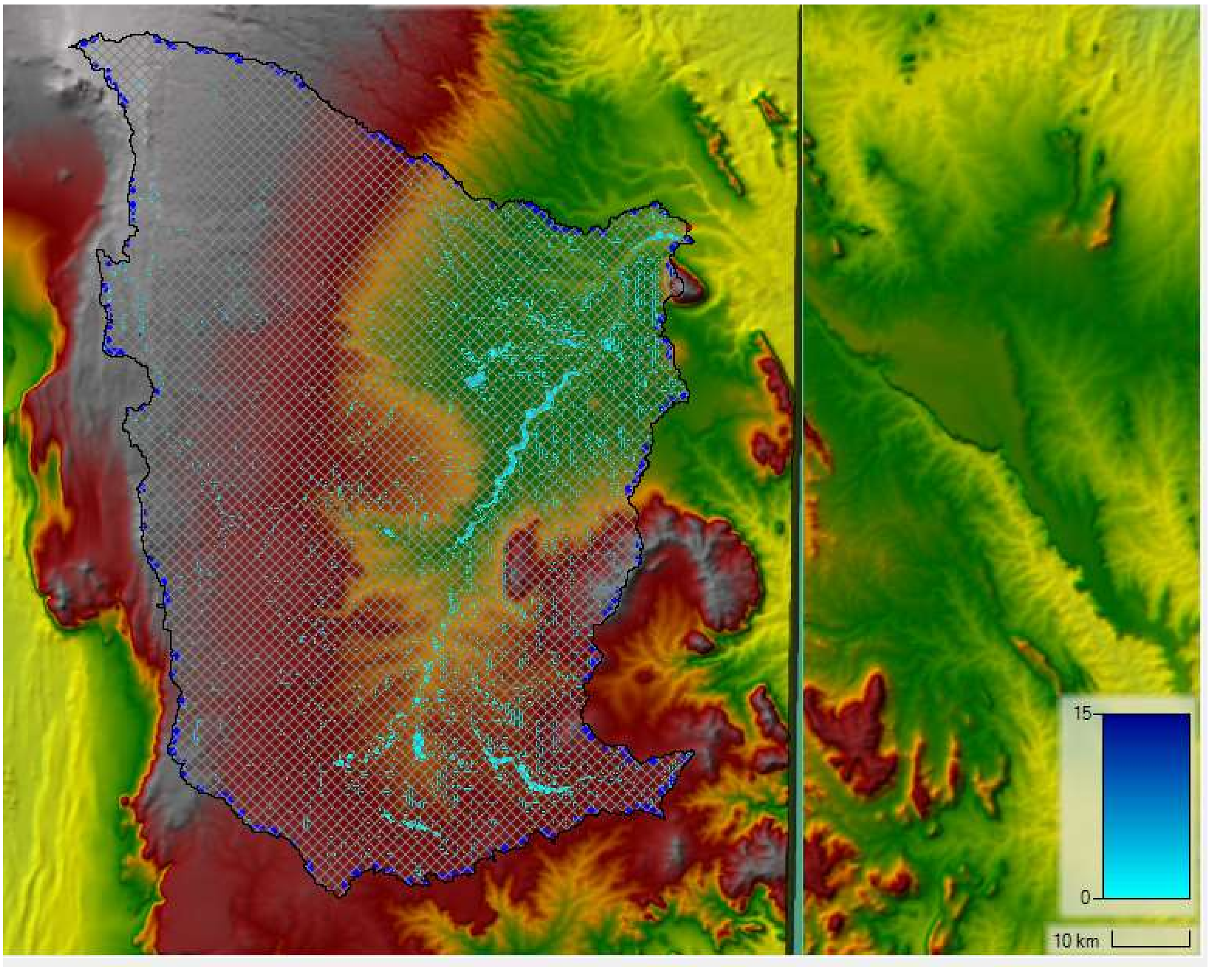

Figure 104. A screenshot from HEC-RAS software showing flood velocity for the S1-Baseline model.

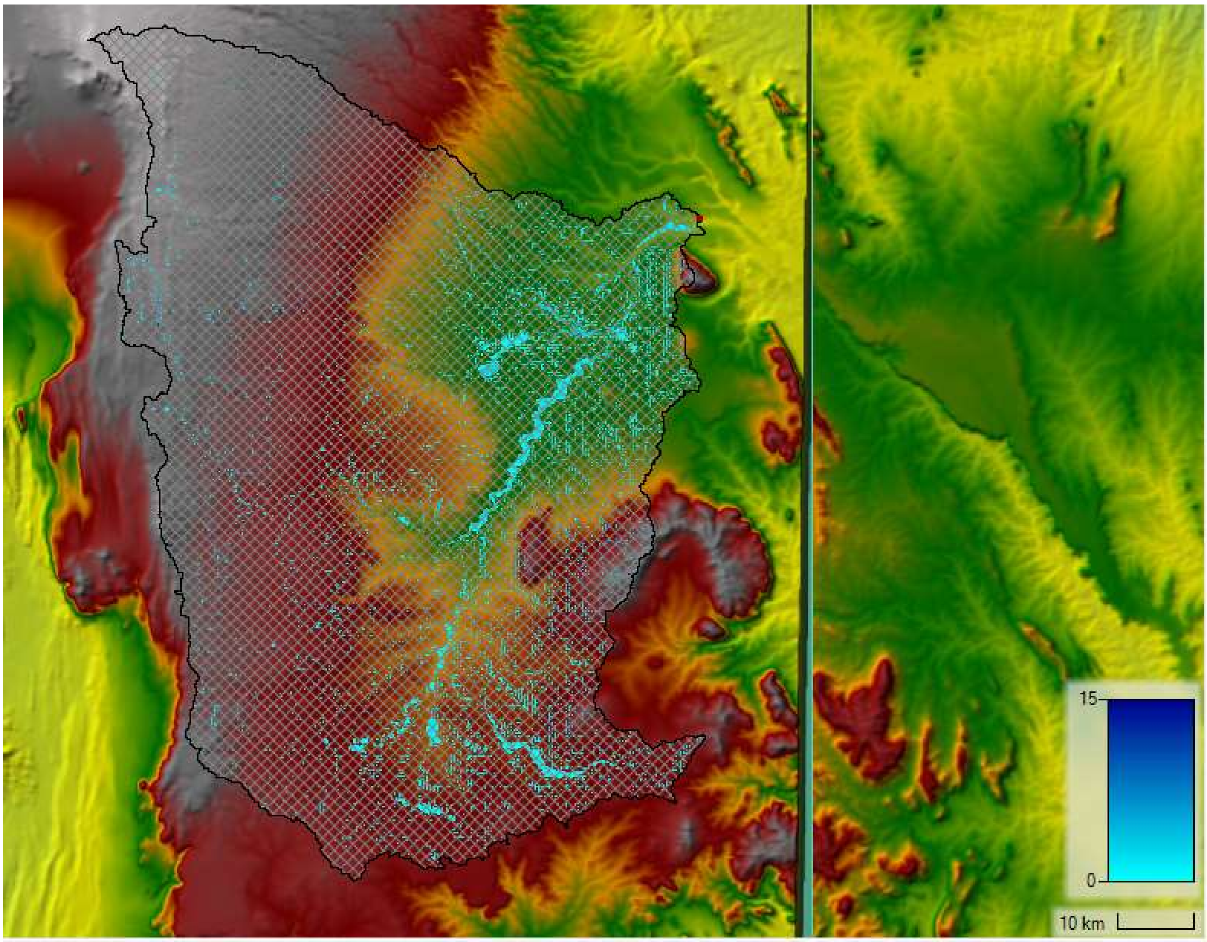

Figure 105. A screenshot from HEC-RAS software showing flood velocity for the S2-2000LU model.

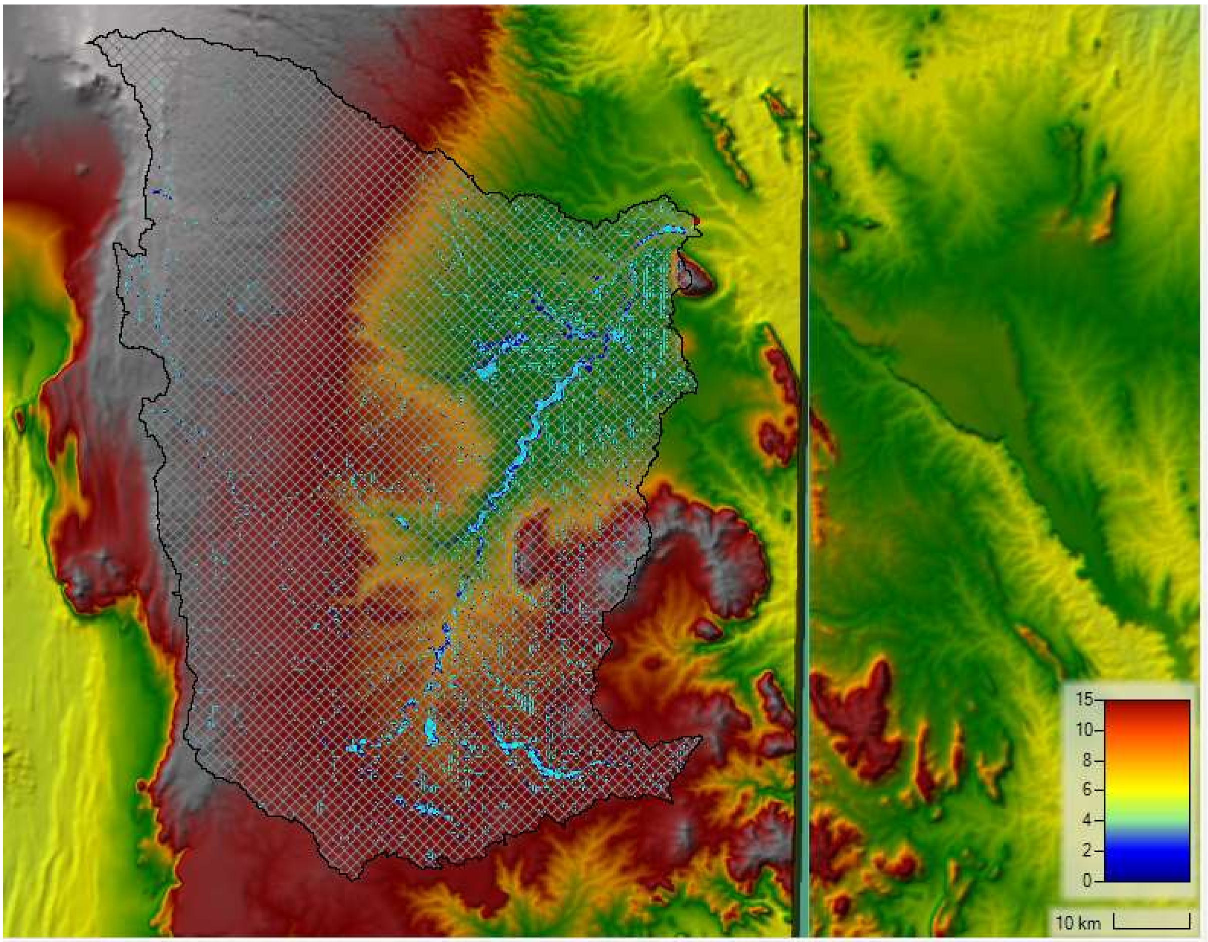

Figure 106. A screenshot from HEC-RAS software showing flood velocity for the S3-CP4uplift model.

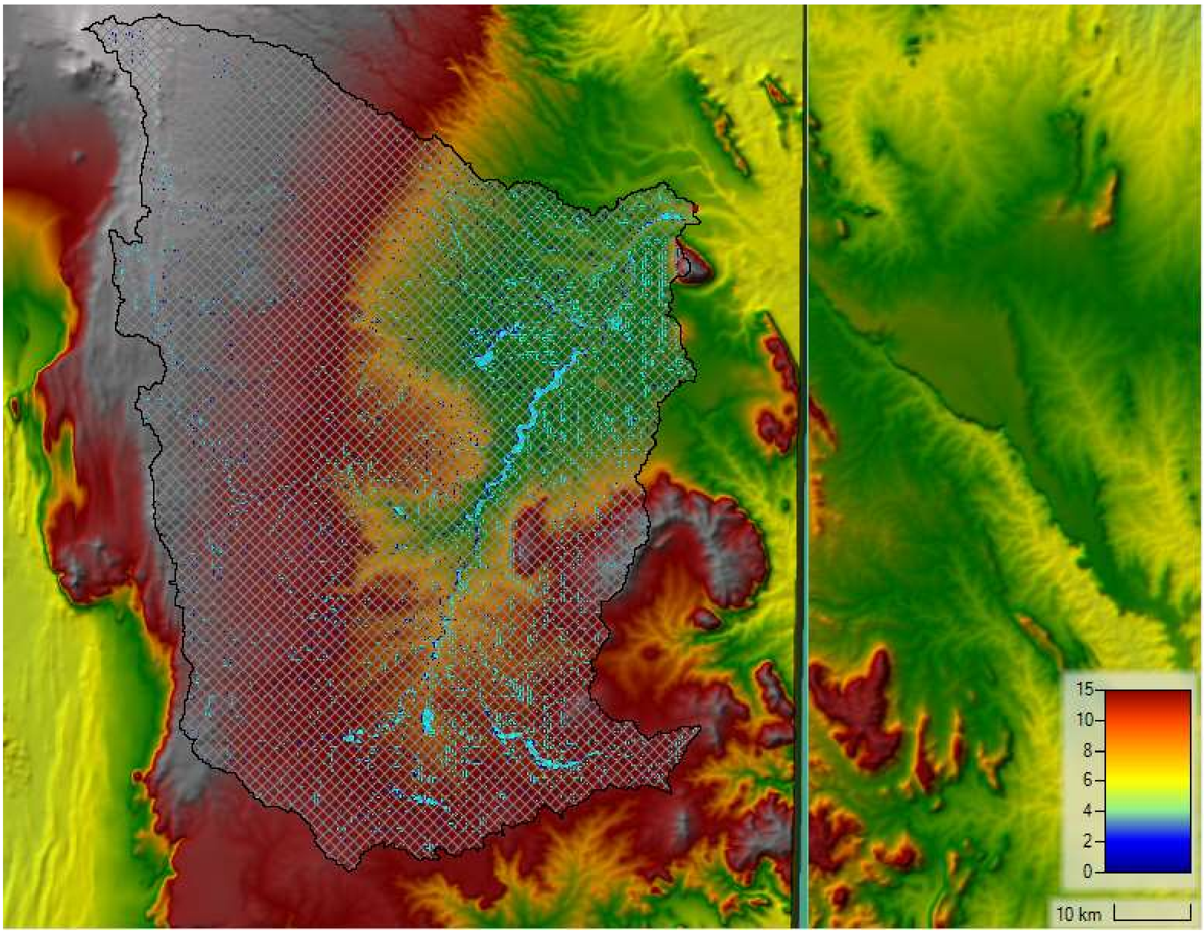

Figure 107. A screenshot from HEC-RAS software showing flood velocity for the S4-P25uplift model.

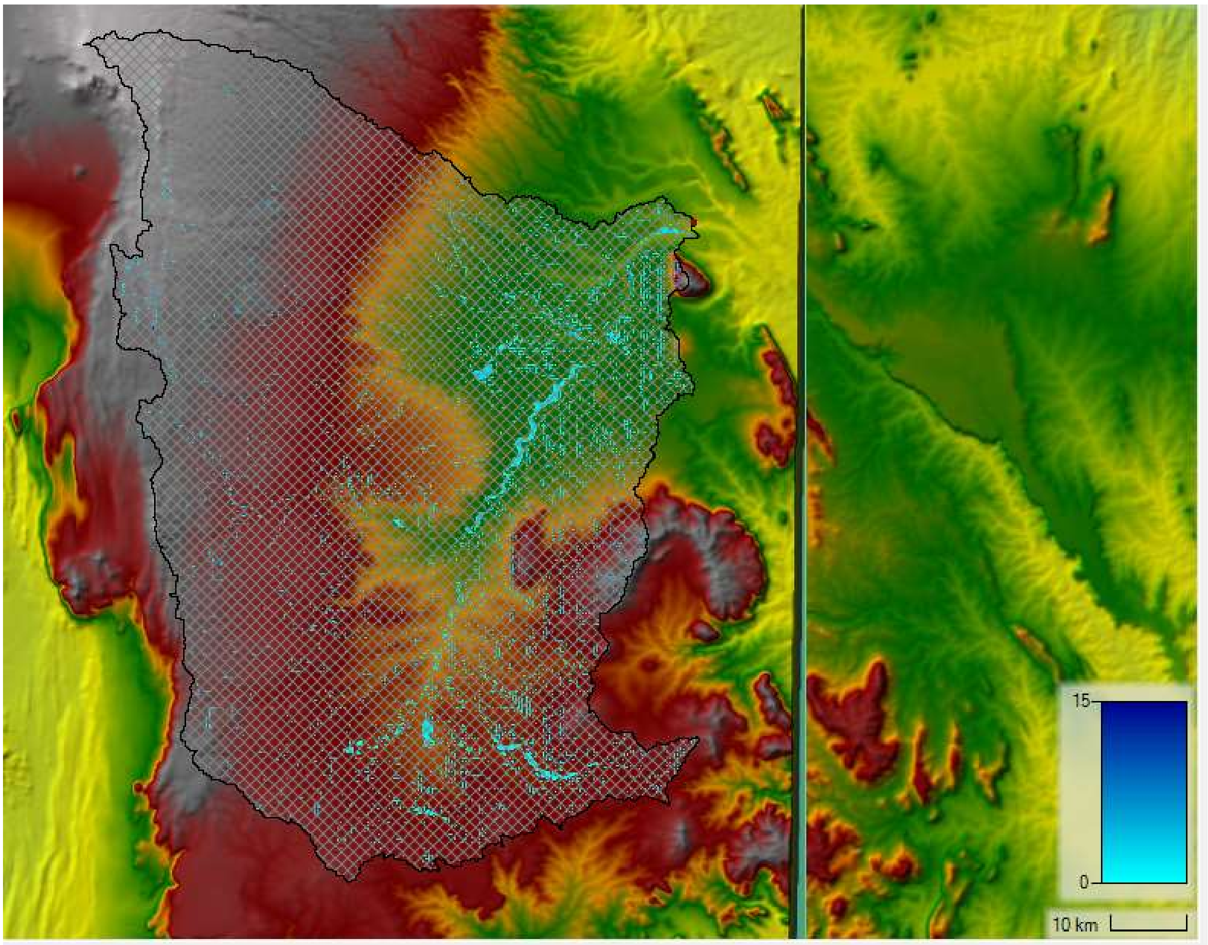

Figure 108. A screenshot from HEC-RAS software showing flood velocity for the S5-RawDEM model.

Table 55: Aim 1: Identification of global datasets and models that could be used for modelling of city scale-pluvial flood hazard in data scarce areas.

Aim 1: Identify global datasets and models that could be used for modelling of city scale-pluvial flood hazard in data scarce areas – (ACHIEVED)		
Objectives	Method	Data
Identify types of data required to build a city scale model	Review literature, attend conferences and workshops, read model documentation.	Journal/conference papers and model manuals.
Identify appropriate, usable global datasets.	Modelled and remote sensing-based sources for: climate change rainfall, digital elevation model (DEM), and urban land use. Create matrix of datasets with pros. and cons.	DEMs: MERIT, ALOS, Tandem-X Precipitation: CP4 and Hycrystal climate output. City change: remotely sensed land use change.
Identify appropriate numerical flood model for city scale urban flood modelling	Identify physical processes that are required in model, and their appropriate application scale. Compare available models for computation speed, and process representation.	HEC-HMS and HEC-RAS hydrologic and hydraulic models.
Select and prepare DEMs for use in a city model.	Process and test available DEMs for use in urban areas. Examine noise error, bias corrections and urban structure artefacts. Test against locally available data (eg Lidar). Process DEM for model input.	ASTER DEM 90m, MERIT DEM, ALOS DEM, NASADEM, Tandem-X DEM.

Table 56: Aim 2: Derivation of urban corrected DEMs with global datasets using Nairobi as a test city

Aim 2: Derive urban corrected DEMs with global datasets using Nairobi as a test city – (ACHIEVED)		
Objectives	**Method**	**Data**
(2.1) Pre-process DEM raster data using Nairobi as a case study.	Process chosen global DEMs (six). Resample all DEMs to 90m resolution and transform DEMs (TanDEM-X 12 & 90m) referenced to the WGS84 (G1150) ellipsoid to EGM96 Geoid using the NOAA's VDatum transformation tool, version 4.0.1 accessible via (https://vdatum.noaa.gov/).	DEM (O1.4), JICA DEM.
Calculate global DEM error	Use QGIS raster algebra tool to calculate the vertical accuracy for the six global DEMs and create error maps. Produce error rasters by subtracting elevations of the JICA reference DEM with higher vertical accuracy.	DEM (O1.4), JICA DEM.
Calculate building density	Process the Facebook high-resolution settlement layer data (HRSL) and the Sentinel-1 SAR urban footprint map to generate building density maps.	Facebook high-resolution settlement 30m layer data (HRSL) LIST building density data.
(2.4) Determine DEM error relationship with building density	Establish a relationship between DEM error and building density by using QGIS tools. Created plots of DEM error versus building density for all six global DEMs.	DEM error maps. Building density maps.
(2.5) Apply error relationship to derive urban corrected global DEM	Remove fraction of vertical error component associated with building density by subtracting the building density error raster from global DEMs.	Original global DEMs Building density error raster.

Table 57. Aim 3: Build and test a city scale urban pluvial flood model with global datasets using Nairobi as a test city

Aim 3: Build and test a city scale urban pluvial flood model with global datasets using Nairobi as a test city **(ACHIEVED)**		
Objectives	**Method**	**Data**
(3.1) Build a city scale model using Nairobi as a test location.	Process chosen datasets (O1.1 & O1.2) for inclusion in chosen model (O1.3), develop and run baseline scenario/s. Examine historical flood events for appropriate baseline model run date/s.	DEM (O1.4), synthetic drainage network (O1.5), Precipitation time series (O1.6). Historical reports of flooding.
(3.2) Collect local data for Nairobi City	Visit city officials and other organisations with Nairobi City to identify and collect relevant local datasets related to urban flooding and drainage with which to test model.	Local city plans, drainage information, flooding hotspots. Rainfall datasets for four stations across Nairobi and environs: Dagoretti, JKIA, Thika, & Machakos.
(3.3) Quantify sensitivity of model behaviour / results to choice of datasets and assumptions made in model build	Vary parameters/datasets in model build (eg DEM urban artefact correction factor/method.) Rerun baseline model and analyse differences in results.	All relevant datasets identified in Aim 1. Test global datasets against locally available data (e.g. rain gauges).
(3.4) Model validation	Comparison of baseline model results with historical flooding observations.	Observations of flooding hotspots recorded by local authorities, news, social media etc. Satellite observations of historic flooding.

Table 58. Aim 4: Test if model is suitable for exploring factors affecting pluvial urban flooding by scenario analysis.

Aim 4: Test if model is suitable for exploring factors affecting pluvial urban flooding by scenario analysis. **(ACHIEVED)**		
Objectives	**Method**	**Data**
Investigating the climate change impacts on pluvial flooding.	Apply uplift factor from future climate rainfall model. Run future climate scenarios and compare to baseline.	Regional Climate Model: CP4 & P25 future climate rainfall datasets for Nairobi. HYCRYSTAL
Investigating the impact of urbanization on pluvial flooding.	Develop a new drainage network for 2030 based on projections of urban growth. Run scenario and compare to baseline.	Globeland30 land use change data capturing urban land transition between 2000 and 2020ization and population growth.